O'Shea, Kerry J. (2010) *Putting a leash on the domain wall: A TEM investigation into the controlled behaviour of domain walls in ferromagnetic nanostructures.* PhD thesis.

http://theses.gla.ac.uk/2123/

# Putting a leash on the domain wall: A TEM investigation into the controlled behaviour of domain walls in ferromagnetic nanostructures

Kerry J. O'Shea MSci

Presented as a thesis for the degree of Ph.D. at the
Department of Physics and Astronomy, University of Glasgow
May 2010

# Abstract

Domain walls may be treated as single entities that can be used to convey bits of information in potential magnetic memory devices such as magnetic logic and racetrack memory, which use controlled domain wall movement in complex magnetic nanowire networks. Greater understanding and control over certain aspects of their behaviour is required, however, before such devices can be realised. The structure of magnetic domain walls in ferromagnetic nanowires is both material and geometry dependent, thus providing an extremely large parameter space to explore. The structure and control of magnetic domain walls in permalloy nanostructures is investigated throughout this thesis using static and pulsed magnetic fields in combination with deliberately fabricated pinning features using Lorentz microscopy.

The effect of an abrupt corner on the structure of domain walls is investigated with the use of a castellated wire geometry. Two different domain wall structures are observed at the corners of the wire, and a completely different domain wall is observed in a straight segment of the wire. Additionally, the reversal behaviour observed is entirely different depending on the direction of the applied field. Reproducibility experiments are also performed to asses the suitability of this geometry for potential use in magnetic memory applications.

The ability to control the behaviour of both vortex and transverse domain walls in nanowires with deliberately fabricated defects is also explored, using a range of domain wall nucleation techniques. The magnetic spin structure of a vortex domain wall is completely different from a transverse domain wall and as a result their interaction with deliberately fabricated pinning sites differs greatly. Both domain wall types possess a chirality or sense of rotation. In wider wires however, transverse domain walls also possess an asymmetry which acts as an additional degree of freedom in the interaction with a trap. The result of both increasing and decreasing the wire width on a domain wall is investigated by patterning a single or double notch or anti-notch along a permalloy wire.

The propagation of a magnetic domain wall along both a gently tapered and straight wire under the application of a pulsed magnetic field is also investigated, where a distorted vortex domain wall structure is observed to form. The distance a domain wall travels following the application of a short field pulse is measured and a lower limit of the velocity is calculated. Additionally, a domain wall is observed to undergo a number of changes in structure and chirality as it is moved along a wire under pulsed fields. The wire edge roughness also has a significant effect on the domain wall propagation velocity and focused ion beam irradiation is utilised to smooth the wire edges.

# Acknowledgements

First and foremost I would like to thank my supervisors Dr. Stephen McVitie and Professor John Chapman for their excellent guidance, support and encouragement over the course of my PhD, for which I am extremely grateful. I would also like say a huge thank you Dr. Damien McGrouther, my third supervisor, for lots of invaluable discussions in addition to the practical assistance towards achieving in-situ resistance measurements.

I would also like to thank Dr. Sam McFadzean for regularly resuscitating the CM20 and ensuring all microscopes were kept up and running. Thanks must also go to Colin How, Billy Smith and Brian Miller for their technical assistance with various pieces of equipment. I would also like to thank Professor John Weaver for lots of useful input and advice, particularly on circuit design. Thanks must also go to Dr. Stephen Thoms and the staff at the JWNC who provided assistance with nanofabrication. I would also like to thank the late Ray Pallester for his invaluable help in designing and constructing the equipment used for the pulsed field experiments in chapter 6.

In addition, I would like to thank Dr. Dorothee Petit, João Sampaio and Huang Zeng from the Imperial College London and Dr. Lara Bogart from Durham University for their collaborative work and helpful input. I would also like to thank Michael Scheinfein for his invaluable help with LLG. The various members of the Spin@RT network must also be acknowledged for providing valuable input in addition to their excellent hosting skills at their respective institutions.

I would also like to thank all SSP group members past and present who have made my PhD experience thoroughly enjoyable! I would like to thank my office mates Paul and Paolo for their entertaining arguments, and more recently Eleonora, LiQiu and Rumy who made the writing up process a lot more enjoyable. I would also like to give special thanks to Dr. Susan Turnbull for her great company, excellent support and generous hospitality.

Finally, I would like to say a huge thank you to my Mum, Leandro and Liam who have provided me with both financial and emotional support over the last few years, well, maybe just the latter in Liam's case! I am forever indebted to you for all your help throughout my education, I really could not have done this without you. Last but not least, I would like to say a massive thanks to Tom whose endless love and support (and lovely presents) have kept me going right until the very end.

# Declaration

This thesis is a record of the work carried out by myself in the Solid State Physics Group of the Department of Physics and Astronomy at the University of Glasgow during the period 2006 - 2010. The work described herein is my own with the exception of the magnetoresistance measurements in chapter 3, which were carried out by Dr. Adekunle Adeyeye at the National University of Singapore. Micromagnetic simulations of the wires containing notches in chapter 4 were performed by Lara Bogart from the University of Durham. Additionally, the fabrication and micromagnetic simulation of the nanostructures studied in chapter 5, were carried by João Sampaio and Dr. Dorothée Petit from Imperial College London.

Some of the work reported in this thesis can be found in the following papers:

1. **'Direct observation of changes to domain wall structures in magnetic nanowires of varying width'**, K. J. O'Shea, S. McVitie, J. N. Chapman and J. M. R. Weaver, Appl. Phys. Lett. 93, 202505 (2008).
2. **'Dependence of domain wall pinning potential landscapes on domain wall chirality and pinning site geometry in planar nanowires'**, L. K. Bogart, D. Atkinson, K. J. O'Shea, D. McGrouther and S. McVitie, Phys. Rev. B 79, 054414 (2009).
3. **'Magnetic imaging of the pinning mechanism of asymmetric transverse domain walls in ferromagnetic nanowires'**, D. Petit, H. T. Zeng, J. Sampio, E. Lewis, L. O'Brien, A-V. Jausovec, D. Read, R. P. Cowburn, K. J. O'Shea, S. McVitie and J. N. Chapman, in press (2010).

This thesis has not previously been submitted for a higher degree.

# Contents

# 1

# Properties of Thin Ferromagnetic Films and Nanostructures

## 1.1 Introduction

The physics of magnetic thin films and nanostructures has become the focus of intense research activity in recent years due to the trend in science and technology towards the miniaturisation of physical structures into the nanoscale. Novel material properties emerge as the structure dimensions become comparable to certain characteristic length scales, such as the magnetostatic exchange length or the domain wall width [1]. At the nanoscale, the magnetic properties of ferromagnetic materials are governed by the geometry of the material in addition to the intrinsic material properties. As a result, it is possible to appropriately engineer the geometry to tailor the domain structure and switching behaviour, which is particularly true in the case of soft magnetic materials where the effect of magnetocrystalline anisotropy is small. Consequently, a magnetic element can be used to form multidomain states with domain walls trapped at specific locations predetermined by the geometry. Different element geometries were used in this thesis to study the nucleation, propagation and stability of domain walls. The following sections will cover the basic concept of ferromagnetism, the effects of the governing energy terms and magnetisation reversal. The concept of magnetoresistance in ferromagnetic materials is also introduced.

## 1.2 Ferromagnetism in thin films

All forms of matter exhibit magnetism arising from the magnetic moments associated with the atoms or ions that comprise the material. A single electron in an atomic orbital resembles a classical current loop with an associated magnetic moment, according to Ampère's theory of elementary molecular currents [2], however in most materials, electrons are paired in their orbitals with opposite spin and their magnetic effects cancel. This type of material is classed as diamagnetic and a weak magnetisation is displayed, with the application of an external field. Any atom or ion with an incomplete shell or subshell of electrons has an uncompensated magnetic moment and is termed paramagnetic [3]. In paramagnetic materials (figure 1.1a), the magnetisation is proportional to an external magnetic field. In ferromagnetic materials however, figure 1.1b, the magnetic moments of the individual atoms/ions interact strongly with each other, which creates a certain degree of order even in the absence of an applied field. This property of ferromagnets makes them the most useful for applications and will be discussed exclusively in this thesis. In addition to ferromagnetism, antiferromagnetism (figure 1.1c) and ferrimagnetism (figure 1.1d) exist as types of magnetic order in solids. Unlike in paramagnetic materials where the atoms only interact with an external field, the atomic moments in ferromagnetic materials interact with each other and possess a spontaneous magnetisation in the absence of an applied magnetic field. In 1907 Weiss [4] described the origin of this interaction in the form of an inner molecular field, $B_i$, which is proportional to the spontaneous magnetisation.

$$B_i = \lambda M \tag{1.1}$$

where $\lambda$ is known as the molecular field coefficient. Heisenberg later explained the nature of this field in the quantum mechanical exchange effect [5, 6], and is described by the Heisenberg exchange Hamiltonian,

$$H_{ex} = -\sum_{i<j} 2J_{ij}\mathbf{S}_i \cdot \mathbf{S}_j \tag{1.2}$$

where $H_{ex}$ is the exchange energy of the sum of pairs of interacting spins, $\mathbf{S}_i$ and $\mathbf{S}_j$, and $J_{ij}$ is the exchange integral and is material dependent. The exchange interaction is discussed further in section 1.3.1.

The magnetisation of a ferromagnet depends on both external field and temperature, as illustrated in figure 1.2. Below a critical temperature, known as the Curie temperature, spontaneous alignment occurs however the material may exhibit little

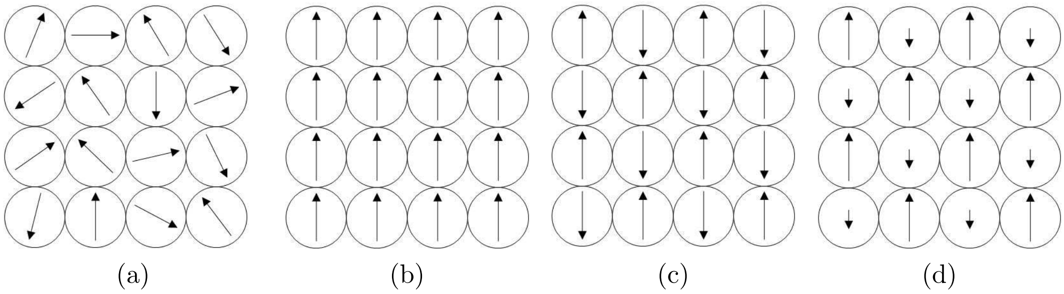

(a) (b) (c) (d)

Figure 1.1: Schematics of the magnetic ordering in (a) paramagnetic, (b) ferromagnetic, (c) antiferromagnetic and (d) ferrimagnetic materials.

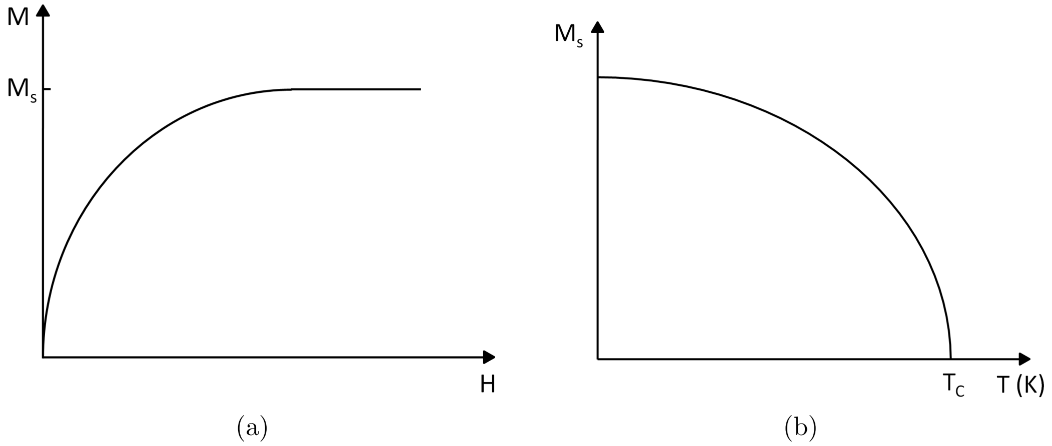

Figure 1.2: Schematic representation of the relationship between magnetisation, M and (a) external field, H and (b) temperature, T.

or no magnetisation. This is due to the material splitting up into regions of uniform magnetisation, referred to as domains and will be discussed further in section 1.3.2. With the application of a magnetic field, the magnetic domains align with the field and increase the magnetisation until saturation occurs at $M_S$, as illustrated in figure 1.2a. Furthermore, the spontaneous magnetisation varies with temperature, which has a maximum value at 0 K and is reduced to zero at the Curie temperature $T_C$, where thermal fluctuations overcome the exchange interaction between the spins and the behaviour becomes paramagnetic. A schematic of the relationship between magnetisation and temperature is given in figure 1.2b. The temperature of a material may increase significantly when performing experiments such as current induced domain wall motion where a high current density (typically ~ $10^{11}$Am$^{-2}$) is passed through a material. In this type of experiment, Joule heating can occur and the material may heat such that the magnetic order is destroyed [7].

## 1.3 Magnetic energy terms

Although ferromagnets possess a non-zero net magnetic moment in the absence of an external field, regions of the material may have very little or no net magnetisation. The reason for this, as mentioned previously, is due to the formation of magnetic domains. The magnetostatic energy is partly responsible for the formation of magnetic domains and is a result of the interaction between the magnetic dipoles within the material and the local magnetic field. The formation of domains however increases the exchange energy which is therefore in direct competition with the magnetostatic energy. These two energy terms govern the domain structures observed in the absence of an external field for a soft magnetic alloy such as permalloy, the material studied in this thesis. Magnetisation processes are also affected by material dependent parameters such as anisotropy and magnetostriction in addition to external magnetic fields. Ultimately, the behaviour of a ferromagnet depends on a number of competing energy terms, described in the following sections.

### 1.3.1 Exchange energy

The Heisenberg Hamiltonian, introduced in the previous section, describes the direct exchange interaction between the atomic spins at lattice sites in metals, and is responsible for the tendency of adjacent spins to align parallel or anti-parallel with one another. The exchange energy is given by,

$$E_{ex} = -\sum_{i<j} 2J_{ij}\mathbf{S}_i \cdot \mathbf{S}_j \tag{1.3}$$

where $\mathbf{S}_i$, $\mathbf{S}_j$ are the neighbouring spins and $J_{ij}$ is the exchange coupling constant. This interaction is responsible for the alignment of neighbouring spins and its value decreases rapidly with increasing distance between atoms. Therefore it is only necessary to consider the exchange interaction between nearest neighbours. Thus the exchange energy contribution for nearest neighbour interactions is

$$E_{ex} = -2JS^2 \sum_{ij} cos\phi_{ij} \tag{1.4}$$

where $S$ is the magnitude of the spin vector and $\phi_{ij}$ is the angle between spins $i$ and $j$. When J is positive, the exchange energy is minimised by a parallel alignment of the adjacent atomic moments, i.e. when $\phi_{ij} = 0$.

### 1.3.2 Magnetostatic energy

The magnetostatic energy arises from magnetic charges at the surfaces of the film or from regions where the magnetisation is discontinuous or divergent. These magnetic charges produce both external and internal sources of field. The external field is referred to as stray field and the internal field is known as the demagnetising field, $\mathrm{H_d}$, and opposes the magnetisation. The magnetostatic field originates from both surface and volume charges, and is expressed as,

$$\mathrm{H_d}(\mathbf{r}) = \frac{1}{4\pi}\int_V \frac{-\nabla \cdot \mathbf{M}}{|\mathbf{r}-\mathbf{r}'|^2} dV + \frac{1}{4\pi}\int_S \frac{\mathbf{M}\cdot\mathbf{n}}{|\mathbf{r}-\mathbf{r}'|^2} dS \tag{1.5}$$

where $\mathbf{n}$ is the outward pointing unit vector, normal to the surface, $\mathbf{r}$ is the position vector for the point at which the field from the charge is evaluated at point $\mathbf{r}'$ in the source. The magnetostatic energy arises from the interaction between the field and the

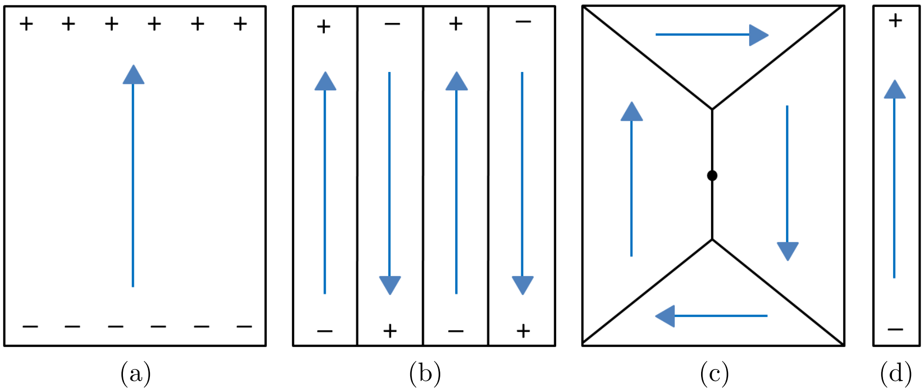

Figure 1.3: Schematic of some of the possible domain configurations in a thin rectangular soft magnetic element. (a) A single domain and (b) a multi domain state with large magnetostatic energy. (c) and (d) flux closure domains and (d) a single domain state induced by shape anisotropy.

magnetisation which it opposes, and is given by,

$$\mathrm{E_d} = -\frac{\mu_0}{2}\int_V \mathbf{M}\cdot\mathbf{H_d}\,dV \tag{1.6}$$

$\mathrm{E_d}$ can be minimised by reducing the amount of magnetic charge that builds up at the edges and surfaces of the material. This is illustrated in figure 1.3 with the example of a theoretical rectangular permalloy element. In the single domain state (figure 1.3a), the exchange energy is minimised with the parallel alignment of neighbouring spins however a large amount of surface charge and associated magnetostatic energy builds up as a result. In reality, this configuration would only be stable under a large magnetic field or if the material possessed a high uniaxial anisotropy. In the absence of these conditions, the system would break up into uniformly magnetised domains, as in figure 1.3b. In this case, the amount of surface charge is reduced at the expense of a significant contribution to the exchange energy. This configuration may be favoured when there is a high uniaxial anisotropy parallel to the long axis of the element. In the absence of a large uniaxial anisotropy, the structure will likely form a flux closure state (figure 1.3c) where little surface charge is generated however an increase in exchange energy is present due to the deviation of spins from a parallel alignment. In figure 1.3d, the shape anisotropy of the element aligns the magnetisation parallel to the long axis and is usually the lowest energy configuration for long magnetic wires in the absence of an external field.

### 1.3.3 Zeeman energy

In the presence of a magnetic field, the moments within a material will attempt to align parallel with the field direction to minimise energy; the different processes by which the magnetisation reversal can occur will be discussed in section 1.5.2. The Zeeman energy describes the effect on the magnetic moments from an externally applied magnetic field, $\mathbf{H_{ex}}$, and is described by

$$E_z = -\mu_0 M_S \int \mathbf{H_{ex}} \cdot \mathbf{m} \, dV \tag{1.7}$$

where $\mu_0$ is the permeability of free space, $\mathbf{m}$ is the unit vector along the direction of magnetisation and is integrated over the volume of material. The Zeeman energy is a minimum for all moments aligned parallel with the direction of external field.

Anisotropy and magnetostriction also affect the behaviour of ferromagnetic materials, however for the permalloy used in this thesis, these effects are minimal. Anisotropy and magnetostriction are fundamental in general magnetic systems however and will be discussed in the following sections.

### 1.3.4 Anisotropy energy

The direction of magnetisation in a material is influenced by the structure of the material and is referred to as anisotropy. Anisotropy energy falls into two categories: magnetocrystalline anisotropy and shape anisotropy. Magnetocrystalline anisotropy is associated with the orientation of magnetic moments with respect to the crystal lattice, however the permalloy studied here has a polycrystalline structure and this effect is negligible. Shape anisotropy arises from magnetostatic effects and is particularly important in patterned magnetic nanoelements as studied in this thesis.

#### Magnetocrystalline anisotropy

Magnetocrystalline anisotropy is caused by the spin-orbit interaction and results in preferred directions for magnetic moments. Atomic orbitals are, in general, non spherical and are linked to the crystal structure which couple to the electron spins and direct the magnetisation along preferred axes within the crystal known as easy axes. To rotate the magnetisation away from the easy axis has an associated energy cost. To align the magnetisation along a hard axis requires the most energy. The anisotropy of hexagonal crystals is a function of only one parameter, the angle $\theta$ between the c-axis and the direction of magnetisation and can be described by the following equation,

$$E_k = \int K_1(1 - m_c^2) + K_2(1 - m_c^2)^2 \, dV \tag{1.8}$$

where $K_1$ and $K_2$ are constants and are temperature dependent and $m_c$ is the direction cosine of the magnetisation along the c-axis. In most hexagonal crystals, the c-axis is an easy axis and in this case $K_1$ is large and positive. If $K_1$ is large and negative however, the easy axis is perpendicular to the c-axis.

In the case of cubic crystals, which posses a higher degree of symmetry, the anisotropy energy can be described by the following

$$E_k = \int K_1(m_a^2 m_b^2 + m_b^2 m_c^2 + m_c^2 m_a^2) + K_2 m_a^2 m_b^2 m_c^2 \, dV \tag{1.9}$$

Where $m_a$, $m_b$ and $m_c$ are the direction cosines along the a, b and c axes, respectively. For Fe, $K_1 = 4.2 \times 10^5$ ergs/cm$^3$ so that the easy axes are along (100), while for Ni, $K_1 = -3.4 \times 10^4$ ergs/cm$^3$ and the easy axes are along the body diagonals (111). These descriptions are only valid however for single crystal materials. The ferromagnetic materials studied in this thesis have a polycrystalline structure with no overall preferred axis. The easy axis of each crystallite is randomly oriented and causes a fluctuation in the magnetisation, a phenomenon known as magnetisation ripple [8]. Despite this, a number of experiments were carried out in the 1950s using thin permalloy films which revealed that applying a large magnetic field during deposition, with or without annealing the sample could induce a uniaxial anisotropy, results of which can be seen elsewhere [9].

### Shape anisotropy

Although most materials display some magnetocrystalline anisotropy, a polycrystalline specimen with no preferred orientation of its grains will display no net magnetocrystalline anisotropy. If the specimen is perfectly spherical, a magnetic field of a fixed value will magnetise the sample to the same extent when applied in any direction. If the specimen is not spherical however, it will be easier to magnetise along a long axis. This phenomenon is known as shape anisotropy and is important for small magnetic elements. When a magnetic element is uniformly magnetised, magnetostatic charges build up at the surfaces and generate sources of external and internal field as introduced previously. The external field is referred to as stray field and the internal field, $\mathrm{H_d}$, opposes the magnetisation. The demagnetising field depends on the material magnetisation and the shape of the element. If we consider an ellipsoid magnetised along its long axis, as depicted in figure 1.4, the resulting magnetostatic charges are separated by a relatively long distance which results in a smaller $\mathrm{H_d}$. When the ellipsoid is magnetised along its short axis however, the magnetic poles are relatively close together, giving a larger $\mathrm{H_d}$ and increasing the anisotropy energy, $\mathrm{E_k}$. The contribution to the anisotropy from the element geometry is given by

$$\mathrm{E_k} = -\int_{\mathrm{V}} \mathrm{K_{eff}} \sin^2\theta \, \mathrm{dV} \tag{1.10}$$

Where $\theta$ is the angle between the long axis and the direction of magnetisation and $\mathrm{K_{eff}}$ is given by

$$\mathrm{K_{eff}} = \frac{1}{2}\mu_0(\mathrm{N_b} - \mathrm{N_a})\mathrm{M_s^2} \tag{1.11}$$

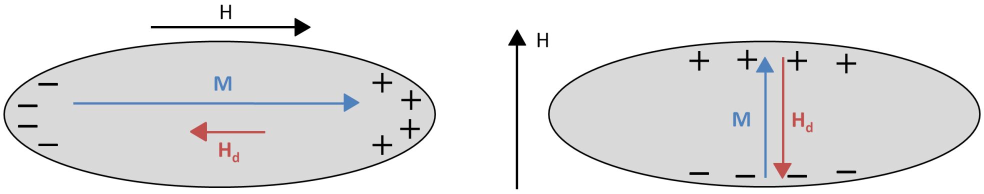

Figure 1.4: A schematic illustration of the demagnetising field that arises depending on whether the ellipsoid is magnetised along the long or short axis. The sizes of the arrows indicate the relative sizes of the demagnetising field.

Where $N_a$ and $N_b$ are the demagnetising factors along the long and short axes, respectively and are geometry dependent. Shape anisotropy is an important factor in the interaction of vortex domain walls with the anti-notches studied in chapter 4. A review of shape effects in elliptical, triangular, square, pentagonal and circular geometries is given in ref [10].

### 1.3.5 Magnetostriction

A change in magnetisation in a ferromagnetic material may also be accompanied by an appreciable change in physical dimensions. This effect is known as magnetostriction and results from a change in separation of adjacent atomic moments. When a crystal of atoms is formed, the electron orbitals lose their spherical symmetry and adopt a shape that reflects the crystal geometry. Given that the atomic moment is dependent on the spin and orbital components of angular momentum, the magnetic properties are affected by the atomic spacing. With the application of an external magnetic field, the atomic moments distort to align with the field which changes the lattice parameters and creates mechanical strain. The magnetostriction, $\lambda$, is defined as the fractional change in length, l, of the material

$$\lambda = \frac{\delta l}{l} \tag{1.12}$$

and has a maximum value $\lambda_S$ known as the saturation magnetostriction and occurs when the magnetisation is saturated in the direction of the applied field. Hence applying a magnetic field to a ferromagnetic material has an associated energy cost, $E_\lambda$, which arises from the induced strain in the material

$$\mathrm{E}_\lambda = \int_V \left(\frac{3}{2}\lambda_S \sigma sin^2\alpha\right) dV \tag{1.13}$$

Where $\alpha$ is the angle between the magnetisation and the stress, $\sigma$, which assumes a mean saturation magnetostriction and small values of $\alpha$. In a similar way, applying strain to a ferromagnetic material changes its magnetisation. For the nanostructures studied in this thesis, magnetostrictive effects were minimal [11].

### 1.3.6 Total energy

The total energy of a ferromagnet is given by summing all the energies discussed in the previous sections

$$\mathrm{E_{tot}} = \mathrm{E_{ex}} + \mathrm{E_{d}} + \mathrm{E_{z}} + \mathrm{E_{k}} + \mathrm{E_{\lambda}} \tag{1.14}$$

A magnetic system will continually attempt to minimise $\mathrm{E_{tot}}$, which often involves the formation of domains in local or global energy minima. The domain structure in zero field depends considerably on the material geometry and properties in addition to the sample history and temperature. When an external magnetic field is introduced, the magnetic state may change irreversibly by domain formation and can be responsible for the material exhibiting hysteresis, as discussed in section 1.5.1.

## 1.4 Magnetic domains and domain walls

The maximum moment of a ferromagnetic material is known as the saturation magnetisation, $\mathrm{M_S}$, and occurs when all the atomic moments are aligned in the same direction by a high enough applied field. After removal of the field, the material may retain a net moment, known as $\mathrm{M_R}$, which is usually significantly lower than $\mathrm{M_S}$. This can be explained by the various energy considerations which cause the magnetisation to break up into magnetic domains. The boundaries separating the domains are known as domain walls and can take various forms depending on the material thickness and competing energies. Within a domain wall the magnetisation rotates coherently from one direction to another typically over a distance in the 1 - 100 nm range.

### 1.4.1 Domain walls in thin films

In bulk materials and thick magnetic films, Bloch type domain walls are favoured where the magnetisation between two anti-parallel domains (known as a 180° domain wall) rotates about an axis perpendicular to the domain boundary, as in figure 1.5a. In this type of wall, the magnetic charges are generated at the surface and are confined to the width of the boundary. Below a critical film thickness (<30 nm [12]) Bloch wall formation becomes extremely energetically costly and Néel walls are more favourable (figure 1.5b). Within Néel walls, the magnetisation rotates about a plane parallel to the plane of the film. Thus the magnetic charges form at the sides of the wall and the stray field is confined within the material. A characteristic difference between domain walls in bulk materials and thin films is the wall width, the width of a Bloch wall scales as the inverse square of the anisotropy constant

$$\delta = \pi\sqrt{\frac{A}{K_U}} \tag{1.15}$$

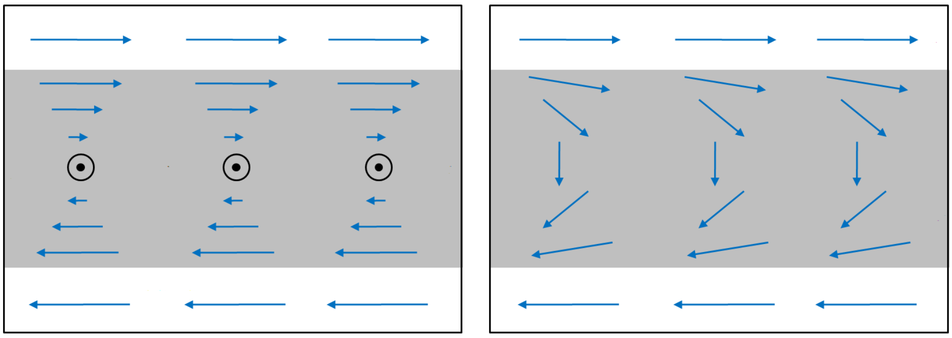

(a) Bloch wall (b) Néel wall

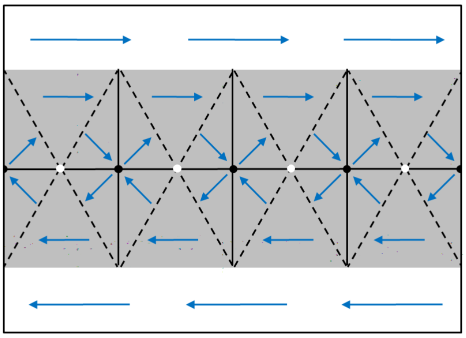

(c) Cross-tie wall

Figure 1.5: Schematic illustration of the typical wall types found in ferromagnetic thin films. (a) Bloch type and (b) Néel type domain walls are favourable in thin films below 50 nm, above this thickness (c) Cross-tie walls are more energetically favourable.

Where $A$ is the exchange stiffness and $K_U$ is the uniaxial anisotropy constant. In thin films the wall width scales as the inverse square of the stray field energy constant

$$\delta = \sqrt{\frac{A}{K_D}} \tag{1.16}$$

Where $K_D = \mu_0 M_S^2/2$ and is known as the stray field energy constant [1]. At intermediate thicknesses a combination of Bloch and Néel wall types can form, known as a cross-tie wall, figure 1.5c. The solid and dashed black lines represent 90° and 45° Néel walls, respectively. The circles represent Bloch lines where the magnetisation is out of plane; black circles are known as cross Bloch lines (cross-ties) and white circles represent circular Bloch lines (vortex cores). The cross-tie wall is a common example of a complicated wall structure occurring as the system tries to minimise the total energy. According to Néel's model [1], a 90° Néel wall has around 12% of the energy of a 180° Néel wall therefore by replacing a 180° Néel wall with a cross-tie wall, the system can save a considerable amount of energy.

## 1.4.2 Domain walls in nanowires

In patterned magnetic structures, the geometry dominates and novel domain wall configurations emerge. In soft magnetic structures, where the magnetocrystalline anisotropy is small, the magnetisation will align with the edges of the element to minimise stray field energy. Hence, in a magnetic nanowire, the magnetisation will align parallel with the wire axis. In the lowest energy configuration the wire will consist of a single domain of uniform magnetisation. With a magnetic domain wall present, the system will comprise two antiparallel domains separated by a 180° head-to-head or tail-to-tail domain wall. The various domain wall configurations that can exist in magnetic wires has been studied by Nakatani et al. [13] where the type of domain wall observed depends on the wire width and thickness (figure 1.6).

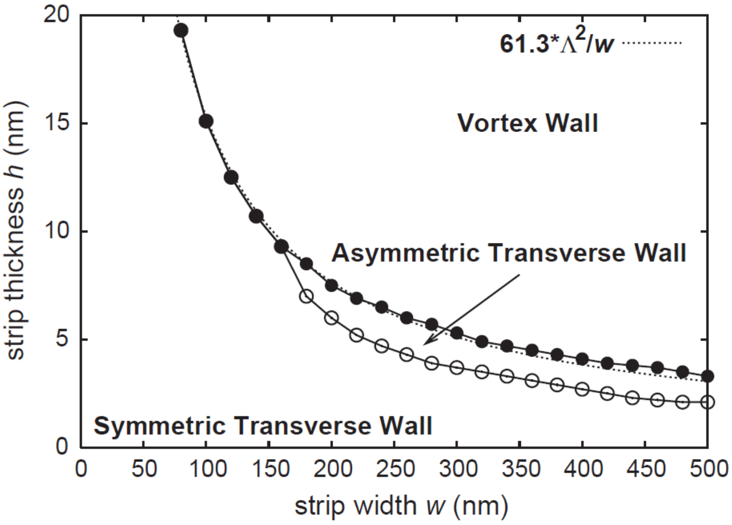

Figure 1.6: Phase diagram of wall types that exist in a planar nanowire of a given width and thickness, taken from Y. Nakatani et al J. Magn. Magn. Mater. **290** (2004).

Figure 1.7 illustrates the wall types introduced by the phase diagram in figure 1.6. The transverse wall comprises, to a first approximation, two 90° walls with the magnetisation in the central domain perpendicular to the wire axis, figures 1.7a,b. As the width or thickness of the wire increases, an asymmetry is introduced in the transverse wall and the central domain has a component of magnetisation parallel to the wire axis, figures 1.7c,d. The vortex domain wall (figures 1.7e,f) consists of three distinct wall sections where the magnetisation rotates about a central vortex core, an out-of-plane magnetisation component.

The structure of the walls described above can be readily transformed into more complex configurations by variations in the wire geometry or by using various external stimuli, such as a magnetic field, spin-polarised current or by thermal activation. A review of head-to-head domain walls in nanowires is given in [14].

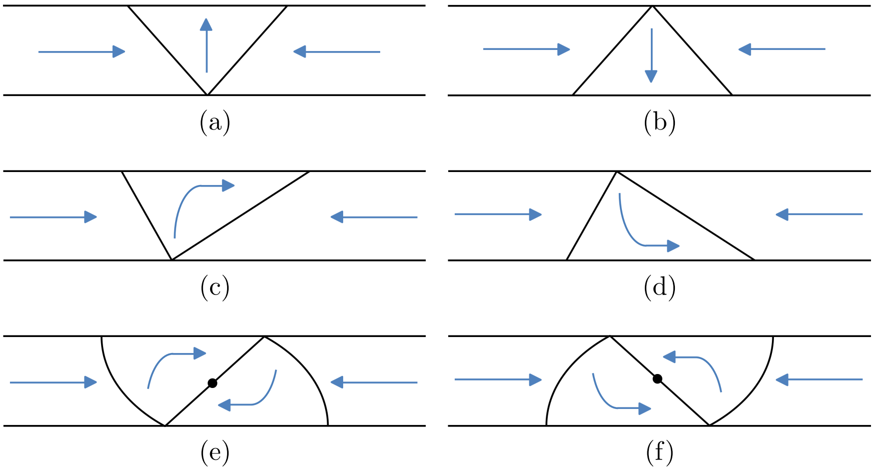

Figure 1.7: Schematic illustration of (a) and (b) transverse domain walls with opposite magnetisation in the central part of the wall, (c) and (d) asymmetric transverse domain walls and (e) a clockwise and (f) a counterclockwise vortex domain wall.

## 1.5 Magnetisation reversal

### 1.5.1 Hysteresis

The magnetic history of a ferromagnet in addition to an applied magnetic field contributes to the magnetisation of a ferromagnet [15]. After deposition, known as the as-grown state, the magnetic moments in a thin film align themselves in such a way that the net magnetic moment is zero. Most magnetic materials fall into one of two classes; either soft or hard magnets. Soft magnetic materials are easily magnetised and demagnetised whereas hard magnets are permanent magnets and require a large field to magnetise them. Ferromagnets may be classified as either hard or soft on the basis of their coercivity; one example of a hard ferromagnet is a NdFeB alloy with a coercivity of the order of 1T. Permalloy has a typical coercivity of 0.04 mT [16]. The coercivity is obtained from the hysteresis loop of a material, an example is given in figure 1.8. With the application of a magnetic field, the material develops a net magnetisation in the direction of the field. At a sufficient field strength, the magnetisation no longer increases and the material reaches saturation, $\mathrm{M_S}$, and all the moments are aligned parallel with the field, $\mathrm{H_S}$. On decreasing the field, the magnetisation also decreases to a value known as the remanence, $\mathrm{M_R}$. A magnetic field in the opposite direction will reduce the magnetisation to zero, the field required to do this is known as the coercivity, $\mathrm{H_C}$. The M-H plot produced as the field is swept in the positive and negative directions is known as a hysteresis loop. The initial increase of M from zero to $\mathrm{M_S}$ is never repeated. The type of hysteresis loop shown in figure 1.8 is known as a major loop as the magnetisation is driven to saturation in both directions. Cycling between smaller field values however, generates a minor loop of which there can exist

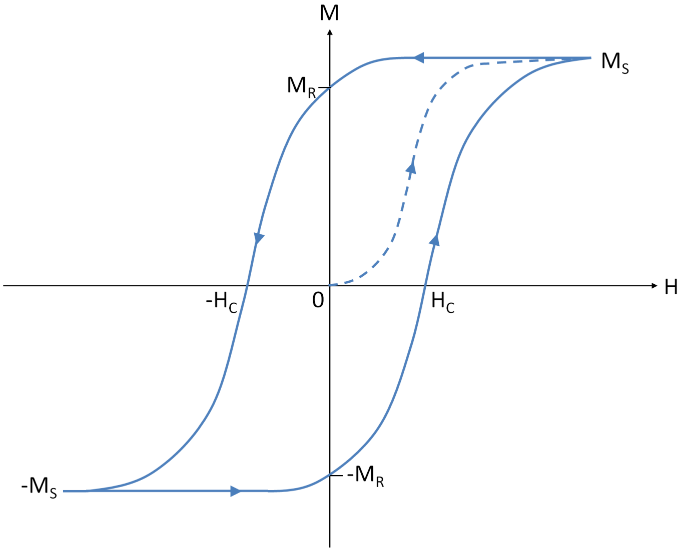

Figure 1.8: Schematic of a typical hysteresis loop for a ferromagnetic material such as permalloy.

an infinite number.

### 1.5.2 Reversal mechanisms

If a magnetic film is placed in a magnetic field, the reversal of the magnetic moments to align with the field may occur by either coherent rotation or by the movement and possible nucleation or annihilation of domain walls. The process of coherent rotation of magnetisation was first presented in a paper by Stoner and Wohlfarth [17] and usually occurs in small single domain particles with uniaxial anisotropy where the introduction of domain walls would cost more energy than spin rotation. It may also be the preferred method of reversal in small elements with no uniaxial anisotropy but with significant shape anisotropy, such as an ellipse. In figure 1.9a, a spherical ferromagnetic particle is given as an example system where coherent rotation of magnetisation is the preferred reversal mechanism. With the applied magnetic field perpendicular to the anisotropy axis, the magnetisation will smoothly rotate to align with the field; the resulting changes in magnetisation are completely reversible. In larger specimens however, it may be more energetically favourable for reversal of magnetisation to occur by the nucleation and subsequent motion of domain walls [18]. In systems comprising multiple domains prior to field application, figure 1.9b, it may not be necessary for the system to nucleate but the existing domains that are favourably oriented with the field will grow at the expense of other domains. At a sufficient field, domains that are unfavourably aligned with the field will be annihilated. The annihilation of domain walls is an irreversible process however the growth/reduction of domains is usually reversible.

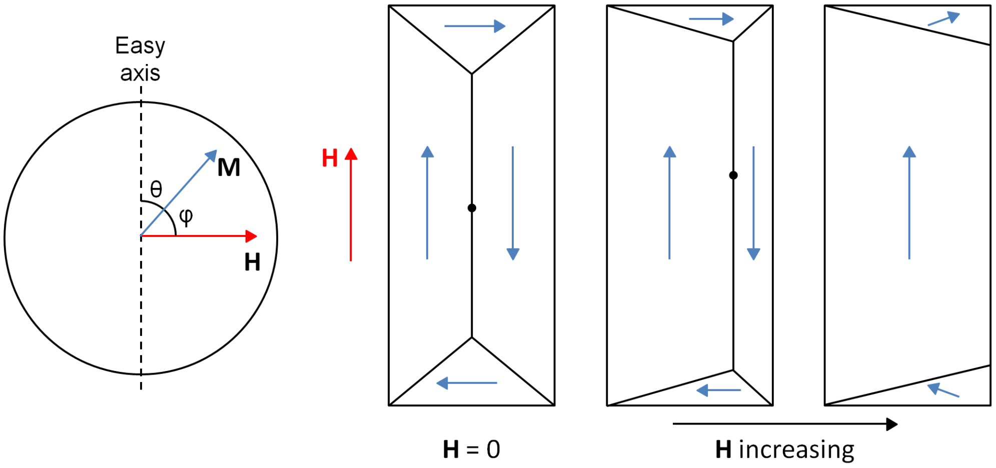

(a) (b)

Figure 1.9: (a) Schematic illustration of a system where reversal of magnetisation occurs by coherent rotation of the magnetisation. (b) Schematic of a system where changes in magnetic structure caused by an external field are irreversible.

## 1.6 Field driven domain wall dynamics

Magnetisation reversal processes that involve the movement of domain walls by the growth/reduction of domains is currently the focus of increased research activity as domain walls may be treated as single entities that can be used to convey information in magnetic storage media, such as magnetic logic [19]. Subsequently, the characterisation of their behaviour under applied magnetic fields is crucial if such devices are to be realised. To compete with other technologies, high speed operation and hence fast domain wall propagation is essential [20]. Domain wall motion in nanowires has only been studied for the past decade and it has been reported that a drastic slowing of domain walls occurs under higher magnetic fields [21–26].

It is well established that domain walls are objects that may be treated as quasi-particles in solids. They propagate under the influence of a magnetic field or electrical current and their motion may be described in terms of velocity and mobility [27]. The velocity-field characteristic of a domain wall in a magnetic nanowire will be discussed here and has two distinct regimes separated by a transition of highly irregular wall motion. The relationship between magnetic field and domain wall velocity is investigated in chapter 6 where a series of short magnetic field pulses were applied to domain walls in long tapered and straight wires.

A key dynamic parameter for magnetic domain wall motion is the wall mobility, $\mu$, which is the rate of change of velocity, $v$ under the influence of an external field, H, and may be written as

$$\mu = \frac{\mathrm{d}v}{\mathrm{dH}} = \frac{\gamma\Delta}{\alpha} \tag{1.17}$$

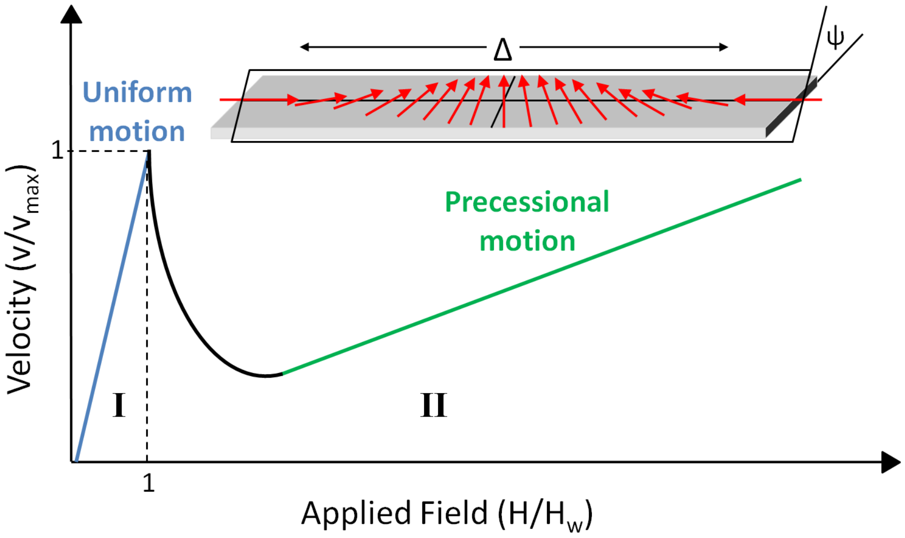

Figure 1.10: Schematic illustration of the two velocity regimes of field driven domain wall motion with inset depicting the wall width, Δ and angle, Ψ.

Where $\gamma$ is the electron gyromagnetic ratio, Δ is the domain wall width and $\alpha$ is the damping parameter. Values of around 30 - 40 ms$^{-1}$ Oe$^{-1}$ are expected for permalloy [28]. A magnetic field applied to a transverse domain wall, for example, in a nanowire will create a torque on the magnetic spins within the central domain of the wall and a component of magnetisation perpendicular to the plane of the wall will be generated. This out-of-plane magnetisation component can be described by an angle, Ψ, as in figure 1.10. For small magnetic fields the domain wall motion is thermally activated and the position of the domain wall changes as successive pinning potentials along the wire are overcome. In this regime, the angle describing the out-of-plane magnetisation component within the wall is constant, i.e. $d\Psi/dt = 0$. Additionally, the domain wall velocity is linearly proportional to the applied magnetic field.

A second regime occurs under applied magnetic fields above the Walker field, $H_w$. Here the stationary value of Ψ is replaced by precessional motion, where $d\Psi/dt \neq 0$. Above $H_w$, Ψ precesses continually leading to oscillatory wall motion and the net average wall velocity decreases with increasing H. When $H >> H_w$, the motion is characterised by a positive linear mobility, similar to that observed in regime I but with a significantly lower value.

$$\mu = \frac{\gamma\Delta}{(\alpha + \alpha^{-1})} \tag{1.18}$$

It has recently been reported that the Walker breakdown process can be suppressed with the application of an in-plane transverse field [29, 30] or by fabricating wires with a certain degree of edge roughness [31]. Another method of suppressing Walker breakdown uses series of transverse arms patterned at regular intervals along the wire [32].

## 1.7 Magnetoresistance

Magnetoresistance refers to the change in electrical resistance of magnetic materials with the application of a magnetic field and was first discovered by William Thomson (Lord Kelvin) in 1851 [33]. Changes in resistance of up to 5% were observed and this discovery was later referred to as Ordinary Magnetoresistance (OMR). More recently giant (GMR) [34], colossal (CMR) [35], anisotropic (AMR) [36] and tunnelling magnetoresistance (TMR) [37] effects have been discovered with larger changes in resistance reported. Only AMR will be discussed here as it forms the motivation for the work in chapter 3.

Many ferromagnetic materials exhibit the anisotropic resistivity effect which is a result of the electron spin-orbit interaction so that the scattering of the conduction electrons is dependent on the orientation of magnetisation with respect to the direction of current flow and is given by the following relation,

$$\rho(\theta) = \rho_0\left(1 + \alpha\cos^2\theta\right) \tag{1.19}$$

Where $\theta$ is the angle between the local magnetisation $\mathbf{M}$ and current $\mathbf{J}$, $\rho_0$ is the resistivity in the absence of AMR and for permalloy $\rho_0 \approx 15$ $\mu\Omega$cm [36] and $\alpha$ is a constant which is between 1 and 5% for permalloy [38]. It follows that a maximum in the local resistivity is observed when there is a parallel or anti-parallel alignment of the current and magnetisation, i.e. when $\theta = 0$. The resistance of a ferromagnetic wire with uniform magnetisation along its length, for example, is at a maximum; the presence of a transverse domain wall will lower the resistance, as the atomic spins within the wall are no longer parallel to the wire axis and hence the direction of current flow, indicated by the red area in figure 1.11. As the thickness of a magnetic film decreases, i.e. as the mean free path of the conduction electrons becomes comparable to the film thickness, the resistivity of the film increases and results from diffuse scattering at the

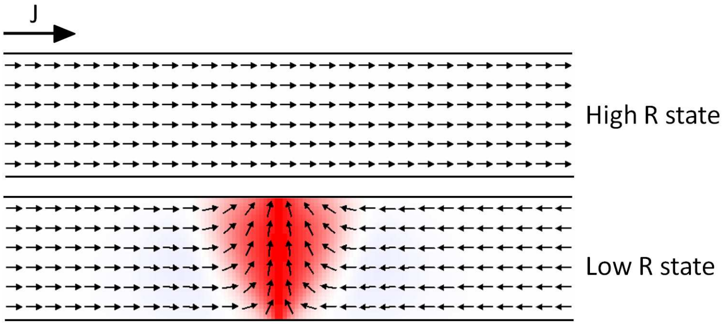

Figure 1.11: Illustration of a high and low resistance state in a ferromagnetic nanowire. The red region indicates the magnetic spins that contribute to the reduction in resistance.

film surface [39]. It has been reported that various film properties, including thickness and grain size and certain preparation dependent parameters including vacuum quality and deposition rate can also affect the magnetoresistance of thin films.

Numerous studies on domain wall resistance (DWR) have been carried out in recent years, which manifests itself as a change in electrical resistance with the presence of one or more domain walls. This effect is of particular interest as it has been predicted to depend on the the structure of the wall, in particular, the wall width [40]. However, at present the sign and magnitude of the DWR is a controversial subject with both positive [41–44] and negative [45–49] values being reported. Positive values of DWR have been predicted by Levy and Zhang [50] and are attributed to spin mistracking during traversal of the rotating magnetisation inside a domain wall. This causes mixing of the spin channels thereby increasing the resistivity and values of a few mΩ have previously been reported. By contrast, it has also been reported that domain walls destroy the electron coherence necessary for weak localisation at low temperature, thus suppressing it. This results in a negative contribution to the resistivity arising from the presence of a domain wall, i.e. negative DWR, and values around 150 mΩ have been reported.

## 1.8 Micromagnetic simulation

Micromagnetic simulation can provide a useful insight into the magnetic behaviour of a given system by allowing the user to simulate various configurations that may be supported as a consequence of the various energy terms in the system. The freely available Object Oriented Micromagnetic Framework (OOMMF) developed at the National Institute of Standards and Technology (NIST) was used in this work [51]. The time dependence of the magnetisation can be obtained directly from the quantum mechanical expression for the precession of magnetisation in a magnetic field,

$$\frac{\mathrm{d}\mathbf{M}}{\mathrm{dt}} = -\gamma \mathbf{M} \times \mathbf{H}_{\mathrm{eff}} \tag{1.20}$$

Where t is the time, $\gamma$ is the gyromagnetic ratio and $\mathbf{H}_{\mathrm{eff}}$ is an effective field,

$$\mathbf{H}_{\mathrm{eff}} = -\frac{1}{\mu_0}\frac{\mathrm{dE_{tot}}}{\mathrm{d}\mathbf{M}} \tag{1.21}$$

Which takes into account the exchange, anisotropy, magnetostatic and external field interactions where $\mathrm{E_{tot}}$ is the total energy of the system. The program evaluates the effective field at each cell in the mesh and the resulting magnetisation by solving the

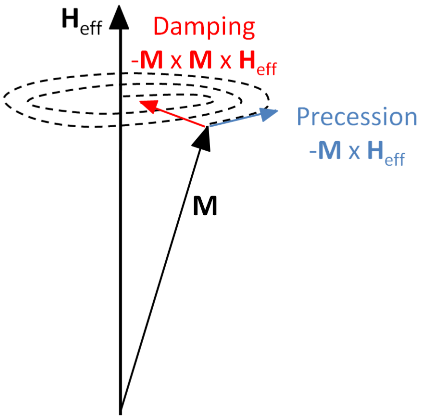

Figure 1.12: Precession of the magnetisation vector **M** around the effective field, $\mathbf{H}_{\mathrm{eff}}$ with damping.

Landau-Lifshitz (LL) equation [52],

$$\frac{\mathrm{d}\mathbf{M}}{\mathrm{dt}} = -\gamma\mathbf{M} \times \mathbf{H}_{\mathrm{eff}} - \frac{\lambda}{\mathrm{M}_{\mathrm{s}}^2}\mathbf{M} \times (\mathbf{M} \times \mathbf{H}_{\mathrm{eff}}) \tag{1.22}$$

Where $\lambda$ is a damping parameter, $\mathbf{H}_{\mathrm{eff}}$ is the effective field and $\mathrm{M}_{\mathrm{s}}$ is the saturation magnetisation. Gilbert proposed a different damping term however to overcome the limitations in the LL equation for ferromagnetic materials with large internal damping to give the Landau-Lifschitz-Gilbert equation (LLG),

$$\frac{\mathrm{d}\mathbf{M}}{\mathrm{dt}} = -\gamma^*\mathbf{M} \times \mathbf{H}_{\mathrm{eff}} + \frac{\alpha}{\mathrm{M}_{\mathrm{s}}}\mathbf{M} \times \frac{\mathrm{d}\mathbf{M}}{\mathrm{dt}} \tag{1.23}$$

With damping coefficient, $\alpha$. The two equations are equivalent provided that $\gamma^* = \gamma(1 + \alpha^2)$ and $\alpha = \lambda/\gamma M_s$. The first term in the equation describes the precession of the magnetisation vector **M** around the effective field, $\mathbf{H}_{\mathrm{eff}}$. The second term describes the dissipation of energy and describes the motion of the magnetisation towards the effective field, $\mathbf{H}_{\mathrm{eff}}$, as illustrated in figure 1.12. With each spin iteration, the equation is re-evaluated until equilibrium is reached. Equilibrium may be defined by a minimum value of the torque, $\mathrm{d}\mathbf{M}/\mathrm{dt}$, typically set to $1 \times 10^{-5}$, or by a limit on the number of iterations or simulation time. This process is repeated with each step-wise increase of the applied field.

An ideal simulation of a nanomagnet would include every atom in the system, realistically however this is not achievable due to constraints on available computing power and time. Instead the nanomagnet may be divided up into a set of discrete 3-dimensional cells of uniform magnetisation. The cell size is an important parameter in determining the outcome of the simulation and is user defined. Typically a cell size close to the exchange length provides realistic results whilst keeping the simulation time to a manageable length. The simulations performed in this thesis used a cell size of 5 nm which is close to the exchange length for permalloy. Additionally, standard material parameters for permalloy were employed throughout, which consist of saturation magnetisation $M_S = 860 \times 10^3$A/m, exchange stiffness $A = 13 \times 10^{-12}$J/m and zero magnetocrystalline anisotropy. A damping parameter of 0.5 was used throughout.

Another factor to be considered is that the cells used in simulations form perfect structures with straight edges and uniform thickness. In reality, element edges will contain a degree of roughness due to limitations of the fabrication process. Such defects are difficult to simulate accurately and must be taken into account when analysing the outcome of a simulation. Finally, the simulations performed here do not take thermal effects into account, which may mean that the field required to depin a domain wall from a constriction, for example, is larger in a simulation than in an experiment performed at room temperature.

## 1.9 Exploiting domain walls in nanowires

Magnetic logic and memory devices rely on the controlled behaviour of magnetic domain walls in complex wire networks under the influence of various external stimuli, such as magnetic field or electrical current. In such devices, information is encoded in the magnetic states of domains; domain wall motion along the wires allows for the access and manipulation of the stored information. A greater understanding over certain aspects of their behaviour is required, however, before such devices can be realised. Key issues include reliable domain wall nucleation, propagation and pinning of domain walls at predefined locations along a nanowire and the ability to reliably depin and annihilate domain walls.

One proposed application for magnetic domain walls in nanowires is a domain wall logic [19] device where a magnetic domain wall is utilised as a mobile interface between two oppositely magnetised domains. The domains themselves form the basis of a binary information representation, whereby a logical ”1” and ”0” are represented by the magnetisation within two oppositely magnetised domains. In such a device, domain walls are moved through a complex network of nanowires by a rotating external magnetic field which acts as both the power source and the clock. Major advantages of using domain walls in such a logic architecture include the production of low power, high speed, and low cost devices with which to build the next generation of computing technology. However, domain wall dynamics are likely to be affected by future miniaturisation, which needs further investigation. Ultimately, the future of magnetic domain wall logic depends on thermodynamic stability in addition to the minimum magnetic field required to power the device, both of which depend on the width of the wires.

Another proposed application for magnetic domain walls in nanowires is magnetic racetrack memory [53]. Tall columns of magnetic material, the racetracks, are arranged perpendicularly on the surface of a silicon substrate and contain a number of magnetic domains to store information. The magnetic domains are separated by a series of head-to-head and tail-to-tail domain walls, the spacing of which controls the bit length. One method of controlling the bit length is the use of artificial pinning sites deliberately fabricated along the wire. Such pinning sites may be introduced by a change in wire dimensions or material properties, for example. In addition to defining the bit length, artificial pinning sites increase the stability of a given domain wall at a pinning site in a nanowire by decreasing the chance of thermal fluctuations or stray fields from adjacent nanowires depinning the domain wall. Magnetic fields are not suitable for driving a series of domain walls along the track as neighbouring domain walls would travel in opposite directions and annihilate one another. Instead, nanosecond current pulses are used to shift the domain walls along the wires. At present, domain walls can be moved under nanosecond long current pulses over a distance of several microns with a velocity exceeding 100 $\mathrm{ms}^{-1}$. Additionally, the direction of motion may be controlled by the sign of the current pulse. Significant challenges still remain however in the development of this technology. These include fabrication of the racetracks normal to the plane of the substrate, reliable motion of a series of 10-100 domain walls along a nanowire and reduction of the critical current density required to move domain walls, whilst maintaining a high velocity. However if the technical challenges for racetrack technology can be overcome, an inexpensive and intelligent 3D memory chip can be built with unsurpassed data storage capacities and no obvious wearout mechanism. Thus, a detailed understanding of the magnetisation dynamics of domain walls and their interaction with deliberately fabricated pinning sites is key for the successful development of racetrack memory.

One of the major challenges associated with all memory devices that rely on the propagation of domain walls is that any physical defects within the wires or material tend to block the propagation of information and thus the performance of the device is also determined by the fabrication quality. Methods for gaining control over the behaviour of domain walls in nanowires are explored in the following chapters, including domain wall nucleation, propagation, pinning and depinning.

# Bibliography

[1] A. Hubert and R. Schäfer, Magnetic Domains, Springer (1998).

[2] D. Jiles, Introduction to Magnetism and Magnetic Materials, Chapman and Hall (1998).

[3] P. Langevin, Ann. Chim. Phys. **5** 70 (1905).

[4] P. Weiss, J. de Phys. **6** 661 (1907).

[5] W. Heisenberg, Z. Phys. **49** 619 (1928).

[6] W. Heisenberg, Z. Phys. **38** 411 (1926).

[7] A. Yamaguchi, S. Nasu, H. Tanigawa, T. Ono, K. Miyake, K. Mibu and T. Shinjo, Appl. Phys. Lett. **86** 012511 (2005).

[8] H. W. Fuller and M. E. Hale, J. Appl. Phys. **31** 238 (1960).

[9] M. Takahashi, J. Appl. Phys. **33** 1101 (1962).

[10] R. P. Cowburn, J. Phys. D: Appl. Phys. **33** R1 (2000).

[11] R. Bonin, M. L. Schneider, T. J. Silva and J. P. Nibarger, J. Appl. Phys. **98** 123904 (2005).

[12] A. Aharoni, An Introduction to the Theory of Ferromagnetism, Oxford University Press (1996).

[13] Y. Nakatani, A. Thiaville and J. Militat, J. Magn. Magn. Mater. **290** 750 (2004).

[14] M. Kläui, J. Phys.: Condens. Matter **20** 313001 (2008).

[15] M. Prutton, Thin Ferromagnetic Films, Butterworths (1964).

[16] Y. Liu, D. J. Sellmyer and D. Shindo, Handbook of Advanced Magnetic Materials, Springer (2006).

[17] E. C. Stoner and E. P. Wohlfarth, Phil. Trans. Roy. Soc. **240** 599 (1948).

[18] D. J. Craik and R. S. Tebble, Ferromagnetism and Ferromagnetic Domains, North-Holland Publishing Co. (1965).

[19] D. A. Allwood, G. Xiong, C. C. Falkner, D. Atkinson, D. Petit and R. P. Cowburn, Science **309** 1688 (2005).

[20] D. Atkinson, D. A. Allwood, G. Xiong, M. D. Cooke, C. C. Faulkner and R. P. Cowburn, Nature Mater. **2** 85 (2003).

[21] G. S. D. Beach, C. Nistor, C. Knutson, M. Tsoi and J. L. Erskine, Nature Mater. **4** 741 (2004).

[22] A. Kunz, IEEE Trans. Magn. **43** 2944 (2007).

[23] J. Y. Lee, K. S. Lee, S. Choi, K. Y. Guslienko and S. K. Kim, Phys. Rev. B **76** 184408 (2007).

[24] E. Martinez, L. Lopez-Diaz, O. Alejos, L. Torres and M. Carpentieri, Phys. Rev. B **79** 094430 (2009).

[25] R. Varga, K. Richter, A. Zhukov and V. Larin, IEEE Trans. Magn. **44** 3925 (2008).

[26] J. Yang, C. Nistor, G. S. D. Beach and J. L. Erskine, Phys. Rev. B **77** 014413 (2008).

[27] A. Mougin, M. Cormier, J. P. Adam, P. J. Metaxas and J. Ferré, EPL **78** 57007 (2007).

[28] S. Konishi, S. Yamada and T. Kusuda, IEEE Trans. Magn. **7** 722 (1971).

[29] M. Bryan, T. Schrefl, D. Atkinson and D. A. Allwood, J. Appl. Phys. **103** 073906 (2008).

[30] S. Glathe, I. Berkov, T. Mikolajick and R. Mattheis, Appl. Phys. Lett. **93** 162505 (2008).

[31] Y. Nakatani, A. Thiaville and J. Miltat, Nature Mater. **2** 521 (2003).

[32] E. R. Lewis, D. Petit, A. V. Jausovec, L. O'Brien, D. E. Read, H. T. Zeng and R. P. Cowburn, Phys. Rev. Lett. **102** 057209 (2009).

[33] S. Chikazumi, Physics of Magnetism, John Wiley & Sons, Inc. (1964).

[34] M. N. Baibich, J. M. Broto, A. Fert, F. N. V. Dau, F. Petroff, P. Etienne, G. Creuzet, A. Friederich and J. Chazelas, Physical Review Letters **61** 2472 (1988).

[35] R. von Hemolt, J. Wecker, B. Holzapfel, L. Schultz and K. Samwer, Phys. Rev. Lett. **71** 2331 (1993).

[36] T. R. McGuire and R. I. Potter, IEEE Trans. Magn. **11** 1018 (1975).

[37] M. Julliere, Phys. Lett. A **54** 225 (1975).

[38] G. Bordignon, T. Fischbacher, M. Franchin, J. P. Zimmerman, A. A. Zhukov, V. V. Metlushko, P. A. J. de Groot and H. Fangohr, IEEE Trans. Magn. **43** 2881 (2007).

[39] K. Fuchs, Proc. Cambridge Philos. Soc. **34** 100 (1938).

[40] M. Viret, D. Vignoles, D. Cole, J. M. D. Coey, W. Allen, D. S. Daniel and J. F. Gregg, Phys. Rev. B **53** 8464 (1996).

[41] T. Y. Chung and S. Y. Hsu, J. Appl. Phys. **105** 07D123 (2009).

[42] R. Danneau, P. Warin, J. P. Attané, I. Petej, C. Beigné, C. Fermon, O. Klein, A. Marty, F. Ott, Y. Samson and M. Viret, Phys. Rev. Lett. **88** 157201 (2002).

[43] J. F. Gregg, W. Allen, K. Ounadjela, M. Viret, M. Hehn, S. M. Thompson and J. M. D. Coey, Phys. Rev. Lett. **77** 1580 (1996).

[44] C. Hassel, S. Stienen, F. M. Römer, R. Meckenstock, G. Dumpich and J. Lindner, Appl. Phys. Lett. **95** 032504 (2009).

[45] N. Giordano and B. Çetin, Phys. Stat. Sol. B **10** 2404 (2004).

[46] T. Nagahama, K. Mibu and T. Shinjo, J. Appl. Phys. **87** 5648 (2000).

[47] U. Rüdiger, J. Yu, S. Zhang and A. D. Kent, Phys. Rev. Lett. **80** 5639 (1998).

[48] G. Tatara and H. Fukuyama, Phys. Rev. Lett. **78** 3773 (1997).

[49] T. Taniyama, I. Nakatani, T. Namikawa and Y. Yamazaki, Phys. Rev. Lett. **82** 2781 (1999).

[50] P. M. Levy and S. Zhang, Phys. Rev. Lett. **79** 5110 (1997).

[51] M. J. Donahue and D. G. Porter, Nistir 6376, Tech. rep., National Institute of Standards and Technology, Gaithersburg, MD (1999).

[52] T. L. Gilbert, IEEE Trans. Magn. **40** 3443 (2004).

[53] S. S. P. Parkin, M. Hayashi and L. Thomas, Science **320** 190 (2008).

# 2

# Sample Characterisation and Fabrication

## 2.1 Introduction

A number of experimental and computational techniques were utilised in this work in order to understand the magnetic behaviour of thin ferromagnetic elements fabricated by electron beam lithography. A description of the various techniques used, from sample preparation to structural and magnetic characterisation by transmission electron microscopy is given in the following sections. The basic principles of a transmission electron microscope (TEM) are described in section 2.2 and the modes of operation used for the structural characterisation are outlined in section 2.3. Various magnetic imaging techniques performed in the TEM, collectively known as Lorentz microscopy, were used to investigate the magnetic behaviour of the structures studied in this thesis, and are discussed in section 2.4. Numerous techniques are available for the fabrication of thin film metallic elements, many of which have origins in microelectronics [1]. Electron beam lithography (EBL) is a sophisticated technique which refers to the transfer of geometrical shapes to a substrate coated with a radiation sensitive substance and was used to fabricate the thin film magnetic elements studied in this thesis; this technique along with the associated processes will be discussed in section 2.5.

## 2.2 The Transmission Electron Microscope

The limit in spatial resolution of an optical microscope is imposed by the wavelength of its illumination. Visible light has a wavelength in the region of 0.5 $\mu$m, allowing optical microscopes to resolve features down to 250 nm at best [2]. A greater resolution is required however to understand the fundamental properties of thin films and consequently electron microscopes were invented in the 1930s to overcome this limit. Modern TEMs are capable of resolving individual columns of atoms in crystals and since their inception have become one of the most efficient tools for the characterisation of materials. The concept of an electron microscope was first proposed by the German physicists Ernst Ruska and Max Knoll shortly after the publication of De

Broglie's famous theory of electron wave-particle duality in 1925 [3]. At this time, it was already known that moving charged particles could be deflected by magnetic fields and the first electron microscope was built in 1931 [4].

The wavelength, $\lambda$, of electrons accelerated by a potential difference, V, is related to their energy,

$$\lambda = \frac{h}{(2m_0eV)^{1/2}} \tag{2.1}$$

where $h$ is Planck's constant and $m_0$ and $e$ are the rest mass and charge of an electron. Modern TEMs typically operate using accelerating voltages in the range 100-300 kV and hence the relativistic kinetic energy of electrons must be taken into consideration; equation 2.1 is modified to become,

$$\lambda = \frac{h}{(2m_0eV(1+\frac{eV}{2m_0c^2}))^{1/2}} \tag{2.2}$$

where $c$ is the speed of light in vacuum. Substituting V = 200 kV, the operating voltage of both of the TEMs used in this work, the wavelength is found to be $\lambda$ = 2.51 pm. Although this wavelength is much shorter than interatomic distances, electron microscopes are not capable of this wavelength limit of resolution due to aberrations in electromagnetic lenses. The drive for better resolution however has meant that since the mid-1970s, commercial TEMs have been capable of resolving individual columns of atoms in crystals with magnifications of several million times [5].

### 2.2.1 The electron source

Electrons are produced in the TEM by two methods: thermionic or field emission. The two microscopes used in this work, a FEI T20 and Philips CM20, use a thermionic and a field emission source respectively. Thermionic emitters, typically tungsten and $LaB_6$, produce electrons when heated sufficiently to overcome the work function of the material. Field emission sources utilise an electric field to extract electrons from the source material. In a field emission gun (FEG) the source material is typically a tungsten needle acting as a cathode with respect to two anodes. The first anode extracts the electrons and the second accelerates them down the microscope column. With field emission, the tip must be free of contaminants which can be achieved by operating under high vacuum conditions ($<10^{-11}$ Torr) and is referred to as cold-field emission. Alternatively, heating the tip acts to preserve its pristine condition and is a process known as Schottky-field emission.

Two useful characteristics of an electron source are the brightness and spatial coherence. The brightness is defined as the current density per unit solid angle of the source and the spatial coherence is related to the source size. The extremely small source size associated with a FEG means that the beam is highly spatially coherent, the current

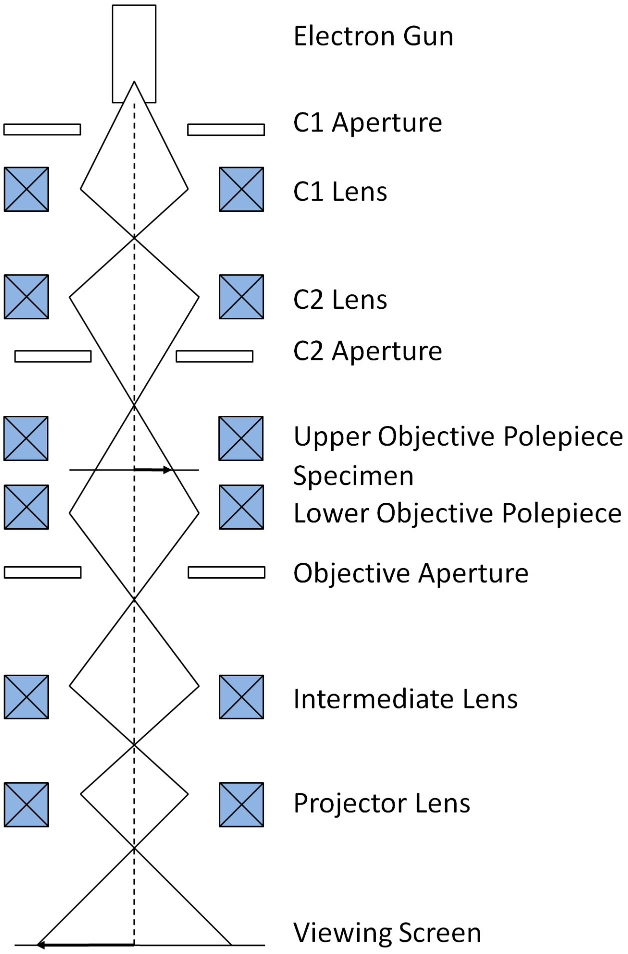

Figure 2.1: Schematic of a typical CTEM column illustrating the positions of the various electromagnetic lenses and apertures used to form an image.

density is extremely large and the brightness is correspondingly high. FEGs are particularly well suited to imaging techniques that require a small probe as in analytical and scanning microscopy. One example is differential phase contrast (DPC) imaging which was used to image the magnetic behaviour of specimens in this thesis and will be described in section 2.4.3. In the case of Fresnel imaging however, the use of a FEG over a thermionic source will not provide significant improvements to the image quality.

### 2.2.2 The microscope column

In a conventional TEM (CTEM) such as the FEI T20, electrons from the gun enter the condenser system which acts to control the electron intensity, spot size and convergence at the sample, with the use of a series of magnetic lenses and apertures, as illustrated in figure 2.1.

The electromagnetic lenses in a TEM are responsible for all the basic operational functions of the instrument, for example, magnifying and focusing the electron beam, the images and diffraction patterns. Magnetic electron lenses are made up of an iron core called a polepiece with a hole drilled through it known as the bore. Most lenses contain an upper and lower polepiece, separated by a gap, each surrounded by a coil of copper wire to provide a magnetic field when a current is passed through it. Electromagnetic lenses contain imperfections however, which limit the resolution of the microscope. Spherical aberration is the key limiting aberration in an electron microscope at high resolution and arises from an inhomogeneous lens field which acts to focus off-axis electrons more strongly than on-axis rays. The result is that the further off-axis an electron is, the more strongly it is bent towards the axis. As a result, a point object is imaged as a disk of finite size surrounded by a series of diffraction rings which limits the resolution of the system and the ability to magnify detail. The effect of spherical aberration can be ignored with Lorentz imaging however as the lens defocus dominates with Fresnel imaging and is responsible for determining the resolution of the system. In the case of DPC imaging, the finite size of the probe, dictated by the condenser system and upper twin lens, is the limiting factor in resolution and not spherical aberration.

On leaving the gun, the condenser lenses are the first lenses encountered by the electron beam. The C1 lens forms a demagnified image of the gun crossover which acts as the object of the illumination system. The user controllable lens, C2, alters the intensity of the illumination by varying the convergence angle of the beam. The C1 aperture controls the spot size of the beam incident on the sample and the C2 aperture defines the maximum convergence angle of the beam. C2 apertures are situated below the condenser lens system and have a diameter typically ranging from 20 $\mu$m to 200 $\mu$m; selecting a smaller aperture provides a beam with greater coherence but reduced current.

In a CTEM, the specimen is situated between the upper and lower polepieces of the objective lens. This is the main imaging lens and determines the resolution of the microscope. Electrons from the condenser system enter the upper polepiece of the objective lens system and are incident on the specimen. Below the objective lens, a series of intermediate and projector lenses are present to further magnify and project the image onto the viewing screen. The intermediate lens is responsible for selecting the mode of operation of the microscope (discussed in section 2.3.1).

### Image acquisition

All electron microscopes must have the capability to detect electrons that have been scattered by the specimen. All electron detectors translate the variations in the scattered electron wavefunction to intensity variations that can be observed by the operator. In CTEMs a viewing screen is usually present at the bottom of the microscope and is coated with a scintillator material which emits light when an electron strikes its surface. In addition to a viewing screen, digital detectors are also used in electron microscopes, the most common being a charge-coupled device (CCD). A scintillator plate, fibre-optically coupled to the CCD, converts the electron beam energy to photons which are sent to the CCD chip. Images captured by the camera are sent to a computer screen for automatic viewing.

## 2.3 Structural characterisation

The two most fundamental operations performed in a TEM are the formation of an image and diffraction pattern. TEM imaging provides information on the size and shape of grains present in a specimen. Electron diffraction provides information on the composition and texture of a specimen and is particularly useful for characterising specimens that are not perfect crystals. Both of these techniques were used to characterise the structures in this work.

### 2.3.1 Diffraction

If two plane waves are incident, at an angle $\theta$, on a set of parallel planes with Miller indices ($hkl$), they will be reflected at an equal angle and may arrive out of phase at the observation point. The path difference between two such waves is 2dsin$\theta$. For constructive interference to occur (i.e. in-phase arrival of the two plane waves), the path difference must be equal to an integral number of wavelengths,

$$\mathrm{n}\lambda = 2\mathrm{d}\sin\theta \tag{2.3}$$

where n is an integer and $\lambda$ is the wavelength of the electrons. In polycrystalline specimens, exclusively studied in this thesis, all possible orientations of crystallites are present and the diffraction pattern consists of concentric rings, figure 2.2a. It can

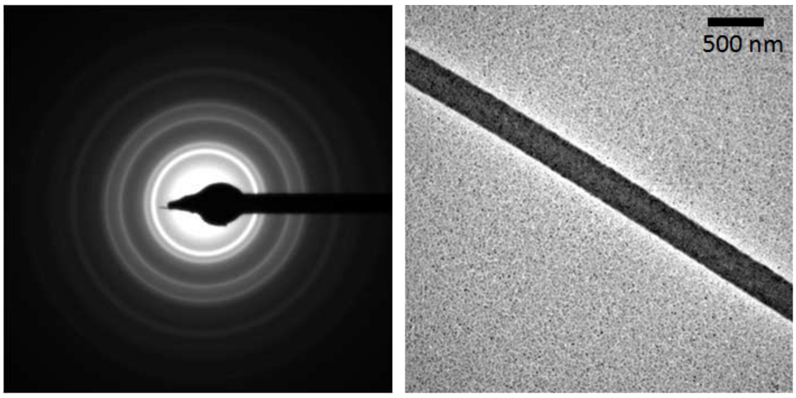

(a) (b)

Figure 2.2: (a) An example diffraction pattern obtained in a CTEM from a 20 nm thick permalloy nanowire and (b) corresponding bright field image.

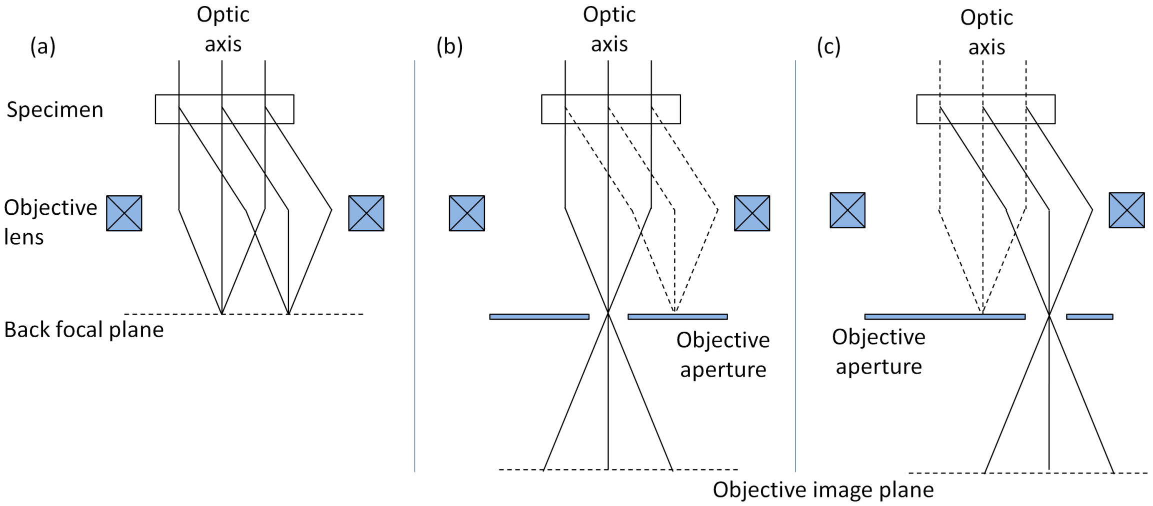

Figure 2.3: Schematic of (a) diffraction, (b) bright field and (c) off-axis dark field imaging modes.

be seen that most of the intensity is in the centre of the pattern, indicating that the majority of electrons are not scattered and travel directly through the specimen. As the scattering probability decreases with angle, the intensity of the rings decreases with distance from the centre of the diffraction pattern. The diffraction pattern may be viewed by changing the strength of the intermediate lens so that the back focal plane of the objective lens becomes the object plane of the intermediate lens, figure 2.3a.

### 2.3.2 Bright and dark field imaging

A diffraction pattern projected onto the viewing screen consists of a bright central spot containing the direct electrons and some scattered electrons and can be used to perform the two most basic imaging operations in the TEM. An image can be formed in the TEM using either the central spot or using some or all of the scattered electrons. Images formed from the bright central spot are known as bright field images; an example is given in 2.2b of a 20 nm thick permalloy nanowire with a thin layer of gold on the surface of the wire and surrounding film. Contrast in the image arises as a result of variations in electron scattering across the specimen. The permalloy wire causes a greater scattering of electrons than the surrounding film, hence the wire appears darker in the image, figure 2.2b. Within the wire, electrons are Bragg scattered from the crystallites that make up the material and grains that appear dark in the bright field image are those that satisfy the Bragg condition.

By inserting an aperture into the back focal plane of the objective lens, most of the diffraction pattern can be obstructed and thus an image is formed using only the fraction of the beam selected by the aperture. A bright field image is produced if the direct beam is selected as discussed above (figure 2.3b); if only scattered electrons are used, a dark field image is produced (figure 2.3c). Dark field imaging is particularly useful for imaging specimens with large variations in mass and thickness as greater electron scattering occurs from thicker areas or from materials with a high atomic number. The electrons selected by the aperture in figure 2.3c travel off-axis and consequently suffer abberations and astigmatism. In order to avoid this, the beam must be tilted onto the specimen at an angle equal to the Bragg angle. The scattered electrons will now travel down the optic axis and this operation is known as centred dark field imaging. Dark field imaging was not often used in this work; bright field imaging and diffraction were the main techniques used for the structural characterisation of the specimens studied in this thesis.

## 2.4 Magnetic imaging

The Philips CM20 FEG TEM/STEM was used for the magnetic characterisation of the samples in this work. This instrument has been optimised for magnetic imaging [6]. In a CTEM, the specimen is situated between the upper and lower polepieces of the objective lens, immersing the sample in a magnetic field of up to 2T. This magnitude of field is sufficient to destroy the magnetic state of most specimens. In the CM20, two additional mini-lenses have been inserted to replace the function of the objective lens and thus create a field-free environment for imaging magnetic specimens in both the Fresnel and differential phase contrast (DPC) imaging modes. The gap between the objective lens pole-pieces has also been widened to allow specialised rods to be inserted such as a magnetising stage (see section 2.4.5). This microscope also has a scanning capability used for the DPC mode of Lorentz microscopy, discussed in section 2.4.3. An 8-segment detector has been fitted below the projector lenses for DPC imaging in addition to a CCD camera for CTEM experiments.

### 2.4.1 Lorentz microscopy

Lorentz microscopy [7, 8] is the name given to a collection of imaging techniques, performed in a TEM, that rely on small deflections of electrons on passing through a magnetic material. These deflections are a result of the Lorentz force and are used to generate contrast in a magnetic sample. Lorentz microscopy was the main technique used for the characterisation of domain walls in magnetic nanostructures in this work. The interaction of electrons with a magnetic specimen can be described by both classical and quantum mechanical approaches as illustrated in the following sections.

#### Classical approach

In Lorentz microscopy, contrast is generated by the deflection of electrons on passing through a magnetic material with a component of induction perpendicular to the elec-

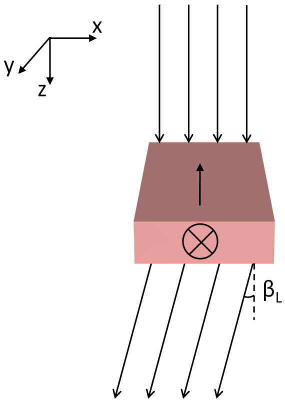

Figure 2.4: Schematic of the deflection of electrons by the classical Lorentz force.

tron trajectory. Electrons travelling along the z-axis through a sample with an in-plane magnetisation, as in figure 2.4, will experience deflection in the x-direction by an angle $\beta_L$,

$$\beta_L(x) = \frac{e\lambda}{h}\int_{-\infty}^{\infty} B_y(x,y)dz \tag{2.4}$$

where $B_y(x,y)$ is the y-component of induction at point $(x,y)$, $e$ is electronic charge, $\lambda$ is the electron wavelength and $h$ is Planck's constant. For a uniform film of thickness $t$, with uniform saturation magnetisation $(M_S)$, the deflection angle can be simplified to

$$\beta_L(x) = \frac{eB_S t\lambda}{h} \tag{2.5}$$

where $B_S$ is the saturation induction $(B_S = \mu_0 M_S)$. The Lorentz deflection for a permalloy film of thickness 20 nm is of the order of 12 $\mu$rad which is significantly smaller than a typical first order Bragg angle around 10 mrad [9].

### Quantum mechanical approach

The classical description above is sufficient to qualitatively explain the principles of Lorentz microscopy however a quantum mechanical approach, using the Aharonov-Bohm effect [10], is necessary where quantitative magnetic information is to be extracted. The quantum mechanical approach is required, for example, when calculating magnetic images as the transfer function of the TEM must be included. This is not possible using the classical approach. Electrons travelling along different paths, $\mathrm{p}_1$ and $\mathrm{p}_2$ as depicted in figure 2.5, will experience a phase shift, $\phi_{\mathrm{m}}$, given by

$$\phi_m(\mathbf{r}) = -\frac{e}{\hbar}\int_{-\infty}^{\infty}(\mathbf{A}\cdot\hat{\mathbf{n}})\mathrm{dz} \tag{2.6}$$

where $\hat{\mathbf{n}}$ is the unit vector parallel to the beam and $\mathbf{A}$ is the magnetic vector potential given by

$$\mathbf{A}(\mathbf{r}) = \frac{1}{4\pi}\iiint\frac{\nabla\times\mathbf{B}(\mathbf{r}')}{|\mathbf{r}-\mathbf{r}'|}\mathbf{d}^3\mathbf{r}' \tag{2.7}$$

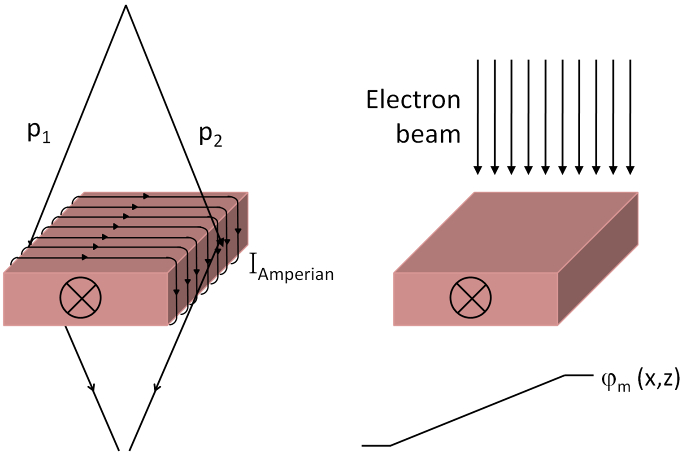

Figure 2.5: Schematic illustration of the interaction of electrons with a bar magnet from a quantum mechanical approach. The associated Ampérian current is also illustrated.

It may be shown that for a beam at normal incidence and in the presence of Ampérian current density only, ignoring conduction and displacement current densities,

$$\phi_m(\mathbf{r}) = -\frac{e\mu_0}{4\pi\hbar r} \otimes \int_{-\infty}^{\infty} (\nabla \times \mathbf{M}) \cdot \mathbf{n}\, \mathrm{d}z \tag{2.8}$$

where r = $|\mathbf{r}|$. Furthermore, assuming the film lies in the xy-plane, the beam is incident along the z-direction and the magnetisation is uniform through the film thickness, $t$,

$$\phi_m(\mathbf{r}) = -\frac{e\mu_0 t}{4\pi\hbar r} \otimes (\nabla \times \mathbf{M}(\mathbf{r})) \cdot \hat{\mathbf{z}} \tag{2.9}$$

This relation can therefore be used to interpret the Lorentz image intensity in relation to the sample magnetisation in Lorentz microscopy, which may also be considered as Ampérian current microscopy [11]. Figure 2.5 also illustrates the Ampérian current associated with a bar magnet with in-plane magnetisation. An additional phase change, $\phi_\mathrm{e}$, will occur regardless of whether the specimen is magnetic and is electrostatic in nature. This arises due to variations in either the thickness, $t$, or in the mean inner potential of the specimen and may be written,

$$\phi_e = \pi \frac{Vt}{\lambda E} \tag{2.10}$$

Where $V$ is the inner potential of the material, 21 V for permalloy, $t$ is the film thickness, $\lambda$ is the electron wavelength and $E$ is the electron accelerating voltage. The total phase change is therefore the sum of the two phase contributions,

$$\phi(\mathbf{r}) = \phi_\mathrm{m} + \phi_\mathrm{e} \tag{2.11}$$

Lorentz microscopy is therefore a branch of phase contrast microscopy and the various modes (including Fresnel, DPC, Foucault) represent different methods of capturing the phase change of an electron beam on passing through a magnetic specimen. Only Fresnel and DPC imaging were used in this work and are described in the following sections.

### 2.4.2 Fresnel imaging

The Fresnel mode of Lorentz microscopy is a powerful technique used to image domain walls in thin ferromagnetic films. In this technique, the main imaging lens is defocused taking its image object from a plane a distance $\Delta$ above or below the sample plane. As illustrated in figure 2.6, electrons passing through an in-plane magnetised film containing 180° anti-parallel domains are either converged or diverged in neighbouring domains. This results in regions of increased or decreased electron intensity at the positions of the domain walls, whilst the domains themselves appear with near-uniform electron intensity. An example of a vortex domain wall in a permalloy nanowire is given in figure 2.6 where a Fresnel image is given at two different defocus values. The central 180° Néel wall and bright vortex core are clearly visible in the centre of the wire; the two darker lower angle sidewalls are just visible at either side of the central 180° wall. To the left of the wall, there is a dark fringe that runs along the lower edge of the wire, disappears at the wall, and runs along the upper edge of the wire to the right of the wall. This indicates that there is a head-to-head magnetisation configuration either side of the wall. The contrast at the edge of the wire is not purely magnetic contrast and is discussed in more detail in section 2.4.6. Comparing the

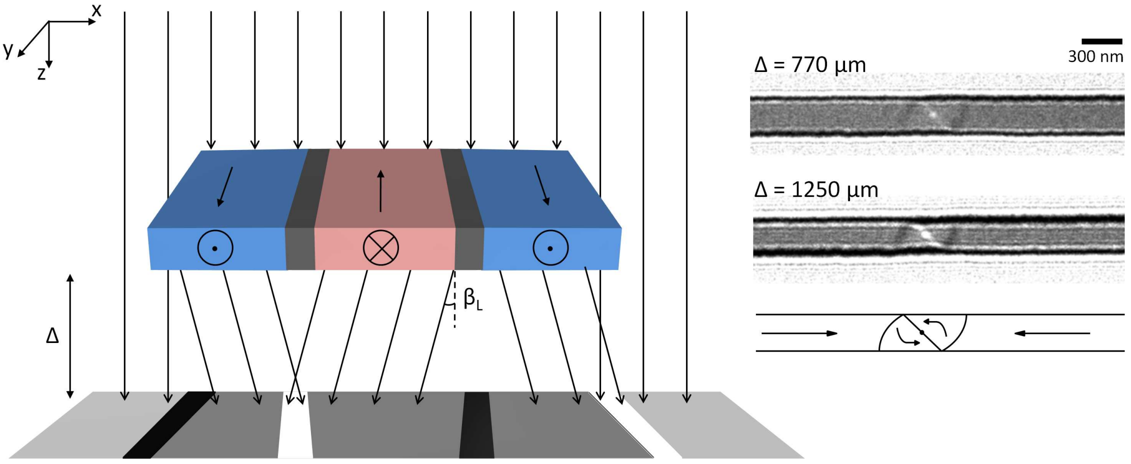

Figure 2.6: Schematic illustration of the Fresnel imaging mode. The main imaging lens is defocused a distance $\Delta$ above or below the specimen plane to reveal contrast at the positions of domain walls and at the edges of the element. Inset shows two Fresnel images of a vortex domain wall at different values of $\Delta$.

Fresnel images at different values of defocus given in figure 2.6, it can be seen that using a larger defocus increases the magnetic contrast, however the image resolution is reduced and hence a compromise must be made in order to maximise the magnetic contrast whilst preserving the image detail. As the dimensions of magnetic elements decrease, imaging the magnetic structure becomes more difficult as a result of limited resolution arising from defocus added to the electrostatic phase which can mask the magnetic contrast. Furthermore, Fresnel imaging is generally considered to be a non-linear imaging technique meaning that quantitative information is difficult to obtain. Recent work however has shown that phase reconstruction is possible using an in focus image and an image either side of focus [12–15].

### 2.4.3 Differential Phase Contrast imaging

The differential phase contrast (DPC) mode of Lorentz microscopy [16] is an effective technique that produces quantitative information on the magnetic induction of thin films. This imaging mode provides a greater spatial resolution than Fresnel imaging as the images acquired are in-focus. In this mode, the microscope is operated in scanning mode and the beam is focused to a small probe. The electron beam is raster scanned

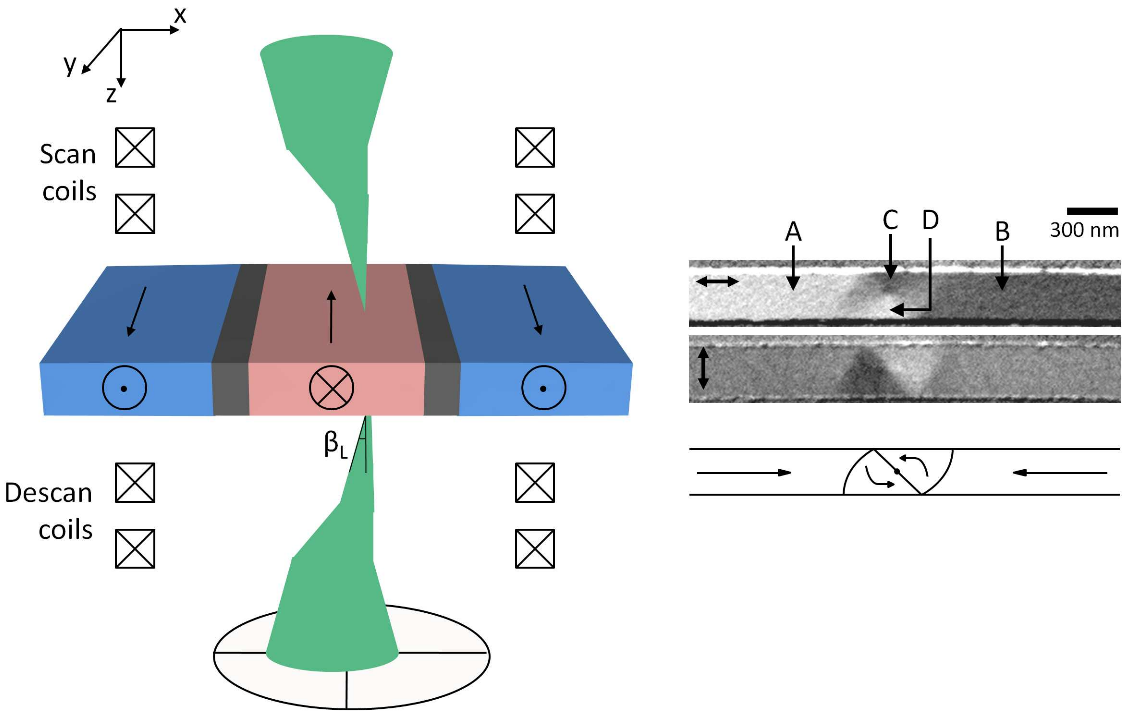

Figure 2.7: In the DPC mode of Lorentz microcopy, the beam is focused to a small probe and is raster scanned across the specimen. The emergent beam will be deflected by angle $\beta_L$ due to the Lorentz force and is not centred on the detector. Taking difference signals from opposite quadrants on the detector provides information on the magnetic induction in the sample. Inset shows an example of a vortex domain wall in a permalloy wire.

across the sample by a set of scan coils and emerges as a cone of illumination which subsequently falls onto a segmented detector, as illustrated in figure 2.7. With a non-magnetic specimen in the path of the beam, the emergent beam remains centered on the detector. When a magnetic sample is placed in the path of the beam however, the Lorentz force deflects the electrons and the emergent beam is not centered on the detector. This results in different signal levels on each of the four quadrants. The deflection of the beam is measured by taking difference signals from opposite sides of the detector, to obtain pairs of images of integrated orthogonal magnetic induction perpendicular to the electron trajectory. A bright field image is also obtained by summing the signals from all four quadrants. Thus the parallel acquisition of magnetic and physical images of the specimen can be achieved. Figure 2.7 shows a pair of orthogonal DPC images of a vortex domain wall in a permalloy nanowire. The uppermost image shows an induction map along the x-axis where it can be seen that the wire is much brighter to the left of the domain wall at position A and darker to the right of the wall at B. This indicates a head-to-head magnetisation either side of the wall.

Within the wall, the intensity level at position C is the same as that at position B indicating both sections are magnetised from right to left. Similarly, the intensity level at positions A and D are comparable indicating both sections are magnetised from left to right. Intensity also appears within the wall with a grey level similar to that of the surrounding film, indicating there is no x-component of induction in these regions. This is confirmed by the lower image where bright and dark regions appear at these positions, indicating a y-component of induction.

The spatial resolution of the images produced is limited by the diameter of the

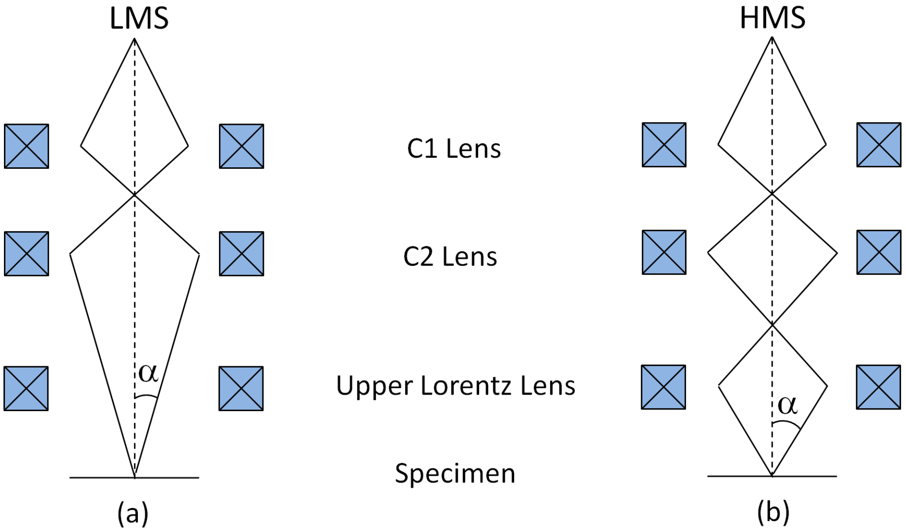

Figure 2.8: Schematic of the high magnification scanning (HMS) and low magnification scanning (LMS) modes. In LMS, the upper Lorentz lens is switched off to form a larger probe at the specimen; in HMS the Upper Lorentz lens is switched on to achieve a smaller probe at the specimen.

probe. This varies depending on the mode of operation, either low magnification scanning (LMS) or high magnification scanning (HMS). LMS was used to image the castellated nanostructures in chapter 3 as it provides greater sensitivity (and higher contrast) to changes in magnetic induction than HMS. As illustrated in figure 2.8, the upper Lorentz lens is switched off in LMS resulting in a larger probe at the specimen and a probe convergence angle, $\alpha$, of around 150 $\mu$rad. In HMS mode, the upper Lorentz lens is switched on to form a smaller probe with a larger probe angle, around 1 mrad. The achievable probe size in LMS mode is better than 50 nm; a probe size <10 nm can be achieved with HMS. Sufficient magnetic information was obtained from the LMS images of the castellated structures in chapter 3 which had a width of 200 nm, therefore HMS was not used for the structures in this work.

### 2.4.4 In-situ magnetising experiments

In addition to imaging the magnetic state of thin magnetic structures, dynamic experiments were also performed by applying magnetic fields in-situ, achieved by weakly exciting the objective lens. This method of field application was routinely used to nucleate domain walls and to drive them from one stable position to another within a magnetic element, for example from a nucleation pad to a notch. The field could then be easily removed and the remanent state imaged. A vertical magnetic field, $\mathbf{H}$, is produced around the sample when a user variable electrical current flows through the objective lens coil, figure 2.9. The direction of the field, either up or down, depends on the direction of current flow through the coil, termed the forward or reverse directions, respectively. With the sample in the horizontal position, the applied field is completely out-of-plane, by tilting the sample by an angle $\theta$, an in-plane component of magnetic field is introduced denoted by $\mathbf{H}_{\parallel}$

$$\mathbf{H}_{\parallel} = \mathbf{H}\sin\theta \tag{2.12}$$

The maximum field that can be applied, at $\theta = 90°$, is determined by the objective lens current and can have a value up to around 7000 Oe. One issue associated with this

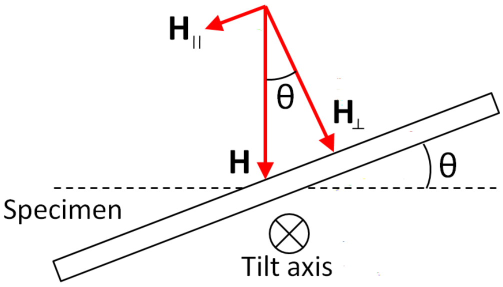

Figure 2.9: Tilting the specimen with the objective lens on introduces parallel and perpendicular components of magnetic field around the specimen.

method is that the perpendicular component of field, $\mathbf{H}_{\perp}$, is also present and may lower the in-plane field required to reverse a particular structure.

### 2.4.5 Pulsed magnetic field experiments

In addition to static magnetic fields, pulsed magnetic fields were also applied to specimens in-situ using a custom designed magnetising stage. This method is particularly useful for generating a large number of statistics in a relatively short time and can provide useful information on the reliability of a specific process. Applying a series of magnetic field pulses to a domain wall can provide information on certain aspects of its behaviour including the propagation field, stopping distance and stability. This magnetising stage was used to characterise the behaviour of domain walls in long wires in chapter 6. The magnetic field is produced by passing a current through a pair of gold wires situated 100 $\mu$m below the sample plane, a schematic is shown in figure 2.10. Using an Agilent Function Generator, arbitrary waveforms of a given frequency and amplitude can be generated which control a 100 A power supply connected to the spec-

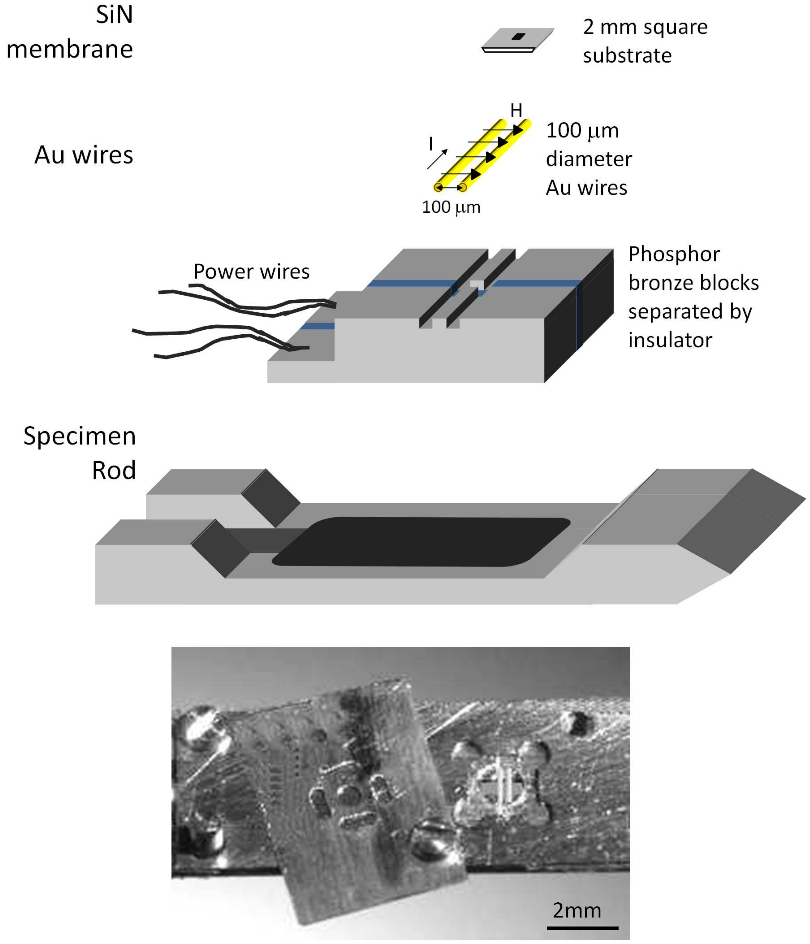

Figure 2.10: Schematic of the various components comprising the specimen end of the magnetising TEM rod with a photograph of the assembled endpiece.

imen rod. Magnetic field pulses of up to around 200 Oe can be applied to the specimen with this set-up, provided the duty cycle is small (1% or lower). The minimum pulse length achievable with this set-up is around 0.1 $\mu$s however at this duration the pulse shape is significantly distorted; the maximum pulse length is 5 $\mu$s. When performing experiments with this TEM rod, the objective lens can still be weakly excited and used as a static field source however the direction of this field is orthogonal to the field from the gold wires.

### 2.4.6 Lorentz image calculation

Micromagnetic simulation packages enable realistic structures to be calculated which, when compared with experimental images, may provide a useful guide for interpreting experimentally observed complex magnetic configurations. One example of this can be seen in chapter 4 where complex magnetic configurations were observed during the interaction of vortex domain walls with anti-notches. The precise magnetic configuration observed was clarified with the aid of micromagnetic simulations. From the results of a given simulation, Fresnel and DPC images may be calculated providing certain microscope parameters are known.

The Lorentz interaction of an electron beam with a magnetic sample is the basis for the generation of contrast in Lorentz microscopy. To recall, the phase is given by

$$\phi_m(\mathbf{r}) = -\frac{e\mu_0}{4\pi\hbar r} \otimes \int_{-\infty}^{\infty} (\nabla \times \mathbf{M}) \cdot \mathbf{n} \, \mathrm{d}z \tag{2.13}$$

A schematic illustration of the phase shift for a magnetic and a non-magnetic sample is given in figure 2.11. The finite width of the domain walls has been neglected and the magnetic phase is represented by a simple triangular wave. For a non-magnetic specimen, the phase shift depends on the sample shape and thickness variations; a rectangular element of uniform thickness is shown in figure 2.11.

The calculation of Lorentz images involves the magnetic phase which includes a convolution between two functions. In real space this is difficult to compute, however in Fourier space the calculation is made easier since a convolution is represented by a straight multiplication of the Fourier transforms of the two functions. Consequently, all image calculations were performed using the Fast Fourier Transform algorithm available in Digital Micrograph™. Scripts were used to calculate the magnetic electron phase, using the algorithm proposed by Mansuripur [17], and were written by Dr. Stephen McVitie and Mr. Gordon White at the University of Glasgow. The calculation of DPC and Fresnel images from the electron phase will now be discussed.

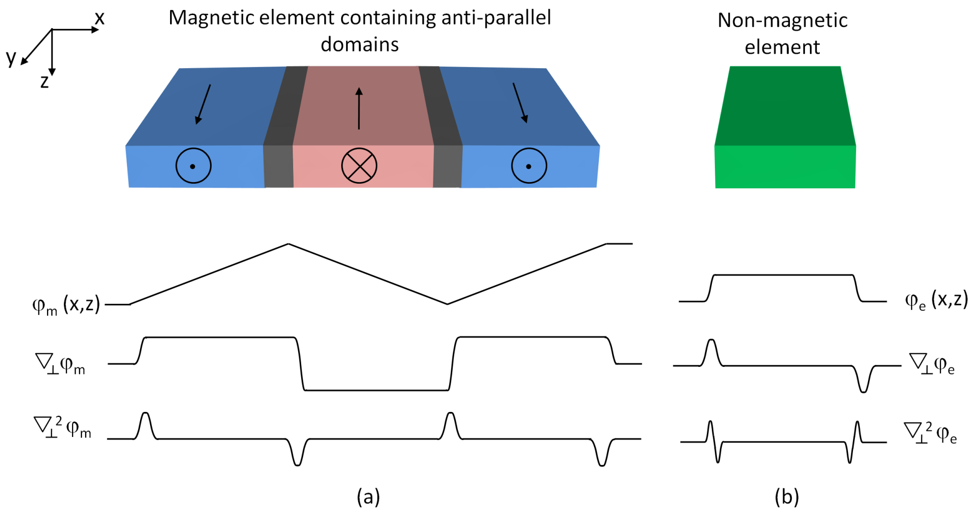

Figure 2.11: Illustration of the phase change electrons undergo on passing through (a) a magnetic and (b) a non-magnetic specimen. The derivative of the phase and the Laplacian, for a small defocus value, are given below.

### DPC image calculation

In differential phase contrast microscopy, the beam is raster scanned across the sample and an image is formed by a segmented detector that converts phase changes into intensity variations. The DPC signal is found by taking the 2D derivative of the electron phase perpendicular to the electron beam,

$$\nabla\phi_m(\mathbf{r}) = -\frac{e}{\hbar}\int_{-\infty}^{\infty}(\nabla\times\mathbf{A})\times\hat{\mathbf{n}}dz \tag{2.14}$$

where $\mathbf{A}$ is the magnetic vector potential and $\hat{\mathbf{n}}$ is the unit vector parallel to the electron beam. Since $\mathbf{B} = \nabla\times\mathbf{A}$, this may be rewritten as,

$$\nabla\phi_m(\mathbf{r}) = -\frac{e}{\hbar}\int_{-\infty}^{\infty}(\mathbf{B}\times\hat{\mathbf{n}})dz = -\frac{2\pi}{\lambda}\beta_L \tag{2.15}$$

Therefore we can say that the DPC image is related to the integrated magnetic induction perpendicular to the beam. Figure 2.11 illustrates the derivative of the phase shift for both a magnetic and non-magnetic specimen along the x-direction. In the case of the magnetic film, a positive phase gradient is observed in the outermost domains and a negative phase gradient in the central domain. Hence brighter regions of intensity will arise in the image corresponding to the outermost domains and a darker region will be observed arising from the central domain. The contribution to the image of the electrostatic phase appears only at the edges of the specimen and no contribution is present within the element. An example calculation is given in figure 2.12 of a vortex domain wall in a permalloy wire, simulated using OOMMF. The magnetisation is given in figure 2.12a-c, with the calculated magnetic and electrostatic electron phase in figure 2.12d,e, where the magnetic phase was calculated using the process detailed earlier.

The electrostatic phase was calculated using equation 2.10 and multiplying by a mask of the wire. The electrostatic phase is more important for Fresnel imaging as it involves defocus and only the magnetic phase was considered here for simplicity. The magnetic phase was then differentiated along the x and y directions to produce the calculated DPC images shown in figure 2.12f. As a direct comparison, experimental DPC images are given in figure 2.12g and show excellent agreement except at the wire edges as the electrostatic phase has been excluded. A colour induction map can also be generated from two orthogonal induction images, figures 2.12h,i. The calculation of

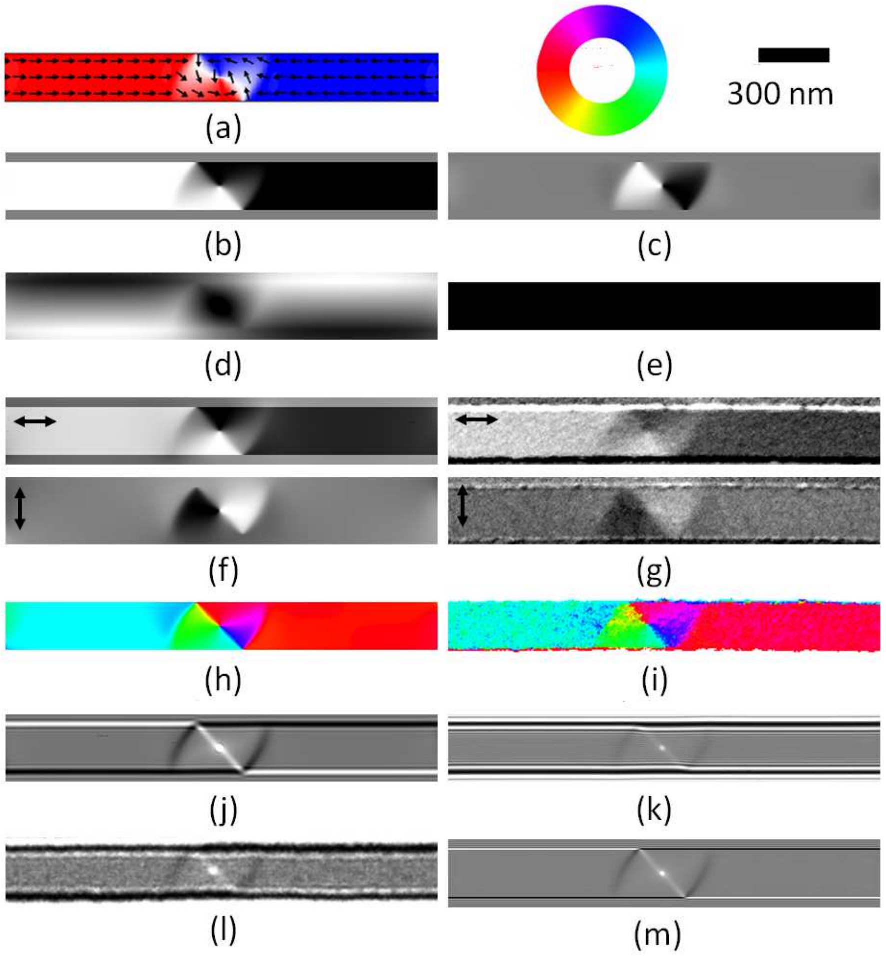

Figure 2.12: A comparison of calculated and experimental Lorentz images of a vortex domain wall in a 20 nm thick permalloy nanowire. (a) The magnetisation as calculated by OOMMF and (b), (c) are the x and y components of magnetisation. From this the (d) magnetic and (e) electrostatic phase are calculated. The magnetic phase is differentiated to give the calculated orthogonal induction maps (f) for comparison with experimental images (g). Arrows indicate the direction of the integrated components. Colour induction maps may be calculated from two orthogonal images (h), (i) where the direction is indicated by the colour wheel. The Fresnel contrast is calculated from purely the magnetic phase (j) and including electrostatic phase and amplitude effects (k). An experimental image is given for comparison (l). The out of plane component of magnetisation curl (m) is in good agreement with the Fresnel contrast.

the Fresnel intensity is discussed in the next section.

### Fresnel image calculation

Fresnel imaging is generally considered to be non-linear, however, under certain constraints the information can be linearly interpreted and used in a quantitative manner [12]. In the linear regime the Fresnel intensity is given by,

$$I(\mathbf{r},\Delta) = 1 - \frac{\Delta\lambda}{2\pi}\nabla_\perp^2\phi(\mathbf{r}) \tag{2.16}$$

Where $\Delta$ is the defocus and $\nabla_\perp^2$ is the Laplacian relating to the in plane co-ordinates. The spatial frequencies in the image determine the validity of this equation for a given defocus. Ignoring conduction and displacement currents, the Laplacian can be expressed as,

$$\nabla_\perp^2\phi(\mathbf{r}) = -\frac{e\mu_0}{\hbar}\int_{-\infty}^{\infty}(\nabla\times\mathbf{M})\cdot\hat{\mathbf{n}}dz \tag{2.17}$$

Reference [12] showed that by inserting this into equation 2.16, and at a small defocus, $\Delta$, for a thin film normal to the beam and assuming the magnetisation is uniform through the film thickness, t, the intensity may be written,

$$I(\mathbf{r},\Delta) = 1 - \Delta\frac{e\mu_0\lambda t}{h}(\nabla\times\mathbf{M}(\mathbf{r}))\cdot\hat{\mathbf{z}} \tag{2.18}$$

Therefore the Fresnel image intensity may be calculated, to a first order approximation, with a knowledge of microscope parameters and the out of plane component of magnetisation curl, where linear imaging is applicable. A schematic illustration of the Laplacian of the phase can be seen in figure 2.11 for a small defocus value and is therefore a representation of linear Fresnel images.

To calculate the Fresnel image, a uniform incident electron wave with unit amplitude is assumed. The exit wave is then calculated by a multiplication of the Fourier transform of the incident wave and the transfer function based on a Lorentz lens with spherical aberration term $\mathrm{C_s} = 8000$ mm in a TEM with an operating voltage of 200 kV and $\lambda = 2.51$ pm. An inverse Fourier transform of the exit wave multiplied by its complex conjugate gives the image intensity.

Returning to the example of the vortex domain wall, the Fresnel intensity is calculated from magnetic phase only and unit amplitude, figure (2.12j), at a defocus of 300 $\mu$m. Good agreement with the experimental image (figure 2.12l) is observed at the position of the domain wall, however there are significant differences at the edges of the wire where the electrostatic phase contribution arises. A better representation of the experimental Fresnel intensity can be achieved if electrostatic phase and amplitude effects are included in the calculation, figure (2.12k). A close representation may also be produced from the out of plane magnetisation curl (figure 2.12m), as indicated in equation 2.18.

## 2.5 Sample preparation

Electron beam lithography was used to fabricate the structures studied in this thesis; this technique and associated processes will be discussed in the following sections. Traditionally lithography is a printing technique using stone or metal with a smooth surface, invented by Senefelder in 1796 [18]. Modern Lithography refers to the transfer of a pattern of geometrical shapes from either a physical or electronic mask to a substrate, usually a Si wafer or semiconductor. The substrate is usually covered in a radiation sensitive material, known as a resist, exposed to radiation and then developed in a chemical which removes either the exposed or un-exposed regions. The types of radiation used include photo lithography (UV), particle lithography (electrons, protons, ions) and x-ray lithography. Electron Beam Lithography (EBL) was routinely used to fabricate thin film elements using an electron beam lithography tool housed in the James Watt Nanofabrication Centre (JWNC), part of the Department of Electronics and Electrical Engineering.

### 2.5.1 TEM membranes

To enable TEM analysis of the magnetic structures in this thesis, the samples must be electron transparent. In most cases, a thickness of less than 100 nm for 200 keV

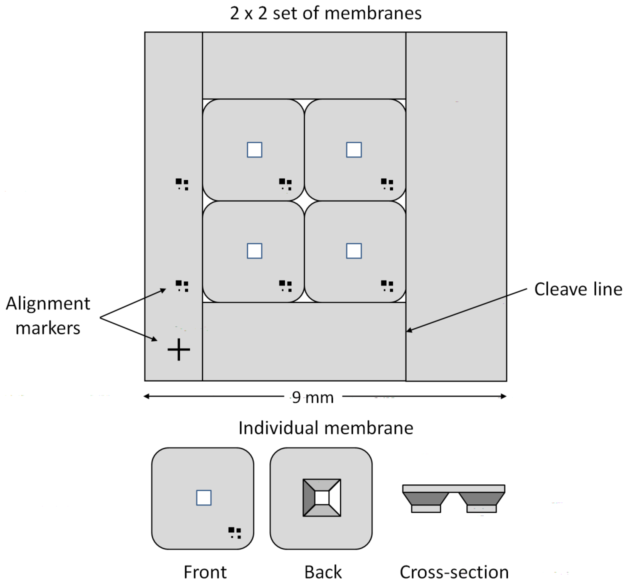

Figure 2.13: A schematic illustration of the substrates used to fabricate thin film elements. A 2×2 membrane set containing etched markers is used for electron beam lithography. Once fabrication is complete the individual membranes are separated for TEM characterisation.

electrons is suitable. The substrates used for the fabrication of the elements studied here are depicted in figure 2.13. They consist of 35 nm thick $Si_3N_4$ supported on a 500 $\mu$m thick silicon frame, with a 100 $\mu$m× 100 $\mu$m electron transparent window [19]. The membranes are fabricated by Kelvin Nanotechnology Ltd (KNT) based in the Department of Electronics and Electrical Engineering at the University of Glasgow. The samples for electron beam lithography are made in 9 mm × 9 mm blocks of $2 \times 2$ membranes. These blocks include etched markers to direct the beam to the desired area and cleave lines ensure clean separation of individual membranes for subsequent TEM analysis.

### 2.5.2 The Vistec VB6 UHR

The tool used for this work was the Vistec VB6 UHR which uses a thermal FEG capable of accelerating voltages of up to 100 kV [20]. The minimum spot size the tool can deliver

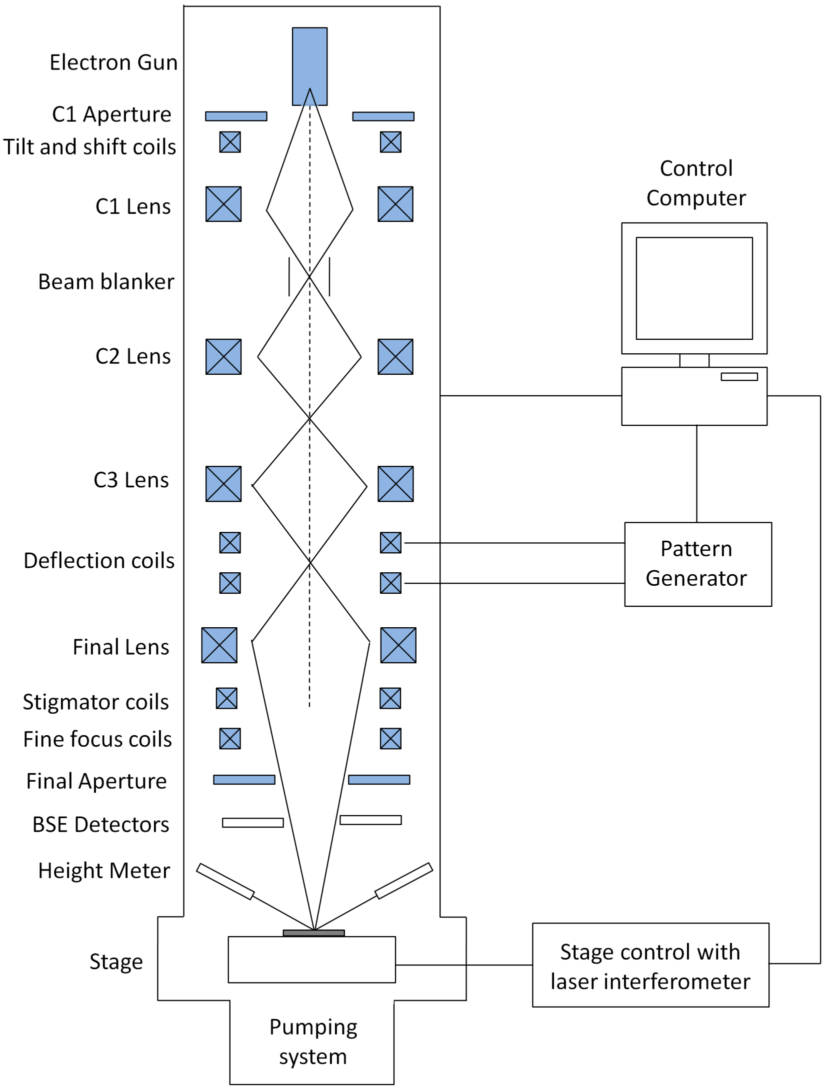

Figure 2.14: Schematic of VB6 beam writer used to pattern the structures studied throughout this thesis.

is around 4 nm, and has been used to write sub-10 nm lines in a negative tone resist [21]. A schematic of the electron optical system is given in figure 2.14, the design is similar to that of scanning electron microscopes. The electrons are generated by a thermally assisted field emission source [22]. The electron beam that emerges from the gun passes through a set of tilt and shift coils, which align the beam along the electron optical axis. The spot size and beam current at the substrate are determined by the lenses C2 and C3. A set of computer controlled deflection coils scan the probe in the x and y directions across the sample during exposure. The final (objective) lens provides the main focus of the beam on the sample whilst fine focusing coils provide correction for beam deflections at the sample and variations in sample height. Stigmator coils correct any astigmatism in the beam and a final aperture defines the beam convergence angle to the substrate. The column is fitted with backscattered electron (BSE) detectors for imaging and the whole system operates under high vacuum to minimise collisions with residual gas molecules.

### 2.5.3 Resist technology

A resist is a material capable of being pattered by exposure to a beam of photons or electrically charged particles. The principal component of a resist is a polymer, which undergoes a change in structure when exposed to radiation. Resists can be classified as either positive tone or negative tone depending on their polarity, figure 2.15. Under exposure, the positive tone polymer is weakened by chain scission to produce organic molecules of a lower molecular weight and consequently the solubility

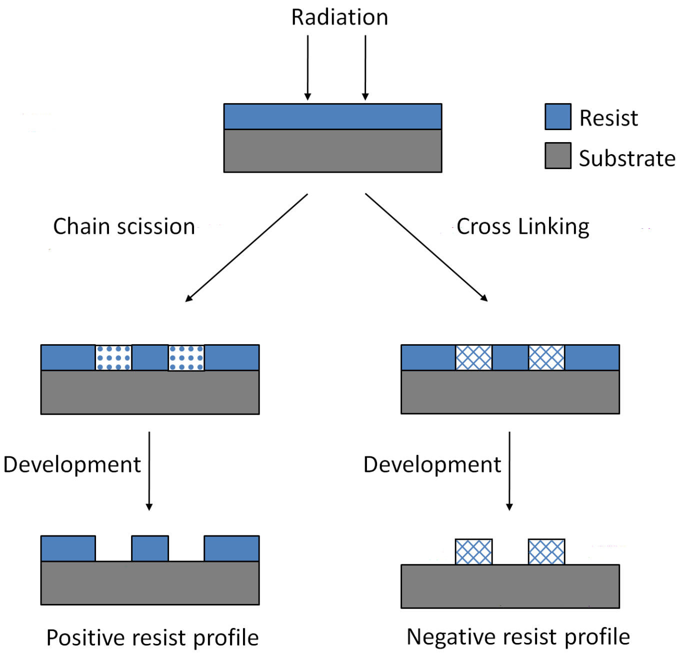

Figure 2.15: Schematic of the resist profile of positive and negative single component resists.

is increased [23]. As a result, the exposed region is removed during the development stage. In the case of negative tone resists, exposure strengthens the polymer by random cross-linkage of main or side polymer chains which renders the exposed parts insoluble. During development, the exposed regions persist whilst the surrounding regions are dissolved. The samples investigated in this thesis were fabricated using the widely available positive tone resist Polymethyl Methacrylate (PMMA) [24]. PMMA has a number of advantages including an extremely high resolution and availability in various dilutions allowing a wide range of resist thicknesses, along with its ease of handling and long shelf life. PMMA is sensitive to electron irradiation of 20 keV and higher.

### 2.5.4 Pattern design and transfer

In order to expose a pattern using the VB6, the design and job specifications must be sent to a control computer. The pattern is initially designed using a CAD program, L-Edit was used for the samples in this thesis, which allows multiple geometrical shapes to be designed and quickly assembled into a complex pattern using a cell hierarchy system. In addition, multiple layers can be used if more than one lithography step is necessary. For example, to fabricate the permalloy nanowires with electrical contacts studied later in this thesis, two lithography steps are required as depicted in figure 2.16. In the first stage, the permalloy nanowires (red elements) are fabricated following a normal EBL procedure. Once this stage is complete another bilayer of resist is spun onto the surface of the wires and membrane to pattern the electrical contacts (light and dark blue layers). A dose around 80% lower is required for the pattern region on the bulk silicon, i.e. off the membrane, due to increased electron backscatter on the bulk material.

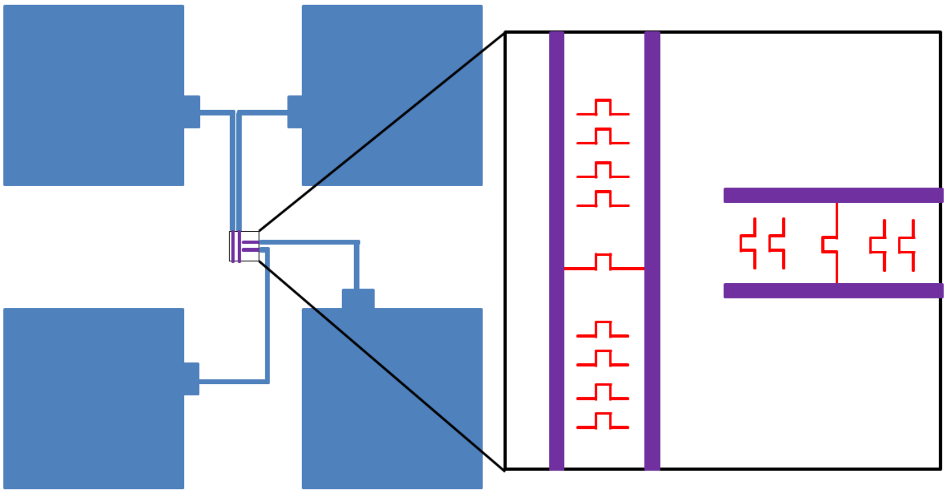

Figure 2.16: An example L-edit layout where the red magnetic elements are patterned in the first stage; the electrical contacts (light and dark blue) are written in the second stage.

The file type L-Edit produces, .gds, is not compatible with the beamwriter, for example a GDSII file has no information on the order in which the shapes are to be stored therefore the tool may have to drive the stage between point A and point B and back again many times which would introduce significant delays. Various steps must therefore be taken offline to eliminate the computationally intense steps and convert the file into a suitable format.

The post-processor used for the work in this thesis is CATS (Computer Aided Transcription System) which divides the pattern into a rectangular grid of fields, the largest area of the pattern that can be written at one time without moving the stage, this value is much larger than the membrane window size and hence the stage was stationary throughout all jobs written. Once a series of parameters have been input along with the .gds file, CATS creates the VB6 compatible file which is sent to the control computer and the job layout program BELLE to produce a final layout file.

### 2.5.5 Metallisation

During the preparation of a sample, techniques such as thermal evaporation and sputtering are used to deposit thin films of metal. Thermal evaporation, as the name suggests, involves heating the material to be deposited whilst sputtering uses energetic ion bombardment.

#### Thermal evaporation

Thermal evaporation was the technique used to deposit the permalloy for all of the elements studied in this work. This technique is performed inside a high-vacuum chamber where the material is heated to the point of evaporation. The material vapour travels through the vacuum in a straight line until it reaches a surface where it condenses in the form of a thin film. The process is carried out under high vacuum, around $5 \times 10^{-6}$ mbar in the Glasgow system, to increase the mean free path of the material being deposited and to minimise contamination from other materials. A schematic of the evaporation system used in this thesis is illustrated in figure 2.17. The target material is placed inside a ceramic boat or crucible through which a large current is passed to heat the material resistively. The substrate is situated directly above the target material and is shielded until any oxide material has been removed and a steady evaporation rate has been achieved. The deposition rate is monitored using the quartz crystal microbalance technique, which undergoes mechanical oscillation at a measured resonant frequency. This resonance is disturbed by the addition or removal of a small mass at the surface of the resonator. For each material, the frequency of vibration is calibrated with material thickness, giving a accurate indication of the material thickness deposited on the substrate. The resulting profile of metal deposited onto the surface of the substrate and resist is shown in the inset for a single layer of positive tone resist.

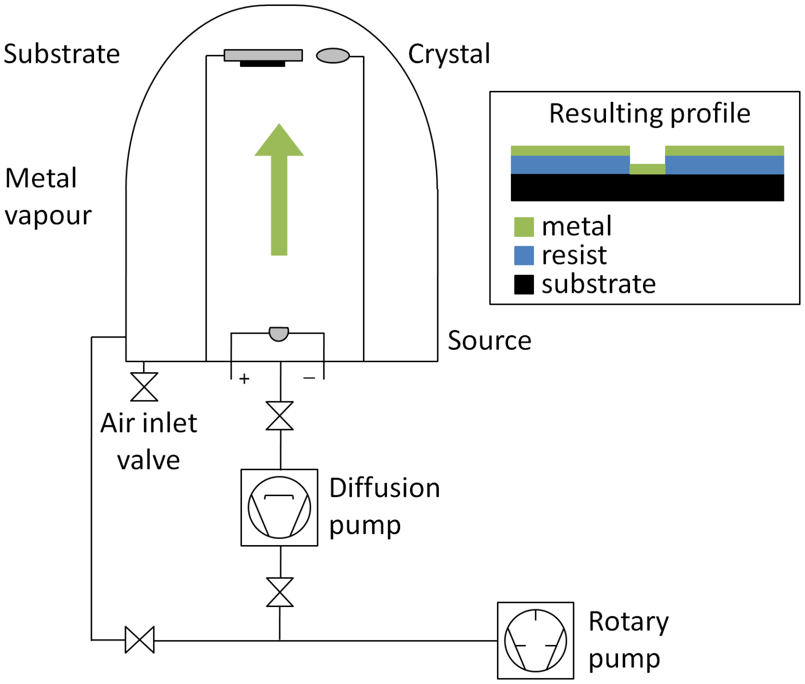

Figure 2.17: Schematic of the thermal evaporator used to deposit thin films in this thesis with an inset of the resulting profile.

### Sputter deposition

Sputter deposition is one of the most common techniques for producing high quality polycrystalline thin films and was used to deposit a thin layer of Au onto the backside of the membranes to prevent charging in the TEM. With this technique, the material to be deposited is bombarded with energetic ions in a glow discharge plasma to remove atoms which are then redeposited on the substrate and build up to form layers. The sputter chamber contains two electrodes, a cathode and an anode and is maintained under vacuum, a schematic is given in figure 2.18. The plasma is formed by the admission of a low pressure inert gas, typically Argon, which is then ionised by electrons from the cathode to form a glow discharge. The positive ions are then accelerated towards the cathode where they strike the surface to cause bond breaking and physical displacement of the atoms. The sputtered atoms condense on the surface of the substrate and on the insides of the chamber to form a thin film. The thickness of film deposited depends on the deposition time and distance from the target material. Again, the resulting profile of metal deposited onto the surface of the substrate and resist is shown in the inset for a single layer of positive tone resist. In this case the metal is deposited onto the surface of the substrate and also onto the sidewalls of the resist to form a continuous film, the implications of which will be discussed in the next section.

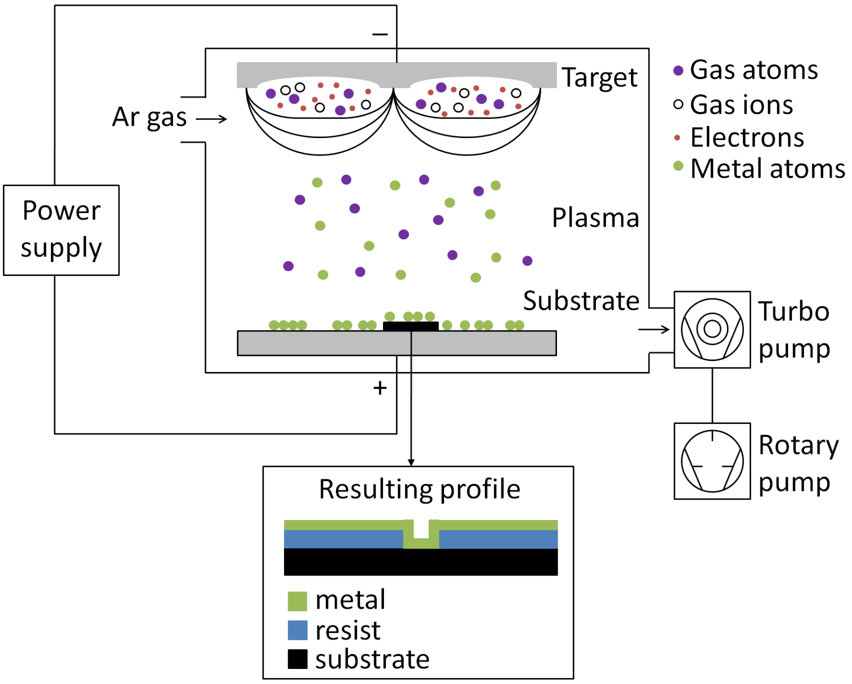

Figure 2.18: Schematic of the sputter coater used to deposit Au layers in this thesis with an inset of the resulting profile.

### 2.5.6 Lift-off

In order to produce the patterned elements as designed in L-edit, the metal film has to be divided into isolated structures. This can be achieved either by chemical etching or by lift-off, the process used to produce the structures investigated in this thesis. Once a pattern has been produced and a metal film deposited over the substrate i.e. covering the resist and regions where the polymer has been cleared, the substrate is immersed in a solvent that dissolves the resist but does not attack the metal film. This ensures the metal is only present in the regions specified by the pattern. The lift-off process is highly dependent on the quality of the resist profile after development. A

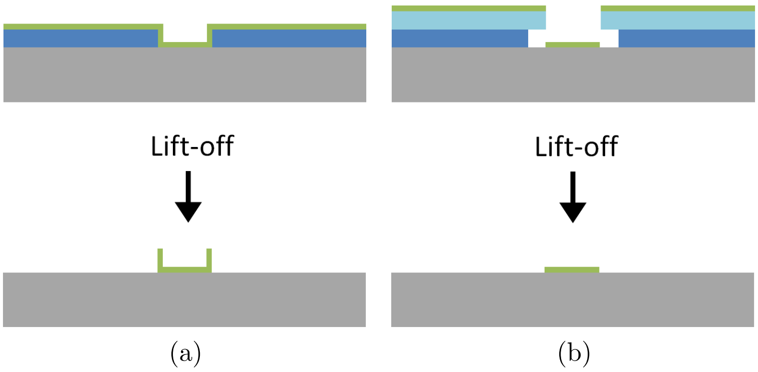

Figure 2.19: An illustration of the resist and deposited metal profile with (a) a single resist layer and (b) a bilayer of resist.

single layer of resist used to define a pattern can be problematic for lift-off as there is a tendency for the deposited metal to adhere to the sidewalls of the resist in addition to the surface to create a continuous film, as indicated in figure 2.19a. This can significantly inhibit lift-off and even after resist removal, the metal coating the sidewalls can remain on the substrate causing an unwanted build up of metal, a process known as flagging. The problem is made worse when the film has been sputter deposited due to an omnidirectional sputtering from the target. A bilayer of resist can enhance lift-off by producing an undercut profile when exposed. A higher molecular weight resist produces narrower linewidths for a given dose thus by depositing a resist with a higher molecular weight on top of a lower molecular weight resist, an undercut profile is achieved. This ensures that the deposited material has a clean separation from the resist, as illustrated in figure 2.19b.

# Bibliography

[1] S. M. Sze, Semiconductor Devices, John Wiley & Sons, Inc (2002).

[2] D. Richards, Philos. Trans. R. Soc. London, Ser. A. **361**, pp. 2843–2857 (2003).

[3] L. De Broglie, Ann. Phys. **3**, pp. 22–128 (1925).

[4] E. Ruska, Rev. Mod. Phys. **59**, pp. 627–638 (1987).

[5] D. B. Williams and C. B. Carter, Transmission Electron Microscopy: A Textbook for Materials Science, Kluwer Academic (1996).

[6] J. N. Chapman, A. B. Johnston, L. J. Heyderman, S. Mcvitie, W. A. P. Nicholson and B. Bormans, IEEE Trans. Magn. **30**, 6, p. 383 (1994).

[7] J. N. Chapman and M. R. Scheinfein, J. Magn. Magn. Mater. **200**, pp. 729–740 (1999).

[8] M. Tanase and A. K. Petford-Long, Microscopy Research and Technique **72**, pp. 187–196 (2009).

[9] L. Reimer, Transmission Electron Microscopy: Physics of Image Formation and Microanalysis, Springer-Verlag (1984).

[10] Y. Aharonov and D. Bohm, Phys. Rev. **115**, pp. 485–491 (1959).

[11] S. McVitie and G. S. White, J. Phys. D: Appl. Phys. **37**, pp. 280 – 288 (2004).

[12] S. McVitie and M. Cushley, Ultramicroscopy **106**, pp. 423 – 431 (2006).

[13] M. Beleggia, M. A. Schofield, V. V. Volkov and Y. Zhu, Ultramicroscopy **102**, pp. 37–49 (2004).

[14] P. Donnadieu, M. Verdier, G. Berthomé and P. Mur, Ultramicroscopy **100**, pp. 79–90 (2004).

[15] D. Paganin and K. A. Nugent, Phys. Rev. Lett. **80**, pp. 2586–2589 (1998).

[16] J. N. Chapman, R. Ploessl and D. M. Donnet, Ultramicroscopy **47**, pp. 331–338 (1992).

[17] M. Mansuripur, J. Appl. Phys. **69**, p. 2455 (1991).

[18] E. Weddige, Lithography, International Textbook Co. (1966).

[19] B. Khamsehpour, C. D. W. Wilkinson, J. N. Chapman and A. B. Johnston, J. Vac. Sci. Technol. B **14**, p. 3361 (1996).

[20] S. Thoms and D. Macintyre, Introduction to ebeam lithography training course (2006).

[21] http://www.jwnc.gla.ac.uk/facility-expertise.htm.

[22] Leica Microsystems Lithography Ltd, Leica Vectorbeam Series Vectorbeam Operator Manual, 4th ed. (2005).

[23] M. T. Goosey, Plastics for Electronics, Springer (1999).

[24] D. R. S. Cumming, S. Thoms, S. P. Beaumont and J. M. R. Weaver, Appl. Phys. Lett. **68**, pp. 322–324 (1996).

# 3

# Characterisation of Castellated Nanowires

## 3.1 Introduction

The ability to control the formation and structure of magnetic domain walls in nanoelements is vital for the success of potential applications such as magnetic racetrack memory [1] as well as providing an insight into their fundamental properties [2, 3]. As the dimensions of nanostructures decrease however, the surface and edge structure play an increasingly important role in determining the possible magnetic configurations that may be supported by a given element. The element geometry investigated here, referred to as a castellated wire, is aimed at controlling the structure of domain walls present in sub-micron wires. This element geometry, introduced in section 3.2, is capable of supporting a number of magnetic configurations at remanence, which are discussed in section 3.3, and as a result the switching fields of the various sections are history dependent. The reversal behaviour of a similar element geometry has been previously deduced using a combination of the anisotropic magnetoresistance (AMR) effect as a probe and micromagnetic simulation [4]. Here the magnetic behaviour is investigated using magnetic imaging techniques (section 3.4) in addition to OOMMF micromagnetic simulation. The reproducibility of the switching behaviour is discussed in section 3.5.1. Finally the results from resistance measurements are presented in section 3.6.

## 3.2 The castellated element

A schematic of the element geometry is given in figure 3.1 where it can be seen that the wire consists of various segments of straight wire connected at right angles. The orientation of magnetisation within two adjoining straight sections of the element is responsible for the domain wall configuration that exists at the intersections. The ends of the wire are tapered to gain more control over the switching of this particular section of the element, referred to as the foot. With flat ends, various degenerate ground states containing end domains can form [5]. During magnetisation reversal, new domain

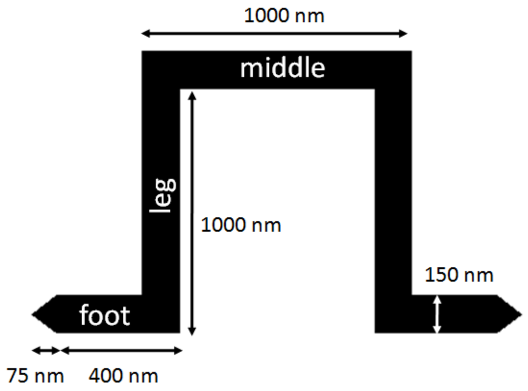

Figure 3.1: A schematic of the castellated wire geometry with section labels for referring to later in the chapter. The element has a thickness of 20 nm.

walls may branch off the end domains and cause the magnetisation to flip abruptly at the switching field [6, 7]. With a tapered end however, the end closure domains are not able to form and instead a quasi-uniform configuration is formed. Reversal of magnetisation occurs abruptly at the switching field after a small rotation of the spins at the pointed ends. Figure 3.2 illustrates two different domain wall formations that arise at the corners, indicated by A and B, along with simplified schematics of the charge distribution at these boundaries. Magnetic charges arise within a material whenever the magnetisation is discontinuous or divergent. Type A walls are higher in energy as a result of a build up of either positive, type A1, or negative, type A2, charge at the boundary. Type B walls are more energetically favourable as opposite charges

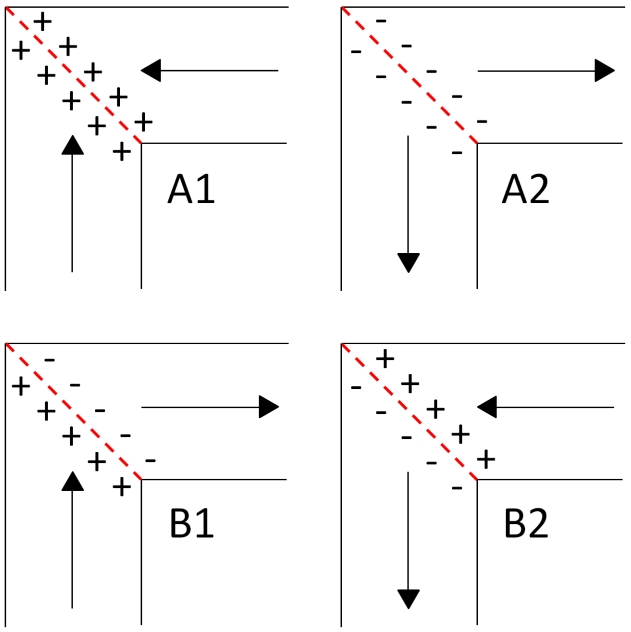

Figure 3.2: A simplified illustration of the different wall types that occur at the corners of the wire. The arrows indicate the magnetisation and the symbols indicate the resulting charge distribution.

are adjacent. A more detailed discussion of the wall types is given in section 3.3.

## 3.3 Micromagnetic simulations

OOMMF micromagnetic simulations were initially performed to identify the various metastable configurations supported by this element. For each simulation, the structure was relaxed from different initial conditions. The results, which do not constitute a complete set, are given in figure 3.3 along with the total energy. Within each of the straight wire sections, the magnetisation aligns parallel to the wire axis; the direction determines the wall configuration at the corners as indicated by figure 3.2. The lowest energy configuration, known as the ground state, is given in figure 3.3a. Here the magnetisation is aligned along the edge of each straight section in such a way that 90° domain walls of type B in figure 3.2 form at each of the four corners. By reversing

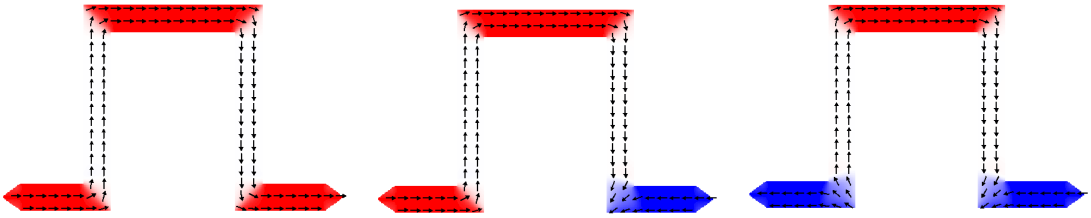

(a) $E_{tot} = 3.29 \times 10^{-17}$J
$E_{ex} = 0.62 \times 10^{-17}$J
$E_{d} = 2.67 \times 10^{-17}$J

(b) $E_{tot} = 5.07 \times 10^{-17}$J
$E_{ex} = 0.56 \times 10^{-17}$J
$E_{d} = 4.51 \times 10^{-17}$J

(c) $E_{tot} = 6.77 \times 10^{-17}$J
$E_{ex} = 0.50 \times 10^{-17}$J
$E_{d} = 6.27 \times 10^{-17}$J

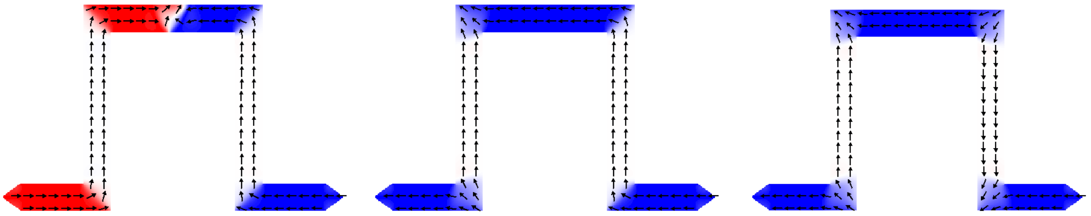

(d) $E_{tot} = 6.97 \times 10^{-17}$J
$E_{ex} = 1.15 \times 10^{-17}$J
$E_{d} = 5.82 \times 10^{-17}$J

(e) $E_{tot} = 7.05 \times 10^{-17}$J
$E_{ex} = 0.50 \times 10^{-17}$J
$E_{d} = 6.55 \times 10^{-17}$J

(f) $E_{tot} = 10.58 \times 10^{-17}$J
$E_{ex} = 0.38 \times 10^{-17}$J
$E_{d} = 10.20 \times 10^{-17}$J

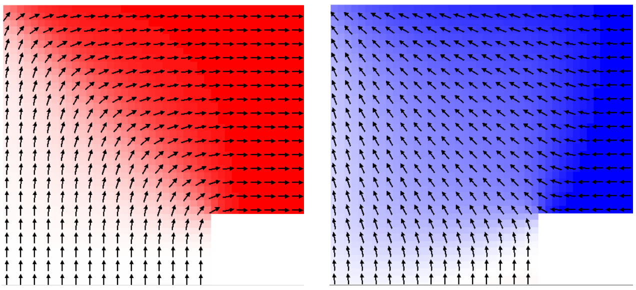

(g) (h)

Figure 3.3: (a)-(f) OOMMF simulations of some of the remanent configurations supported by this structure along with the total energy of each system. The form of the two domain wall types at higher magnification is also given in (g),(h).

the magnetisation within the right foot, a wall of structure A1 in figure 3.2 is formed at the corner, figure 3.3b. The form of this wall decreases the exchange energy due to a greater number of lower angle spins. Conversely, this domain wall creates a large surface charge at the corner leading to an increase in magnetostatic energy and increase in the total energy of the system. In a similar way, the total energy of the system is increased further when the left foot is reversed to form an A2 wall at the corner, figure 3.3c. The configuration in figure 3.3d is formed by relaxing the structure from a state where all the spins are aligned along the positive y-axis to form a head-to-head transverse domain wall in the centre of the middle section. An increase in exchange energy occurs here due to a reduction in the number of parallel spins arising from the 180° domain wall. However the magnetostatic energy is lower than that in figure 3.3c due to the decrease in surface charges at the corners. The total energy of the system is increased further when the type A walls are positioned at either end of the left leg, figure 3.3e. The exchange energy in this system is the same as that in figure 3.3c but the magnetostatic energy is 4% higher. The reason for this small energy difference is unclear however as the magnetostatic charges at either end of the left leg are separated by a larger distance thus leading to a smaller demagnetising field. The highest energy configuration is observed when all four corners of the structure contain either an A1 or A2 type domain wall, figure 3.3f. The magnetostatic energy is at a maximum due to the large number of magnetic charges at the corners however the exchange energy is the lowest in this configuration. Figures 3.3g,h illustrate in more detail the form of the two wall types that exist at the corners.

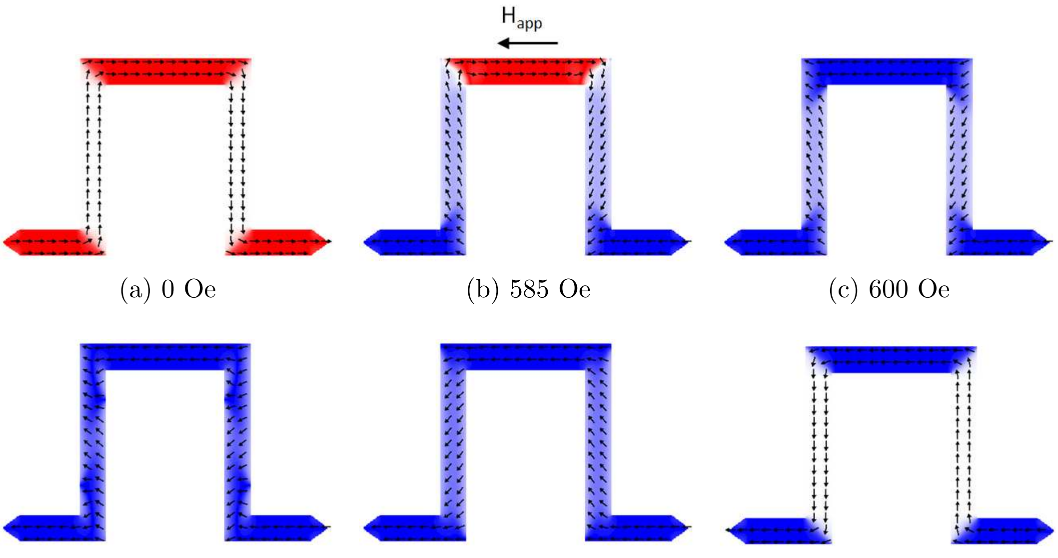

(a) 0 Oe (b) 585 Oe (c) 600 Oe

(d) 954 Oe (e) 955 Oe (f) 0 Oe

Figure 3.4: With the application of an x-axis field, the horizontal sections reverse first; the vertical sections reverse at a significantly larger field to lower the total energy of the system.

With the element in the ground state, a magnetic field applied along the x-axis causes various sections of the magnetic element to switch, as illustrated in figure 3.4. Initially simulations were performed with a field step of 50 Oe to determine the main switching events. The simulation was then refined using field steps of 5 Oe to determine a more accurate value of the switching field. The simulation started from the ground state, figure 3.4a. On increasing the magnetic field along the direction shown, the feet both switch first at the same field of 585 Oe, as expected due to the fact that they are identical in size, figure 3.4b. The middle section switches at a field of 600 Oe, figure 3.4c. With the application of a higher field, the type A domain walls at the corners start to spread into the legs (figure 3.4d) before the vertical sections also switch at a field of 955 Oe (figure 3.4e). This annihilates the A1 and A2 domain walls at the

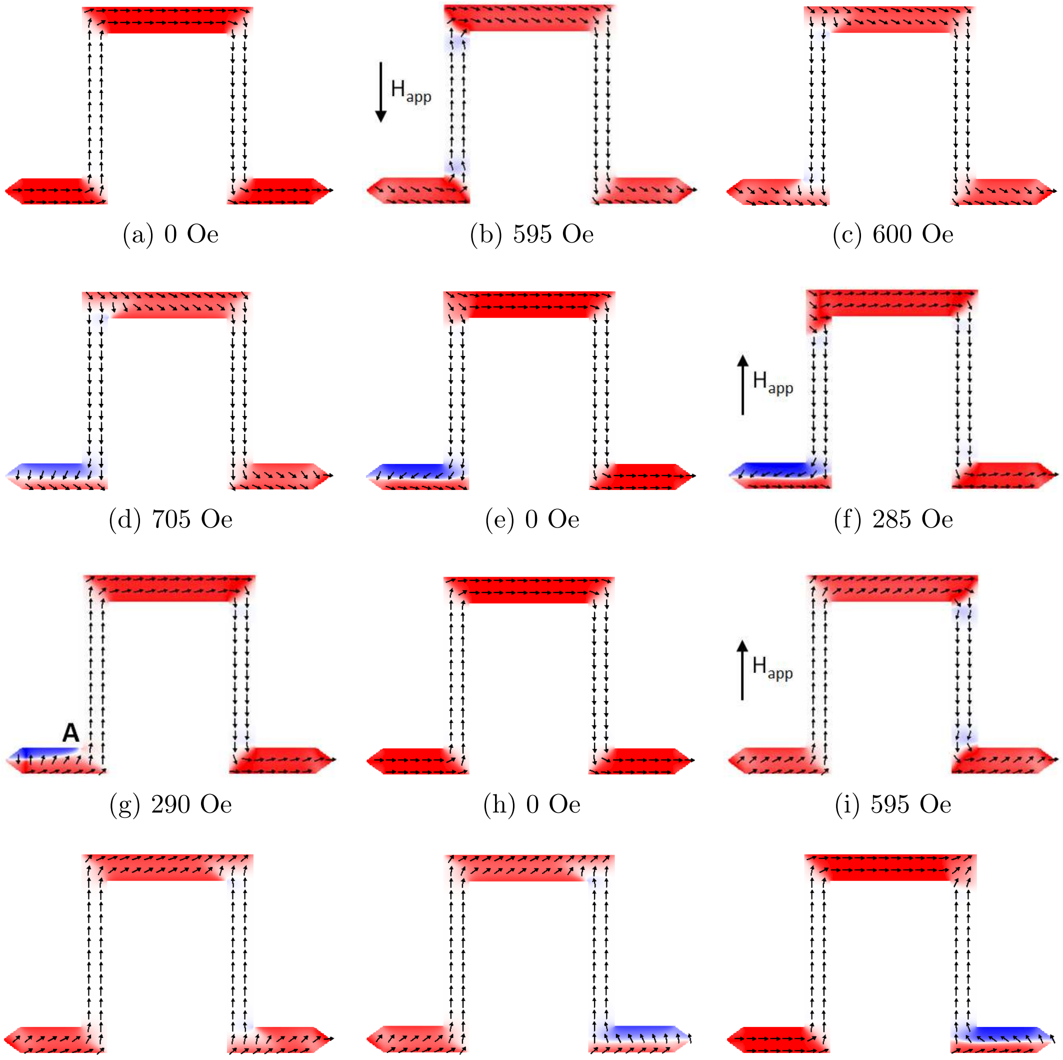

(a) 0 Oe (b) 595 Oe (c) 600 Oe

(d) 705 Oe (e) 0 Oe (f) 285 Oe

(g) 290 Oe (h) 0 Oe (i) 595 Oe

(j) 600 Oe (k) 705 Oe (l) 0 Oe

Figure 3.5: Starting from the ground state, a significant field is required to switch the left leg; a higher field partially switches the left foot. A 180° domain wall forms in the foot at remanence, which is removed with the application and subsequent removal of a reverse field. The same behaviour occurs in the right leg as the structure is symmetric.

corners and once the field is removed, the structure is once again in the lowest energy configuration, figure 3.4f.

The magnetic behaviour of the structure under a y-axis field sequence is illustrated in figure 3.5. Starting from the ground configuration, figure 3.5a, a magnetic field is directed along the vertical axis. As the field is increased, the spins at the two corners either side of the left leg begin to rotate to align with the field, figure 3.5b. Switching of the left leg occurs abruptly at a field of 600 Oe, figure 3.5c. On increasing the field further, the left foot partially switches at 705 Oe (figure 3.5d) creating a domain wall that spans the length of the foot. Surprisingly, this configuration is favourable and the domain wall is still present at remanence, figure 3.5e. The field was then increased in the reverse direction, where the A type domain wall at the upper left corner extends slightly into the left leg, figure 3.5f, before reversing it at a field of 290 Oe, figure 3.5g. The domain wall in the left foot no longer spans the length of the foot and is anchored onto the upper part of the corner between the foot and leg, indicated by **A**. If the field is removed at this stage, this domain wall is no longer favourable and vanishes leaving the foot in a quasi-uniform configuration, figure 3.5h. On increasing the field further, the spins at the two rightmost corners begin to rotate to align with the field, figure 3.5i, similar to the behaviour observed in the left leg as they are identical. Switching of the right leg occurs abruptly at a field of 600 Oe, figure 3.5j. Partial switching of the right foot is also observed at a field of 705 Oe (figure 3.5k) and the configuration is stable at remanence, figure 3.5l.

## 3.4 Characterisation by magnetic imaging

Permalloy elements equal in size to those used in the simulations were fabricated using electron beam lithography and lift off techniques, as outlined in chapter 2, for magnetic characterisation in the TEM. The magnetic reversal of the castellated wires was initially investigated using the Fresnel mode of Lorentz microscopy and is discussed in the following section.

### 3.4.1 Fresnel imaging

Figure 3.6a shows a Fresnel image (left) of the wire in the ground energy configuration with the magnetisation given in the accompanying schematic (right). Here the magnetisation follows the edges of the element, indicated by the thick dark Fresnel fringe which runs along the inner edges of the structure, highlighted along the legs by **A** and **B**. Additionally, two bright spots may be observed at the lowermost corners, indicated by the red arrows. The position of the thick dark Fresnel fringes may be confirmed by looking at a line trace across the two legs, as shown alongside the Fresnel image. The dashed box in the Fresnel image indicates the area over which the line trace was obtained. It can immediately be seen from this plot that the dark fringe is wider on the inside of each leg, indicated by **C** and **D**. Edge contrast also arises whether the wire is magnetic or not and is due to the large phase gradient experienced

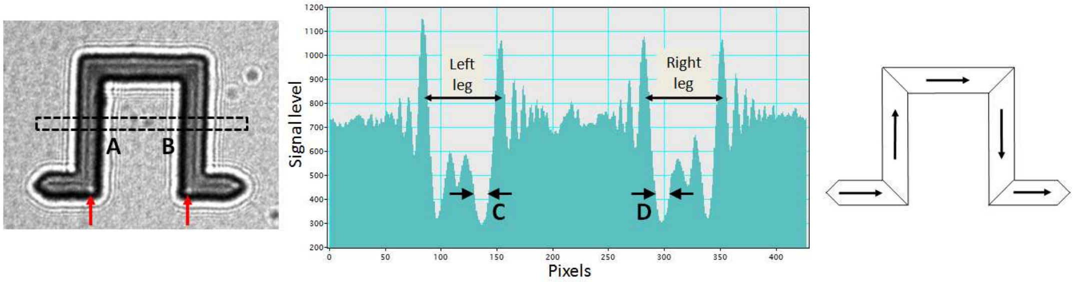

(a) Experimental Fresnel image

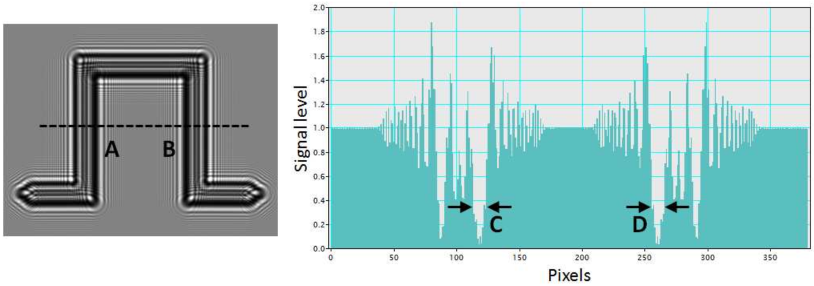

(b) Calculated Fresnel image

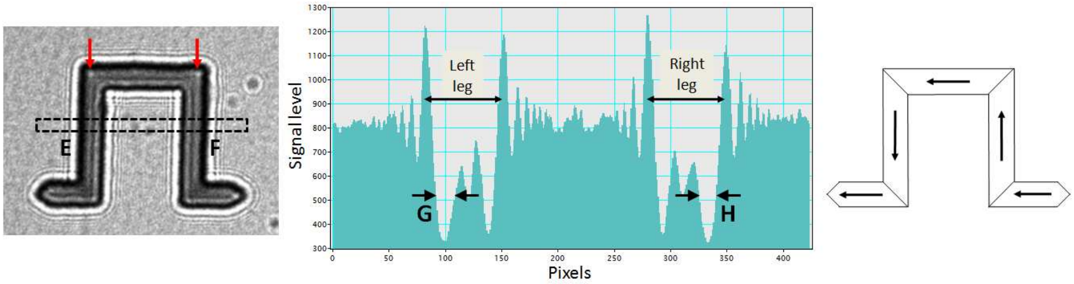

(c) Experimental Fresnel image

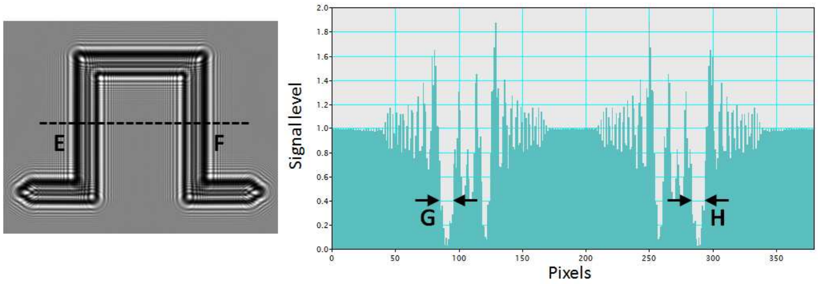

(d) Calculated Fresnel image

Figure 3.6: (a) An experimental Fresnel image of the ground state with a line trace across the legs to highlight the intensity variation across the wire. The schematic displays the magnetisation. (b) A corresponding calculated Fresnel image at a defocus of 1000 $\mu$m with line trace for comparison with (a). (c) An experimental image of an equivalent ground state; the magnetisation is given in accompanying schematic. (d) Corresponding calculated image at 1000 $\mu$m defocus.

by the electron beam between areas containing the magnetic film and those with only the surrounding substrate. The edge contrast observed in the experimental image is therefore a superposition of the magnetic and electrostatic phase contributions. The magnetic configuration of the wire may be deduced by observing the edge contrast alone, however the form of the 90° domain walls within the wire are not visible. A calculated Fresnel image is given along with a line trace to aid interpretation in figure 3.6b; both magnetic and electrostatic phase contributions were included in the calculation. The calculated image is in good agreement with the experimental image. The dark Fresnel fringes, indicated by **A** and **B**, in the calculated image are highlighted in the line trace where it can be seen that the dark fringe is thicker on the inside of each leg at **C** and **D**, as in the experimental image. On complete reversal of the structure, the magnetisation within each of the wire sections is of an opposite sense, figure 3.6c. This is confirmed by observing that the dark Fresnel fringe is now along the outer edges of the structure, indicated along the legs by **E** and **F**. Again the line trace highlights the position of the thicker dark Fresnel fringe, i.e. on the outer edge of each leg at **G** and **H**. Additionally the bright spots are now at the two uppermost corners, again indicated by the red arrows. The calculated Fresnel image in figure 3.6d provides additional confirmation that magnetisation reversal has occurred as the thicker Fresnel fringe is also on the outer edges of the structure, indicated by **E** and **F** in the calculated image and **G** and **H** in the line trace. Clearly the switching of the various sections of the element can be observed using this technique; however the form of the domain walls within the structure could not be determined. DPC imaging was therefore also used to probe the magnetic structure further.

### 3.4.2 DPC imaging

#### Reversal behaviour under an x-axis field

The magnetic switching behaviour was investigated using the differential phase contrast mode of Lorentz microscopy in low magnification scanning (LMS) mode where the particular form of the domain walls at the corners of the structure was also revealed. Figure 3.7 shows a sequence of images acquired at remanence after the switching of various sections of the structure with the application of a horizontal field. The field was increased until a section switched, the field was then removed and an image was acquired. This process was repeated until a full reversal had occurred. The structure was only imaged at remanence in order for the domain walls to be clearly observed and subsequently compared with that calculated by the simulation. Additionally, the large fields needed to reverse the various sections of the structure introduced a significant distortion to the appearance of the structure in the images owing to the large tilt angle. Figure 3.7a shows the initial configuration of the structure, where two orthogonal greyscale images are given, mapping the x and y components of magnetic induction. A colour vector map of induction, calculated from the two greyscale images is given along

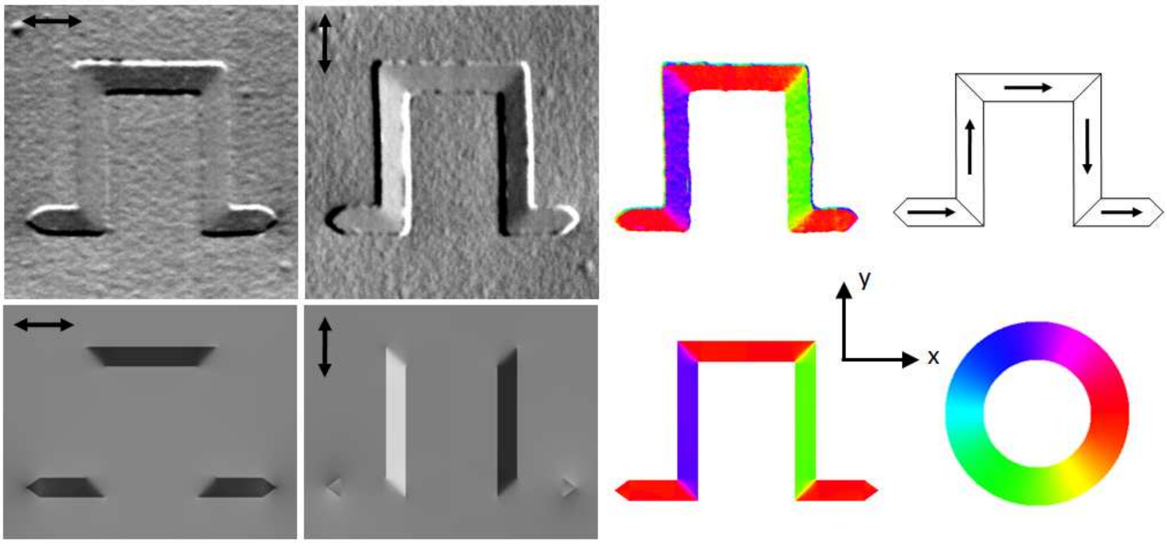

(a) 0 Oe

(b) 0 Oe, right foot switched at 232 Oe, simulated value is 585 Oe

(c) 0 Oe, left foot switched at 279 Oe, simulated value is 585 Oe

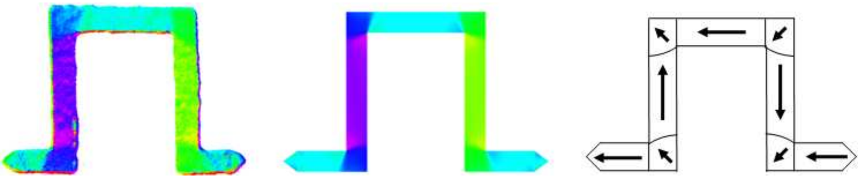

(d) 0 Oe, middle switched at 288 Oe, simulated value is 600 Oe

(e) 0 Oe, after the application of a 500 Oe field, simulated value is 955 Oe

Figure 3.7: DPC image sequence of the x-axis reversal behaviour; each image was acquired at remanence.

with a simulated DPC colour map for comparison. From figure 3.7a it can be seen that the structure is initially in the ground energy state. With the application of a magnetic field, the right foot switches first at a field of 232 Oe, figure 3.7b; a significantly larger field of 279 Oe was required to switch the left foot, figure 3.7c. The middle switched at 288 Oe (figure 3.7d) and the application of a 500 Oe field was sufficient to switch the magnetisation in the legs, figure 3.7e. The fields at which the various sections of the structure are predicted to switch differ from those observed in experiment, however the form of both A and B type domain walls at the corners of the structure are in good agreement with those calculated from the simulation.

### Reversal behaviour under a y-axis field

Figure 3.8 shows DPC images from a y-axis field reversal where the images were also acquired at remanence. The structure was in the ground state at the start of the sequence, figure 3.8a. A pair of orthogonal induction maps are again given along with the colour map generated from these two images. Calculated DPC images from the OOMMF simulations in figure 3.5 are also included for comparison. The magnetic field was initially increased along the negative y-axis where at a field of 279 Oe, the left leg

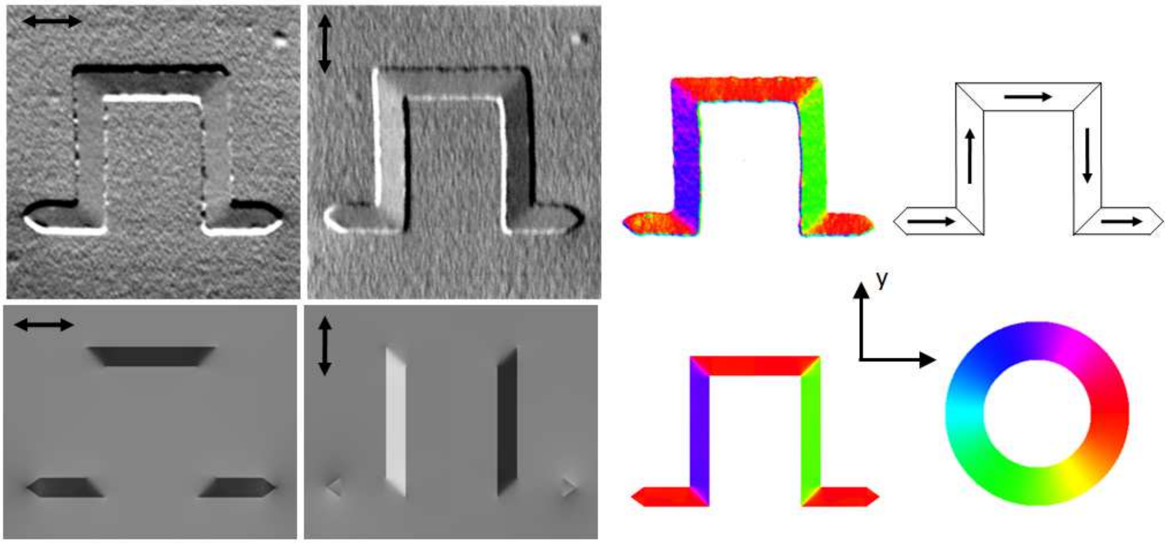

(a) 0 Oe

(b) 0 Oe, left leg switched at 279 Oe, simulated value is 600 Oe

Figure 3.8: DPC image sequence of the structure under a y-axis field cycle. The foot partially reverses in each direction to leave a 180° domain wall at remanence. Figure continues on the following page.

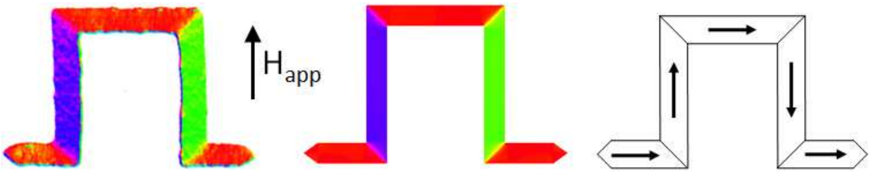

(c) 0 Oe, left leg switched at 119 Oe, simulated value is 290 Oe

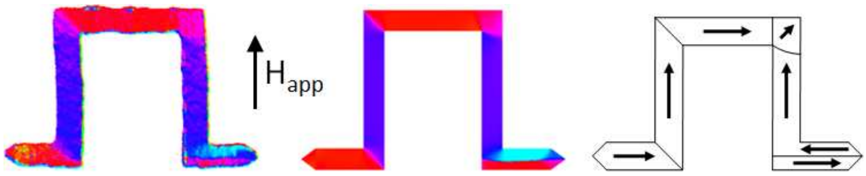

(d) 0 Oe, right leg switched at 306 Oe, simulated value is 600 Oe

Figure 3.8: DPC image sequence of the structure under a y-axis field cycle. The foot partially reverses in each direction to leave a 180° domain wall at remanence.

switched. An image of the remanent state was acquired, where the left foot consisted of a 180° domain wall spanning the length of the section. A reverse magnetic field was then applied and a field of 119 Oe was required to switch the left leg to form the ground energy state, thus annihilating the 180° domain wall in the foot, also predicted by simulation (figure 3.8c). A field of 306 Oe was required to switch the magnetisation within the right leg and once more this created a 180° domain wall in the foot. To return the structure to the ground energy state, a field of 103 Oe was required to reverse the magnetisation within the right leg and force the foot back into a single domain configuration, not shown here. Again, the field values calculated by simulation differ from those observed in experiment, however each experimentally observed magnetic configuration is in good agreement with the corresponding calculated DPC image.

## 3.5 Discussion

Although there is excellent agreement between the calculated and experimental DPC images, there is however a large discrepancy between the switching fields predicted by OOMMF and the experimentally observed values. As discussed in chapter 1, the OOMMF simulations do not take thermal or time dependent effects on the magnetisation into consideration, which must be taken into account when comparing OOMMF simulations with experiment. Additionally, the experimental setup used here involves the use of a large vertical field of 590 Oe around the sample; the switching fields observed are a result of tilting the sample to introduce an in-plane field component. The presence of the large vertical field was not included in the previous OOMMF simulations and may reduce the magnitude of the field required to switch a particular section of the element. These issues will be addressed in the following sections in addition to discrepancies caused by geometrical differences between the simulated and fabricated structures. A series of modifications to the original simulation will now be presented for the x-axis field cycle, modifications to the y-axis field cycle will be discussed later.

### 3.5.1 Modifications to the x-axis simulation

In addition to the quantitative differences observed between the reversal fields, the simulation also predicted that the feet switch at the same field; this was not observed in experiment. The dimensions of each foot and leg were then measured for 5 different structures to get an indication of the spread in values. Bright field images of the structures were obtained, an example of which is given in figure 3.9, along with a line trace of the leg. The width of the leg, in pixels, was obtained from the full width at half maximum (FWHM), as illustrated in figure 3.9. By inserting a cross grating with known dimensions into the microscope, and using the same imaging conditions, the width in nanometres was calculated. A summary of the results is given in table 3.1. In all 5 structures, the left foot was narrower than the right foot; in 4 out of 5 structures the left leg was narrower than the right leg. Additionally, the actual dimensions of the structures were considerably larger than intended. The spread in measured widths for each section is similar.

The simulations were then modified so that the structure had a width of 200 nm instead of the previously used 150 nm, the results of which are given in figure 3.10. The reversal behaviour of the structure was identical to that observed with the 150 nm wide structure, however the switching fields were significantly lower. The switching fields for the feet and middle decreased by around 20%; the switching fields of the legs dropped by around 40%. However, these values are still considerably higher than those observed experimentally.

Subsequently, the effect of the large vertical field around the specimen during magnetising experiments was considered in the OOMMF calculation. A simulation incorpo-

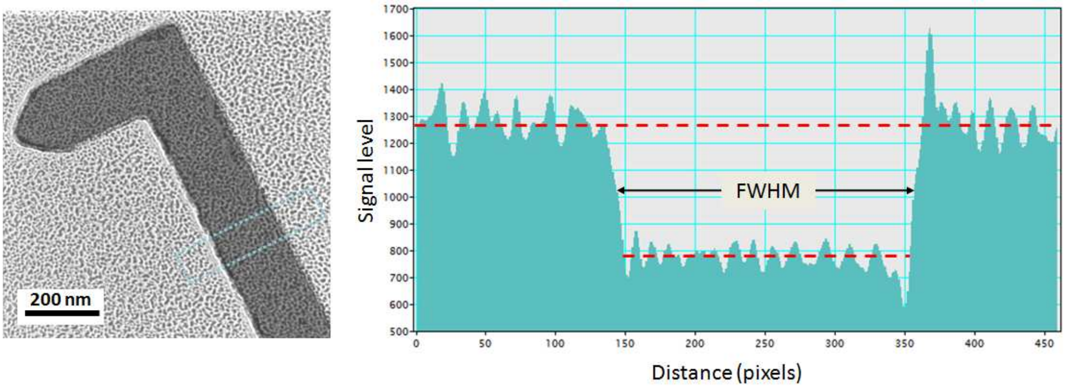

Figure 3.9: A bright field image of the right leg and foot of a castellated wire with a line trace across the leg. The width in pixels was converted to nanometres using a cross grating for calibration.

| Structure | Left Foot | Right Foot | Left Leg | Right Leg |
|---|---|---|---|---|
| 1 | 192 ± 2 | 204 ± 2 | 188 ± 2 | 204 ± 2 |
| 2 | 196 ± 2 | 209 ± 2 | 198 ± 2 | 203 ± 2 |
| 3 | 201 ± 2 | 211 ± 2 | 192 ± 2 | 195 ± 2 |
| 4 | 204 ± 2 | 207 ± 2 | 194 ± 2 | 197 ± 2 |
| 5 | 197 ± 2 | 214 ± 2 | 197 ± 2 | 195 ± 2 |
| Mean | 198 | 209 | 194 | 199 |
| $\sigma$ | 5 | 4 | 4 | 4 |

Table 3.1: The width, in nanometres, of each foot and leg from 5 different structures along with the mean and standard deviation for each section.

rating the cosine variation of the vertical field (590 Oe) was performed with an in-plane field increment of 5 Oe, however no difference in switching field of the various sections of the structure was observed with this field resolution. The out-of-plane field is therefore thought to have a negligible effect on the reversal fields obtained experimentally.

Due to a difference being observed between the reversal fields of the feet, the simulations were subsequently modified to introduce the measured physical differences between the feet and legs. It has been reported that the coercivity of small elements decreases rapidly with increasing element width, whilst the length of the element has little effect on the coercivity [8, 9]. Consequently, altering the length of the feet did not have any effect on the switching field (not shown here). From the values in table 3.1, it is evident there is a mean difference of 11 nm in the widths of the feet and a mean difference of 5 nm between the legs. Therefore, the mask file of the structure was adjusted such that the left foot was 11 nm narrower than the right and the left

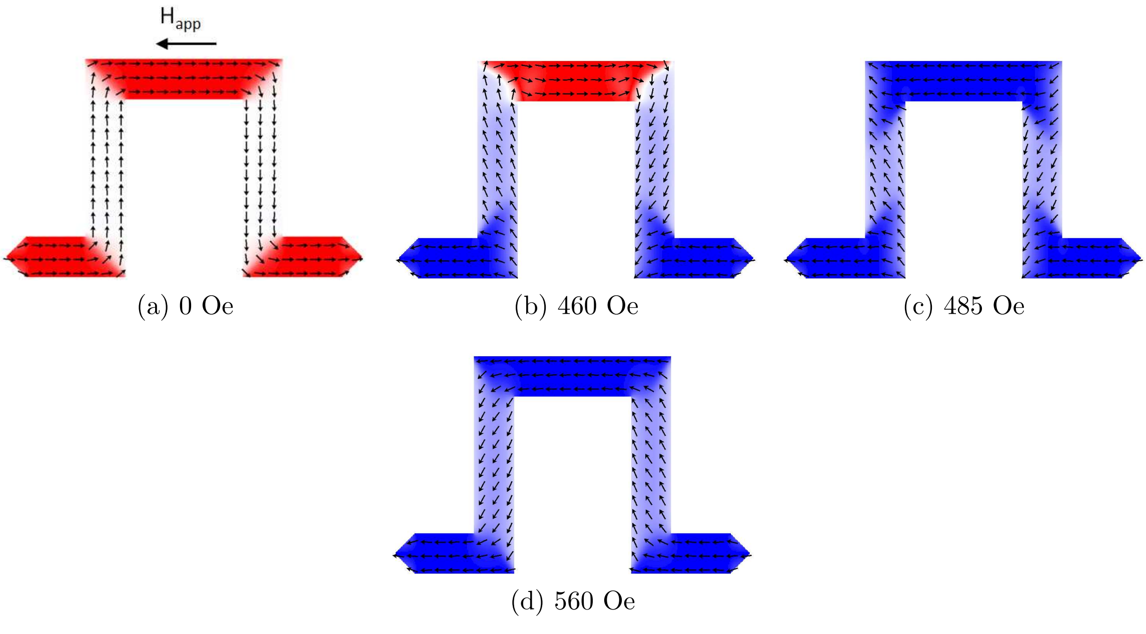

(a) 0 Oe (b) 460 Oe (c) 485 Oe

(d) 560 Oe

Figure 3.10: Result of a simulation of a 200 nm wide structure under an x-axis field cycle. Qualitatively the behaviour is unchanged, however the reversal fields are lower.

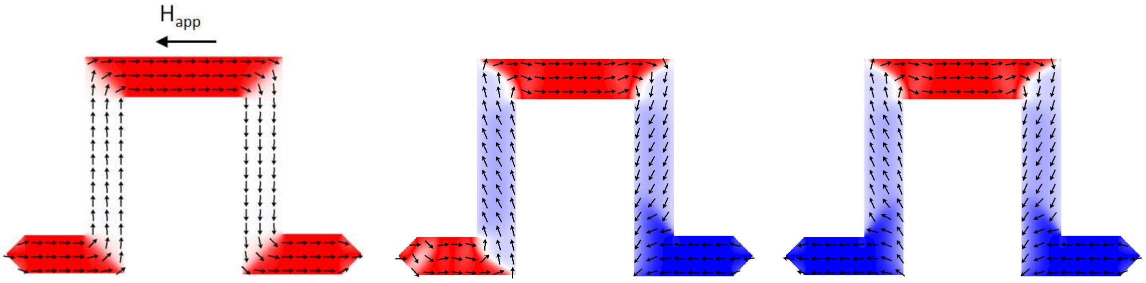

(a) 0 Oe (b) 460 Oe (c) 475 Oe

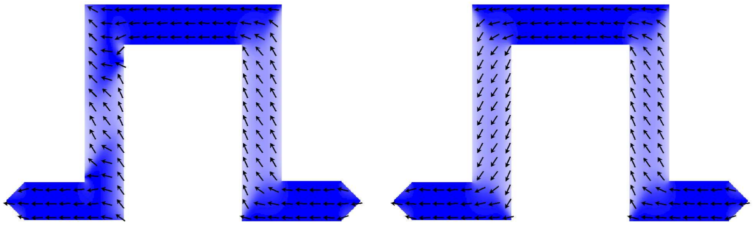

(d) 560 Oe (e) 565 Oe

Figure 3.11: By modifying the simulation to introduce a difference in width between the feet and legs, a difference in switching field between these sections is predicted.

leg was 5 nm narrower than its right counterpart. The results of the simulation are given in figure 3.11, which show that a 15 Oe difference in switching field between the feet is introduced if the width is altered by 11 nm, figures 3.11b,c. A much larger field difference of 47 Oe was observed in experiment. A smaller difference in switching field, of just 5 Oe, is predicted when there is a 5 nm difference in width between the legs, figures 3.11d,e. The reversal field of each leg was not determined in the experiment shown earlier, however is measured in the next section where the reproducibility of the switching behaviour is investigated.

In order to try to improve the agreement between experiment and simulation further, a final micromagnetic simulation was performed using a more realistic geometry. This simulation utilised a bright field image of the structure to generate the mask file instead of the ideal mask used initially, and is shown in figure 3.12. Each pixel was set to 5 nm, thus the structure had a width of ~200 nm. Additionally, the edges of the structure in the mask file are not smooth; a close-up of the upper right corner is given in figure 3.12b. The x-axis simulation was set up in the same way as for the ideal simulation; the structure started from a ground energy state and the magnetic field was then increased until a full reversal had occurred, figure 3.13. The field was then removed and the remanent state calculated. The modified simulation predicted that the right foot switched first a field of 405 Oe (figure 3.13b), a field slightly closer to but still considerably higher than the experimentally observed value of 232 Oe. However, the simulation also predicted that the middle switched after the right foot at a field of 420 Oe, figure 3.13c which was not observed in the experiment presented earlier where this section reversed after both feet had switched. The left foot was predicted to reverse

(a) (b)

Figure 3.12: (a) Image of the mask file used in the modified simulation. A close-up of one of the corners is given in (b) where the detailed edge structure is revealed.

at a field of 450 Oe, figure 3.13d. A considerably higher field of 660 Oe was required to reverse the magnetisation within the right leg and a value almost twice as large, of 1295 Oe, was required to reverse the magnetisation within the left leg. On removal of

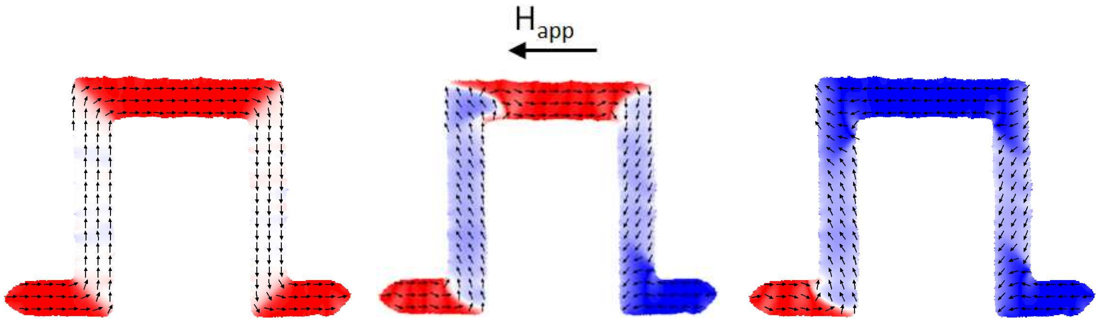

(a) 0 Oe (b) 405 Oe (c) 420 Oe

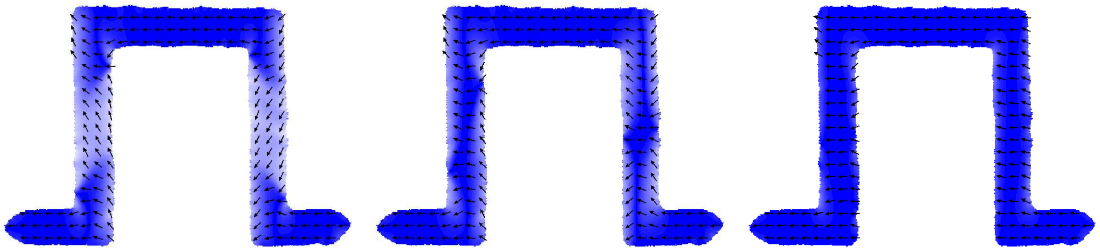

(d) 450 Oe (e) 660 Oe (f) 1295 Oe

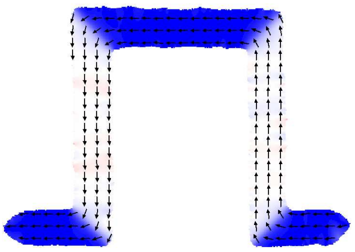

(g) 0 Oe

Figure 3.13: With the application of an x-axis field, the horizontal sections reverse first; the vertical sections reverse at a significantly larger field to lower the total energy of the system.

the field from the configuration in 3.13f, the structure relaxed to the ground energy state, figure 3.13g. It must be noted that the reversal fields of each section obtained experimentally correspond to just one experiment carried out for a single structure and are therefore not representative of this geometry as a whole. A series of repetitions were subsequently carried out to give an idea of the reproducibility of this behaviour and will now be discussed.

### Reproducibility

One of the limiting factors in the development of magnetic memory devices is the fact that not all elements can be fabricated to be identical leading to a variability in switching field between nominally identical structures [10]. The reversal behaviour must be reproducible not only for a given structure over many repetitions but over a number of structures over a large number of repetitions.

The switching field distribution of 24 nominally identical elements was investigated using Fresnel imaging, the results from an x-axis field cycle are presented in figure 3.14. The structures were all in the ground energy state before the field was applied. The field was then increased incrementally, in steps of around 9 Oe, and the number of switching events per field increment was recorded. The switching field for each horizontal section of the structure has a finite width as expected due to small variations between structures as a result of the fabrication process. It is immediately clear from this figure that in addition to each switching field possessing a finite width, the distributions also overlap one another.

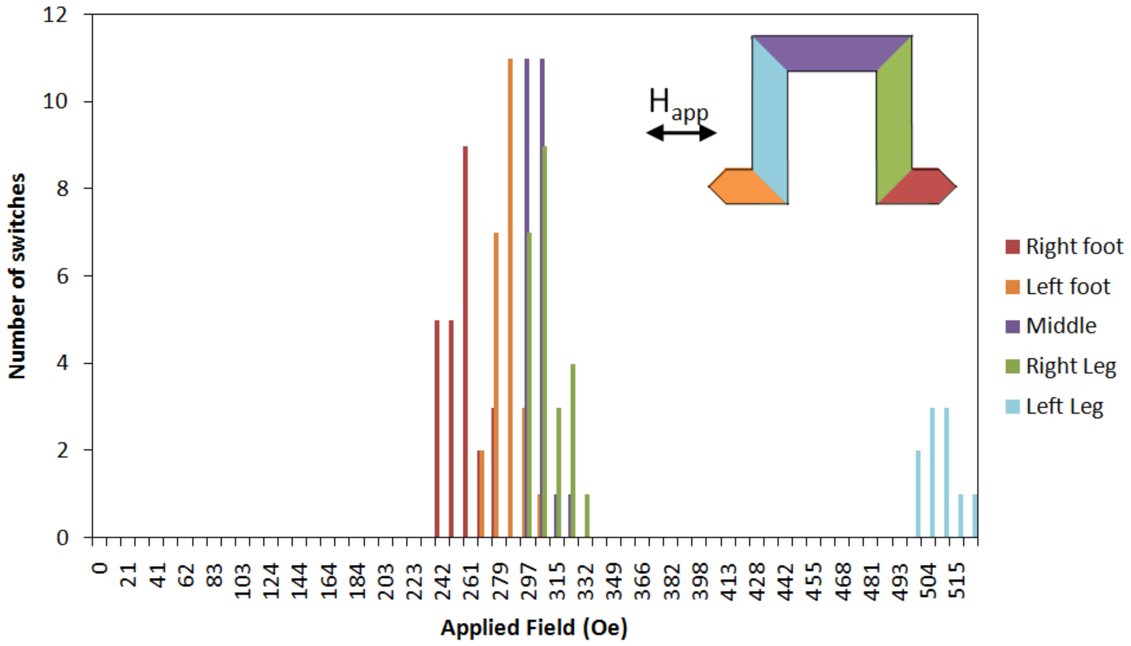

Figure 3.14: The switching field distribution from 24 structures under an x-axis field cycle.

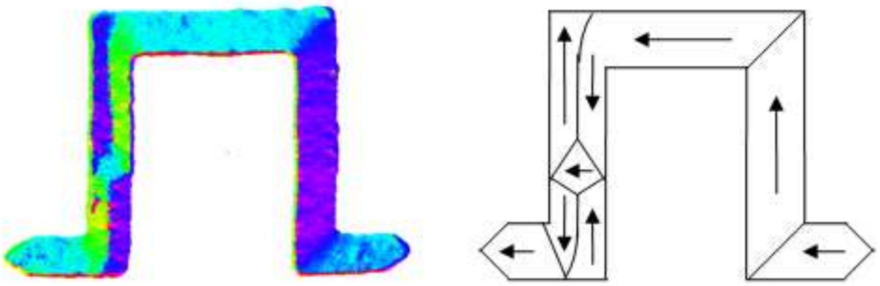

Figure 3.15: In some cases during an x-axis field reversal the left leg did not fully reverse and a multidomain configuration formed at remanence.

The distributions of the right and left feet have a very similar width of 37 Oe, and 36 Oe, respectively. As the feet were designed to have the same dimensions, it was expected that the distributions would completely overlap, however from figure 3.14 it is clear that in 19 out of the 24 cases, the right foot switches at a lower field. From the measurements of the dimensions of the feet in section 3.4.2 however, it was discovered that the left foot was narrower than the right in the 5 structures measured, leading to a higher reversal field for this part of the structure. The switching field distribution of the middle is 27 Oe and for all but one of the structures, the right leg switches within the same field range as the middle. The reason for this is unclear, however it must also be noted that these experiments were carried out in a slightly different way from the initial experiments. In the original experiment, the magnetic field was increased steadily whilst simultaneously observing the element for a reversal event, however in the reproducibility experiments, a magnetic field was applied incrementally for a significant time duration as all 24 structures had to be closely inspected for a switching event. This effect in combination with temperature dependent effects may cause the reversal field of a given section to be lower.

The switching distribution for the left leg occurs over a field range of 21 Oe, however the left leg did not fully reverse in all of the structures. In 14 out of the 24 structures, this section only partially switched and a multidomain configuration formed at remanence, shown in figure 3.15. It was also expected that the legs would switch at the same field as they were also designed to be identical, however, an average difference in width of 5 nm between the legs was measured in the previous section.

A table summarising the critical reversal fields obtained from both experiment and simulation is given in table 3.2. The experimental field values reported are taken as the average value of each section from the distribution in figure 3.14.

It may be noted that a quantitative agreement between the simulated and experimental reversal fields was not achieved with the various modifications made to the simulation, however a closer agreement between them was obtained. By using a wire width of 200 nm and introducing a difference in width between the feet and legs, the order in which each section of the structure reversed was correctly predicted, with fields closer to those obtained experimentally. The presence of the significant vertical field around the specimen was found to have no effect on the reversal fields. By using a bright field image as the mask file for the simulation, slightly different reversal behaviour was observed where the middle section reversed following reversal of the right foot. This was not observed in the DPC imaging experiment, however from the switching field distribution in figure 3.14, there is a degree of overlap between the reversal fields of the left foot and middle, therefore on some occasions the middle may have reversed before the left foot. Additionally, a significant difference between the switching fields of the right and left legs was calculated, in agreement with the reproducibility experiment. The same set of modifications applied to the y-axis field cycle will now be discussed.

| **X-axis Field** | Real Structure | Simulation | | | | |
|---|---|---|---|---|---|---|
| | | | Width = 200 nm | | | |
| | | Width = 150 nm | Symmetric | Vertical field = 590 Oe | Narrow Leg and Foot | Real Structure |
| Right Foot | 258 | 585 | 460 | 460 | 460 | 405 |
| Left Foot | 286 | 585 | 460 | 460 | 475 | 450 |
| Middle | 303 | 600 | 485 | 485 | 485 | 420 |
| Right Leg | 309 | 955 | 560 | 560 | 560 | 660 |
| Left Leg | 508 | 955 | 560 | 560 | 565 | 1295 |

Table 3.2: The reversal fields, in Oe, of the various sections of a castellated structure under an x-axis field observed in experiment and simulation with a series of modifications to try to reproduce the experimental results.

## 3.5.2 Modifications to the y-axis simulation

As it was established in the previous section that the presence of the vertical field had no effect on the reversal behaviour or switching field of the structure, this modification was omitted from the simulations presented here. In the experiments investigating the reversal behaviour under a y-axis field, it was observed that on reversal of the left and right legs, the left and right feet also partially reversed. In the simulation however, a field of 105 Oe higher than that to switch the legs was required to partially reverse the feet. From the measurements carried out in the previous section on the widths of the feet and legs, it is clear that the structure used in the simulation in figure 3.5 is not representative of the actual structure observed in experiment. A modified simulation was therefore performed using a 200 nm wide symmetric structure and is presented in figure 3.16. The reversal behaviour in addition to the field values were modified by

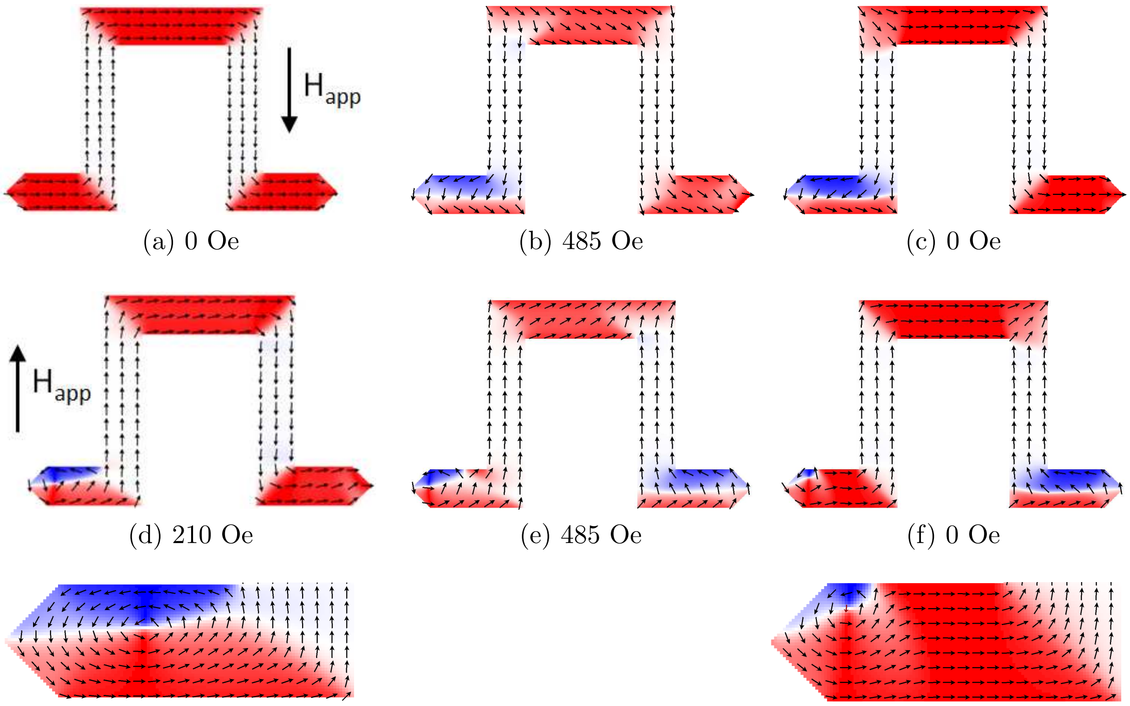

(a) 0 Oe (b) 485 Oe (c) 0 Oe

(d) 210 Oe (e) 485 Oe (f) 0 Oe

(g) 0 Oe (h) 0 Oe

Figure 3.16: Simulation of a 200 nm wide castellated structure under a y-axis field cycle. There is a vortex remanent state within the left foot. (g),(h) are magnified views of the left foot.

using a better representation of the actual structure dimensions. Starting from the ground state, figure 3.16a, a magnetic field along the direction indicated reversed the magnetisation in the left leg at a field of 485 Oe. Simultaneously, the magnetisation within the left foot partially reversed which, at remanence, produced a 180° domain wall in this segment in agreement with experiment, figure 3.16c. With the application of a reverse field, the magnetisation within the left leg reversed at a field of 210 Oe (figure 3.16d). The 180° domain wall was not completely removed with the application of this field and formed a vortex in the foot at remanence, a close-up is given in figure 3.16g. As this is a symmetric structure, the right and left legs switched at the same field, therefore the right leg switched at a field of 485 Oe, figure 3.16e. Again a 180° domain wall was formed in the foot at remanence, figure 3.16f. On reversal of the right leg, the vortex structure in the left foot changed significantly; a close-up is given in figure 3.16h. The remanent vortex in the left foot was not observed in experiment, however as mentioned previously, the DPC images only correspond to one experiment and therefore may not be representative of this structure.

Subsequently, a simulation was performed to include the measured differences between the feet and legs (see table 3.1). The result of this simulation is given in figure 3.17. Only the reversal of the left leg was simulated, as the dimensions of the right foot and leg were kept at 200 nm. The same qualitative behaviour was observed under

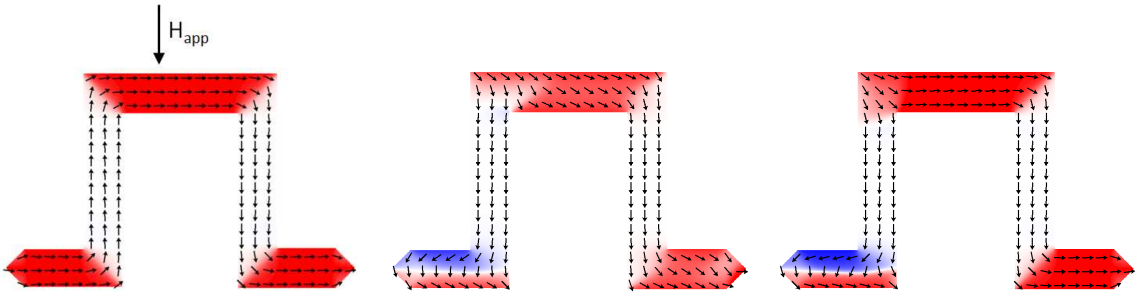

(a) 0 Oe (b) 490 Oe (c) 0 Oe

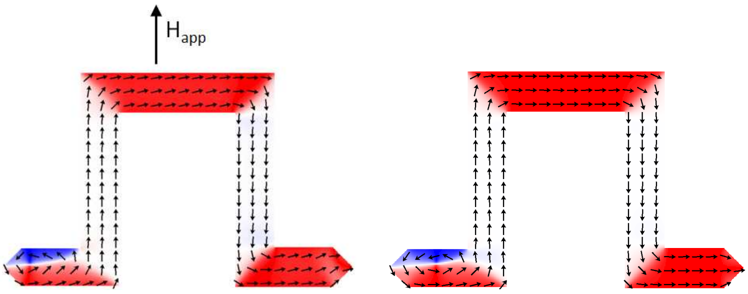

(d) 215 Oe (e) 0 Oe

Figure 3.17: By modifying the simulation to introduce a difference in width between the feet and legs, a difference in switching field between these sections is predicted.

a y-axis field cycle, however a field of 5 Oe higher was required to reverse the left leg in both field directions, owing to its reduced width. Additionally, a similar vortex magnetic structure remained in the left foot at remanence.

The final simulation of a y-axis field cycle involved the use of a bright field image as the mask of the structure, the same mask used for the x-axis field cycle was utilised here. Starting from the ground state, figure 3.18a, the simulation predicted that reversal of the left leg occurred with the application of 400 Oe, figure 3.18b. This nucleated a 180° domain wall in the foot at remanence, as observed in experiment, figure 3.18c. With the application of a reverse field, the left leg switched at a field of 170 Oe (figure 3.18d), where the 180° domain wall in the foot was not completely removed. A close-up of the foot is given in figure 3.18g. Reversal of the right leg occurred at a field of 460 Oe, figure 3.18e, a field of 60 Oe higher than that to reverse the left leg. On removal of the field, a 180° domain wall formed in the right foot as observed in experiment, figure 3.18f. However, a vortex structure still remained in the left foot, figure 3.18h, which was not observed in the experiment presented previously, however the results of an experiment investigating the reproducibility of a series of structures are presented in the next section.

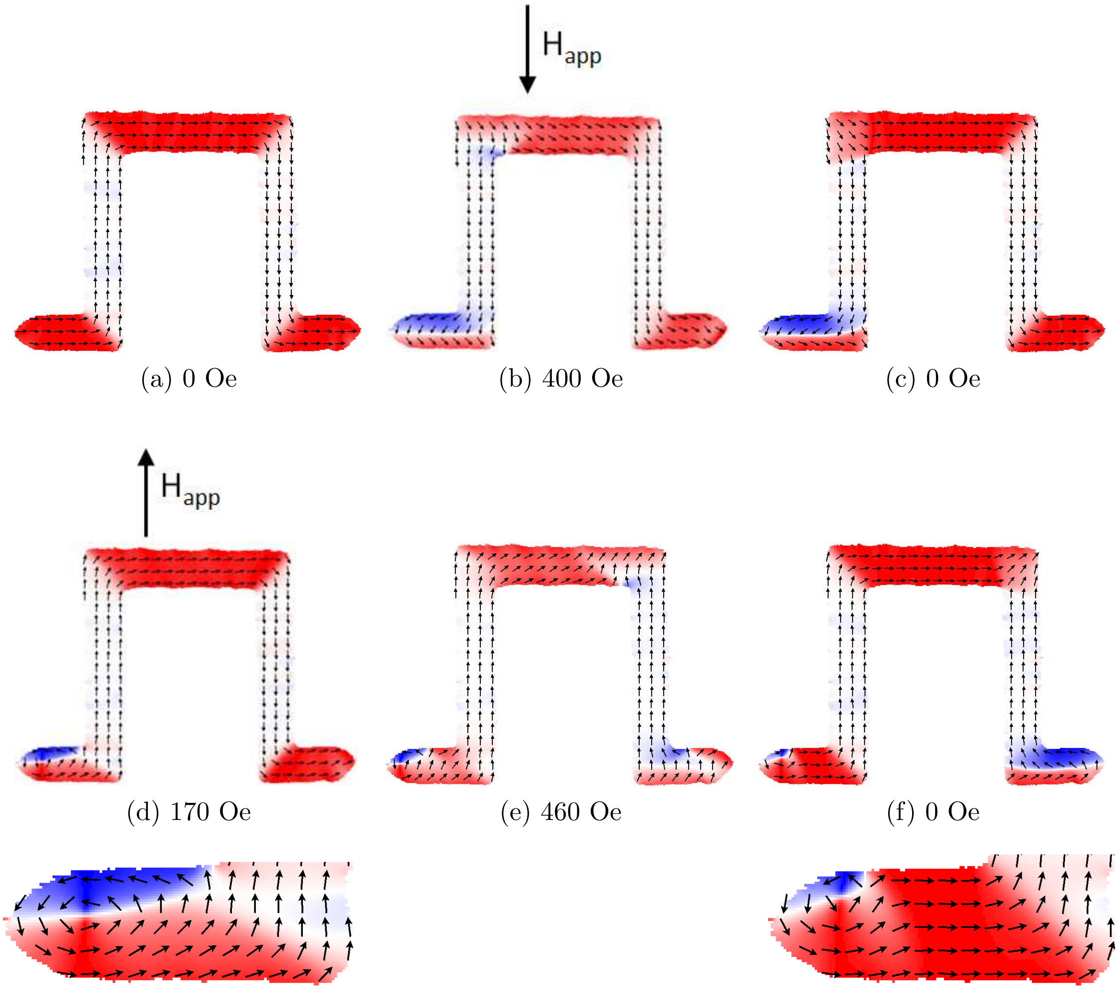

(a) 0 Oe (b) 400 Oe (c) 0 Oe

(d) 170 Oe (e) 460 Oe (f) 0 Oe

(g) 170 Oe (h) 0 Oe

Figure 3.18: (a) starting from the ground state, an applied field along the negative y-axis switches the left leg first, (b), creating a domain wall in the left foot at remanence, (c). Under a positive y-axis field, the left leg switches first, (d), leaving a multidomain configuration in the left foot, (g). The right leg switches at a significantly larger field, (e), which does not completely remove the domain wall in the left foot, (f),(h).

### Reproducibility

In a similar manner to the x-axis field cycle, the reversal fields of the legs under a y-axis field cycle were measured for 24 nominally identical structures, and are presented in figure 3.19. In this case, a large field along the negative y-axis was applied and all of the structures were in the remanent configuration given in figure 3.18c. The field was then increased along the positive y-axis and the switching field of both vertical sections was recorded for the 24 structures. The switching field distributions of the left and right legs occur over a field range of 21 Oe and 35 Oe, respectively, with the switching field of the right leg being a factor of around three higher than for the left leg. On reversal of the left leg, the 180° domain wall remained in the left foot in 3 out of the 24 structures. In 7 of the remaining structures, the remanent configuration

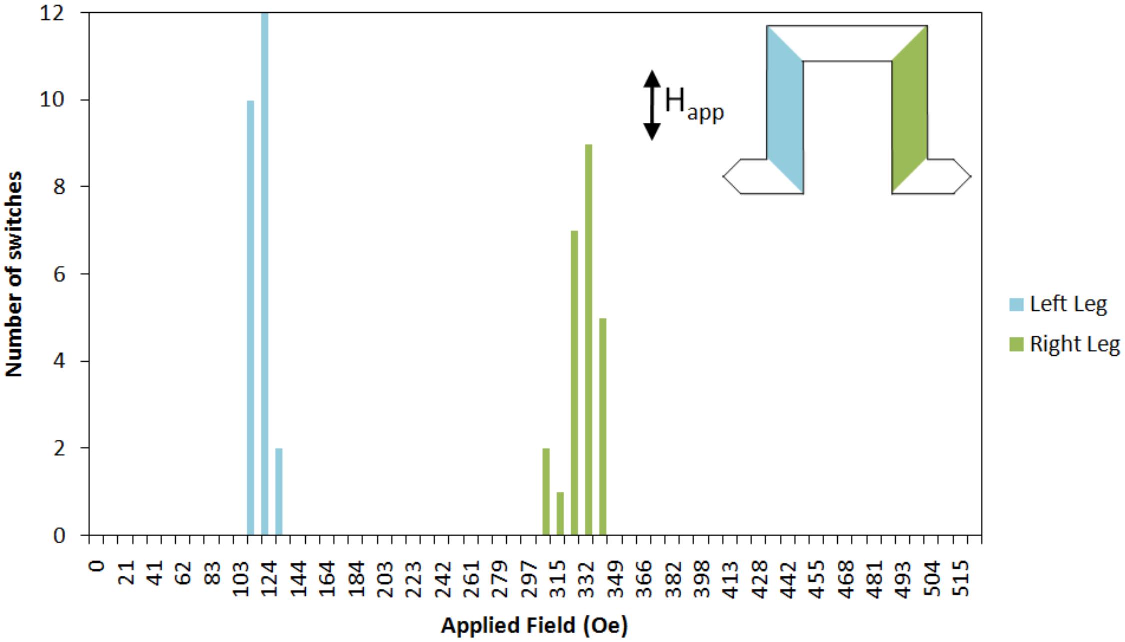

Figure 3.19: The switching field distribution from 24 structures under a y-axis field cycle.

in the foot could not be determined. The 180° domain wall was completely removed in the remaining cases. The simulation of the real structure presented in the previous section illustrates a possible remanent configuration for the left foot that could not be determined in this experiment. A table summarising the critical reversal fields of the legs is given in table 3.3, where again the field values for the real structures are taken as the mean value from the reproducibility measurements. The closest agreement was achieved by utilising a mask file of the real structure in the simulation instead of an ideal structure with straight and symmetrical sections. Although quantitative agreement was not achieved, the relative difference in switching field of the vertical sections was similar. The field required to reverse the right leg was 2.7 times higher than that required to reverse the left leg both experimentally and obtained from the

| **Y-axis Field** | Real Structure | Simulation | | | | |
|---|---|---|---|---|---|---|
| | | Width = 150 nm | Width = 200 nm | | | |
| | | | Symmetric | Vertical field = 590 Oe | Narrow Leg and Foot | Real Structure |
| Left Leg | 120 | 285 | 210 | - | 215 | 170 |
| Right Leg | 329 | 600 | 485 | - | 485 | 460 |

Table 3.3: The reversal fields, in Oe, of the various sections of a castellated structure under a y-axis field observed in experiment and simulation with a series of modifications to try to reproduce the experimental results.

simulation of the real structure.

Clearly, the dimensions and edge profile are absolutely key in determining the reversal behaviour of each section of this structure. Small differences in the width of two nominally identical sections leads to a significant difference in reversal field between them. As such, this wire geometry may not be suitable for use in magnetic memory devices where well defined and highly reproducible reversal behaviour is essential. In the next section, a different technique to probe the reversal behaviour of these structures is described.

## 3.6 MR measurement

As discussed in the introduction, the AMR effect has previously been used to probe the magnetic reversal behaviour of a similar wire geometry. The magnetoresistive technique is a viable method of monitoring the reversal behaviour of sub-micron sized magnetic elements and is advantageous for systems of reduced dimensions where the resistance is larger and therefore easier to measure [11, 12]. Magnetoresistance measurements have also been performed on Co [13] and NiFe [14] zigzag wire geometries, i.e. structures containing 90° intersections as in the castellated wires, to extract the domain wall contribution to the resistivity in a magnetic nanowire. A micromagnetic simulation of an x-axis magnetoresistance curve was initially performed using the package LLG Micromagnetics Simulator™, developed by Michael Scheinfein [15]. The LLG Micromagnetics simulator solves the Landau-Lifschitz-Gilbert equation using finite differences and permits the calculation of the magnetoresistance behaviour. The simulations were performed using the standard parameters for permalloy with a cell size of 5 nm. The resistance of each cell in the mesh is calculated by applying +1V to the entry side and -1V to the exit side and computing the current flow using finite differences. The resistance of the whole structure is computed using a complex network of series and parallel resistors handled by the finite difference matrix.

The result of the simulation is given in figure 3.20, where various points along the curve have been numbered to give a corresponding micromagnetic configuration. The resistance of the wire is at a maximum at zero applied field. In both field directions, two distinct jumps in resistance may be observed, one at a field of ±560 Oe and the other at a field of ±1040 Oe. There is also a smooth general decrease in resistance with increasing applied field. As the magnetic field is increased along the x-axis, the magnetisation within the legs will gradually rotate to align with the field, in other words, there is a continual decrease of the magnetisation component parallel to the direction of current flow. This has the effect of continually lowering the resistance. The discontinuous jumps along the otherwise smooth curve are explained as follows. At 480 Oe, given by 2 in figure 3.20, the structure is still in the original configuration, however the large

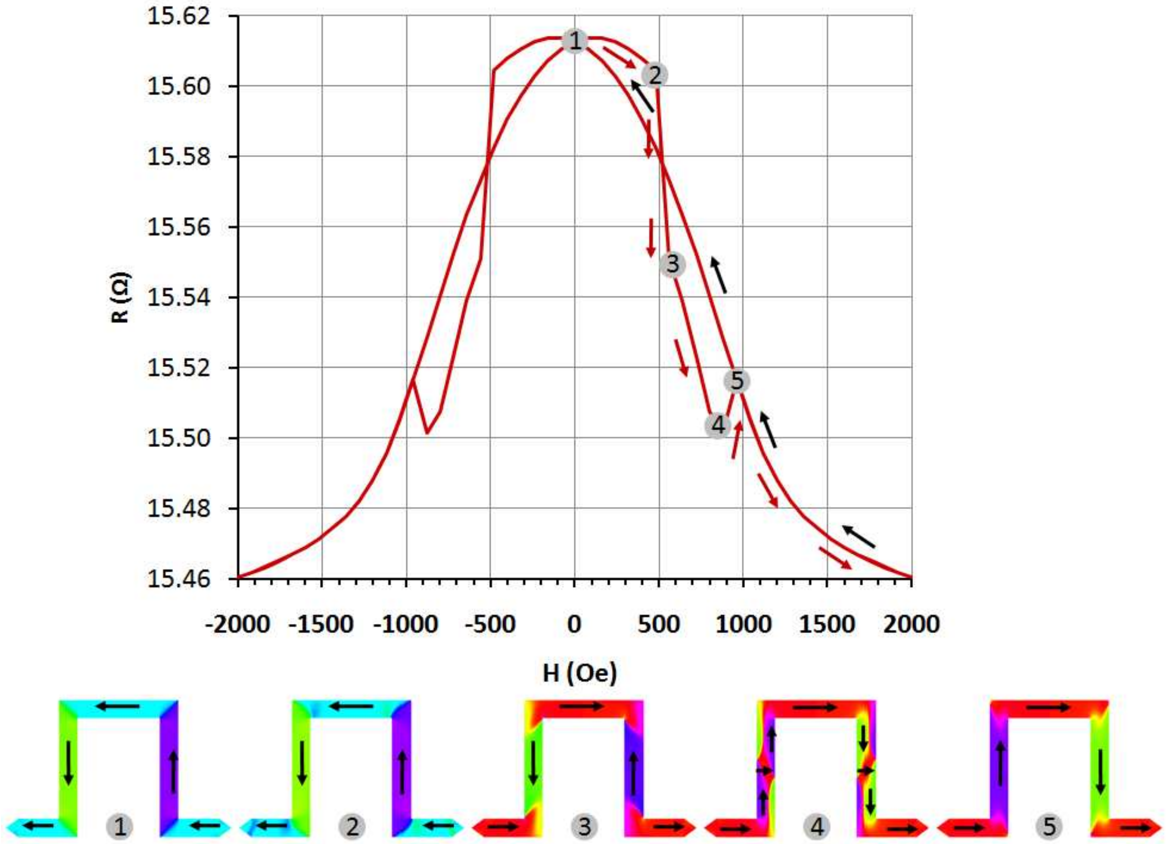

Figure 3.20: The magnetoresistance curve was simulated for the structure in an x-axis field cycle. The red arrows indicate the outward resistance path; the black arrows refer to the return curve. Calculated DPC images corresponding to various resistance values are also given.

magnetic field forces the spins away from their equilibrium position and they are no longer exactly parallel with the edges of the structure. At 560 Oe, there is a significant drop in resistance (see 3 in figure 3.20). At this applied field, the horizontal sections of the structure have reversed, creating regions of high magnetic charge density at each corner. The magnetisation is still parallel to the direction of current flow in the main part of each straight segment, however the magnetic spins are now perpendicular to the current direction at the corners. It is therefore only the change in magnetisation at the corners that contributes to this sudden reduction in resistance. At a field of 960 Oe, the legs begin to switch, see 4 in figure 3.20, which results in an increase in resistance when they fully reverse at 1040 Oe, 5 in figure 3.20. This increase is a result of the annihilation of the head-to-head and tail-to-tail domain walls at the corners, thus creating 90° domain walls in their place. The current and magnetisation are now more favourably aligned at the corners however the presence of the large magnetic field means the spins are forced considerably away from their equilibrium position to align with the field, hence the resistance is not at the maximum value as at zero field.

Magnetoresistance measurements using similar structures were also carried out by

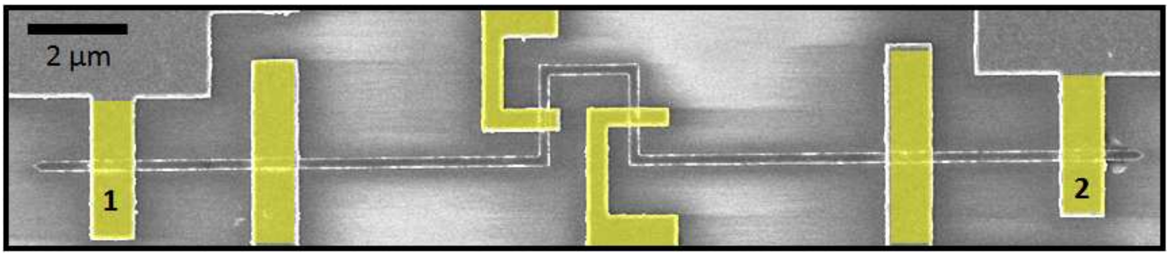

Figure 3.21: SEM image of the castellated wire sample with gold contacts deposited on top for performing magnetoresistance measurements.

Dr. Adekunle Adeyeye at the National University of Singapore (NUS). Figure 3.21 is an SEM image of the permalloy castellated wire with gold electrical contacts, highlighted by false colour. The resistance measurement was performed using contacts labelled 1 and 2, i.e. across the whole structure. The 20 nm thick $Ni_{80}Fe_{20}$ wires were fabricated by Dr. Adekunle Adeyeye using electron beam lithography and lift off techniques. Electrical contacts were fabricated using optical lithography, metallisation and lift off of Cr(2 nm)/Au(50 nm). The only deliberate geometrical difference between the wires on this sample and the wires studied previously is that the feet are significantly longer to allow space for the contacts to be placed. A current of 30 $\mu$A was passed through the structure and a resistance measurement obtained from an x-axis field cycle is presented in figure 3.22. There is good agreement between the experimental magnetoresistance measurement presented in figure 3.22 and the simulated curve in figure 3.20. The

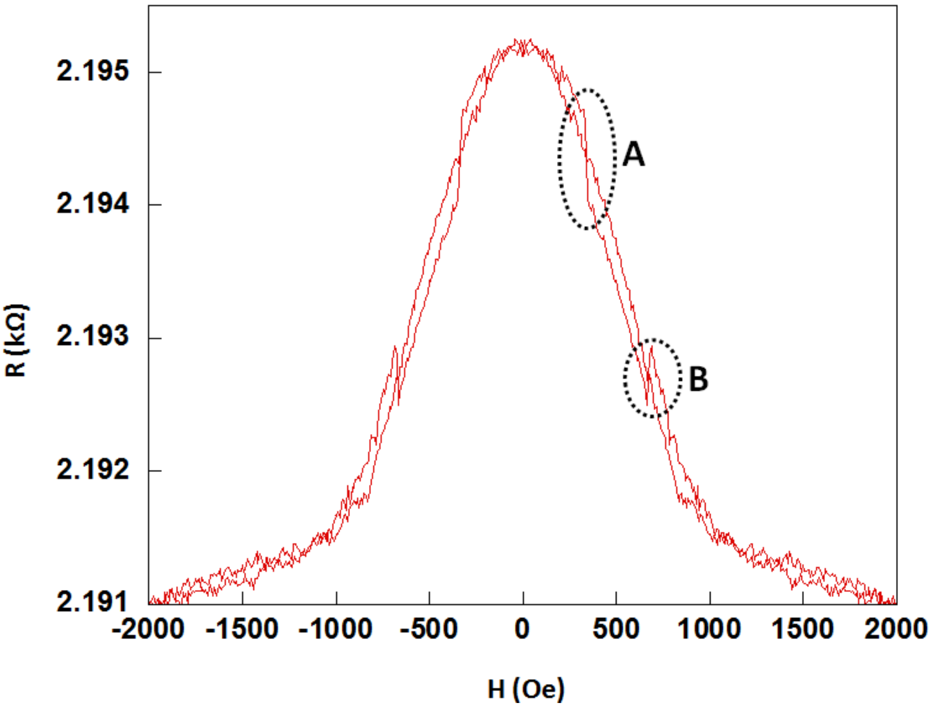

Figure 3.22: Resistance measurement of the castellated wire under an x-axis field cycle. Characteristic features of the curve are highlighted by **A** and **B**.

resistance had a maximum value at 0 Oe, and there was a general decrease in resistance with increasing applied field, as observed in the simulation. Two characteristic features of the resistance curve, occurring at fields of ±400 Oe and ±700 Oe, highlighted by **A** and **B** respectively, also appear in the simulated resistance curve and correspond to reversal of various segments of the structure. There was a smooth decrease in resistance as the applied field was increased until a field of 400 Oe, where there was a significant drop in resistance at **A**. A similar abrupt decrease in resistance was observed in the simulation corresponding to the reversal of the horizontal sections of the structure. As the field was increased further, the resistance continued to gradually decrease until a field of 700 Oe was reached where a small increase in resistance occurred at **B**. This jump in resistance was also predicted by the simulation, which corresponds to the reversal of the vertical sections of the element. At this point the structure had undergone a complete reversal however was still under the influence of a large magnetic field; increasing the field further continued to gradually lower the resistance. The resistance returned to a maximum value on removal of the field.

The resistance of the fabricated structure was considerably higher than that of the simulated structure, however the size and quality of the electrical contacts used to conduct the measurement affect the total measured resistance [16]. In the simulation, the current was specified to enter the structure from the tapered end of the foot, giving a contact size of 15 × 20 nm$^2$. A considerably larger electrical contact was required for the measurement on the fabricated structure, leading to a larger total resistance. Additionally, the simulation was performed at 0 K whereas the experiment was performed at room temperature, which also further increases the measured resistance. Quantitative agreement between the switching fields of the simulated and fabricated structure is not expected from the results presented previously, however good qualitative agreement was obtained where the characteristic features were clearly reproduced.

A sample was fabricated with the aim of performing in-situ MR measurements at Glasgow University, however due to time constraints, the experiment could not be completed. Given that the AMR is directly linked to the magnetic domain structure, it follows that combining Lorentz microscopy with MR measurements can provide a greater understanding of the complex transport properties of magnetic nanostructures [17, 18] and provides the basis of an exciting project to be carried out in the future. The proposed experimental setup and generation of resistance measurements is outlined in the following section.

In order to measure the resistance of the castellated structures, the existing sample had to be modified to include electrical contact pads connected to the ends of the wires. Fabrication of the sample required a two stage lithography process whereby the the permalloy wires were fabricated in the first stage and a second lithography step produced gold electrical contacts. This lithography process is outlined in chapter

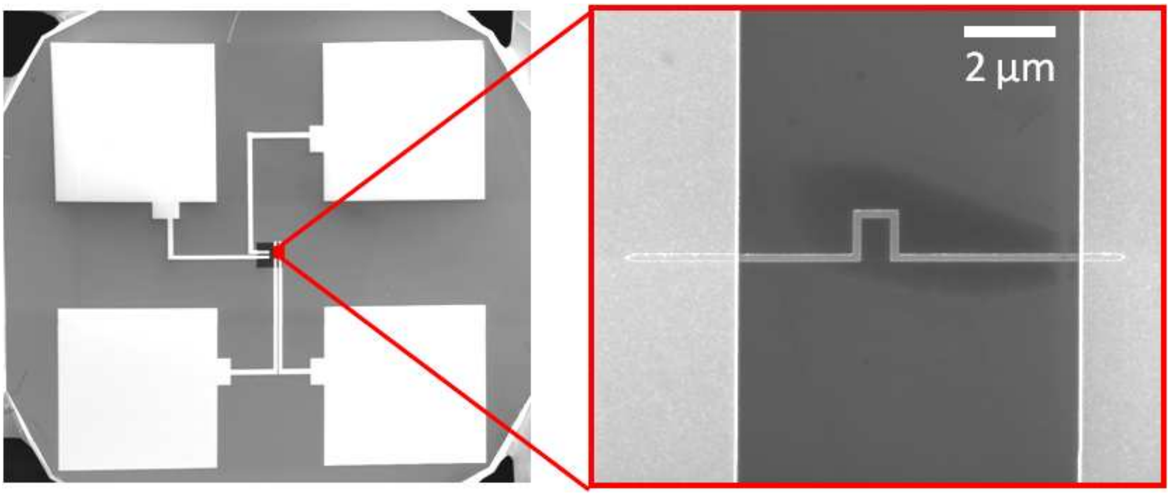

Figure 3.23: SEM image of the castellated wire sample with gold contacts deposited on top for performing magnetoresistance measurements.

2. Figure 3.23 shows an image of the sample, the inset gives a higher magnification image of one of the castellated structures with the gold contacts on either side. The only deliberate geometrical difference between the wires on this new sample and the wires studied previously is that the feet are significantly longer to allow space for the contacts to be placed. Four large gold contact pads may be seen on the surface of the sample, the lower two of which are connected to the structure given in the inset. The upper two contact pads are connected to an identical wire that is orientated at a 90° angle to the structure shown in the inset. This allows for the resistance measurement of a structure under both an x- and y-axis field cycle without the need to remove the rod from the TEM, disconnect the sample and rotate it 90°, thus risking the possibility of damaging the sample.

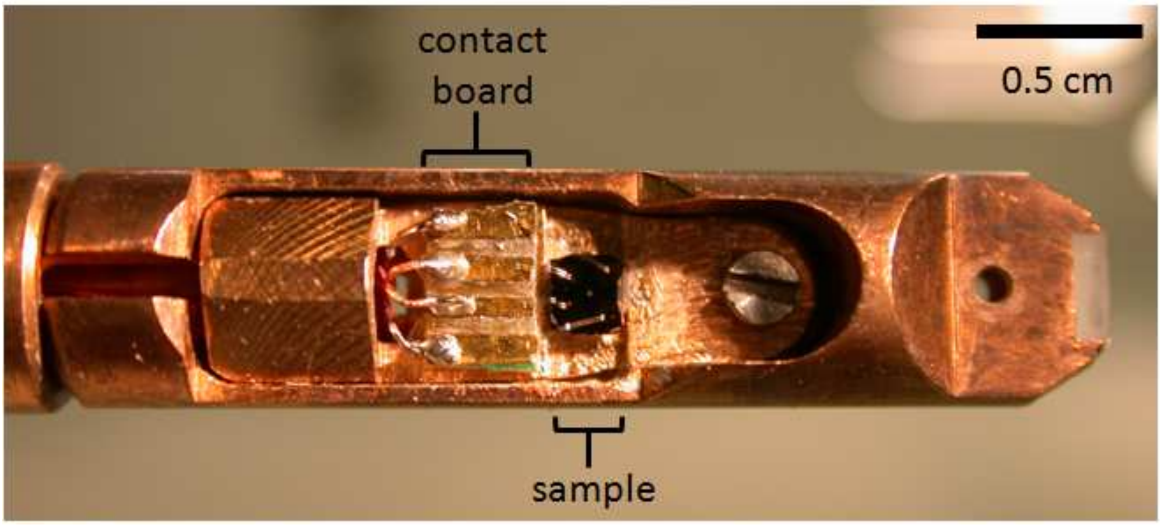

Figure 3.24: Photograph of the end of the TEM rod used to perform in-situ resistance measurements with a sample bonded ready for measurements.

In order to carry out resistance measurements in-situ, a different TEM rod had to be used specifically to suit this type of measurement. A photograph of the end of the TEM rod, containing the sample, is given in figure 3.24. Performing in-situ resistance measurements is particularly challenging due to space limitations. For example, the part of the TEM rod labelled 'contact board' in figure 3.24 has an area of just 0.5 × 0.4 $cm^2$ and is made from a printed circuit board. The wires connected to the left side of the contact board are manually soldered in place. The membrane containing the castellated structures, labelled 'sample' in figure 3.24, is secured in place by a small quantity of glue and is connected to the contact board by ultrasonic bonding.

Furthermore, the specimen is sensitive to electrostatic discharge which can damage the sample; this occurred frequently and is the main reason these experiments were not completed in the duration of this thesis. The dramatic effect of this on the specimen is illustrated in figure 3.25. Figure 3.25a is a Fresnel image of the wire prior to the resistance measurements and figure 3.25b illustrates the damage caused to a castellated wire by electrostatic discharge. Consequently, extra precautions need to be taken to ensure the durability of the sample, for example, the use of an antistatic wrist strap and antistatic floor mats, a large resistor may also be connected into the circuit whilst the sample is being connected to prevent large currents from flowing through the specimen. Additional wires were patterned on the membrane, not connected to the gold contacts, to ensure the membrane could be re-used if one of the structures was damaged. Tungsten deposition using the FIB was used to connect a spare wire to the gold contacts either side of the structure, as illustrated by figure 3.26. Figure 3.26a is an SEM image of a damaged wire; an additional castellated structure connected to the gold contacts by tungsten deposition is given in figure 3.26b.

As the change in resistance being measured is extremely small, it is also essential

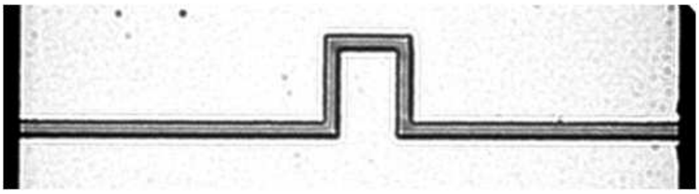

(a)

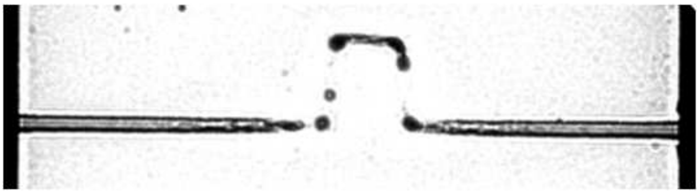

(b)

Figure 3.25: Fresnel image of the castellated wire (a) prior to resistance measurements and (b) following electrostatic discharge.


(a)

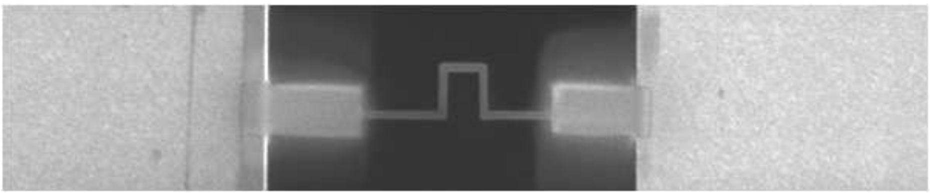
(b)

Figure 3.26: (a) SEM image of a castellated wire damaged by electrostatic discharge. (b) SEM image of a repaired wire connected to the gold electrical contacts by W deposition using the FIB.

to ensure a good electrical contact is made to reduce the signal-to-noise ratio. It was found that loose electrical contacts gave rise to a large variation in the base resistance value, which masked any changes in resistance due to magnetoresistance. Therefore it is essential to ensure the contact board and the contacts on the membrane are clean and smooth. It was found that a loose electrical contact could be improved by dropping a small piece of solder onto the connection. This is challenging however due to the close proximity of the contacts to the membrane window where the castellated wires are situated and additionally, the solder flux easily spread across the surface of the membrane, resulting in extremely poor image contrast. However, if all of the challenging aspects of this experiment described above can be overcome, a highly useful capability of assigning characteristic features in a resistance curve to magnetic configurations of a structure will be achieved.

## 3.7 Discussion

The results presented here have shown that the castellated wires are able to support a variety of remanent configurations that include a combination of two different wall types, A and B, at the intersection of each straight wire section. The strong shape anisotropy was intended to influence the domain wall structure and stabilise a particular spin configuration. The form of the domain wall depends on whether there is a high or low magnetic charge density at the corner where the two straight sections meet. When there is a high charge density (type A walls), there is an increase in magnetostatic energy along with a reduction in the exchange energy as the wall contains lower angle spins. With a low magnetic charge density at the corner (type B walls), the magnetostatic energy is at a minimum with the formation of a 90° domain wall. The formation of this type of wall however has an increase in exchange energy associated with it due to its reduced width compared with type A walls.

Micromagnetic simulations were used to predict the behaviour of the structure under an x- and y-axis field cycle and DPC imaging was used to directly observe the magnetic structure. DPC images were also calculated from the micromagnetic simulations at remanence and are in excellent agreement with the experimental images. The form of the domain walls at the corners and the remanent configurations in the feet were clearly observed. However, the field at which each section reversed was not correctly predicted by the simulation. Although the structures were designed to have identical feet and legs, in reality this is difficult to achieve due to the nature of the fabrication process. Therefore the differences between experiment and simulation were thought to most likely be attributed to minor geometrical differences between sections intended to be identical. After measuring the widths of various sections of 5 structures, the simulations were modified to take geometrical differences into account. A more suitable prediction of the experimental behaviour was produced, however the critical field values still differed greatly from experiment. The closest agreement between experiment and simulation was achieved by using a bright field image as the mask file in order to account for edge roughness and more accurate geometrical variations. Thermal effects on the magnetisation were not included in the simulation and are thought to be the major cause of the remaining difference [19].

Furthermore, the permalloy used in the fabrication of these structures was deposited in a system with a base pressure of $5 \times 10^{-6}$ mbar, which increased considerably during deposition, meaning that the risk of contamination during deposition was increased and quality of the permalloy may be compromised. Properties of the material that may be affected include the saturation magnetisation, $M_S$, and the coercivity. The saturation induction, $B_S = \mu_0 M_S$, is directly related to the Lorentz deflection angle introduced in chapter 2, section 2.4, and therefore may be calculated using DPC imaging. The saturation induction of permalloy, $B_S = 1.0$ T. A study has previously been carried out to investigate the effects of ion irradiation on permalloy films, by Mr. Martin Stäerk at the University of Glasgow [20]. It was found that the unirradiated permalloy, deposited using the thermal evaporator at Glasgow University, had a saturation induction of around 0.5 T. A final modification to the original x-axis simulation to alter the value of $M_S$ from $860 \times 10^3$ Am$^{-1}$ to just $430 \times 10^3$ Am$^{-1}$ produced considerably lower switching fields, as displayed in table 3.4. A field increment of 5 Oe was used for the simulations. The average switching fields for the real structure are also included for comparison. Using a lower value of $M_S$ in the simulation clearly provides a better comparison with the real structure. The simulated structure used did not include the imperfections observed with the real structures and therefore some differences still exist. The compromised quality of the permalloy due to the deposition

| | Right Foot | Left Foot | Middle | Right Leg | Left Leg |
|---|---|---|---|---|---|
| $M_S = 860 \times 10^3$ Am$^{-1}$ | 585 | 585 | 600 | 955 | 955 |
| $M_S = 430 \times 10^3$ Am$^{-1}$ | 295 | 295 | 305 | 675 | 675 |
| Real Structure | 258 | 286 | 303 | 309 | 508 |

Table 3.4: Table of switching fields, in Oe, of the various elements of the structure under an x-axis field for two simulations with different values of saturation magnetisation, $M_S$. The average switching fields of the real structure are also included for comparison.

system may therefore provide an additional explanation for the difference between the experimentally observed and simulated switching field values.

A considerable spread in reversal fields was found in the switching fields of 24 nominally identical structures. As mentioned previously, this is to be expected as not all elements can be fabricated to be identical. In the case of the x-axis reversal, the switching values of all sections except the left leg are not distinct and all reversed within a field range of 110 Oe, with a considerable degree of overlap between various sections. This property is clearly undesirable for memory devices, where a clear characteristic switching field of each section is necessary. The switching fields of the left and right legs under a y-axis field are well defined however and separated by a large field of 209 Oe. One issue that would prove problematic for magnetic memory applications is the partial switching of the feet, where stable multidomain configurations form at remanence. By increasing the length of the feet, figure 3.27, the magnetostatic energy would be decreased due to a greater separation of the magnetic charges that arise at the ends and hence a flux-closure state may be less likely to form. The increased shape anisotropy would also ensure that a single domain state is more energetically favourable.

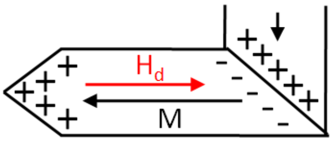

(a)

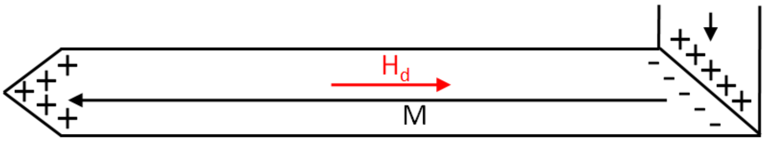

(b)

Figure 3.27: (a) with a low aspect ratio of the foot, there is a short distance separating the magnetic charges, hence the demagnetising field is large which may encourage a flux-closure state to form. (b) by increasing the length of the foot, the magnetic charges are separated by a larger distance hence reducing the demagnetising field.

The experimental magnetoresistance measurement performed by Dr. Adeyeye was in good agreement with that predicted by the simulation, in particular, the shape and characteristic features of the curve were reproduced well. Discrepancies between the total resistance of the structure were attributed to the thermal effects and contact resistance. These results highlight the feasibility of this technique for the characterisation of magnetic nanostructures.

It may be concluded that the types of domain walls that form in these wires are distinct and highly reproducible, however the fields required to create and annihilate them vary from one structure to another. It may be possible to achieve a characteristic switching field for each section if a greater geometrical distinction between sections is made. Additionally, greater control over certain aspects of the fabrication process, such as lift off, may produce a narrower spread in switching field between nominally identical structures and hence may make this element desirable for use in magnetic memory applications.

# Bibliography

[1] S. S. P. Parkin, M. Hayashi and L. Thomas, Science **320** 190 (2008).

[2] M. Kläui, J. Phys.: Condens. Matter **20** 313001 (2008).

[3] C. H. Marrows, Adv. Phys. **54** 585 (2005).

[4] A. O. Adeyeye and R. L. White, J. Appl. Phys. **95** 2025 (2004).

[5] A. B. Johnston, J. N. Chapman, B. Kamsehpour and C. D. W. Wilkinson, J. Phys. D: Appl. Phys. **29** 1419 (1996).

[6] K. J. Kirk, M. R. Scheinfein, J. N. Chapman, S. McVitie, M. F. Gillies, B. R. Ward and J. G. Tennant, J. Phys. D: Appl. Phys. **34** 160 (2001).

[7] T. Schrefl, J. Fidler, K. J. Kirk and J. N. Chapman, J. Magn. Magn. Mater. **197** 193 (1997).

[8] R. D. McMichael, J. Eicke, M. J. Donahue and D. G. Porter, J. Appl. Phys. **87** 7058 (2000).

[9] M. Ruhrig, B. Khampsehpour, K. J. Kirk, J. N. Chapman, P. Aitchison, S. McVitie and C. D. Wilkinson, IEEE Trans. Magn. **32** 4452 (1996).

[10] X. Zhu, P. Grütter, V. Metlushko and B. Ilic, Phys. Rev. B **66** 024423 (2002).

[11] T. R. McGuire and R. I. Potter, IEEE Trans. Magn. **11** 1018 (1975).

[12] A. B. Oliveira, S. M. Rezende and A. Azevedo, Phys. Rev. B **78** 024423 (2008).

[13] T. Taniyama, I. Nakatani, T. Yakabe and Y. Yamazaki, Appl. Phys. Lett. **76** 613 (2000).

[14] J. L. Tsai, S. F. Lee, Y. D. Yao, C. Yu and S. H. Liou, J. Appl. Phys. **91** 7983 (2002).

[15] http://llgmicro.home.mindspring.com/.

[16] M.-F. Lai, Z.-H. Wei, C.-R. Chang, J. C. Wu, J. H. Kuo and J.-Y. Lai, Phys. Rev. B **67** 104419 (2003).

[17] T. Haug, K. Perzlmaier and C. H. Back, Phys. Rev. B **79** 024414 (2009).

[18] T. Haug, A. Vogl, J. Zweck and C. H. Back, Appl. Phys. Lett. **88** 082506 (2006).

[19] A. Himeno, T. Okuno, T. Ono, K. Mibu, S. Nasu and T. Shinjo, J. Magn. Magn. Mater. **286** 167 (2005).

[20] M. Stäerk, private communication (2010).

# 4

# Pinning Vortex Domain Walls using Wires of Varying Width

## 4.1 Introduction

The previous chapter illustrated that a certain degree of control over the behaviour of domain walls can be achieved by patterning 90° corners into an otherwise straight wire. The structure of the domain walls was highly reproducible however the external magnetic fields required to create and annihilate them were variable from one structure to another. In this chapter an alternative method of controlling domain walls is explored. Straight magnetic wires are investigated here and a variation in the wire width, i.e. either a constriction or protrusion is used as a means of controlling domain walls propagating along the wire. Vortex domain walls are expected to form in the straight segments of these wires, however the local energy landscape will change in regions where the wire width varies and more complex domain wall configurations are expected.

Various techniques have recently been used to investigate the interaction of domain walls with notches and anti-notches including MOKE magnetometry [1–3], where the the interaction of domain walls in triangular and semi-circular notches and anti-notches were investigated. It was found that the depinning field generally increased with increasing trap depth [1]. Additionally the strength of pinning was found to depend on the notch geometry and the chirality of the incoming domain wall [2]. Allwood et al. [3] demonstrated the use of a triangular shaped anti-notch as a domain wall diode, a geometry only allowing the propagation of a domain wall in one direction along a nanowire. This may be particularly advantageous for domain wall experiments where precise control over the location of a domain wall is desirable or for memory applications that may benefit from an intrinsically defined propagation direction through the diode.

Recent studies utilising micromagnetic simulations have revealed order-of-magnitude differences in the depinning fields of oppositely magnetised walls travelling in the same direction through a diode [4]. Furthermore, in one study [5], only domain walls of a specific chirality were pinned by a triangular notch. This geometry may be used as a highly effective domain wall chirality filter. Another study has modelled the effect of the notch angle on the formation of a domain wall in a triangular notch structure for various materials [6], which was found to have a significant effect on the resulting domain wall structure in some cases. Additionally, the interaction of domain walls with notches under the influence of spin-polarised currents and magnetic fields has also been modelled where a phase diagram has been developed to describe the effect on a domain wall trapped at a notch depending on the magnitude of the field and current [7].

Magnetic imaging techniques have recently been used to reveal the magnetic structure of both vortex and transverse domain walls pinned at triangular [8–10] and rectangular [11] notches. The asymmetric nature of vortex domain wall pinning was clearly revealed when both wall chiralities are incident on a triangular notch in one study using Lorentz microscopy [8]. The magnetic structure of both vortex and transverse domain walls at a triangular notch have been imaged using magnetic force microscopy (MFM), where it was also demonstrated that the form of the wall including its chirality could be readily detected from its unique resistance value [9]. Photoemission electron microscopy has also been used to image the pinning of domain walls at triangular notches along permalloy wires [10], where vortex domain walls were observed with different chiralities in successive experiments. This study also highlights the stochastic nature of domain wall injection. The effectiveness of an elongated rectangular notch has also been probed using MFM, where multiple stable locations for a pinned domain wall were found [11]. This is significant when considering various geometries for use in magnetic memory devices involving pinning domain walls at specific locations along nanowires.

Finally, electrical measurements, based on the GMR effect, have been used to detect the occurrence and motion of a domain wall in a nanowire containing a triangular notch [12] or anti-notch [13]. The depinning field was found to depend on the direction of motion of the domain wall along the wire in the case of the anti-notch, similar to that observed for a domain wall diode [3].

Although numerous studies have been carried out to investigate the interaction of domain walls with notches and anti-notches, the precise evolution of a domain wall as it progresses through an artificial pinning site has not been directly observed. In this chapter, Lorentz microscopy has been used to directly observe the interaction of vortex domain walls with various lithographically defined constrictions and protrusions, referred to hereafter as notches and anti-notches, respectively.

## 4.2 Pinning vortex domain walls with asymmetric notches

The micromagnetic structure of a domain wall is determined by an energy minimisation process that includes various material dependent properties in addition to the material geometry. The nanowires studied in this chapter are made from permalloy ($Ni_{80}Fe_{20}$), therefore the magnetisation is largely constrained by magnetostatic effects and tends to align parallel with the edges of the structure. When structural features such as notches are patterned along the wire, the local spin structure tends to align along the edges of these features. A notch or anti-notch therefore comprises a particular spin structure which can present either a potential barrier or a well and in some cases a combination of both, to an incoming domain wall depending on its micromagnetic spin structure. The behaviour of vortex domain walls propagating along a nanowire containing a narrower section of wire, i.e. a notch, will be investigated in the following section.

### 4.2.1 Formation of a head-to-head domain wall

In order to study the interaction of domain walls with a notch, it is essential to have a reproducible method of nucleating domain walls. The geometry used here was designed to achieve this and consists of a rectangular nucleation pad attached to a 17 $\mu$m long nanowire with a tapered end, as depicted in figure 4.1. The advantage of including a tapered end to a wire was introduced in chapter 3 and prevents end domains forming at the far end of the wire, which may reduce the reversal field. Prior to domain wall injection, the magnetisation in the wire was set by the application of a magnetic field

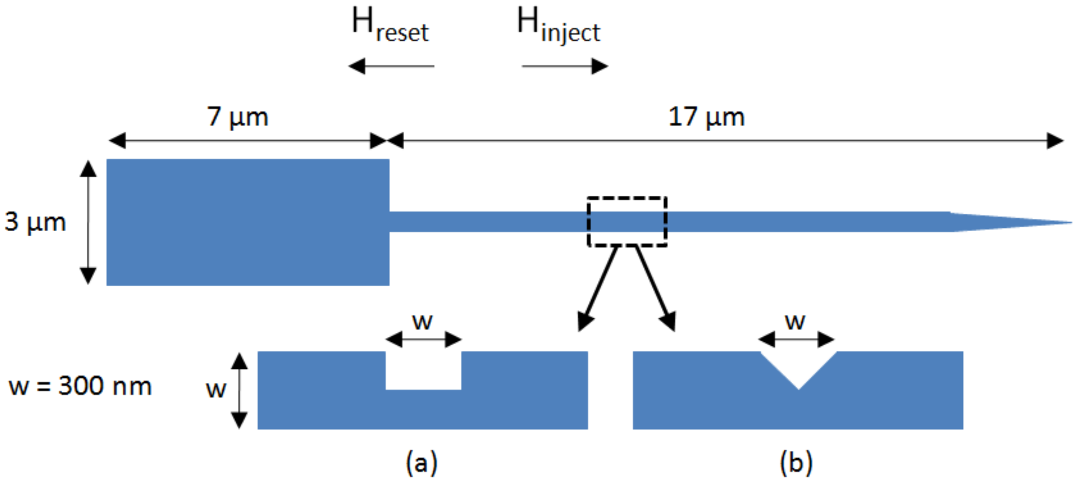

Figure 4.1: A schematic diagram of the wire geometry used to study the interaction of vortex domain walls with (a) rectangular and (b) triangular constrictions. The notch depth is approximately 50% of the wire width. The length of the wire is 17 $\mu$m. The width of the notch is equal to the wire width.

along the direction indicated by $H_{reset}$ in figure 4.1. This ensured that the magnetisation in the wire was uniform with no domain wall at the notch prior to experiment. The rectangular injection pad possesses a lower coercivity than the wire, therefore it reverses at a lower field than the wire and is used to inject a domain wall into the wire. A domain wall was injected by applying a magnetic field ~12 Oe along the direction indicated by $H_{inject}$. The injected wall immediately travelled to the notch (indicated by the dashed line) and was pinned by it, however on removal of the field, the structure of the wall could be identified easily. The form of the domain walls injected into these wires were vortex domain walls, which is the predicted domain wall configuration for a straight wire of these dimensions, as illustrated in the domain wall phase diagram in figure 4.2. It is possible to control the chirality of the injected domain wall using this geometry with the application of a small transverse field [5], however this was not employed in the experiments performed here. A deliberately fabricated pinning feature, in the form of either a triangular or rectangular notch, was patterned along one side of the wire, figures 4.1a,b. The nanowires were 12 nm thick and were fabricated by electron beam lithography and lift off techniques, as described in chapter 2. The wire width was nominally 300 nm with a notch width equal to the wire width and a depth approximately 50% of the wire width.

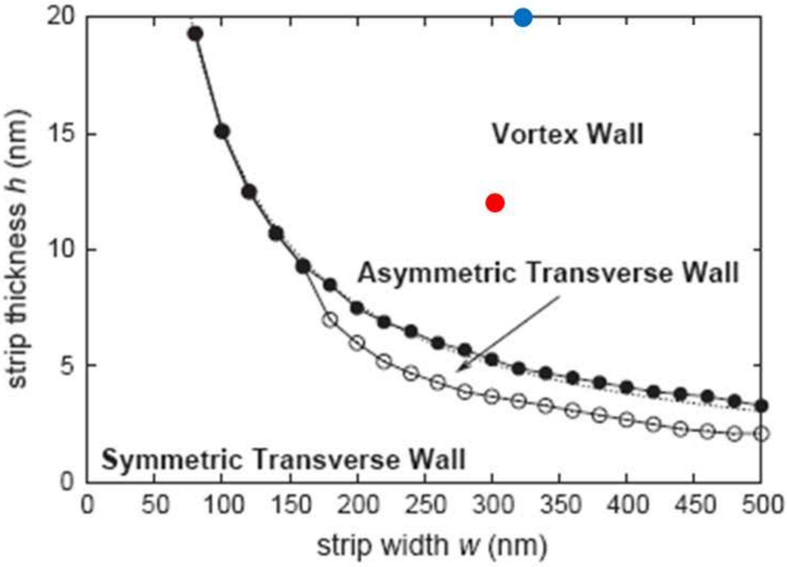

Figure 4.2: The red circle indicates the location within the domain wall phase diagram of this wire geometry. The blue circle refers to the wires studied in section 4.3. Plot taken from Y. Nakatani et al J. Magn. Magn. Mater. **290** (2004).

### 4.2.2 Vortex domain wall interaction with triangular traps

Fresnel imaging was initially used to characterise the magnetic behaviour of these wires, however the domain wall contrast was weak due to the reduced thickness of the structures. DPC imaging was therefore used to characterise the magnetic behaviour and also to clearly identify the domain wall structures. Additionally, OOMMF micromagnetic modelling, carried out by Lara Bogart at the University of Durham, was used to investigate the interaction of domain walls with the notches. In the simulation, standard parameters for permalloy were employed as discussed in chapter 1, section 1.8. As described above, a magnetic field of 12 Oe was required to inject a wall into the wire. The field was then removed and the form of the injected wall was inspected at remanence. The field was then increased to observe the propagation of the domain wall through the trap. Each experiment was repeated 5 times to determine the reproducibility of the interaction. The simulations were set up in a similar way; the field was removed once the wall was pinned at the notch, the field was then increased in steps of 2 Oe until the wall had depinned.

Figure 4.3 shows the interaction of a clockwise (cw) and counterclockwise (ccw) vortex domain wall with a triangular notch. As a result of the lack of control over the chirality of the injected domain walls, the cw and ccw vortex domain walls were observed in different wires. Furthermore, the wire in which a ccw vortex domain wall was observed had a larger notch depth than for the wire where a cw vortex domain wall was observed. On measuring the dimensions of each notch, it was found that the depth of the triangular notch was 131 nm for the cw case and 208 nm for the ccw case. The simulation of the ccw vortex domain wall was therefore carried out in a wire with a greater depth of notch, a value of 75% of the wire width was used. In each sub-figure, the uppermost colour image is the experimental DPC image, a corresponding calculated image and schematic are given below. In figure 4.3a, I and II are the orthogonal greyscale induction images along the x and y axes, respectively; III is the corresponding colour induction map calculated from I and II, as described in chapter 2.4.6. At remanence, both a cw (figure 4.3a) and a ccw (figure 4.3c) vortex domain wall were pinned on the left side of the notch, i.e. the side nearest the injection pad. The calculated DPC images below are in good agreement with the experimental images. With the application of a magnetic field, figure 4.3b, the vortex core moved downwards towards the lower edge of the wire as indicated by the arrows in figures 4.3a,b; the leading part of the domain wall was still pinned at the same location. The extent of the wall visibly reduced and the wall depinned abruptly at 18 ± 2 Oe. In the simulations, the wall also abruptly depinned from the notch but at a significantly higher field value of 84 Oe.

In figure 4.3c, the central wall of the ccw vortex domain wall is approximately parallel with the left edge of the notch, confirmation of this is given by the schematic below. The leading wall is pinned at the notch apex and the wall does not extend beyond this point. As the applied magnetic field was increased, figure 4.3d, the core of the vortex was forced upwards due to the growth of the domain favourably aligned with the field, i.e. the lower part of the wall. The ccw vortex domain wall significantly

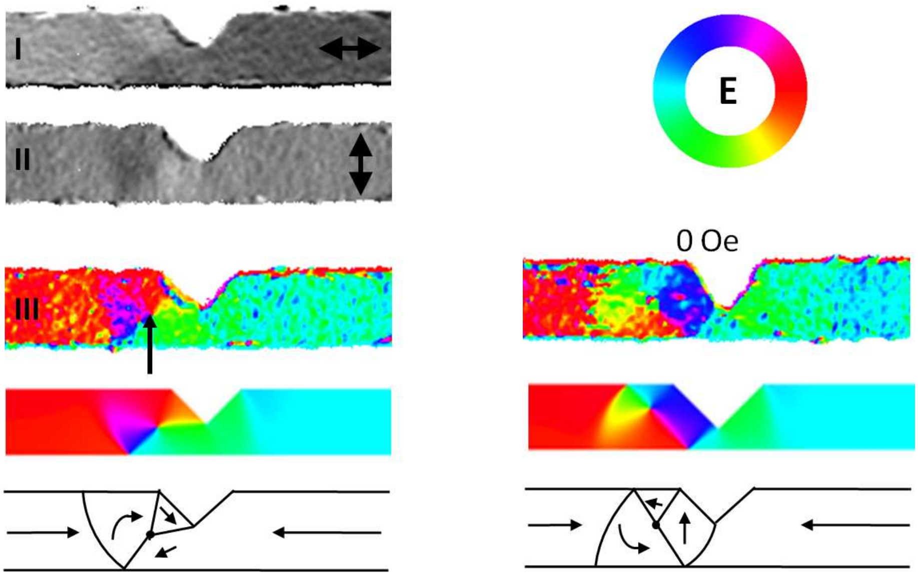

(a) 0 Oe

(c) 0 Oe

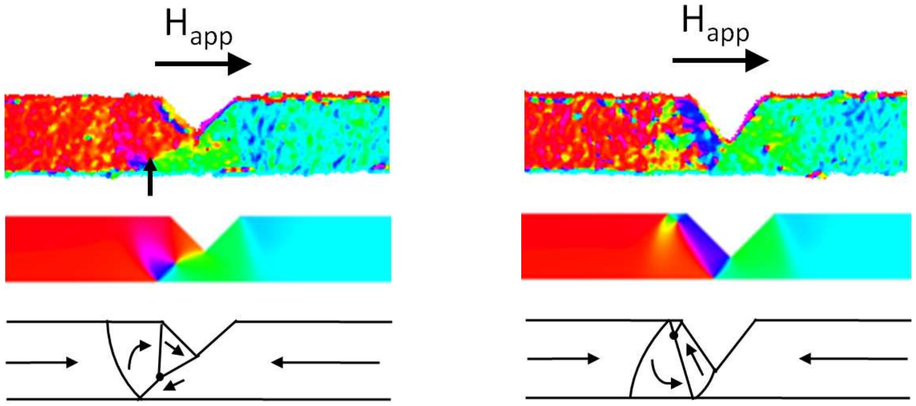

(b) In-situ field is 15 Oe, simulated field is 82 Oe. Wall depins at 84 Oe (simulation) and 18 Oe (experiment).

(d) In-situ field is 27 Oe, simulated field is 78 Oe. Wall depins at 190 Oe (simulation) and 31 Oe (experiment).

Figure 4.3: I and II are the two greyscale images mapping the magnetic induction in the x and y directions, respectively. III is the colour induction map calculated from I and II. The images show the interaction of a cw and ccw vortex domain wall with a triangular notch. Images (a) and (c) show the domain wall pinned at remanence, (b) and (d) illustrate the behaviour prior to depinning. Calculated DPC images and schematics of the magnetisation are also included. The colour wheel is given by E.

distorted at a field of 27 Oe as the vortex core was displaced to the upper edge of the wire. As observed in the cw vortex domain wall case, the wall did not travel further than the notch apex, and a significantly higher field of 31 ± 2 Oe was required to depin the ccw vortex wall from this notch. The simulation predicted that at a field of 90 Oe, the ccw vortex domain wall completely lost its original structure and transformed to a transverse domain wall, as illustrated in figure 4.4. A considerable field of 190 Oe was required to depin it from this notch. A summary of the experimental and simulated depinning fields of the cw and ccw vortex domain walls from both notches

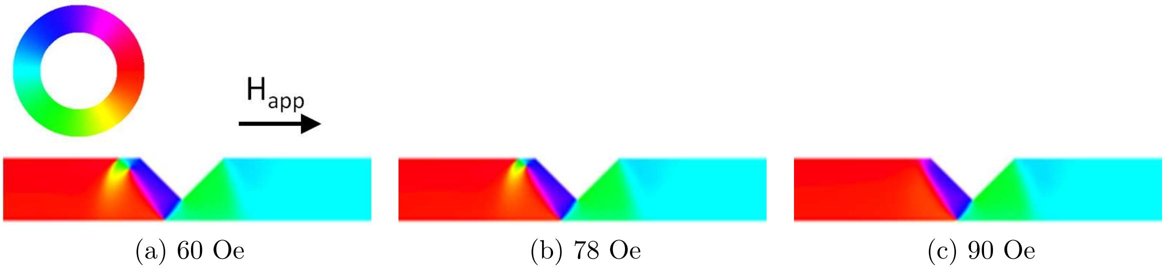

(a) 60 Oe (b) 78 Oe (c) 90 Oe

Figure 4.4: A series of DPC colour images illustrating the expulsion of the vortex core as the ccw vortex domain wall is transmitted through the triangular notch. At a field of 90 Oe, the vortex domain wall transforms to a transverse domain wall.

is given in table 4.1. From the simulation, the field at which the ccw vortex domain wall transformed to a transverse domain wall is included, however this field could not be determined experimentally.

| | Triangular notch | | | Rectangular notch | | |
|---|---|---|---|---|---|---|
| | Experiment | Simulation | | Experiment | Simulation | |
| | Depin | Transform | Depin | Depin | Transform | Depin |
| cw | 18 ± 2 | - | 84 | 24 ± 2 | - | 84 |
| ccw | 31 ± 2 | 90 | 190 | 22 ± 2 | 66 | 170 |

Table 4.1: Table of depinning fields, in Oe, of cw and ccw vortex domain walls from triangular and rectangular notches obtained from both experiment and simulation.

It is evident that under an applied field, the core of the vortex domain wall travels either downwards (figure 4.3b) or upwards (figure 4.3d) depending on the alignment between the direction of the applied field and the magnetisation either above or below the vortex core, respectively. This is illustrated schematically in figure 4.5.

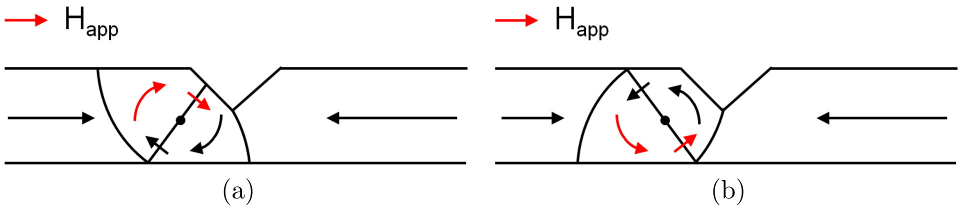

(a) (b)

Figure 4.5: Schematic illustration of the movement of the vortex core prior to depinning. The red arrows within each vortex domain wall are favourably aligned with the applied field hence this domain increases in size with an increasing field. Consequently, the vortex core in (a) travels downwards and in (b) travels upwards.

### 4.2.3 Vortex domain wall interaction with rectangular traps

The significance of the shape of the notch was then explored and a more abrupt geometry, namely a rectangular notch, was used to pin domain walls. Figure 4.6 illustrates

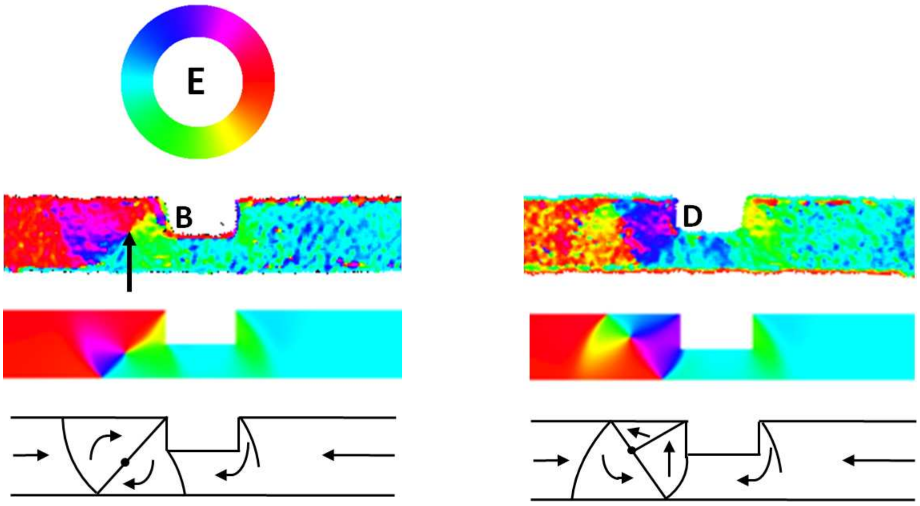

(a) 0 Oe

(c) 0 Oe

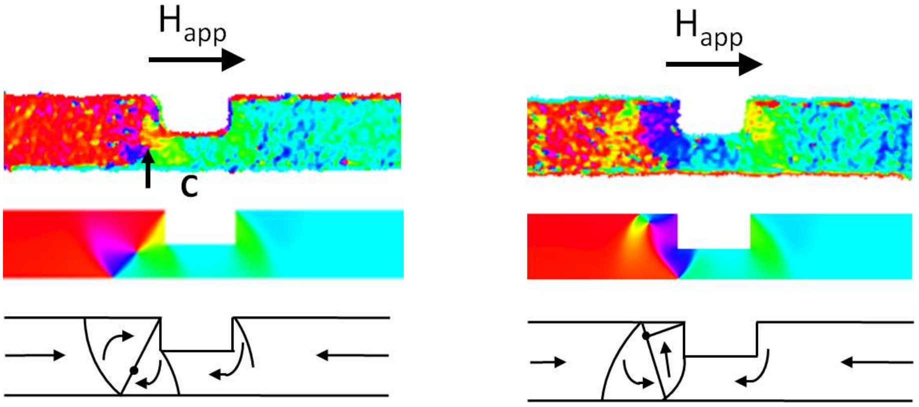

(b) In-situ field is 21 Oe, simulated field is 82 Oe. Wall depins at 84 Oe (simulation) and 24 Oe (experiment)

(d) In-situ field is 18 Oe, simulated field is 60 Oe. Wall depins at 170 Oe (simulation) and 22 Oe (experiment)

Figure 4.6: DPC colour images showing the interaction of a cw and ccw vortex domain wall with a rectangular notch. Images (a) and (c) show the domain wall pinned at remanence, (b) and (d) illustrate the behaviour under an applied field. Calculated DPC images and schematics of the magnetisation are also included. The colour wheel is given by E.

the interaction of a cw (figures 4.6a,b) and ccw (figures 4.6c,d) vortex domain wall with such a notch. The experiments were performed in the same way as for the triangular notch, that is the field was removed after nucleation to study the injected wall structure. Subsequently, the field was increased to observe the propagation of the domain wall through the notch. At remanence, the vortex wall was again pinned on the left side of the notch in both cases; the abrupt edge of the notch prevented the vortex walls from travelling beyond this point. In both cases the leading wall of each vortex domain wall was pinned by the leading edge of the notch, indicated by **B** and **D** in figures 4.6a,c. As the magnetic field was increased, the experimental image illustrates very clearly that the core of the cw vortex domain wall moved downwards, again indi-

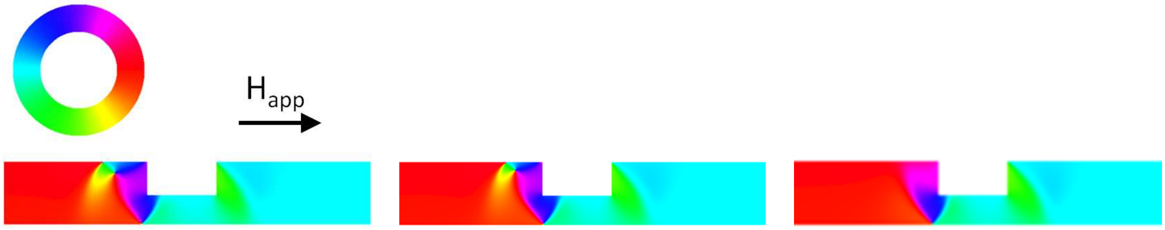

(a) 48 Oe (b) 60 Oe (c) 66 Oe

Figure 4.7: A series of DPC colour images illustrating the expulsion of the vortex core as the ccw vortex domain wall is transmitted through the rectangular notch. At a field of 66 Oe, the vortex domain wall transforms to a transverse domain wall.

cated by the arrows, whilst the wall compressed significantly at a field of 21 Oe. The geometry of the notch however only allowed for modest penetration of the leading wall into the notch at **C**, figure 4.6b. A modest field of 24 ± 2 Oe was required to depin the cw vortex wall in experiment, however a field of 84 Oe was predicted by simulation, see table 4.1.

The ccw vortex domain wall behaved in a similar manner in both a triangular and rectangular notch under an applied field. At a field of 18 Oe the wall width reduced whilst simultaneously forcing the vortex to the upper edge of the wire, significantly distorting the original wall structure, figure 4.6d. At an applied field of 22 ± 2 Oe, the ccw vortex domain wall abruptly depinned from the notch. The movement and subsequent expulsion of the vortex core out of the wire is again illustrated by the simulation in figure 4.7. No significant difference in depinning field of the cw and ccw vortex domain walls was observed for the rectangular notch, however the simulation predicted that the ccw wall was depinned at a field of 170 Oe.

### 4.2.4 Discussion

In all cases, the notch effectively interrupted the propagation of the domain wall along the wire, as the domain wall did not travel beyond the extent of the constriction following injection into the wire. In the case of cw vortex domain walls, the vortex core travelled downwards towards the lower edge of the wire under an increased field, prior to depinning from the notch. In the case of ccw vortex domain walls, the vortex core travelled towards the upper edge of the wire under an applied field, hence the domain wall changed structure more significantly before depinning, appearing with a largely transverse structure due to the large displacement of the vortex core. These experiments also demonstrated that the interaction is relatively insensitive to the notch geometry.

The triangular notch provided a stronger pinning for a ccw vortex domain wall than for a cw vortex domain wall, however on closer inspection of the notch geometry, it was clear that there was a significant difference in the notch depth. It has been well established that the depinning field of a domain wall increases with increasing notch depth [1], therefore the observed difference in depinning field for a ccw vortex domain wall may be largely attributed to a deeper constriction rather than the wall spin structure. The simulation predicted that a field of 168 Oe is required to depin a ccw from a 50% notch depth. However, this figure rises to 190 Oe when the notch depth is 75%. No difference in the depinning field for a cw and ccw vortex domain wall from a rectangular notch was observed within the precision of the applied field. This was not predicted by the simulation, where a field approximately twice as large was required to depin a ccw than a cw vortex domain wall from a rectangular notch.

As introduced in the previous chapter, it is expected that the depinning fields will be lower experimentally as OOMMF does not include thermal effects on the magnetisation. One study has reported a strong temperature dependence of the depinning field of domain walls from triangular notches [14]. Additionally, in chapter 3, the effect of the out-of-plane field, present in the in-situ magnetising experiments, was investigated and was found to have a negligible effect on the switching field. The discrepancy observed here is therefore attributed to temperature dependent effects. Although the depinning fields have not been accurately predicted by the OOMMF simulations, the qualitative behaviour is in good agreement with that observed experimentally.

## 4.3 Pinning vortex domain walls with symmetric anti-notches

It is evident that the spin structure of an incoming wall is the main feature responsible for the type of interaction a domain wall undergoes with a trap. Here the effect of altering the local energy landscape in a slightly different way is investigated, in this case by patterning protrusion i.e. an anti-notch, on both sides of the wire. The anti-notch is symmetric in this case and also allows the magnetisation to deviate from the mean direction in the straight part of the wire. Additionally, the method of domain wall nucleation used in the previous section provided no control over the chirality of the injected domain wall, the method used here aims to generate a certain degree of control.

### 4.3.1 The symmetric triangular anti-notch structure

In order to gain more control over domain walls, it is desirable to have a method of domain wall nucleation that is separate from domain wall propagation. The geometry used in the previous section utilised a uniaxial field to inject a domain wall into the wire which subsequently travelled towards the pinning site. The geometry used here required a pair of orthogonal fields to firstly nucleate a domain wall at a specific location

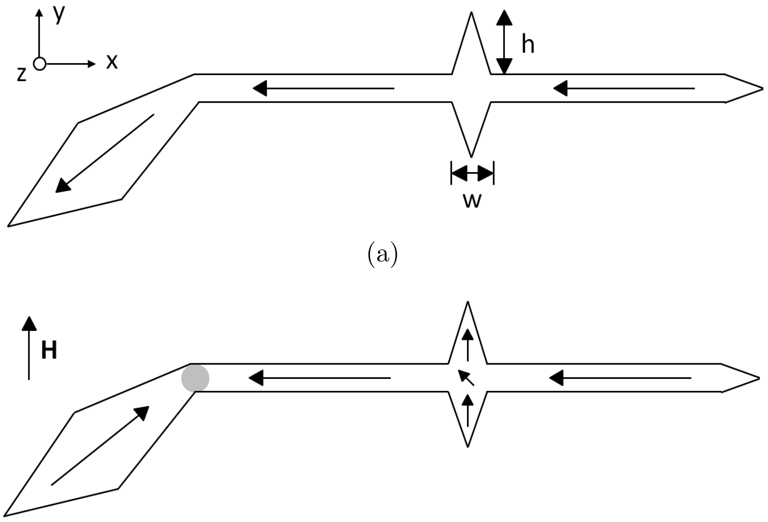

(a)

(b)

Figure 4.8: (a) A schematic of the wire containing an anti-notch in the as-grown state. The application of a hard axis field reverses the magnetisation within the pad and generates a domain wall at the pad-wire junction, (b).

and secondly to drive it towards the trap. It consisted of a diamond shaped nucleation pad connected to a wire of width 320 nm with a symmetric triangular anti-notch patterned half way along its length, as shown in figure 4.8a. The wires were 20 nm thick, therefore vortex domain walls were expected to form, indicated by the blue point in figure 4.2. The interaction of vortex domain walls with a pair of anti-notches of heights 100 nm and 675 nm with a fixed width of 400 nm were initially investigated. In subsequent experiments however, the effect of varying the width of the anti-notch was also investigated. The anti-notches are characterised by their width $w$ and height $h$, and will be referred to as $(w,h)$ anti-notches with $w$ and $h$ specified in nanometers. The diamond shaped nucleation pad was situated at one end of the wire; the method of domain wall nucleation is explained in the next section. The other end of the wire was tapered to avoid domain wall nucleation from this end, as discussed previously. The shape anisotropy associated with the wire and nucleation pad ensured that, at remanence, the magnetisation was directed along the long axis of the wire and along the length of the pad, as indicated by the arrows in figure 4.8a. Although the magnetisation is directed from left to right in this figure, it is equally likely that the opposite case would form as-grown. Starting from the configuration in figure 4.8a, a domain wall was formed between the pad and wire by the application of a magnetic field along the direction indicated in figure 4.8b. It is also important to note that the direction of magnetisation within the anti-notch (where h = 675 nm) was also set by the nucleation field, as illustrated by the arrows in figure 4.8b.

### 4.3.2 Formation of a head-to-head domain wall

The initial magnetic configuration of the anti-notch was a quasi-uniform state with no domain wall where the wire joins the pad. A Fresnel image of this configuration is given in figure 4.9a, where the thick dark Fresnel fringe runs along the upper edge of the wire and diamond nucleation pad. Formation of a domain wall was achieved by applying a magnetic field of ~300 Oe close to the y-axis and then removing it. The magnitude of the applied field was not large enough to saturate the structure but was sufficient to nucleate a domain wall by switching the magnetisation of the diamond nucleation pad.

From 100 nucleations along this direction, involving 20 wires each subjected to appropriate field sequences 5 times, a transverse domain wall was nucleated 68% of the time, a Fresnel image of this outcome is shown in figure 4.9b. The thicker fringe now runs along the lower edge of the pad at **E**, indicating the magnetisation within this area

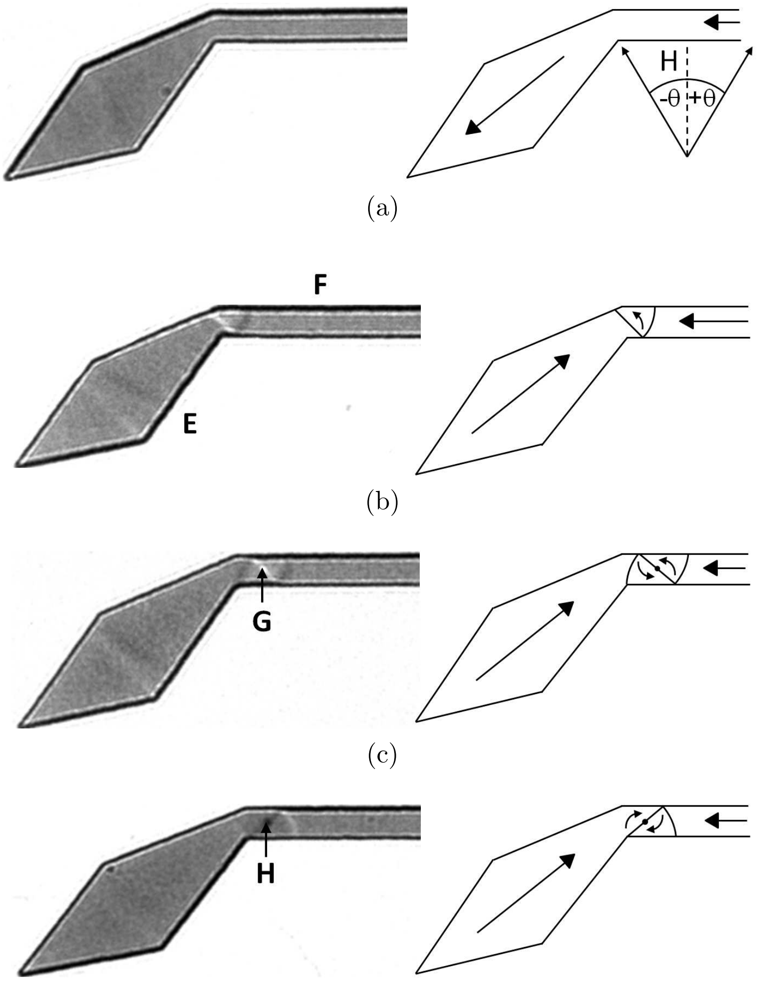

(a)

(b)

(c)

(d)

Figure 4.9: Fresnel images of (a) the wire in the quasi-uniform state and the various domain walls nucleated at the pad-wire junction which consist of (b) a transverse domain wall, (c) a counterclockwise and (d) a clockwise vortex domain wall

has reversed. The dark Fresnel fringe is still present along the upper edge of the wire at **F**, consistent with a domain wall appearing at the junction. In the remaining 32% of injections, a counterclockwise (ccw) vortex domain wall was produced, figure 4.9c. The appearance of the vortex core, i.e. white in this case indicated by **G**, is indicative of the sense of rotation of magnetisation around it. Additionally, under a small field in the x-direction the transverse domain wall transformed into a ccw vortex domain wall as it moved into the uniform section of the wire. The direction of the nucleation field was subsequently varied to investigate the types of domain walls supported by this structure [15]. Ten field orientations counterclockwise from the y-axis and five clockwise from the y-axis were investigated where each structure was subjected to a field along the x-axis to generate a quasi-uniform state, then a field was applied close to the y-axis and removed. Observations were made in zero field. The results can be seen in figure 4.10.

It can immediately be seen that the most common wall type to form at this junction is a transverse domain wall, referred to here as an 'up' transverse domain wall due to the direction of magnetisation within its central domain. By rotating the direction of field away from the y-axis in a clockwise direction (positive values of $\theta$ in figure 4.10) by just one degree, the probability of nucleating a ccw vortex domain wall increased by 10%; the probability of nucleating a transverse domain wall fell by 27%. In the remaining 17% of nucleations, the domain wall formed in the anti-notch. On increasing the

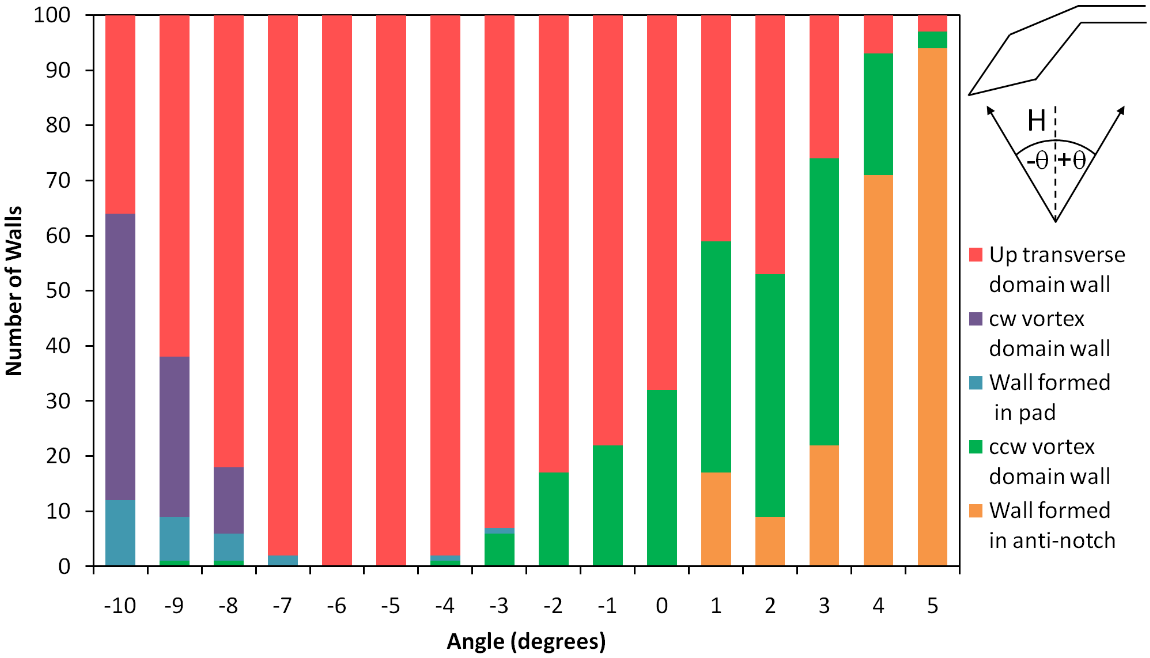

Figure 4.10: The frequency of nucleating each wall type for a variety of field orientations close to the y-axis. The angles are measured with respect to the element short axis, as illustrated in figure 4.9a. Angles above +5° were not investigated as it was assumed that most of the walls would form in the anti-notch.

nucleation field angle further, the probability of nucleating a ccw vortex domain wall increased steadily until a tilt angle of 4° and 5° where the probability dropped to just 22% at 4° and 3% at 5°. The probability of the wall forming in the anti-notch however increased to 71% and 94%, respectively. Field angles above 5° were not investigated as it was assumed that most of the walls would form in the anti-notch.

By rotating the direction of the field in a counterclockwise direction, the probability of nucleating a ccw vortex domain wall decreased steadily to zero at an angle of -5°, where, at this angle and at -6°, a transverse domain wall formed in every case. As the field angle was increased further, the number of transverse domain walls nucleated decreased to 36% at -10°. At -8°, 12% of nucleations resulted in a cw vortex domain wall, a Fresnel image is given in figure 4.9d. This number increased steadily to 52% at -10°, as did the number of domain walls that formed in the nucleation pad.

The processes leading to the formation of a cw and a ccw vortex domain wall are illustrated schematically in figure 4.11. With the application of a magnetic field at a small value of $-\theta$, a transverse domain wall forms in the corner of the wire, i.e. at the junction between the nucleation pad and wire, figure 4.11a(**I**). On removal of the field, the domain wall indicated by the dashed line becomes the central Néel domain wall of the resulting cw vortex domain wall. The remaining domain wall fades as the magnetisation rotates to align with this central Néel wall and a cw vortex wall is formed, figure 4.11a(**II**).

With the application of a magnetic field along the y-axis or at a small value of $+\theta$, a transverse wall forms in the straight part of the wire, figure 4.11b(**I**). The magnetisation in the small section of straight wire between the diamond pad and the transverse wall will rotate to align parallel with the straight edges of the wire and in some cases will rotate further to form a vortex domain wall, indicated by the blue domain wall and arrow in figure 4.11b(**II**). Figure 4.11b(**III**) is a schematic of the resulting ccw vortex

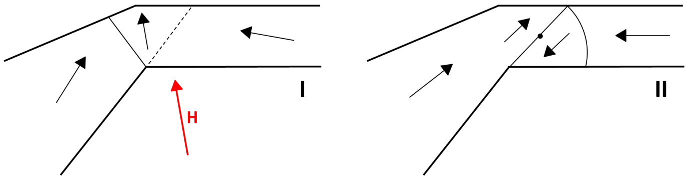

(a) Formation of a cw vortex domain wall

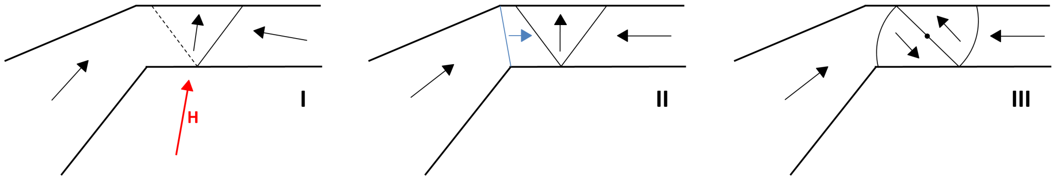

(b) Formation of a ccw vortex domain wall

Figure 4.11: Schematic illustration of the formation of (a) a cw and (b) a ccw vortex domain wall depending on the applied field orientation, highlighted in red.

domain wall.

### 4.3.3 Vortex domain wall interaction with triangular anti-notches

Following the domain wall nucleation process, the element was rotated by 90° in the TEM to apply a magnetic field to drive the domain wall towards, and eventually through, the anti-notch. Fresnel image sequences displayed in the following sections show the various wall transitions during propagation along the wire.

#### Interaction of vortex domain walls with a low anti-notch

The interaction of a cw and ccw vortex domain wall with a (400, 100) anti-notch is given in figures 4.12 and 4.13. At a relatively small field of 8 Oe, the cw vortex domain wall was driven into the anti-notch, figure 4.12a. Here the central 180° Néel wall spans diagonally across the anti-notch as the domain wall width (i.e. the extent of the complete domain wall packet) is comparable to the wire width. The domain wall structure did not change when the field was removed at this stage, indicating that the anti-notch acted as an effective potential well to the domain wall. Under an increased field, the vortex domain wall distorted significantly and extended beyond the anti-notch and into the far side of the wire, figure 4.12b. Simultaneously, the vortex core was forced further into the apex of the anti-notch prior to de-pinning at a field of 54 Oe, figure 4.12c. Here the domain wall contrast has disappeared and the dark edge fringe runs along the lower edge of the wire, confirming that magnetisation reversal has occurred. The behaviour observed is very similar for a domain wall of the opposite chirality, figure 4.13. Again, the anti-notch acted as a potential well to the incoming domain wall which easily entered it at a field of 13 Oe, figure 4.13a. At a field of

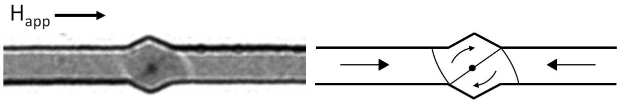

(a) 8 Oe

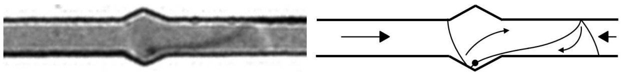

(b) 37 Oe

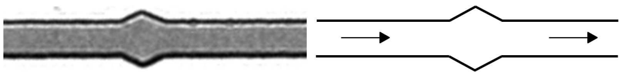

(c) 54 Oe

Figure 4.12: Fresnel image sequence of the cw vortex domain wall (a) inside, (b) being pulled away from and (c) depinned from the (400, 100) anti-notch along with corresponding schematics.

48 Oe, the leading domain wall extended a large distance beyond the anti-notch whilst the trailing wall was pinned by the apex of the anti-notch, (figure 4.13b). The domain wall de-pinned at a field of 57 Oe, figure 4.13c.

(a) 13 Oe

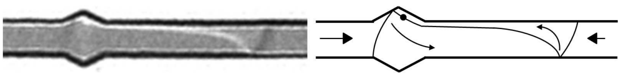

(b) 48 Oe

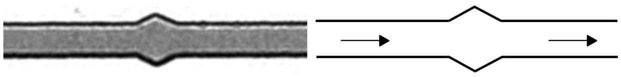

(c) 57 Oe

Figure 4.13: Fresnel image sequence of the ccw vortex domain wall (a) inside, (b) being pulled away from and (c) depinned from the (400, 100) anti-notch along with corresponding schematics. The observed behaviour is similar to that observed for the cw vortex domain wall.

### Interaction of vortex domain walls with a high anti-notch

The interaction of vortex domain walls with a high anti-notch differed considerably from that observed with a low anti-notch. Figure 4.14 shows a Fresnel image sequence of a cw vortex domain wall interacting with a (400, 675) anti-notch. At a field of 10 Oe, the wall approached the anti-notch but stopped in front of it, figure 4.14a. Here the anti-notch acted as a potential barrier to the incoming wall and prevented it from travelling beyond this point. As the field was increased, the vortex domain wall compressed slightly (figure 4.14b) whilst the vortex core simultaneously shifted downwards, before depinning occurred abruptly at a field of 60 Oe, figure 4.14c.

The ccw vortex domain wall interacted entirely differently with a (400, 675) anti-notch than its cw counterpart, figure 4.15. At a field of 13 Oe, the ccw vortex domain wall easily entered the anti-notch and completely lost its characteristic form in doing so, figure 4.15a. With a field of 48 Oe, the domain wall extended beyond the anti-notch in a similar sense to that in the (400, 100) anti-notch, figure 4.15b. The wall de-pinned from the anti-notch at 55 Oe, figure 4.15c.

This behaviour may be understood by considering the following. The initial field in the y-direction set the magnetisation in the 675 nm high anti-notch vertically upwards, confirmation of which is obtained by noting that the fringe is thicker on the right hand side of the anti-notch (locations **J** and **K** in figure 4.14b). For a cw vortex domain wall, the upwardly directed magnetisation in the anti-notch is opposite to that in the leading domain of the incoming wall (see figure 4.16a) and, as such, a prominent domain wall

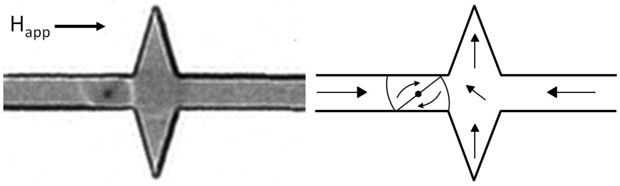

(a) 10 Oe

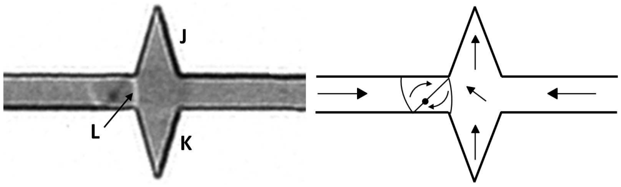

(b) 25 Oe

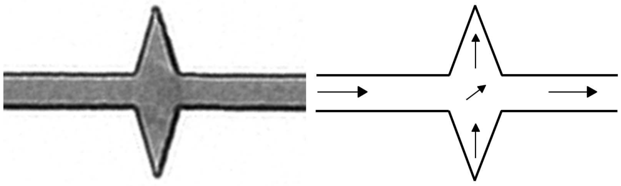

(c) 60 Oe

Figure 4.14: Fresnel image sequence of the ccw vortex domain wall (a) pinned outside the (400, 675) anti-notch, (b) with an increased magnetic field and (c) depinned from the anti-notch, along with corresponding schematics.

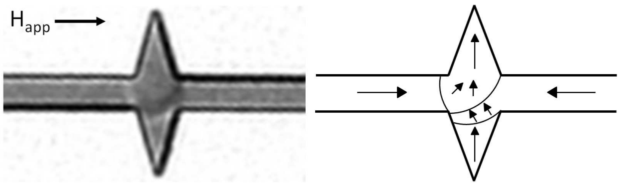

(a) 13 Oe

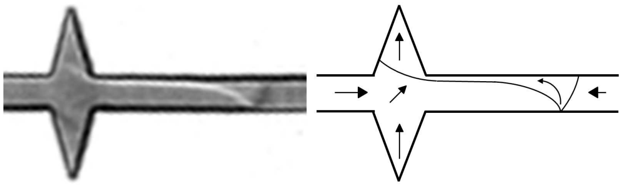

(b) 48 Oe

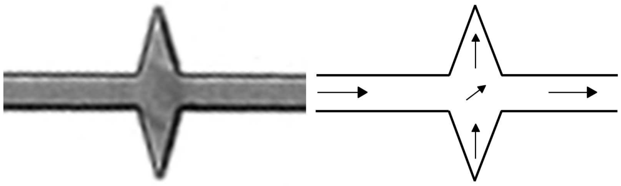

(c) 55 Oe

Figure 4.15: Fresnel image sequence of the cw vortex domain wall as it is being pulled away from and the (400, 675) anti-notch along with corresponding schematics.

formed at **L**, figure 4.14b. It is clear from the schematic in figure 4.14b that for the domain wall to enter the anti-notch, it would have to overcome the energy barrier constituted by the upwardly directed magnetisation within the anti-notch.

However, it is not energetically favorable for the cw vortex domain wall to enter the anti-notch and, as such, does not occur. By contrast, in the case of a ccw vortex domain wall incident on the same anti-notch, the magnetisation of the leading domain in the vortex domain wall has a component pointing perpendicularly upwards and hence in a similar sense to the magnetisation in the anti-notch, figure 4.16b. Thus the vortex domain wall enters the 400 nm wide anti-notch, albeit losing its original form in such a way that the total energy is reduced.

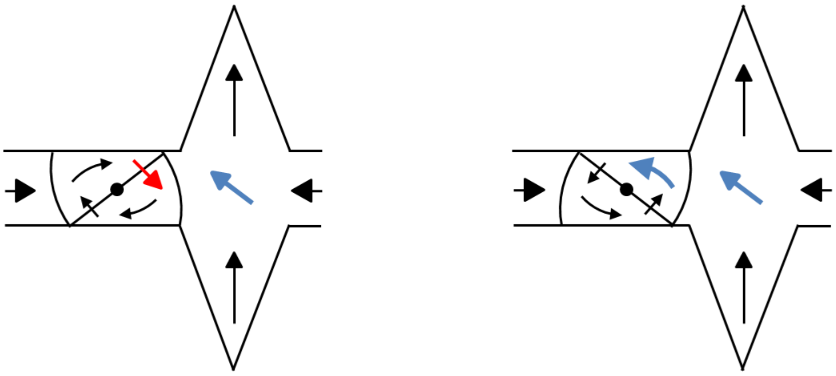

(a) cw vortex domain wall (b) ccw vortex domain wall

Figure 4.16: The relative orientation between the magnetisation in the leading domain of the vortex domain wall and the magnetisation within the anti-notch determines whether the anti-notch acts as a potential (a) barrier or (b) well.

OOMMF micromagnetic simulations were also performed to gain a better understanding of the modification of the domain walls as they progressed through the anti-notches. Standard parameters for permalloy were used with a square cell size with a side of 5 nm in the plane of the wire; a field increment of 5 Oe was used. From the simulations, the corresponding Fresnel images were also calculated using a defocus of 500 $\mu$m. For simplicity, only the magnetic contribution to the phase was included in the calculation. In the simulation, the domain wall was initialised to the left of the anti-notch and a field was applied to propagate it through the anti-notch.

In the case of the shallow anti-notch, figure 4.17, the ccw vortex domain wall was easily accommodated by the anti-notch where this configuration is shown at remanence, figure 4.17a. On increasing the field, the vortex core travelled upwards, further into the apex of the anti-notch, as observed in experiment (figure 4.17b). Simultaneously, the wall extended significantly into the far side of the wire, depinning at a field of 115 Oe (figure 4.17c). The interaction of a cw vortex domain wall with a (400, 100) anti-notch was not simulated as it was expected to be equivalent to the ccw case. There is good agreement between the calculated and experimental Fresnel images.

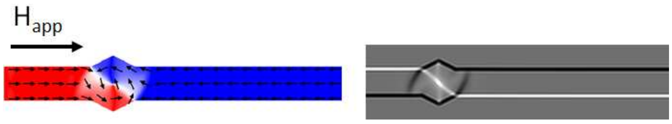

(a) 0 Oe

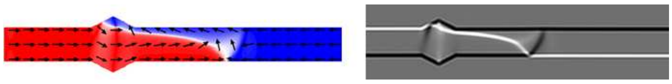

(b) 105 Oe

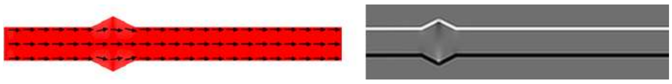

(c) 115 Oe

Figure 4.17: OOMMF simulation (left) and corresponding calculated Fresnel images (right) of the ccw vortex domain wall as it is being pulled away from and the (400, 100) anti-notch. The equilibrium position for the wall at remanence is inside the anti-notch and the wall distorts significantly before depinning.

Figure 4.18 shows the result of an OOMMF simulation of the cw vortex domain wall interacting with a (400, 675) anti-notch under an applied field. The corresponding calculated Fresnel images again at a defocus of 500 $\mu$m are included. After the initialisation of a cw vortex wall to the left of the anti-notch, a field of 25 Oe was required to drive the wall towards the pinning site, figure 4.18a. As observed in experiment, the wall did not enter the anti-notch and was instead pinned in front of it. With an increasing field, the vortex core moved progressively towards the lower edge of the wire (figure 4.18b) and abruptly depinned at a field of 175 Oe, figure 4.18c.

Figure 4.19 shows an OOMMF simulation of a ccw vortex domain wall interacting with the same anti-notch. The vortex domain wall was initialised to the left of the anti-notch and subsequently travelled towards and into the anti-notch at remanence, figure 4.19a. Here, the vortex core is not distinguishable and the wall has completely lost its vortex structure. As the field was increased, the magnetic configuration within the anti-notch changed noticeably and a domain wall started to emerge at a field of 95 Oe, figure 4.19b. The wall did not extend any further however and depinned at a field of 100 Oe, figure 4.19c. In experiment, a greater extension of this domain wall prior to depinning was observed, similar to that observed in figure 4.17b. The complete transformation of the domain wall on entering this anti-notch however is in good agreement with that observed experimentally.

As introduced earlier, it is expected that the depinning field values observed in experiment will be lower than those predicted by simulation due to the fact that the experiments were performed at room temperature [16]. Although the depinning fields have not been accurately predicted by the OOMMF simulations, the qualitative behaviour is in excellent agreement with that observed experimentally.

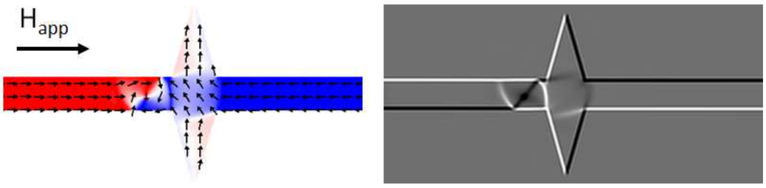

(a) 25 Oe

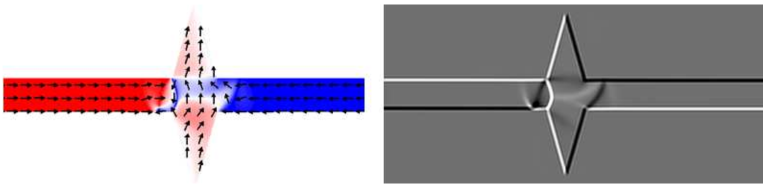

(b) 170 Oe

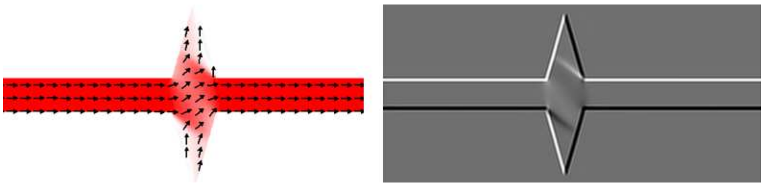

(c) 175 Oe

Figure 4.18: OOMMF simulation (left) and corresponding calculated Fresnel images (right) of the cw vortex domain wall interacting with a (400, 675) anti-notch. The wall does not enter the anti-notch.

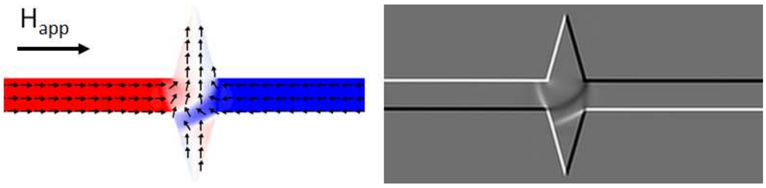

(a) 0 Oe

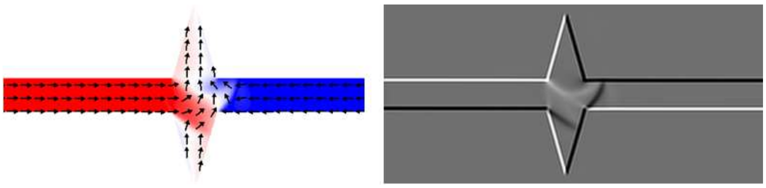

(b) 95 Oe

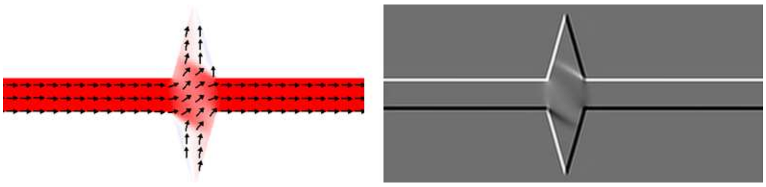

(c) 100 Oe

Figure 4.19: OOMMF simulation (left) and corresponding calculated Fresnel images (right) of the ccw vortex domain wall as it is being pulled away from the (400, 675) anti-notch. The equilibrium position for the wall at remanence is inside the anti-notch.

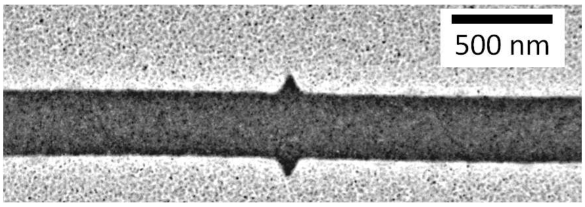

Figure 4.20: Bright field image of the (100, 100) anti-notch.

### 4.3.4 Variation of the anti-notch width

In the next set of experiments, the effect of reducing the width of the anti-notch from 400 nm to 100 nm was investigated, a bright field image of the (100, 100) anti-notch is given in figure 4.20. Figure 4.21 shows a ccw vortex domain wall interacting with a (100, 100) anti-notch. At a field of 10 Oe, the leading domain wall of the vortex domain wall entered the anti-notch, one end extending slightly beyond the anti-notch at **M**, while the other end remained on the original side at **N**. The trailing domain wall remained quite distant from the anti-notch and the overall geometry of the vortex domain wall was substantially unchanged, figure 4.21a. The behaviour of the domain wall under an increasing field is illustrated in figures 4.21b-4.21d. First the vortex core moved closer to the upper edge of the wire and the total domain wall structure compressed (figure 4.21b), then under a field of 34 Oe the vortex core could no longer be distinguished and one end of a wall was pinned in the upper part of the anti-notch, the remainder of the structure resembling an asymmetric transverse domain wall, figure 4.21c. A significant increase in field to 49 Oe was required to complete the reversal, figure 4.21d.

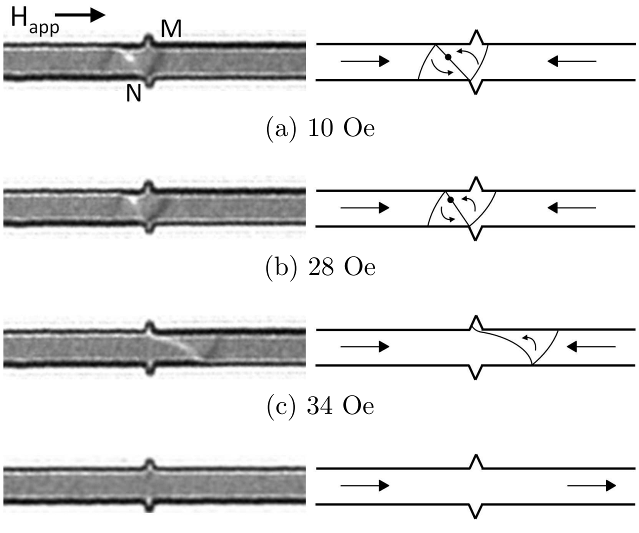

(a) 10 Oe

(b) 28 Oe

(c) 34 Oe

(d) 49 Oe

Figure 4.21: (a) Fresnel image of the ccw vortex domain wall pinned at the (100, 100) anti-notch. (b)-(d) Fresnel image sequence of the ccw vortex domain wall as the applied field is increased. Corresponding schematics are also included.

The behaviour of a cw vortex domain wall with a (100,100) anti-notch was more variable, figure 4.22. It was observed that the cw domain wall was pinned by the (100, 100) anti-notch in one of two similar but subtly different ways, figures 4.22a,d. In figures 4.22a, the cw vortex domain wall was pinned in front of the anti-notch in a similar manner to that observed in the ccw vortex domain wall case. In figure 4.22d however, the vortex domain wall stopped in front of the anti-notch and no part of the wall entered or extended beyond the anti-notch. As the field was increased, the behaviour observed was similar in both cases, that is the vortex core moved further down towards the lower edge of the wire, figures 4.22b,e. The configuration observed in figure 4.22b is equivalent to that observed for the ccw vortex domain wall. However, the domain wall did not emerge as a transverse domain wall in this case but was abruptly de-pinned at a field of 39 Oe, figure 4.22c. In figure 4.22e, the domain wall also compressed with an increased field however still no part of the vortex domain wall entered the anti-notch. In this case the anti-notch acted as a potential barrier, in a similar sense to that observed in the (400, 675) anti-notch. The domain wall abruptly depinned at a field of 51 Oe, figure 4.22f. In the majority of cases involving a cw vortex domain wall however, observed in 9 out of 15 experiments, most of the vortex domain wall passed through the anti-notch, and it was the trailing wall that was pinned at the lower part of the anti-notch, figure 4.22g. Here, the pinning was weaker than observed in any other case, with magnetization reversal being completed at a field of 24 Oe.

OOMMF simulations performed on these structures showed that a ccw vortex domain wall (figure 4.24a) is pinned by the lower part of the (100, 100) anti-notch, whilst

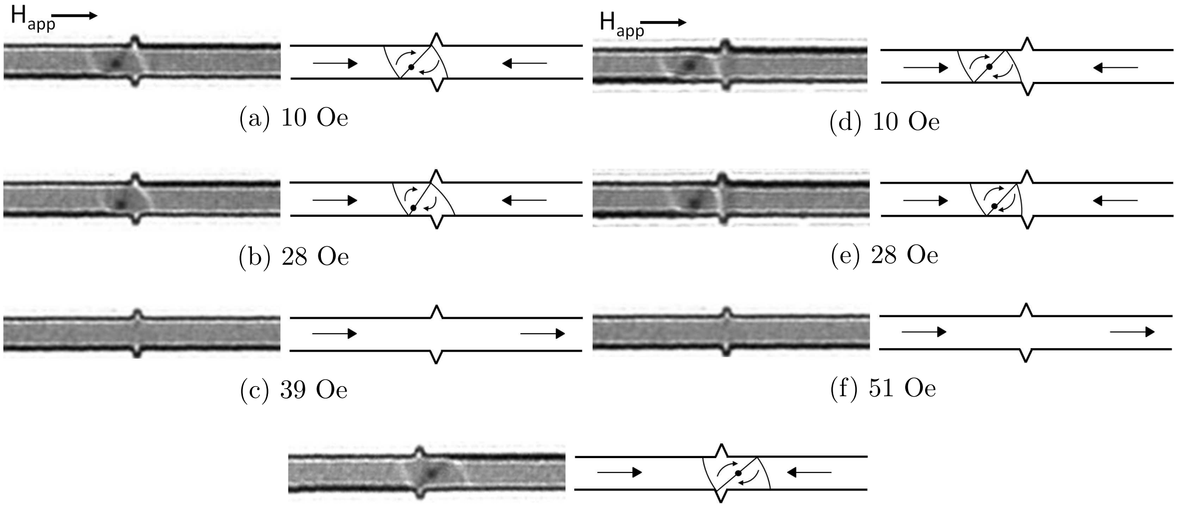

(a) 10 Oe

(d) 10 Oe

(b) 28 Oe

(e) 28 Oe

(c) 39 Oe

(f) 51 Oe

(g) 10 Oe

Figure 4.22: (a)-(c) Fresnel image sequence of the cw vortex domain wall being driven through the (100, 100) anti-notch. (d)-(f) Fresnel image sequence of the cw vortex domain wall being driven through the (100, 100) anti-notch in a subsequent experiment. (g) Fresnel image of the cw vortex domain wall pinned by its trailing wall, observed in a different experiment. Corresponding schematics are also included.

part of the leading wall extends beyond the anti-notch, as observed in experiment. A close-up of the magnetisation within the anti-notch is also given in each sub-figure. As the field was increased, the vortex core moved slightly upwards, figure 4.23b, but then the whole wall abruptly moved further along the wire whilst keeping its original structure; the vortex core moved downwards to occupy a more central location within the vortex domain wall. Now the trailing part of the wall is pinned by the upper part of the anti-notch (figure 4.23c); the magnetisation within the lower part of the anti-notch reversed during this process. The wall depinned from this configuration at a modest field of 50 Oe, figure 4.23d, where the magnetisation in the upper part of the anti-notch also reversed. The extent of the transformation undergone by the wall as observed in experiment, was not predicted by the simulation, however the key aspects of the pinning and depinning process were portrayed. The distortion of the

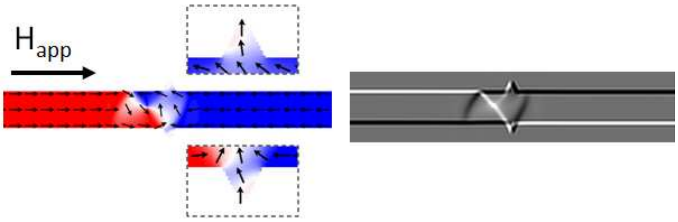

(a) 10 Oe

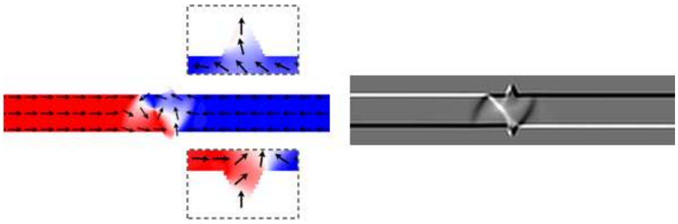

(b) 25 Oe

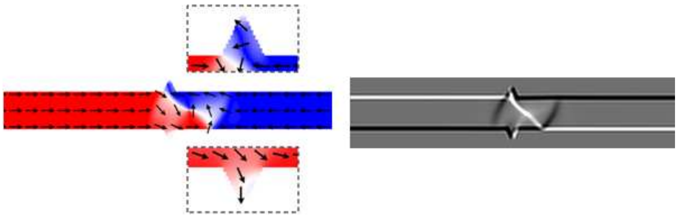

(c) 45 Oe

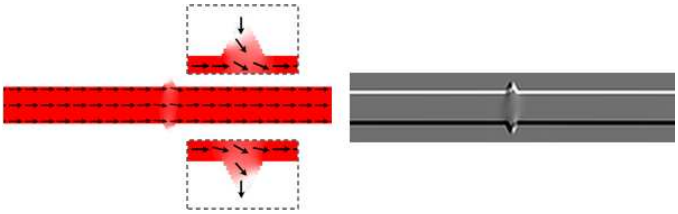

(d) 50 Oe

Figure 4.23: OOMMF simulation (left) and corresponding calculated Fresnel images (right) of the ccw vortex domain wall interacting with a (100, 100) anti-notch.

wall as it was pulled away from the anti-notch was slight compared with that observed experimentally, as the structure of the domain wall was largely preserved in the simulation. The magnetisation within the anti-notch was not preserved as the domain wall depinned, however this could not be compared with experiment as the magnetisation within the anti-notch could not be determined.

Figure 4.24 shows the results of an OOMMF simulation of a cw vortex domain wall interacting with a (100, 100) anti-notch. The leading wall does not enter into or extend beyond the anti-notch with the application of a small field to drive the wall towards it, figure 4.24a, however it may be observed that the magnetisation within both the upper and lower part of the anti-notch is directed vertically upwards. With an increased field, figure 4.24b, the wall compressed against the anti-notch with still no part of the wall extending beyond it. A large field of 115 Oe was required to depin the wall from the notch, figure 4.24c. That the interaction of a cw and a ccw vortex domain wall with a (100, 100) anti-notch differs, suggests that the magnetisation within the anti-notch can be set in a similar manner to that in a high anti-notch. From the simulation, a ccw vortex domain wall depins at a significantly lower field than a cw vortex domain wall. In experiment however, the opposite was the case; in most cases a cw vortex domain wall had travelled across most of the anti-notch before being pinned by the lower part of the anti-notch.

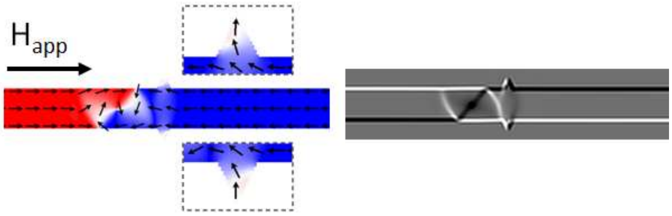

(a) 10 Oe

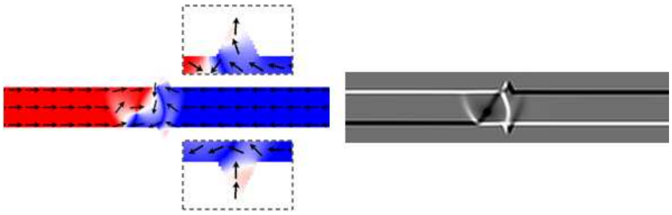

(b) 110 Oe

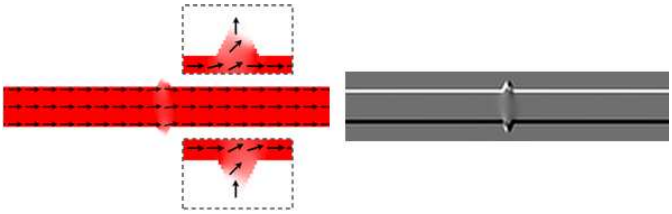

(c) 115 Oe

Figure 4.24: OOMMF simulation (left) and corresponding calculated Fresnel images (right) of the cw vortex domain wall interacting with a (100, 100) anti-notch.

Following this, the simulation was modified to investigate the strength of the pinning when the domain wall was pinned at the trap by the trailing wall, as observed in the majority of experiments. Figure 4.25a is the image used as the initial magnetisation, where the red and blue regions represent areas where the magnetisation is directed towards the right and left, respectively. This configuration was relaxed in the absence of an applied field to give the configuration in figure 4.25b. The domain wall is not stable at this location at remanence however and adjusts such that the leading wall is pinned by the upper part of the anti-notch. In this configuration, it may be observed

(a)

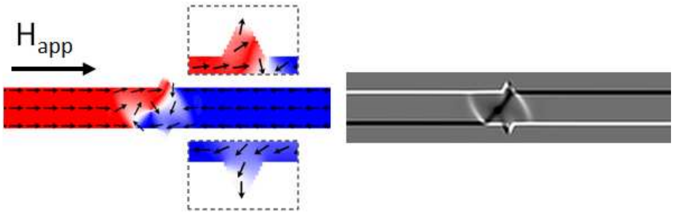

(b) 0 Oe

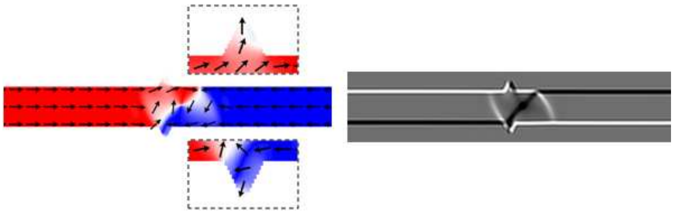

(c) 15 Oe

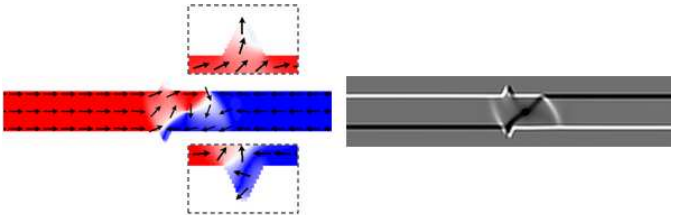

(d) 45 Oe

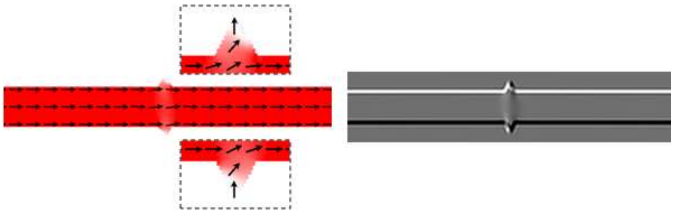

(e) 70 Oe

Figure 4.25: (a) a schematic of the initial magnetisation. (b)-(e) OOMMF simulation (left) and corresponding calculated Fresnel images (right) of the cw vortex domain wall interacting with a (100, 100) anti-notch when the leading wall has passed through the upper part of the anti-notch.

that the upper and lower parts of the anti-notch are oppositely magnetised. A modest field of 15 Oe was required to move the domain wall across the notch where it was pinned by the lower part of the anti-notch, as observed in experiment. A slight extension of the wall can be seen at a field of 45 Oe, figure 4.25d. The simulation also indicated that the wall was strongly pinned at this location with a field of 70 Oe needed to depin it (figure 4.25e), 20 Oe higher than that needed to depin a ccw vortex domain wall from the same anti-notch.

The interaction of vortex domain walls with anti-notches of intermediate widths was also studied; the Fresnel image sequences are not shown here. However, values of depinning fields for the full range of anti-notch geometries studied are summarised in figure 4.26. The values shown are averaged over eight experiments using two structures of each geometry. In the case of the cw vortex domain wall interacting with a (100, 100) anti-notch, the fields are an average of the most favourable type of interaction, i.e. most of the domain wall passes through the anti-notch and is pinned by its trailing wall as in figure 4.22g. For ccw vortex domain walls (red points), rather similar values were obtained throughout; however, this was not the case for the cw vortex domain walls (blue points). For the anti-notches of greatest height (figure 4.26a), the strength of the potential barrier increased approximately linearly with decreasing anti-notch width, the field required to push a cw vortex domain wall through a 100 nm wide anti-notch being 66% greater than for a 400 nm wide anti-notch. In the case of the lowest anti-notches, figure 4.26b, depinning fields were generally comparable to those for ccw vortex domain walls, other than for the narrowest anti-notch where especially weak pinning was observed as noted earlier.

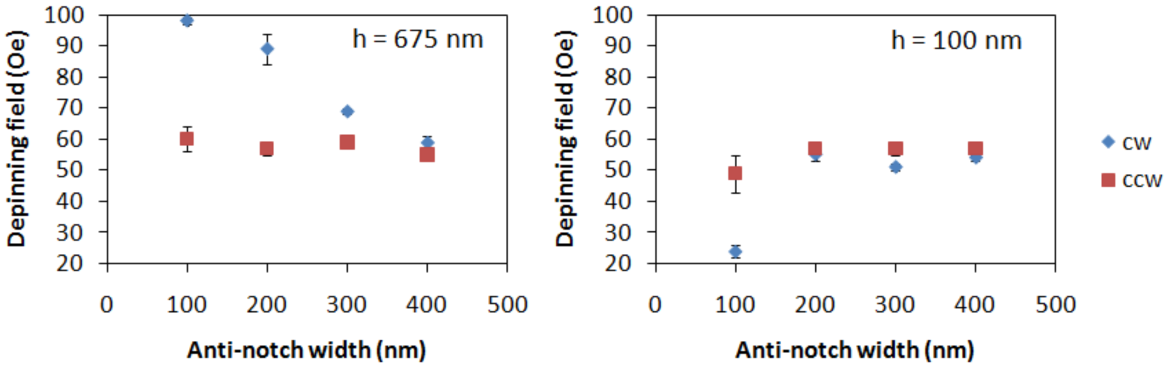

(a) (b)

Figure 4.26: Depinning fields of vortex domain walls from (a) a high anti-notch and (b) a low anti-notch.

Fresnel images of both cw and ccw vortex domain walls pinned at each of the anti-notch geometries studied, at remanence, are given in figure 4.27. For 675 nm high anti-notches, it is clear that the anti-notch acts as either a potential well or a potential barrier to incoming walls. A barrier is observed for cw vortex domain walls where

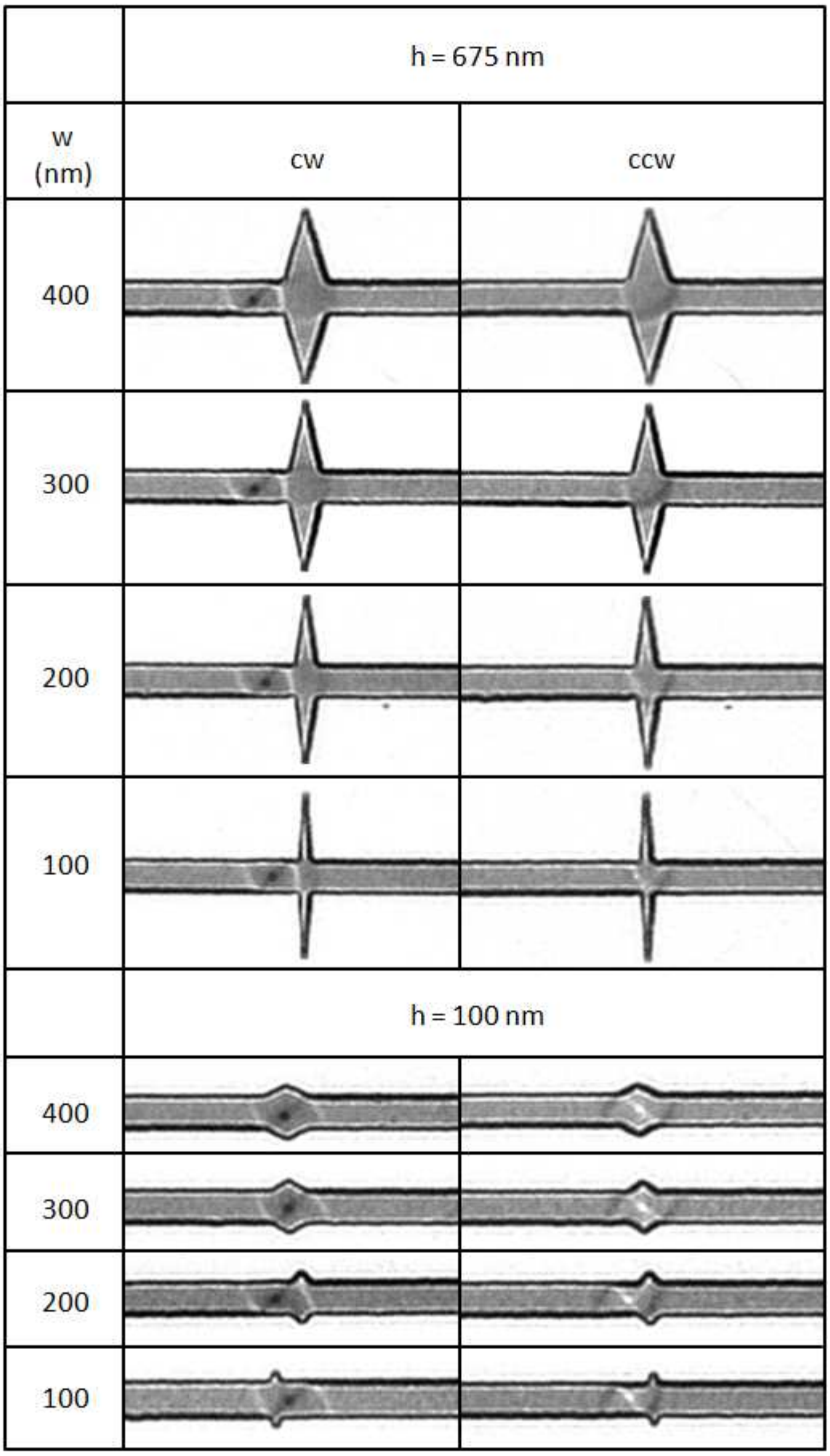

Figure 4.27: Fresnel images of both cw and ccw vortex domain walls pinned at the (400-100, 675) and the (400-100, 100) anti-notches at remanence.

the wall sits in front of the anti-notch and a well is observed for ccw vortex domain walls where the wall sits inside the anti-notch. This behaviour is observed for all anti-notch widths investigated. In the case of 100 nm high anti-notches, rather different conditions pertain. Within the anti-notch, the deviation of the magnetisation from the mean direction is less marked and, at least for the wider anti-notch, there is no memory of the direction of the initial magnetising field. As such the behaviour of vortex domain walls of different chiralities is less marked, any differences being most significant when the anti-notch is narrow. For anti-notch widths ≤ 200 nm, the extent of the wall is considerably larger than the anti-notch and a significant compression of the wall would have to occur if it were to enter it and instead either the leading or trailing wall is pinned by either the upper or lower part of the anti-notch.

## 4.4 Discussion

It is clear that all notch and anti-notch geometries investigated here arrest the progress of incoming vortex domain walls regardless of wall chirality. This is a consequence of the preferred local direction of magnetisation being no longer parallel to the wire as it is in regions where the width of the nanowire is constant. Additionally, by varying the geometry of the notch or anti-notch, the potential a domain wall experiences can be modified. In the case of notches, the behaviour observed did not appear to depend on the shape of the notch but instead on the chirality of the incident domain wall. For cw vortex domain walls, the vortex core shifted downwards with an external field prior to depinning from the notch. For ccw vortex domain walls however, the vortex core was forced upwards until eventually forced out of the wire, rendering the vortex domain wall a transverse wall before depinning could take place. That a significantly higher field was required to depin a ccw vortex domain wall from a triangular notch than a cw from the same pinning geometry was attributed to differences in notch depth; the depinning fields in the rest of the experiments were similar. A greater probability of nucleating one chirality of domain wall over another using this set-up is possible however, by using a slightly different injection pad geometry [8, 17] or by applying a small transverse field during injection [5].

In the case of triangular shaped anti-notches, the deviation of the magnetisation from the mean direction in the wire became more marked as the height of the anti-notch increased [18], while the sense of the deviation was dependent on the direction of the initial magnetising field. This in turn led to different behaviour when cw and ccw vortex domain walls were incident on the anti-notch. A similar study has been carried out using a pair of attached wires as an effective domain wall gate to interrupt the propagation of vortex domain walls [19].

The results presented here also show that the depinning process is complex with very extended highly asymmetric transverse-like wall structures forming before reversal is completed. This is clearly a consequence of the high stability of the domain wall within its preferred location in the anti-notch. Since one end of the wall is fixed firmly, the system has to balance the decrease in energy achieved by increasing the volume of spins which align with the applied field against the increase in energy incurred by a longer length of domain wall. The new equilibrium is determined by this balance up to the point where the field is sufficiently strong to depin the wall at which point reversal of the remainder of the element is abrupt.

In using low anti-notches, the overall structure of the domain wall is preserved and provides a reproducible method of trapping vortex domain walls of both chiralities. In using high anti-notches the structure of the ccw vortex domain wall is completely lost however the cw vortex domain wall is preserved and presumably a reverse field would reproducibly move the domain wall back to the diamond pad. In conclusion, by using an anti-notch rather than a notch, a greater degree of control is achieved. An additional degree of control is achieved when the height of the anti-notch is significant. The behaviour observed here may be particularly useful in devices where knowledge of the chirality of the domain wall is important.

# Bibliography

[1] C. C. Falkner, M. D. Cooke, D. A. Allwood, D. Petit, D. Atkinson and R. P. Cowburn, J. Appl. Phys. **95** 6717 (2004).

[2] D. Petit, A. Jausovec, D. Read and R. P. Cowburn, J. Appl. Phys. **103** 11 (2008).

[3] D. A. Allwood, G. Xiong and R. P. Cowburn, Appl. Phys. Lett. **85** 2848 (2004).

[4] M. T. Bryan, T. Schrefl and D. A. Allwood, Appl. Phys. Lett. **91** 142502 (2007).

[5] D. Atkinson, D. S. Eastwood and L. K. Bogart, Appl. Phys. Lett. **92** 022510 (2008).

[6] G. D. Li, Y. Zhai, P. K. J. Wong, D. X. Niu, Y. Lu, S. Lepadatu and Y. B. Xu, IEEE Trans. Magn. **43** 2830 (2007).

[7] T. Komine, H. Murakami, T. Nagayama and R. Sugita, IEEE Trans. Magn. **44** 2516 (2008).

[8] D. McGrouther, S. McVitie, J. N. Chapman and A. Gentils, Appl. Phys. Lett. **91** 022506 (2007).

[9] M. Hayashi, L. Thomas, C. Rettner, R. Moriya, X. Jiang and S. S. P. Parkin, Phys. Rev. Lett. **97** 207205 (2006).

[10] L. Thomas, C. Rettner, M. Hayashi, M. G. Samant and S. S. P. Parkin, Appl. Phys. Lett. **87** 262501 (2005).

[11] D. Lacour, J. A. Katine, L. Folks, T. Block, J. R. Childress, M. J. Carey and B. A. Gurney, Appl. Phys. Lett. **84** 1910 (2004).

[12] A. J. Zambano and W. P. Pratt, Jr., Appl. Phys. Lett. **85** 1562 (2004).

[13] A. Himeno, T. Okuno, S. Kasai, T. Ono, S. Nasu, K. Mibu and T. Shinjo, J. Appl. Phys. **97** 066101 (2005).

[14] P. Lendecke, R. Eiselt, G. Meier and U. Merkt, J. Appl. Phys. **103** 073909 (2008).

[15] C. Brownlie, S. McVitie, J. N. Chapman and C. D. W. Wilkinson, J. Appl. Phys. **100** 033902 (2006).

[16] A. Himeno, T. Okuno, T. Ono, K. Mibu, S. Nasu and T. Shinjo, J. Magn. Magn. Mater. **286** 167 (2005).

[17] K. He, D. J. Smith and M. R. McCartney, Appl. Phys. Lett. **95** 182507 (2009).

[18] M. Herrman, S. McVitie and J. N. Chapman, J. Appl. Phys. **87** 2994 (2000).

[19] M. Hara, J. Shibata, T. Kimura and Y. Otani, Appl. Phys. Lett. **89** 192504 (2006).

# 5

# Pinning Transverse Domain Walls using Wires of Varying Width

## 5.1 Introduction

Geometrically confined domain walls in which the spin structure of the wall can be controlled via lateral dimensions and film thickness are currently the focus of intense research due to the associated exciting physical phenomena and the potential for device applications [1, 2]. From the results shown in the previous chapter, it is clear that the detailed domain wall spin structure plays a very important role in determining the pinning at lateral traps (notches and anti-notches). That is, a given trap will disturb the propagation of a vortex domain wall in a manner that is dependent on its chirality. Additionally, it was observed that the strength of the pinning is also chirality dependent in some cases. As the dimensions of thin films and nanostructures decrease, towards the realisation of cheaper and faster devices, interesting thickness dependent domain wall phenomena emerge. Below a critical nanowire width or thickness, the favoured domain wall structure is no longer vortex and is instead either a symmetric or asymmetric transverse domain wall structure. The spin structure of a transverse domain wall is entirely different from a vortex domain wall and consists, to a first approximation, of two 90° domain walls, in contrast to three connected domain walls with an out-of-plane component of magnetisation at the core in the case of a vortex domain wall, as introduced in chapter 1. This in turn will produce entirely different phenomena when such a wall nears a constriction or protrusion. Previous studies, using various techniques, have already been carried out to determine the potential disruption presented to a transverse domain wall by a constriction or protrusion [3–9], however, the detailed interaction of the transverse domain wall as it was transmitted through the trap was not directly observed. Additionally, micromagnetic simulations have been utilised to observe the magnetic structure of transverse domain walls in the vicinity of notches [10, 11]. In this chapter, the interaction of transverse domain walls with both symmetric and asymmetric traps is investigated. In particular, the role of the characteristic V shape of the domain walls [12] will be explored. Additionally, in wider wires, the transverse domain wall takes on an asymmetric form [13], that is, it has a component of magnetisation parallel to the wire edge. This creates an additional degree of freedom which may play a role in the depinning of such walls from a trap.

## 5.2 Pinning transverse domain walls using a transverse arm

Figure 5.1 illustrates the characteristic V shape of a transverse domain wall packet, that is, a transverse domain wall is wider on one side than the other, as depicted in figures 5.1a,b. Throughout the rest of this chapter, the term transverse domain wall will refer to the complete domain wall packet, that is two domain walls at approximately 90° to one another. It will be clearly stated when either of the individual domain walls that make up the complete packet are referenced. In these experiments the nature of the interaction when both the wide side and the vertex of the transverse domain wall are on the same side of the wire as the trap is presented; the structure geometry and trap configuration are introduced in the next section. Lorentz microscopy was utilised to characterise the magnetic behaviour in conjunction with OOMMF micromagnetic modelling to aid interpretation of the results.

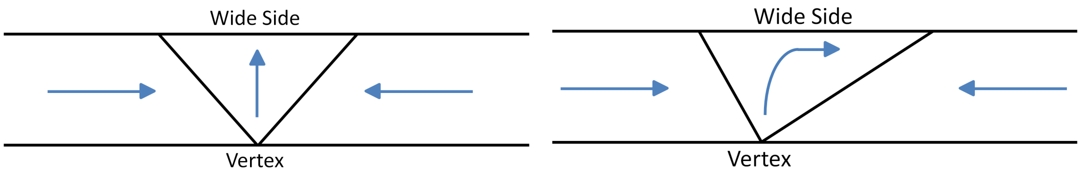

(a) (b)

Figure 5.1: Schematic illustration of (a) a transverse and (b) an asymmetric transverse domain wall with the definitions of the wide side and the vertex.

### 5.2.1 The T-shaped trap structure

The wire geometry used here is presented in figure 5.2 and utilises a T-shaped trap, indicated by **A**, to control the propagation of domain walls. This structure not only provides a nucleation method that is separate from that used for propagation of the wall along the wire but also allows the magnetisation in the trap to be set by the nucleation field. The left end of the wire is curled into a hook for domain wall nucleation, detailed in the next section, and the other end is tapered. Figures 5.2a-c show schematics of the orientation of the trap with respect to the rest of the wire in three different cases studied. In figures 5.2a,b, the T is patterned on either the upper or lower edge of the

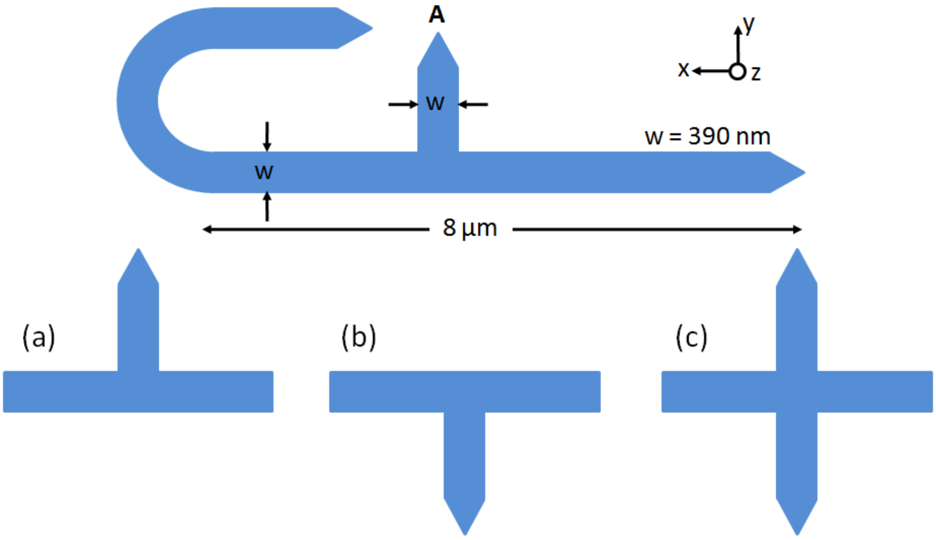

Figure 5.2: Schematic of the structure used to investigate the interaction of transverse domain walls with a T-shaped trap. (a),(b) Schematics of two different orientations of the T and (c) a double-T trap.

wire. In 5.2c, the trap comprises a double T structure, i.e. a T patterned on both sides of the wire to form a symmetric trap. The wires are 9 nm thick and were made from thermally evaporated permalloy. Fabrication of the wires was carried out by João Sampaio from Imperial College London using electron beam lithography and lift off techniques.

A head-to-head transverse domain wall was nucleated by the following method. With the application of a magnetic field parallel to the long axis of the wire, i.e. along the x-axis in figure 5.2, the magnetisation in the upper and lower part of the hook is forced to align with the field, thus creating a head-to-head transverse domain wall in the centre of the hook. Vortex domain walls are expected to form in wires of these dimensions, however, the section of wire in which the domain wall is nucleated is not a straight segment of wire and the nucleation field sets the magnetisation within the central domain of the transverse domain wall. The magnetisation within the transverse arm may relax to be either along the positive or negative y-axis. By applying the nucleation field ~ 45° away from the horizontal axis however, this degeneracy was removed. With the application of the nucleation field described above, a head-to-head transverse domain wall forms with its wide side on the outer edge of the hook, as illustrated in figure 5.3a. It would be unfavourable for the domain wall to form with its vertex towards the outer edge of the hook, as in figure 5.3b, due to a build up of positive charge at the domain wall.

The structure of the nucleated domain wall is therefore identical in every case however it is the ability to control the magnetisation within the T that allows different symmetries of domain wall to be studied for a given trap, as illustrated by the DPC images in figures 5.4a,b. In figure 5.4a, a field of ~290 Oe was applied along a direction

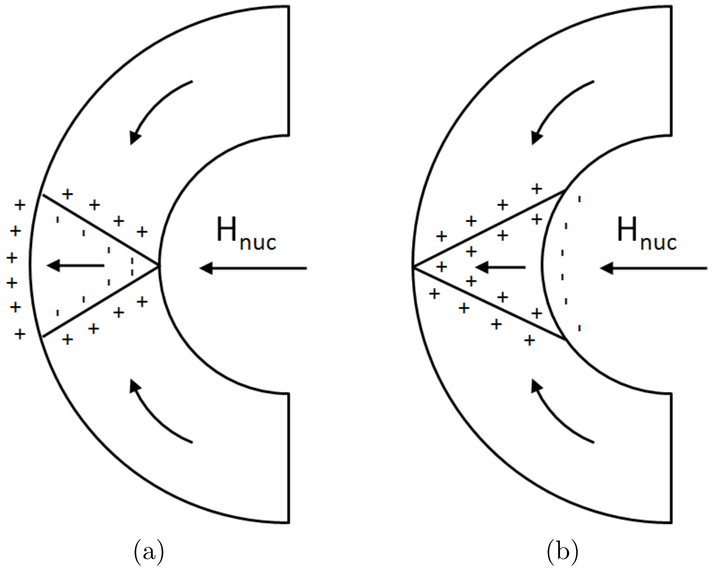

Figure 5.3: (a) The nucleated transverse domain wall forms with its wide side at the outer edge of the hook. (b) an unfavourable transverse domain wall configuration.

approximately 45° clockwise away from the x-axis, which resulted in the nucleation of a head-to-head transverse domain wall in the centre of the hook at remanence. Additionally, the magnetisation in the transverse arm was set by this process to be aligned along the positive y-axis. In a similar way, with the application of the same field along a direction ~ 45° counterclockwise away from the x-axis, as indicated in

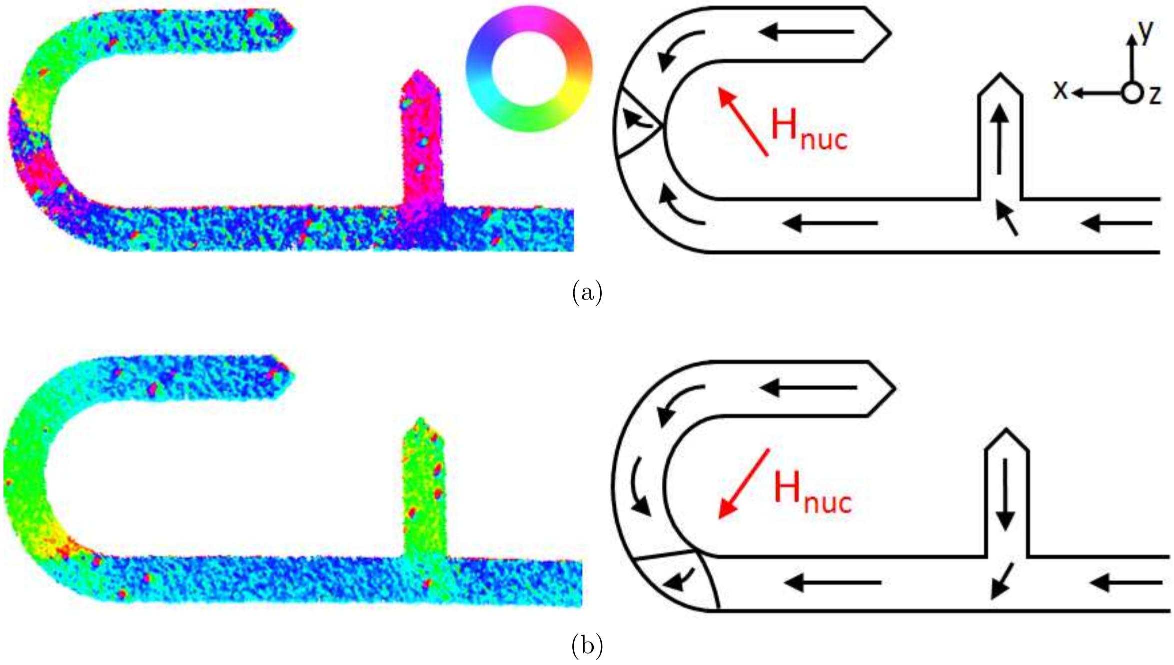

Figure 5.4: Experimental DPC colour images (left) and corresponding schematics (right) of the resulting domain wall and trap configurations following the application of a nucleation field at an angle of 45° (a) clockwise and (b) counterclockwise away from the x-axis.

figure 5.4b, a transverse domain wall with the same structure as in figure 5.4a was formed however the magnetisation within the transverse arm was opposite, i.e. along the negative y-axis. From this structure, the interaction of a transverse domain wall with its vertex nearest the transverse arm was studied. By patterning the transverse arm on the opposite side of the wire (figure 5.2b), the interaction of the same wall with its wide side nearest the trap was also probed.

### 5.2.2 Micromagnetic simulations of T structure

Micromagnetic simulations using the OOMMF package detailed in chapter 1 were performed on similar structures by João Sampaio from Imperial College London. Figure 5.5a shows a schematic of the mask used in the simulations. The hooked end of the wire was omitted to reduce the simulation time and instead a domain wall was initialised to the left of the T and subsequently driven towards it. With rectangular ends however, the magnetostatic energy dominates causing the magnetisation to align along the edges of the structure. This can produce end domains and may cause more complex behaviour to occur than would otherwise be observed in the fabricated structures. To avoid this, the stray field from 2 $\mu$m long tracks either side of the wire was included in the simulation as a fixed Zeeman field to act as a continuation of the wire. In effect, this removes the demagnetising field from the ends of the wire. Furthermore, in some cases the domain wall extended significantly whilst being pulled away from the trap and consequently reached the end of the wire before depinning. To overcome this, the section of wire to the right of the T was doubled in length, detailed in figure 5.5b. The input parameters were standard parameters for permalloy as discussed in chapter 1, section 1.8, with a mesh size of $5 \times 5 \times 9$ nm$^3$. The field increment was initially set to

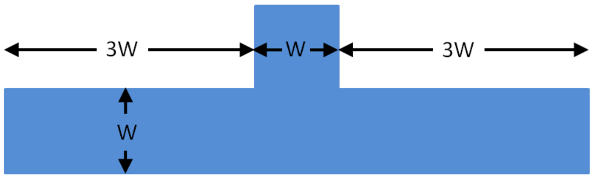

(a)

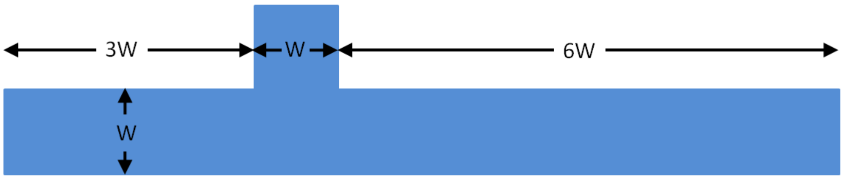

(b)

Figure 5.5: (a) Schematic of the mask used to simulate the interaction of transverse domain walls with a T. (b) in some cases the domain wall extended beyond the T whilst still pinned by it and the length of the wire had to be increased.

20 Oe to observe the complete interaction; the field increment was then reduced to 5 Oe to obtain a more accurate depinning field value. The simulations were set up to investigate the behaviour when the magnetisation in the central part of the transverse domain wall was both parallel and anti-parallel to the magnetisation in the T and double T, and are presented in the following sections.

### Parallel alignment between the central domain of the transverse domain wall and trap

Three different simulations were performed for a parallel alignment between the magnetisation in the central domain of the transverse domain wall and the T, and are detailed in figure 5.6. The three simulations performed reflect the interaction of a transverse domain wall with a T when both the vertex (figure 5.6a) and the wide side (figure 5.6b) of the domain wall packet are incident on the T, and when the transverse domain wall is faced with a double T (figure 5.6c).

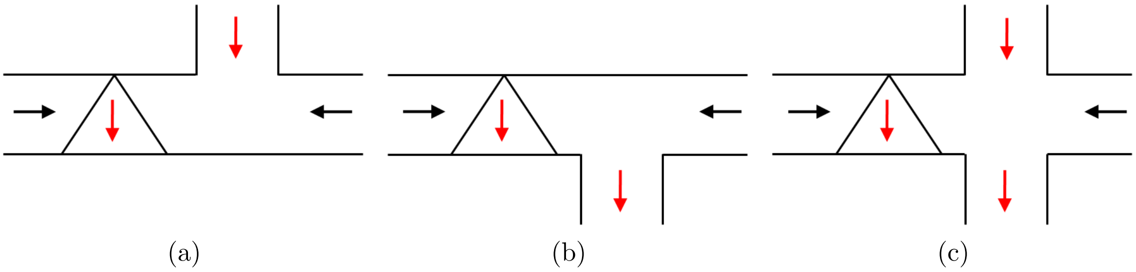
(a) (b) (c)

Figure 5.6: Schematics of the three domain wall configurations with respect to the trap for a parallel alignment between the central magnetisation of the wall and the trap.

The result of the configuration in figure 5.6a is given in figure 5.7, where the initial transverse domain wall can be seen to the left of the trap at remanence, figure 5.7a. A field increment of 1 Oe was used here due to a particularly weak interaction being observed. The transverse domain wall progresses towards the trap at a field of 9 Oe (figure 5.7b) and the vertex becomes pinned by the right corner of the trap at 10 Oe, figure 5.7c. The transverse domain wall remains pinned at this location for a further 2 Oe (figure 5.7d) before it is depinned at 13 Oe, figure 5.7e. It is evident that in this configuration, the T is not an efficient pinning site as the transverse domain wall easily propagates beyond it under a modest applied field.

The interaction is significantly different if the wide side of the transverse domain wall is on the same side of the wire as the T, as presented in figure 5.8. At its wide side, the extent of the domain wall packet is comparable to the width of the T, allowing the transverse domain wall to be easily accommodated by the trap at remanence, figure 5.8a. With the application of a magnetic field, the vertex of the transverse domain wall travels into the far side of the wire whilst the trailing wall is strongly anchored to the

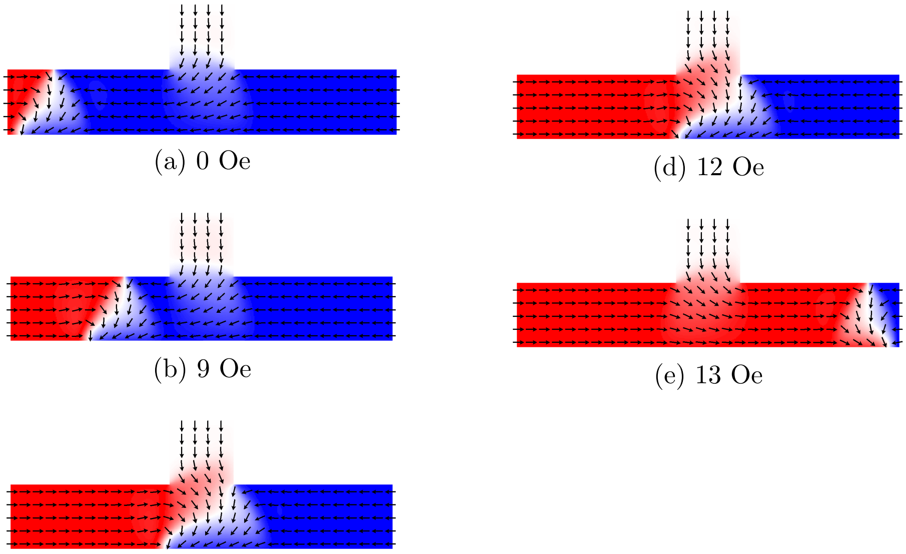

(a) 0 Oe

(d) 12 Oe

(b) 9 Oe

(e) 13 Oe

(c) 10 Oe

Figure 5.7: Result of a micromagnetic simulation when there is a favourable alignment between the magnetisation in the central domain of the transverse domain wall and the T. In this case the vertex of the domain wall is on the same side of the wire as the T.

T, figure 5.8b, significantly distorting the original transverse domain wall structure. The wall packet distorts further at a field of 50 Oe (figure 5.8c), with a significantly higher field of 80 Oe required to depin it, figure 5.8d.

Furthermore, with a double T, figure 5.9, the strength of the pinning is identical to that observed for a single T when the wide side of the transverse domain wall is on the same side of the wire as the T. The transverse domain wall easily enters the double T at remanence, figure 5.13a, and spans across it. The vertex of the wall is also faced with a T in this case and therefore must increase in width to accommodate it. As the applied magnetic field is increased, the vertex of the transverse domain wall becomes

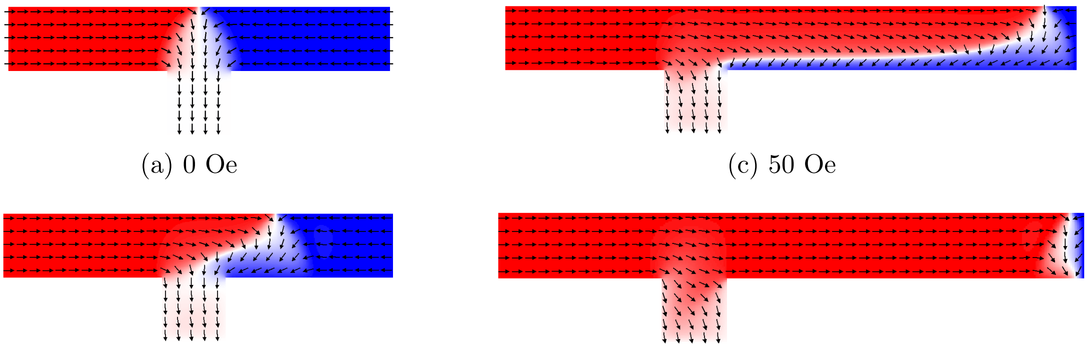

(a) 0 Oe

(c) 50 Oe

(b) 45 Oe

(d) 80 Oe

Figure 5.8: Result of a micromagnetic simulation when there is a favourable alignment between the magnetisation in the central domain of the transverse domain wall and the T. In this case the wide side of the domain wall is on the same side of the wire as the T.

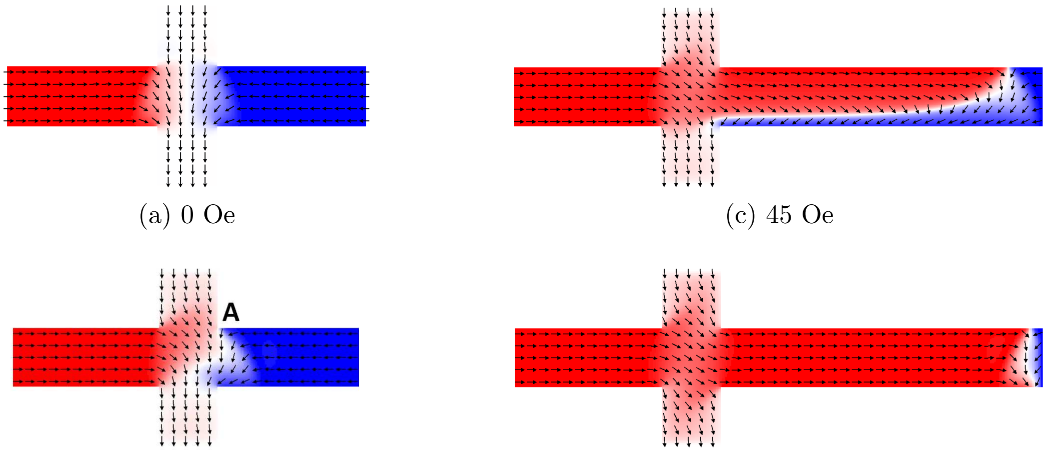

(a) 0 Oe (c) 45 Oe

(b) 40 Oe (d) 80 Oe

Figure 5.9: Result of a micromagnetic simulation when there is a favourable alignment between the magnetisation in the central domain of the transverse domain wall and the double T.

pinned at the upper right corner of the double T, at **A** in figure 5.9b. With a slight further increase of the applied field, the domain wall extends significantly beyond the trap (figure 5.9c) and is depinned with a field of 80 Oe, figure 5.9d.

### Anti-parallel alignment between the central domain of the transverse domain wall and trap

Similarly, three different simulations were performed to observe the interaction of a transverse domain wall with a T when there is an anti-parallel alignment between the magnetisation in the central domain of the transverse domain wall and the T. These cases are outlined in figure 5.10.

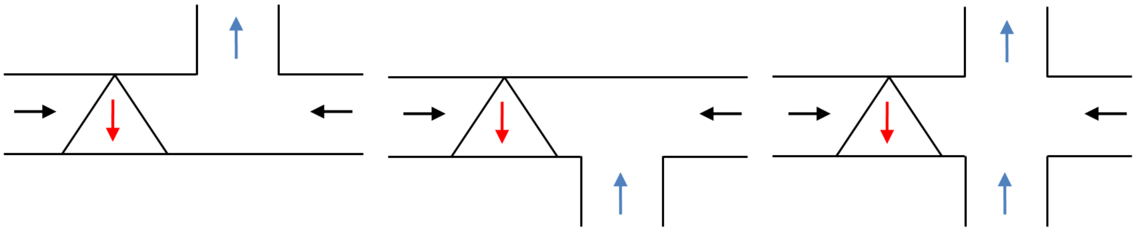

(a) (b) (c)

Figure 5.10: Schematics of the three domain wall configurations with respect to the trap for an anti-parallel alignment between the central magnetisation of the wall and the trap.

The interaction when the vertex of the transverse domain wall is on the same side of the wire as the T is presented in figure 5.11. At remanence, the wide side of the transverse domain wall is level with the first edge of the trap; the vertex is situated a small distance to the left of the T. No part of the transverse domain wall enters the

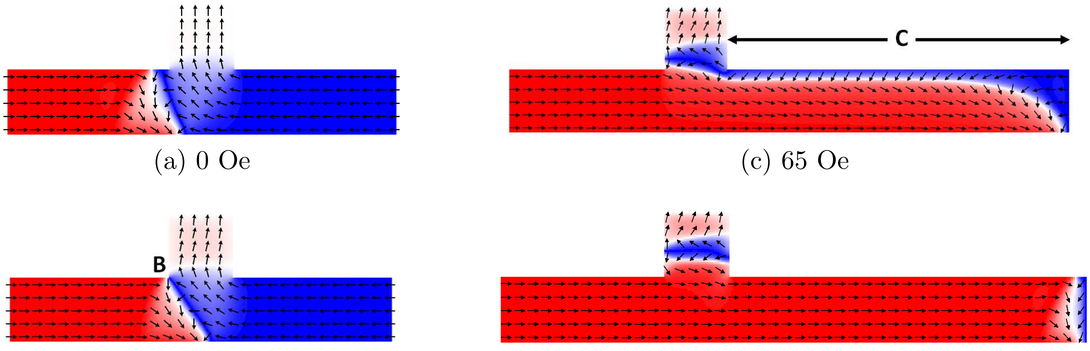

(a) 0 Oe (c) 65 Oe

(b) 40 Oe (d) 105 Oe

Figure 5.11: Result of a micromagnetic simulation when there is an unfavourable alignment between the magnetisation in the central domain of the transverse domain wall and the T. In this case the vertex of the domain wall is on the same side of the wire as the T.

T at this stage, figure 5.11a. As the field is increased, the whole domain wall packet travels towards the T and the vertex is pinned at the first corner of the T, at **B** in figure 5.11b. The leading domain wall now extends across the T. As the field is increased further, it is clear that the transverse domain wall is strongly anchored at this location

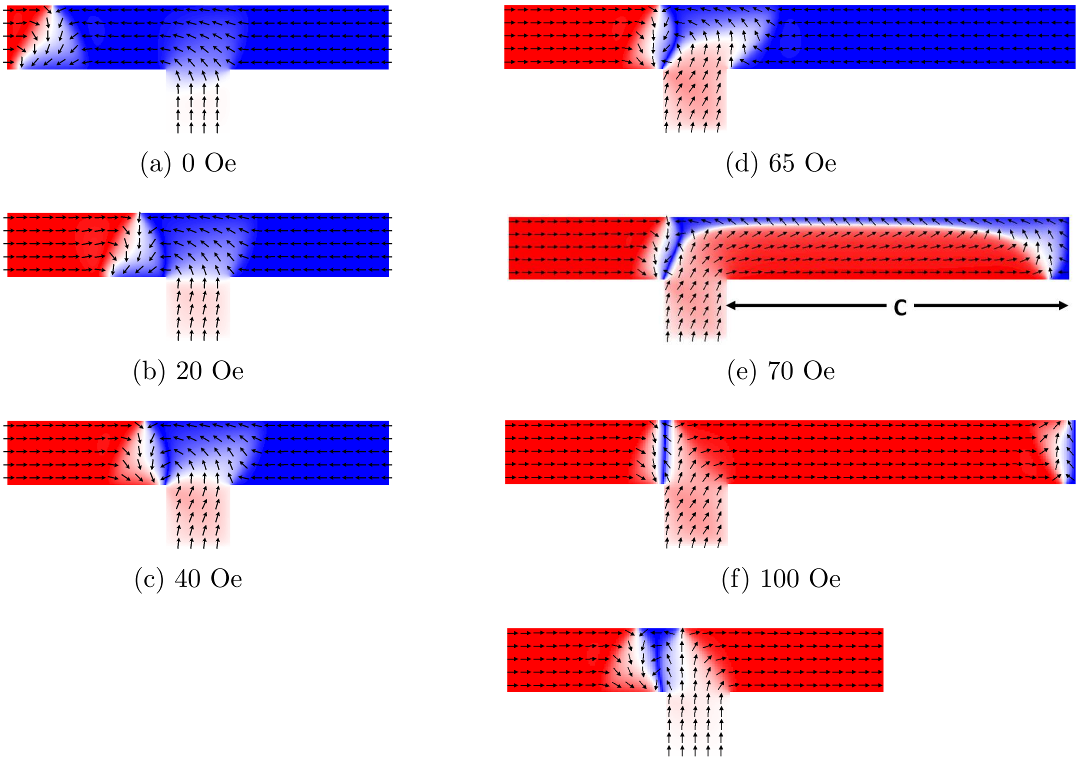

(a) 0 Oe (d) 65 Oe

(b) 20 Oe (e) 70 Oe

(c) 40 Oe (f) 100 Oe

(g) 0 Oe

Figure 5.12: Result of a micromagnetic simulation when there is an unfavourable alignment between the magnetisation in the central domain of the transverse domain wall and the T. In this case the wide side of the domain wall is on the same side of the wire as the T.

and the leading wall extends a large distance into the far side of the wire, labelled by **C** in figure 5.11c. The central domain of the transverse domain wall has now rotated to align with the direction of the applied field and a new domain wall is nucleated in the T as the original wall is depinned from the T at 105 Oe, figure 5.11d.

If the wide side of the transverse domain wall is on the same side as the T, figure 5.12a, a field of 20 Oe is required to move the domain wall packet towards the trap, where it stops in front of it, figure 5.12b. As the field is increased further, figures 5.12c,d, the transverse domain wall visibly compresses and it is evident that, in this configuration, the T presents a strong energy barrier to an incoming transverse domain wall. A new domain wall is nucleated from the T at a field of 70 Oe, figure 5.12e, which reverses the far side of the wire, indicated by **C**, at a field of 100 Oe (figure 5.12f) thus creating a 360° domain wall to the left of the T. On removal of the field, the 360° domain wall expands significantly, figure 5.12g.

The interaction observed is very similar when a double T is used to pin a transverse domain wall, figure 5.13. A small field is required to move the transverse domain wall towards the double T, figure 5.13b. As the field is increased, figures 5.13c,d, the wall compresses noticeably; however, in this case the right side of the wire, indicated by **C**, abruptly reverses at a lower field of 80 Oe (figure 5.13e). This again creates a 360° domain wall to the left of the T which increases in width slightly at remanence as

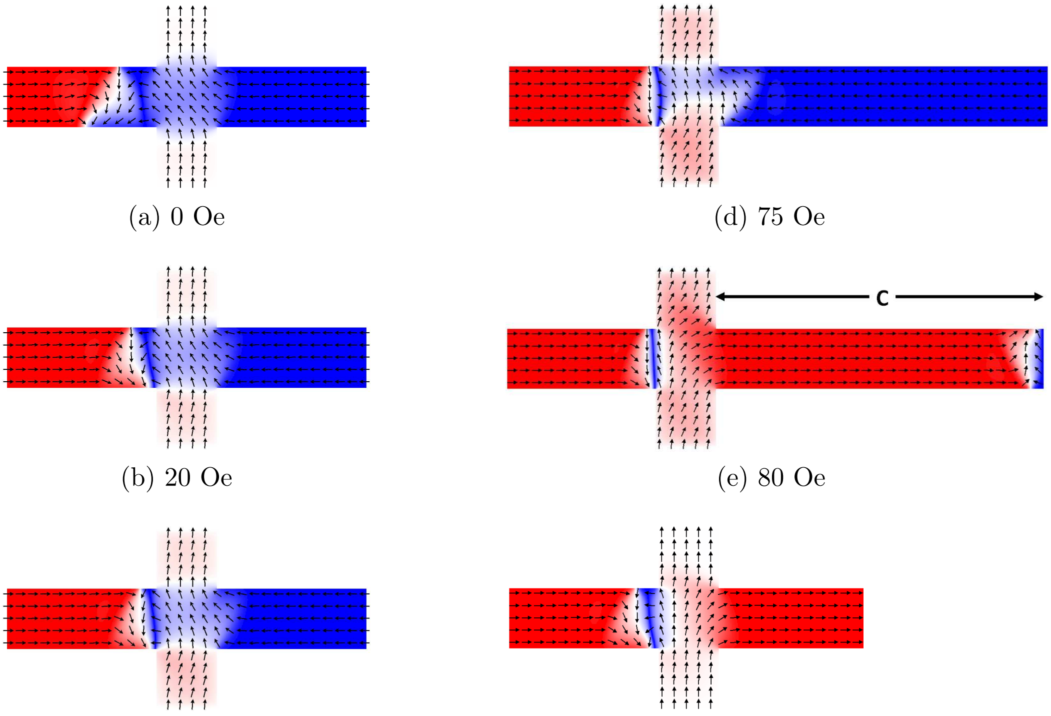

(a) 0 Oe

(d) 75 Oe

(b) 20 Oe

(e) 80 Oe

(c) 40 Oe

(f) 0 Oe

Figure 5.13: Result of a micromagnetic simulation when there is an unfavourable alignment between the magnetisation in the central domain of the transverse domain wall and the double T.

shown in figure 5.13f.

These simulations have shown that transverse domain walls display a rich variety of behaviour when interacting with both symmetric and asymmetric traps. A table summarising the critical fields involved in the interactions simulated here is given in table 5.1. The errors displayed in the table were obtained from half the field step used, as the magnitude of the field step was not consistent across all simulations. The orientation of the magnetisation within the central domain of the transverse domain wall with respect to the magnetisation in the transverse arm is key to the type of interaction observed. Additionally, it is evident that the interaction, and therefore strength of pinning, is dependent on whether the wide side or vertex of the transverse domain wall meets the trap. This is especially important for a parallel alignment between the wall and T, where this orientation ultimately determines the effectiveness of the T as a pinning site. With the vertex incident on the T, the transverse domain wall requires a small field to drive it towards the T and is pinned by it for a field of just 2 Oe before depinning. With its wide side incident on the trap however, the transverse domain wall is easily accommodated by the T and is trapped by it at remanence. A significant field is required to depin it from the T. With a double T, the behaviour observed is similar to that when the wide side of the transverse wall meets the single T, with no difference observed in the depinning field. Furthermore, the transverse domain wall was observed to readily distort and extend a large distance into the far side of the wire before depinning.

When there is an anti-parallel alignment between the wall and T, the wall is faced with a repulsive force, constituted by the magnetisation within the T opposing that

| | Parallel DW and T | |
|---|---|---|
| | DW Extension | Depinning |
| Vertex incident on T | - | 12.5 ± 0.5 |
| Wide side incident on T | 47.5 ± 2.5 | 77.5 ± 2.5 |
| DW incident on double T | 42.5 ± 2.5 | 77.5 ± 2.5 |
| | Anti-parallel DW and T | |
| | DW Extension | Depinning |
| Vertex incident on T | 62.5 ± 2.5 | 102.5 ± 2.5 |
| Wide side incident on T | 67.5 ± 2.5 (N) | 97.5 ± 2.5 (N) |
| DW incident on double T | - | 77.5 ± 2.5 (N) |

Table 5.1: A table summarising the critical fields, in Oe, including the field at which the domain wall extends a significant distance away from the T and the field at which it depins from the T, determined from the simulations only. In some cases a new domain wall was nucleated before the original domain wall depinned from the trap, indicated by (N).

within the central domain of the transverse domain wall. The strength of the interaction is similar regardless of whether the wide side or vertex of the transverse domain wall is incident on the T. The behaviour of the transverse domain wall as it is depinned from the T differs however depending on the orientation of the wall with respect to the T. When the vertex is incident on the T, a significant extension of the leading domain wall beyond the trap into the far side of the wire is observed prior to depinning. Conversely, when the wide side of the domain wall is incident on the T, the transverse domain wall does not travel beyond the T before the far side of the wire reverses via the nucleation and subsequent propagation of a domain wall from the T. There is just 5 Oe separating the field required to depin the domain wall in the former case and to nucleate a new domain wall in the latter case. Furthermore, with the addition of a second transverse arm, a similar interaction is observed to the case where the wide side of the wall meets the T. The far side of the wire reverses by the nucleation of a domain wall from the trap, albeit at a notably lower field. In all three cases, the trap is an effective pinning site for a transverse domain wall when there is an antiparallel alignment between the domain wall core and the trap.

### 5.2.3 Direct observation of domain wall pinning by a T

Fresnel imaging was initially used to study the magnetic behaviour of the fabricated structures; however, the domain wall contrast was weak and the magnetic configuration was difficult to determine in most cases. Therefore, the DPC mode of Lorentz microscopy was used instead to investigate the behaviour of transverse domain walls in the configurations detailed above. The results are presented in the following sections.

#### Parallel alignment between the central domain of the transverse domain wall and trap

Figure 5.14 illustrates the interaction of a transverse domain wall with a T with the vertex of the wall encountering the trap. At remanence, the transverse domain wall is situated in the hook to the left of the T and is shown in figure 5.14a. A schematic of the magnetisation is given alongside the experimental DPC image. Only DPC images

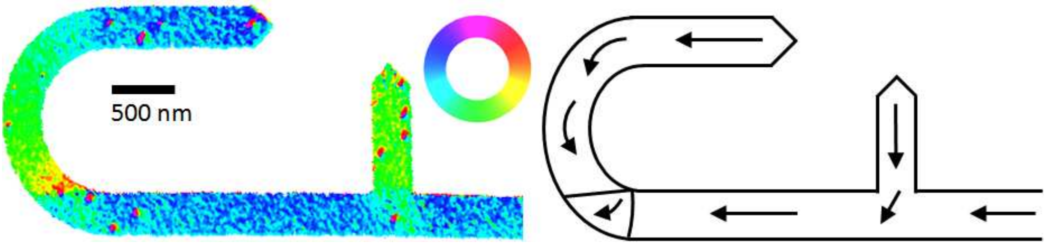

(a) After domain wall nucleation

Figure 5.14: Figure continues on the following page.

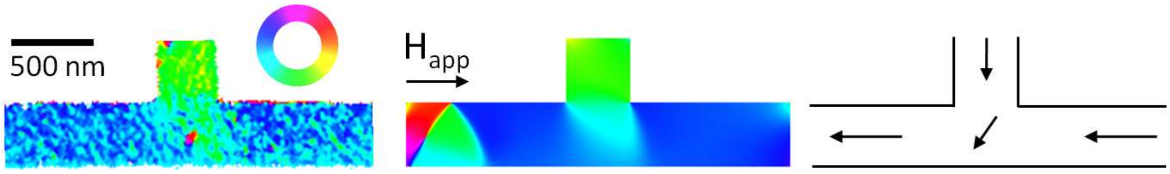

(b) Experimental field is 0 Oe, simulated is 0 Oe

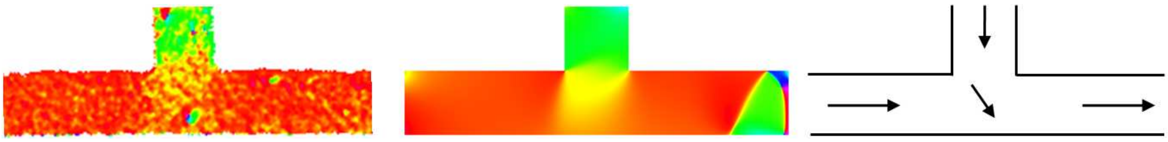

(c) Experimental field is 7 Oe, simulated is 20 Oe

Figure 5.14: Experimental DPC colour images (left) and corresponding calculated DPC images (middle) of the interaction of a transverse domain wall favourably aligned with a transverse arm with its vertex nearest the T. A schematic of the magnetisation is also given to aid interpretation (right).

of the trap and surrounding wire minus the hook will be shown hereafter; the form of the nucleated domain wall was the same in every case. Figure 5.14b shows a magnified DPC image of the trap and adjoining wire at remanence, i.e. the same configuration as in figure 5.14a. The experimental DPC image is shown at the left of each subfigure and the corresponding calculated DPC image (generated from the simulation) is shown in the centre. A schematic of the magnetisation is given at the right of each subfigure to aid interpretation. The direction of magnetisation within the main body of the wire and within the T are clearly visible, with good agreement between the calculated and experimental images. The transverse domain wall can be seen in the simulated image to the left of the T; it is out of view in the experimental image. With the application of a magnetic field, figure 5.14c, the transverse domain wall progressed beyond the T and into the far side of the wire at an applied field of 7 Oe, thus reversing it. In other words, the T did not successfully pin the transverse domain wall.

When the wide side of the transverse domain wall was incident on the T, the domain wall travelled towards and into the trap at a field of 7 Oe, figure 5.15a. As the extent of the transverse domain wall is comparable to the width of the trap, the trap acted as a potential well. As the applied field was increased, the vertex moved along the wire in the direction of the applied field, whilst the trailing wall was strongly anchored to the first corner of the T. The wall no longer appeared symmetric and progressed beyond the extent of the trap into the far side of the wire, figure 5.15b, before depinning at a field of 25 Oe, figure 5.15c. The evolution of the transverse domain wall through the transverse arm is in good agreement with that calculated by the simulation, in particular the extension of the domain wall into the far side of the wire prior to depinning, however the fields at which the process occurs differ considerably.

When the transverse domain wall was faced with a double T, figure 5.16, a field of 6 Oe was required to move the domain wall into the trap, which was subsequently

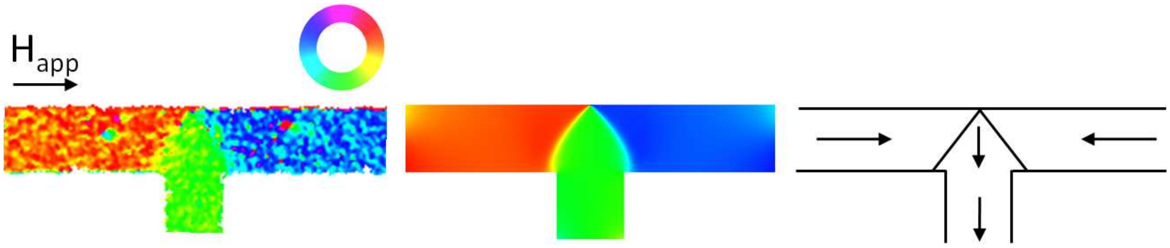

(a) Experimental field is 0 Oe, simulated is 0 Oe

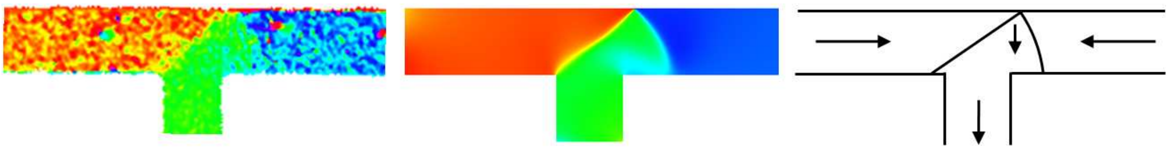

(b) Experimental field is 23 Oe, simulated is 40 Oe

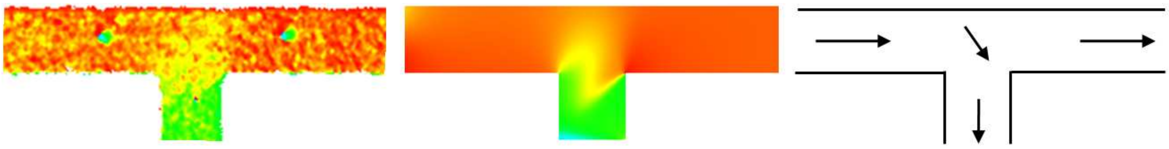

(c) Experimental field is 25 Oe, simulated is 80 Oe

Figure 5.15: DPC colour images (left) of a transverse domain wall interacting with a T when the wide side of the wall is on the same side of the wire as the trap. Calculated DPC images are given (centre) calculated from the micromagnetic simulation. Schematics of the magnetisation are also given (right) to aid interpretation.

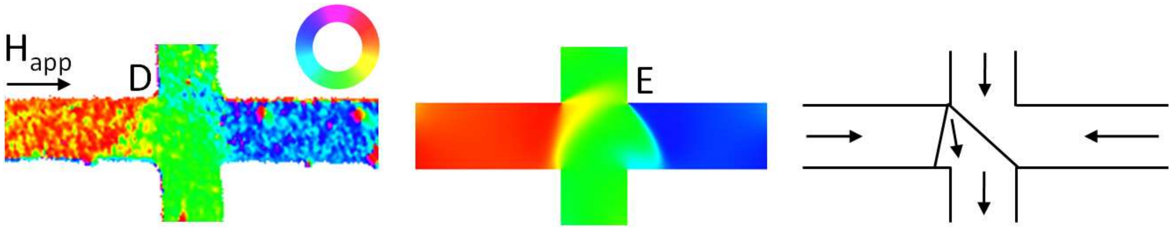

(a) Experimental field is 0 Oe, simulated is 0 Oe

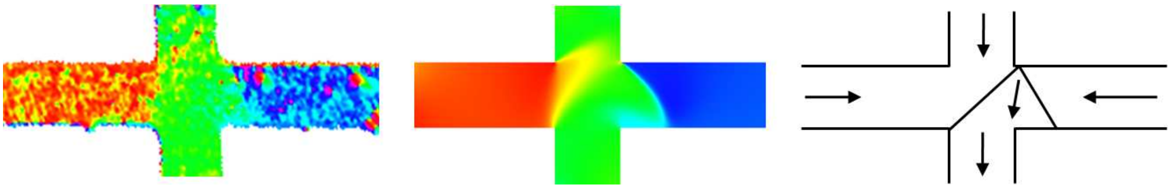

(b) Experimental field is 18 Oe, simulated is 40 Oe

(c) Experimental field is 25 Oe, simulated is 60 Oe

Figure 5.16: Figure continues on the following page.

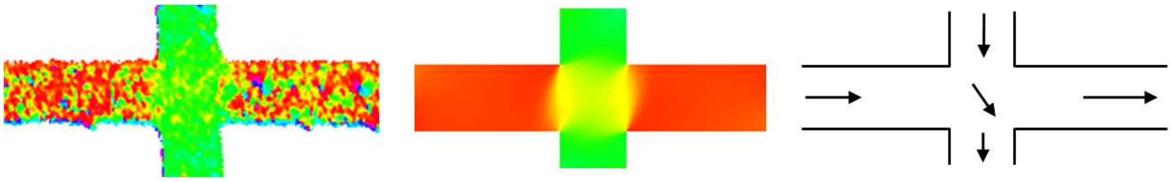

(d) Wall depinned at 37 Oe. Experimental field is 0 Oe, simulated is 0 Oe

Figure 5.16: Experimental and corresponding calculated DPC images of a transverse domain wall interacting with a double T when there is a parallel alignment between the magnetisation in the double T and the central domain of the transverse domain wall.

removed to observe the magnetic configuration at remanence, displayed in figure 5.16a. There is a subtle difference between the experimentally observed and calculated magnetic configurations of the transverse domain wall pinned by the double T. In the experimental image, the vertex of the domain wall is pinned at the left corner of the T at **D**. In the calculated image, the vertex is pinned by the right corner of the T, at **E**, at remanence. As the field is increased however, the vertex of the domain wall moves in the direction of the applied field and becomes pinned by the right corner of the T, figure 5.16b, in agreement with the calculated image. At an experimental field of 25 Oe, the transverse domain wall extends a significant distance away from the double T into the far side of the wire before depinning at a field of 37 Oe, figure 5.16d.

### Anti-parallel alignment between the central domain of the transverse domain wall and trap

In these experiments, the magnetisation within the T was reversed such that there was an unfavourable alignment between the magnetisation in the central domain of the transverse domain wall and the transverse arm. The form of the nucleated domain wall was identical, however the location of the nucleated domain wall meant that a small field of around 6 Oe was required to navigate the domain wall around the hook so that it could subsequently be driven towards the T. The magnetisation within the transverse arm was not reversed by the application of this field.

The interaction of a transverse domain wall with its vertex incident on the T is presented in figure 5.17. A small field of 6 Oe was required to drive the transverse domain wall towards the T, where at remanence the wall packet was located a short distance in front of the trap, figure 5.17a. The leading wall of the transverse domain wall was approximately level with the first corner of the trap. As the applied field was increased, the vertex moved to the first corner of the trap (figure 5.17b); the leading wall extended across the full width of the trap. Further extension of the transverse domain wall was not observed experimentally, prior to depinning at a field of 32 Oe, figure 5.17c.

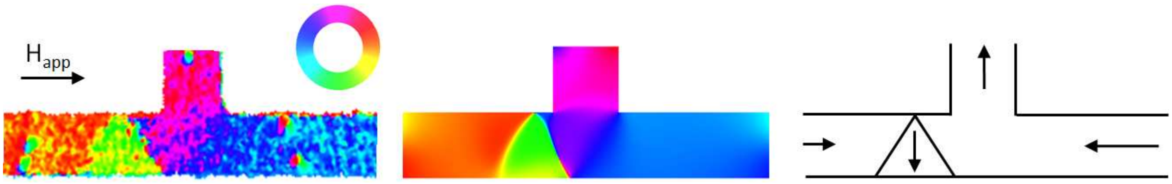

(a) Experimental field is 0 Oe, simulated is 0 Oe

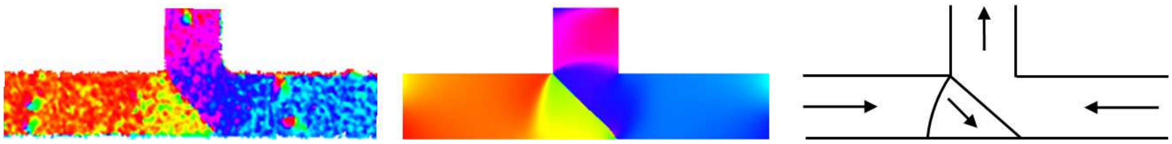

(b) Experimental field is 23 Oe, simulated is 60 Oe

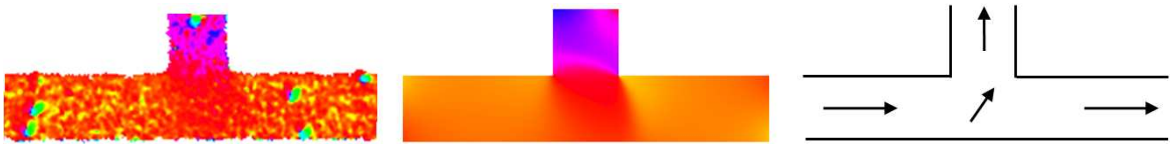

(c) Wall depinned at 32 Oe. Experimental field is 0 Oe, simulated is 0 Oe

Figure 5.17: Experimental and corresponding calculated DPC images of a transverse domain wall interacting with a T when there is an antiparallel alignment between the magnetisation in the T and the central domain of the transverse domain wall. Here the vertex of the domain wall is incident on the T.

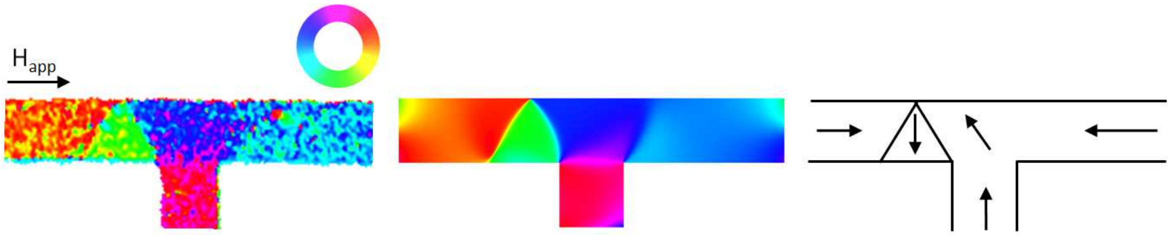

(a) Experimental field is 15 Oe, simulated is 20 Oe

(b) Experimental field is 24 Oe, simulated is 60 Oe

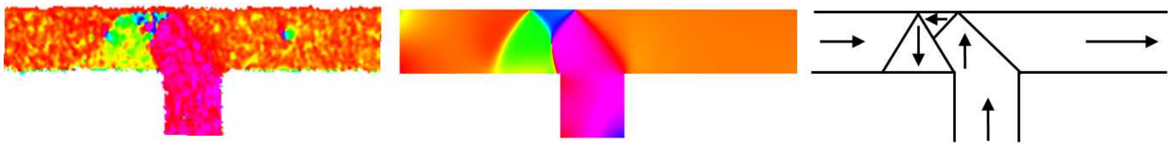

(c) Far side of wire reversed at 30 Oe. Experimental field is 0 Oe, simulated is 0 Oe

Figure 5.18: Experimental and corresponding calculated DPC images of a transverse domain wall interacting with a T when there is an antiparallel alignment between the magnetisation in the T and the central domain of the transverse domain wall. Here the wide side of the domain wall is incident on the T.

A potential barrier was also observed when the wide side of the transverse domain wall was incident on the T, figure 5.18. A slightly higher field of 15 Oe was required to move the transverse domain wall to the T, figure 5.18a. The leading wall of the domain wall packet was pinned at the first corner of the T. If the field was removed at this stage, the transverse domain wall travelled back along the wire to the hook, not shown here. On increasing the field, the transverse domain wall clearly compressed as it moved further towards the trap, figure 5.18b. At a field of 30 Oe, the far side of the wire abruptly reversed thus creating a 360° domain wall to the left of the T at remanence, as shown in figure 5.18c. The behaviour observed here is in good agreement with that observed in the simulation, which also predicted the formation of a 360° domain wall to the left of the T.

With a transverse arm patterned on both sides of the wire, figure 5.19, the progress of the domain wall was efficiently obstructed in a manner similar to that observed when the wide side of the wall met the T. A small field of 6 Oe was required to move the domain wall towards the trap where the field was then removed and the domain wall configuration observed, figure 5.19a. At remanence, the leading wall stopped at the left corner of the double T, the same location observed for the single T case in figure 5.18. As the field was increased, the vertex travelled further towards the trap, thus

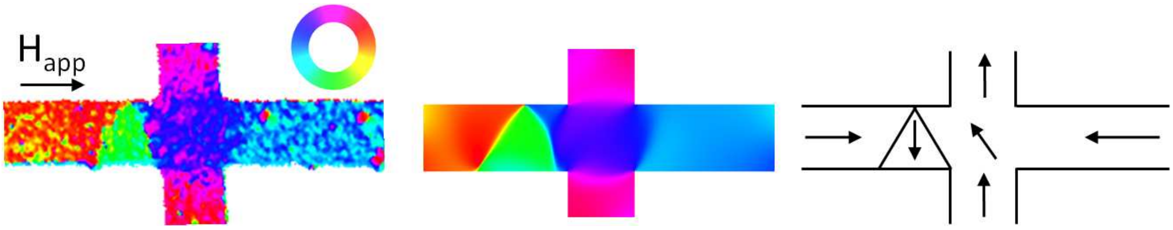

(a) Experimental field is 0 Oe, simulated is 0 Oe

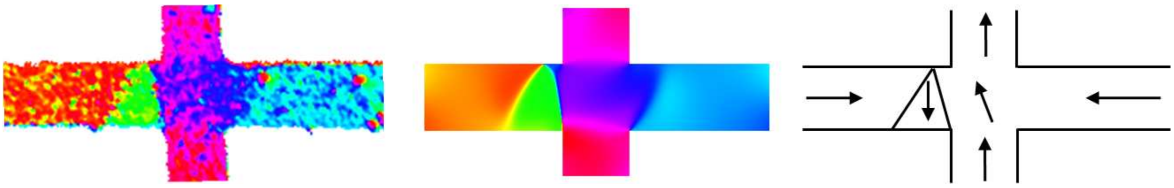

(b) Experimental field is 20 Oe, simulated is 40 Oe

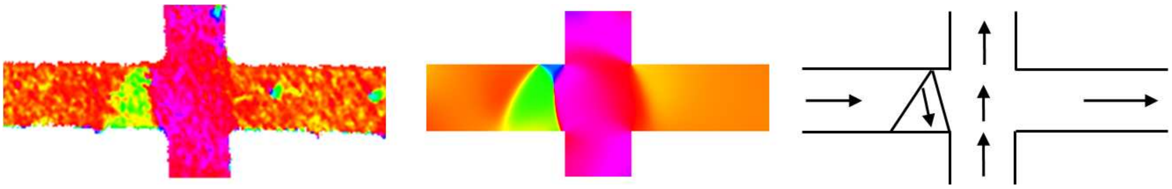

(c) Far side of wire reversed at 40 Oe. Experimental field is 0 Oe, simulated is 0 Oe

Figure 5.19: Experimental and corresponding calculated DPC images of a transverse domain wall interacting with a double T when there is an antiparallel alignment between the magnetisation in the double T and the central domain of the transverse domain wall.

reducing the extent of the transverse domain wall, figure 5.19b. The far side of the wire abruptly reversed at a field of 40 Oe before the original transverse domain wall was transmitted through the T, figure 5.19c. Consequently, a 360° domain wall was formed to the left of the double T, as observed in figure 5.18. Here the double-T acted as an effective energy barrier for the incoming wall with a slightly higher field required experimentally to reverse the far side of the wire.

### 5.2.4 Discussion

In summary, the interaction of transverse domain walls with both single and double transverse arms was studied where the relative orientation between the magnetisation in the central domain of the transverse domain wall and the transverse arm was both parallel and anti-parallel. With an unfavourable alignment, the T acted as a strong potential barrier to a transverse domain wall regardless of whether the wide side or vertex of the wall was incident on the T. With a favourable alignment however, the interaction was more varied. A table summarising the critical fields observed in both simulation and experiment is given in table 5.2. A considerable extension of the wall was observed for a transverse domain wall being pulled from a double T when there was a parallel alignment of the magnetisation in the wall core and trap, however an extension of the wall was not observed in all cases where this was predicted to occur by simulation. One possible reason for this may be due to the fact that the experiments were performed at room temperature and may cause the domain walls to depin more

| | Parallel DW and T | | |
|---|---|---|---|
| | Simulation | | Experiment |
| | DW Extension | Depinning | Depinning |
| Vertex incident on T | - | 12.5 ± 0.5 | - |
| Wide side incident on T | 47.5 ± 2.5 | 77.5 ± 2.5 | 25 ± 2 |
| DW incident on double T | 42.5 ± 2.5 | 77.5 ± 2.5 | 37 ± 2 |
| | Anti-parallel DW and T | | |
| | Simulation | | Experiment |
| | DW Extension | Depinning | Depinning |
| Vertex incident on T | 62.5 ± 2.5 | 102.5 ± 2.5 | 32 ± 2 |
| Wide side incident on T | 67.5 ± 2.5 (N) | 97.5 ± 2.5 (N) | 30 ± 2 (N) |
| DW incident on double T | - | 77.5 ± 2.5 (N) | 40 ± 2 (N) |

Table 5.2: The critical fields, in Oe, involved in the interaction of transverse domain walls with T shaped traps observed from both simulation and experiment. Only the depinning fields are included experimentally. The entries containing (N) indicate where a new domain wall was nucleated prior to depinning.

easily due to thermal activation [14]. As a result, only the depinning fields obtained from experiment are given in the table. Additionally, a depinning field for a parallel alignment of the transverse domain wall and T where the vertex met the T could not be determined as the T was not observed to pin the transverse domain wall.

It is evident from experiment, that in the parallel case, the addition of a second transverse arm increases the field required to depin the domain wall, or in the anti-parallel case, the field to reverse the far side of the wire; this was not observed in the simulations however. In the simulation, the addition of a second transverse arm did not alter the depinning field for a parallel alignment between the domain wall and trap. Furthermore, a lower depinning field was calculated with the addition of a second T in the anti-parallel case. However, the length of the structures used in the simulation was decreased to reduce the simulation time and therefore the simulated structures differ considerably from the fabricated structures. Unfortunately, due to time constraints, simulations of the full structures could not be performed. Furthermore, quantitative agreement between the simulated and experimental reversal fields is not expected, as the simulations do not include the effect of temperature, whilst the experiments were performed at room temperature. Good qualitative agreement was observed between the simulations and experiment however, and cases where the simulation predicted depinning by nucleation of a domain wall from the trap were also reproduced experimentally.

It is clear that this type of pinning geometry acts as an effective trap to an incoming transverse domain wall in most cases, particularly with the addition of a second transverse arm. The experimental DPC images have clearly revealed the nature of the interaction between the transverse domain walls and the T shaped pinning sites, in good agreement with the calculated DPC images from simulation.

## 5.3 Role of the domain wall asymmetry in relation to pinning

In the previous section, the interaction of transverse domain walls with both a single and double transverse arm was studied for a variety of domain wall-trap configurations. However, the asymmetry of the transverse domain wall was not considered in these experiments and may play a role in the interaction, especially in cases where the pinning is weak. The experiments in the following section aim to probe the significance of the asymmetry in the transverse domain wall.

In this section, a more rounded trap geometry with a significantly reduced height was employed with the aim of preserving the overall structure of the domain wall as it was transmitted through the constriction. The structures were fabricated by electron beam lithography, thermal evaporation of 9 nm permalloy and lift-off performed by

João Sampaio from the Imperial College London. The Fresnel mode of Lorentz microscopy was used to characterise the magnetic behaviour of transverse domain walls in these structures. Although the thickness of the wires here is the same as the wire thickness in the previous section, where DPC imaging was used, the width of these wires is significantly larger and as a result the domain wall contrast was greater for these structures using Fresnel imaging.

## 5.4 The domain wall trap structure

A schematic of the wire used for these experiments is given in figure 5.20a. The structures are 600 nm wide arcs of radius 7.5 $\mu$m, spanning an angle of 60°. The domain wall trap was a semicircle of radius, $R_{\text{trap}}$, equal to half the wire width, w. The wire thickness was 9 nm. A trap was patterned on both sides of the wire, as in the previous section, to investigate the interaction of domain walls of different symmetries, i.e. when the magnetisation in the central domain is either up or down, with respect to the trap. Using this system, both the wide side and vertex of the wall interact with the trap, as in the first section of this chapter. The four different trap configurations, comprising either a constriction or protrusion, are given in figures 5.20b-e.

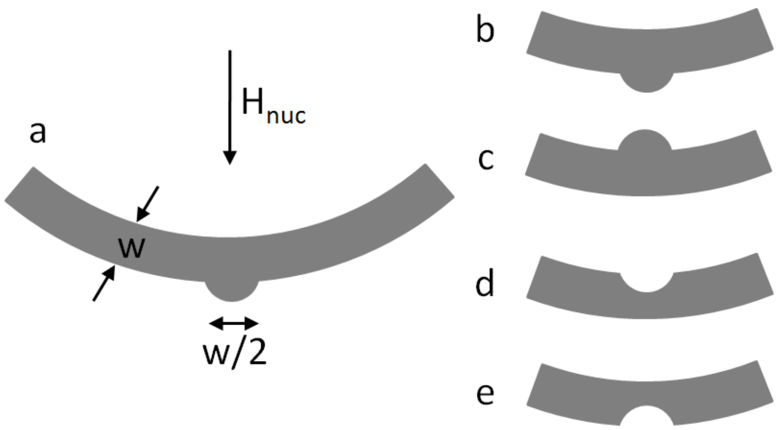

Figure 5.20: Schematic of the curved wires containing constrictions and protrusions. The width of the wires, w = 600 nm. With the application of a nucleation field along the direction indicated, a domain wall forms at the trap.

A domain wall was formed by applying a large magnetic field along the direction shown in figure 5.20 to force the magnetisation in the wire either side of the arc downwards thus creating a head-to-head domain wall at the trap. The wire dimensions used here (the wire width is 600 nm; thickness is 9 nm) suggest that a vortex domain wall is the favourable domain wall configuration for a straight segment of wire [15], however the wires used in this study are curved. Additionally, the nucleation field sets the magnetisation within the central domain leading to the formation of asymmetric

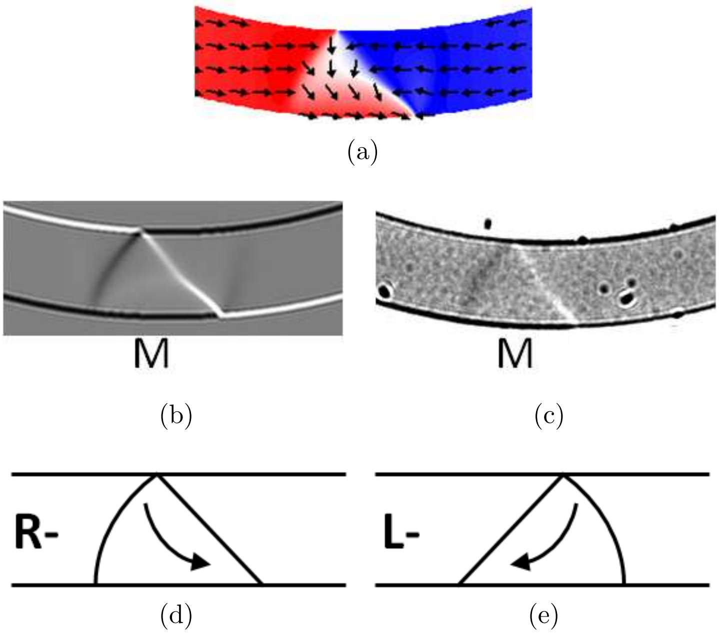

Figure 5.21: An asymmetric transverse domain wall (a) calculated by OOMMF, (b) corresponding calculated Fresnel image and (c) an experimental Fresnel image. Schematic illustrations of an asymmetric transverse domain wall with the asymmetry towards (e) the right and (d) the left are also given.

transverse domain walls on removal of the field.

The transverse domain walls observed here also have an asymmetry, i.e. the central domain also has a component of magnetisation parallel to the wire edge i.e. either to the right (R-) or left (L-). The direction of this asymmetry could not be controlled in the experiments performed here however it may be detected by observing the Fresnel contrast along the edges of the wire. Figure 5.21a shows the result of a simulation of a R-asymmetric transverse domain wall in an arc with no constriction or protrusion. Figures 5.21b,c show the corresponding calculated Fresnel image, using only the magnetic phase, and an experimental Fresnel image of an equivalent transverse domain wall. The nature of the asymmetry is determined by observing the Fresnel contrast along the outer edge of the wire, at M in both images. To the right of the wall, the thick dark Fresnel fringe runs along the inner edge of the arc, ending at the vertex of the wall. This indicates that the magnetisation is directed along the arc from right to left. To the left of the wall, the thicker Fresnel fringe runs along the outer edge of the arc, indicating the magnetisation is directed from left to right. This Fresnel fringe also appears along the wire edge where the central domain of the transverse domain wall is situated at M, indicating there is a component of magnetisation within the domain that is also directed from left to right. A schematic of the magnetic configuration of both a R- and L-asymmetric transverse domain wall is given in figures 5.21d,e.

### 5.4.1 Interaction of asymmetric domain walls with constrictions

In the following sections, the nature of the interaction of transverse domain walls with constrictions first of all, followed by protrusions is presented using Fresnel imaging in conjunction with micromagnetic simulation. OOMMF simulations using masks of the fabricated structures were performed by Dr. Dorothée Petit from Imperial College London using standard parameters for permalloy and a cell size of $5 \times 5 \times 9\,\mathrm{nm}^3$. Mask files obtained from SEM images of the arcs were used to include any effects arising as a result of edge roughness or random defects in the structure. Fresnel images were calculated from the results of the simulation and included to aid interpretation of the experimental images. In order to differentiate the effect of the asymmetry from the effect of other sources of asymmetry such as random defects in the structure or misalignment of the arc with the applied field, straight, smooth and perfectly symmetrical structures of identical dimensions (referred to as ”perfect” structures) were also simulated. The detailed processes involved in the depinning of an asymmetric transverse domain wall in both directions was the focus of these experiments, thus a purely qualitative comparison was made with the results of these simulations. The experiments were carried out as follows. A domain wall was nucleated at the pinning site with the application of a large field along the direction given in figure 5.20. An image was then acquired of the domain wall pinned by the trap at remanence. Subsequently, a magnetic field was applied in both the forward and reverse horizontal directions to determine the nature of the potential profile presented by the pinning site, detailed in the next sections.

#### Constriction on outer edge of arc

Figure 5.22 illustrates the behaviour of a transverse domain wall in an arc with the constriction on the same side of the wire as the wide side of the wall. In each sub-figure, a Fresnel image is given in (I) with corresponding schematic in (II). The corresponding calculated Fresnel image at a defocus of 1730 $\mu$m, the value used in experiment, is given in (III) obtained from the simulation in (IV). The Fresnel images shown in figure 5.22 were calculated using the magnetic contribution to the phase only, ignoring electrostatic effects and as a result some differences in contrast appear along the wire edges, for example, the bright white line appearing along the wire edge in the calculated image does not appear in the experimental image due to the additional superimposed electrostatic contribution. Following nucleation, a magnetic field was applied in both the forward, +H$_{\mathrm{app}}$, and reverse, $-$H$_{\mathrm{app}}$, directions to observe the behaviour of the domain wall as it was both transmitted through and pulled away from the trap. In addition to the remanent state, the magnetic configuration is also displayed at a field value close to $H_d^+/2$ and $H_d^-/2$, where $H_d^+$ and $H_d^-$ are the depinning fields in the forward and reverse directions, respectively.

At remanence, the transverse domain wall occupied a position to the left of the trap, figure 5.22a(I), and comprised a horizontal component of magnetisation directed from left to right. Confirmation of this is obtained by observing the thick dark fringe along the lower edge of the arc, which is present along the lower edge of the arc to the right of the wall and along the edge of the constriction at **B**, indicating the magnetisation

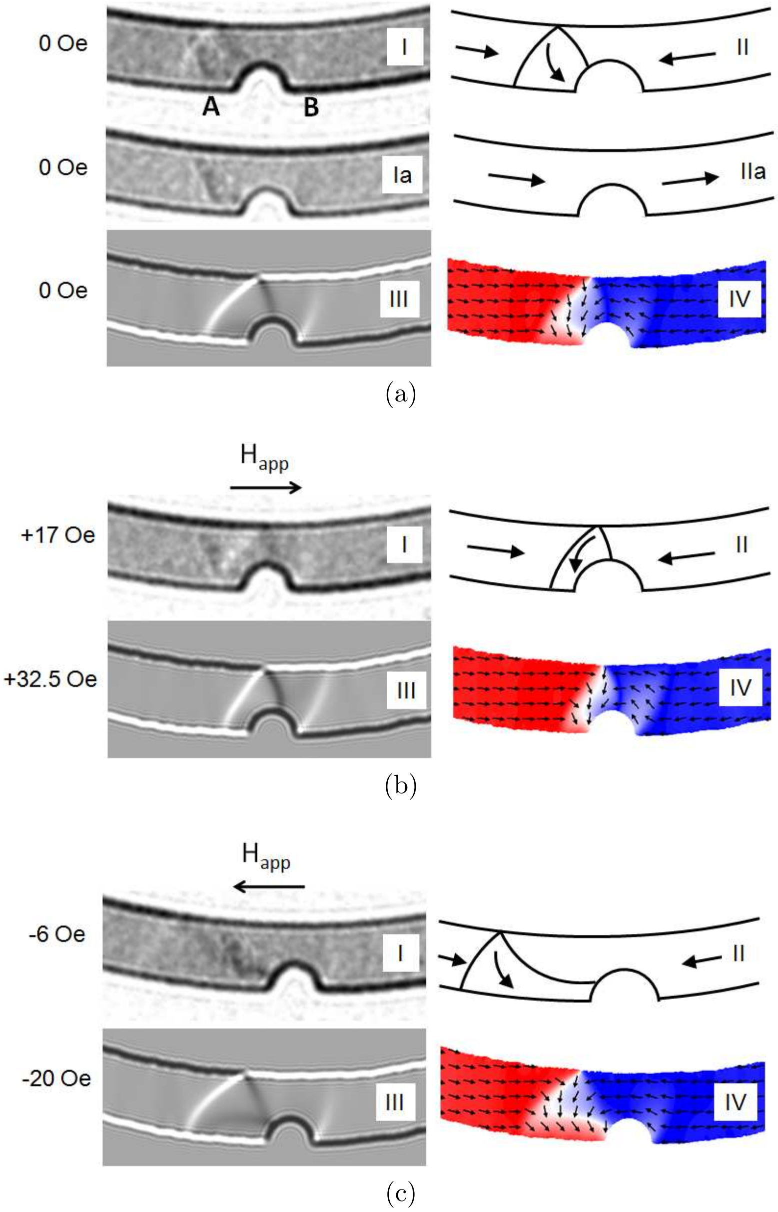

Figure 5.22: In each sub-figure (I) is an experimental Fresnel image, (II) is a corresponding schematic. (Ia) and (IIa) illustrate the appearance of the wire containing no domain wall, revealing a defect to the left of the constriction. (III) is the corresponding calculated Fresnel image obtained from the micromagnetic simulation given in (IV). (a) illustrates the form of the domain wall in the trap at remanence. (b), (c) illustrate the depinning of the domain wall at a field $\approx H_d/2$ in both the forward and reverse directions, respectively.

here is directed from right to left parallel to the edge of the structure. That there is no dark fringe along the wire where the wide side of the wall is located at **A** suggests that there is a component of magnetisation within the wall that is opposite in direction, i.e. directed from left to right. A schematic illustration is given in figure 5.22a(II). Contrast also arises within this particular wire to the left of the constriction, close to **A**, that is not magnetic. Confirmation of this is given by a Fresnel image of the wire in a uniformly magnetised state in figure 5.22a(Ia). A schematic of the magnetisation is given in figure 5.22a(IIa). It is clear from this Fresnel image that the dark band appearing on the left side of the wire is not magnetic and should be ignored in the remaining images in figure 5.22. A simulation was also performed for a transverse domain wall with a horizontal component of magnetisation directed from right to left, which showed that this type of domain wall is not stable on the left side of the constriction and immediately transforms to a R-asymmetric domain wall. The calculated Fresnel image given in 5.22a(III) is in good agreement with the experimental Fresnel image. An image of the remanent state obtained from OOMMF is given in figure 5.22a(IV).

At a field of +17 Oe ($\approx \mathrm{H}_\mathrm{d}^{+}/2$), the width of the transverse domain wall reduced significantly, figure 5.22b and it mainly occupied the left side of the trap at this field value. A significantly higher field of 32 Oe was required to depin the transverse domain wall; the wall packet continued to compress and abruptly depinned at this field value without travelling beyond the constriction.

Under a reverse field of -6 Oe ($\approx \mathrm{H}_\mathrm{d}^{-}/2$), the overall width of the transverse domain wall increased noticeably whilst the trailing domain wall remained strongly pinned to the left side of the trap. The transverse domain wall depinned at a field of -11 Oe. The simulation predicted a modest expansion of the domain wall as it was pulled from the constriction, however thermal effects in the experiment may help to overcome weak pinning by random defects in the structure and allow for a greater distortion of the wall. The simulations of these structures predicted depinning fields of >+65 ± 5 Oe/-36 ± 4 Oe in the forward and reverse directions, respectively. In the simulated case the whole structure reversed before the transverse domain wall depinned, hence only the lower boundary of the depinning field could be determined.

The simulation of the perfect structure indicated that a transverse domain wall is stable at a position to the side of the constriction with its asymmetry directed towards

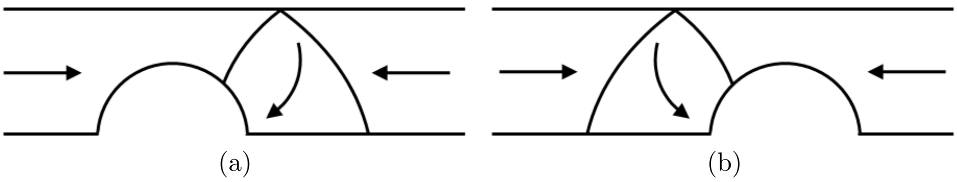
(a) (b)

Figure 5.23: Schematic illustration of the remanent configuration for (a) a L- and (b) a R-asymmetric transverse domain wall in the vicinity of a constriction.

the trap, i.e. a L-asymmetric transverse domain wall ends up on the right of the trap and a R-asymmetric wall ends up on the left, as illustrated in figure 5.23.

### Constriction on inner edge of arc

When the vertex of the transverse domain wall interacts with a constriction, the equilibrium position of the domain wall is close to the centre of the trap, however, the domain wall asymmetry forces the domain wall to occupy a position slightly to the left of the trap, figure 5.24a. It can be noted that the asymmetry in the domain wall is directed from right to left from the dark Fresnel fringe that runs along the lower edge of the wire, where the wall is located at **C**. The simulation also predicted that

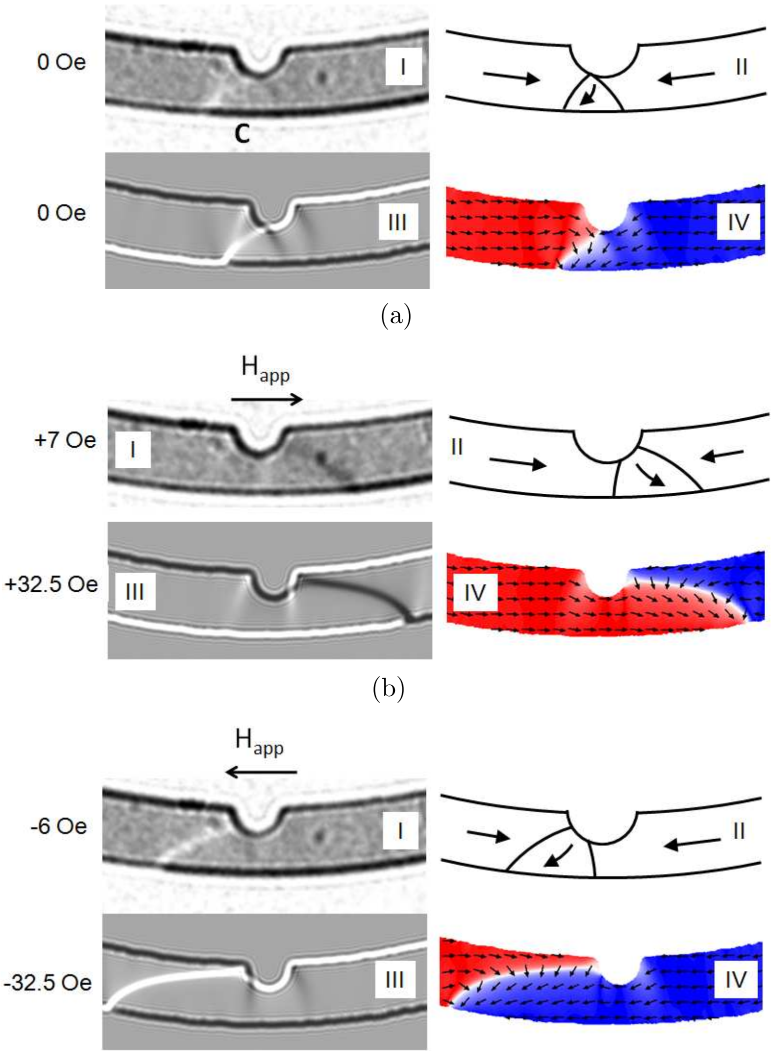

(a)

(b)

(c)

Figure 5.24: In each sub-figure (I) is an experimental Fresnel image, (II) is a corresponding schematic. (III) is the corresponding calculated Fresnel image obtained from the micromagnetic simulation given in (IV). (a) illustrates the form of the domain wall in the trap at remanence. (b), (c) illustrate the depinning of the domain wall at a field $\approx H_d/2$ in both the forward and reverse directions, respectively.


(a) +12 Oe


(b) -10 Oe

Figure 5.25: With the application of a higher field, the domain wall extended a greater distance away from the constriction.

a transverse domain wall with its asymmetry directed towards the left will be pinned at a location close to but slightly left of the centre of the constriction. The calculated Fresnel image is in good agreement with the experimental image.

With the application of a magnetic field of +7 Oe (≈ $H_d^+/2$) in the forward direction, figure 5.24b, the wall extended significantly beyond the constriction and into the far side of the wire; the asymmetry in the transverse domain wall also switched from left to right as it progressed through the trap. The simulation predicted a larger extension of the domain wall into the far side of the wire at a field ≈ $H_d^+/2$, figure 5.24b(IV). The wall depinned at a field of +13 Oe.

A similar deformation of the wall structure was observed when a reverse field was applied to the transverse domain wall, figure 5.24c, whereby the wall extended considerably into the wire to the left of the trap. The extent of the domain wall expansion was modest compared with that predicted by the simulation. However, the domain wall extended a larger distance away from the trap with the application of a higher field, as illustrated in figure 5.25. The domain wall depinned at a field of -11 Oe. The simulated depinning fields were calculated at +36 ± 4/-45 ± 5 Oe. The reason for this discrepancy is unclear as no difference in depinning field was predicted for the perfect structures.

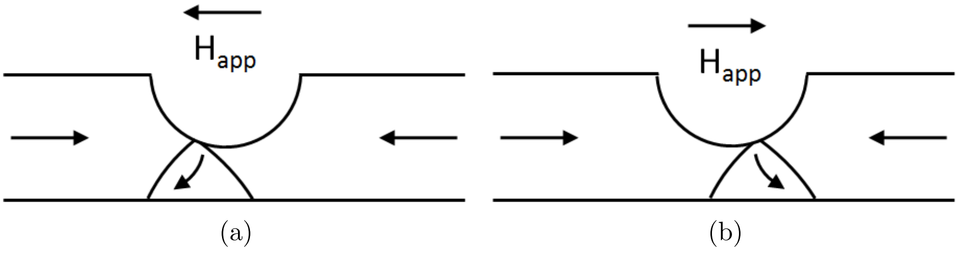

(a) (b)

Figure 5.26: Schematic illustration of two equivalent cases. In (a) pulling a L-asymmetric transverse domain wall away from a constriction is equivalent to pushing a R-asymmetric transverse domain wall through the same constriction, as in (b).

Simulations of the perfect structures indicated that the behaviour of a R-asymmetric transverse domain wall under $+H_{app}$ is equivalent to the behaviour of a L-asymmetric transverse domain wall under $-H_{app}$, as illustrated in figure 5.26. Additionally, the simulations indicated that the behaviour of a L-asymmetric domain wall under the action of $-H_{app}$ is equivalent to its interaction under $+H_{app}$, above a critical field, $+H_c$. $+H_c$ is the field at which the L-asymmetric transverse domain wall transforms to a R-asymmetric transverse domain wall under a positive field, and was calculated to be ±12.5 Oe. Above $+H_c$, both configurations mirror each other, as in figure 5.25, leading to the same depinning field of ±22.5 Oe.

In summary, a constriction acts as either a potential well or potential barrier depending on the orientation of the incoming wall with respect to the constriction. The potential profile presented to a domain wall depends on whether it is energetically favourable for the domain wall to sit in the centre of the trap as illustrated in figure 5.27. If so, an attractive potential well is observed (figure 5.27) otherwise a repulsive potential barrier occurs due to the build up of positive charge as in figure 5.27b. In the following section, the interaction of transverse domain walls with protrusions is investigated.

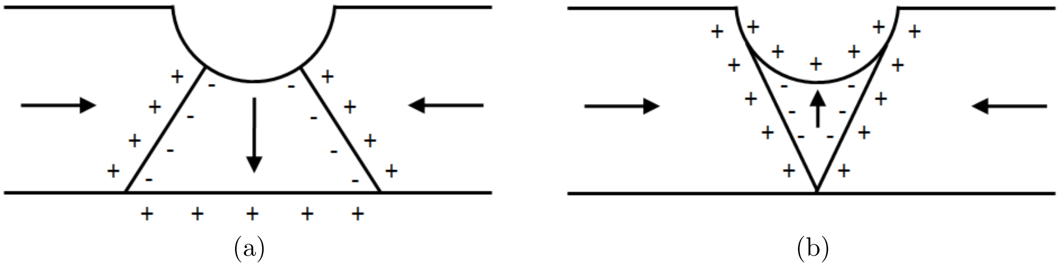

Figure 5.27: Schematic illustration of the distribution of magnetic charge when transverse domain walls of either chirality are placed in the centre of a constriction. The configuration in (a) is energetically favourable and the domain wall experiences a potential well. In (b), the configuration is unstable due to the generation of uncompensated charges along the trap edge. The domain wall experiences a potential barrier and spontaneously moves to the side of the constriction.

## 5.4.2 Interaction of asymmetric domain walls with protrusions

### Protrusion on outer edge of arc

Quite different behaviour was observed when the wall was faced with a protrusion rather than a constriction. At remanence, figure 5.28a, the equilibrium position of the domain wall is close to the centre of the trap and due to the similarity in the width of the transverse domain wall packet and the extent of the trap, the protrusion acts as a potential well for the domain wall. A component of magnetisation within the wall, following the edge of the structure from right to left, is also detected by observing the Fresnel contrast along the edge of the protrusion. A similar component of magnetisation parallel to the edge of the structure is also present in the calculated Fresnel image in (III), confirmed by observing the magnetisation given in (IV). There is good agreement between the calculated and experimental Fresnel images.

At a field of +5 Oe ($\approx \mathrm{H}_{\mathrm{d}}^{+}/2$), the domain wall remained unchanged and is clearly

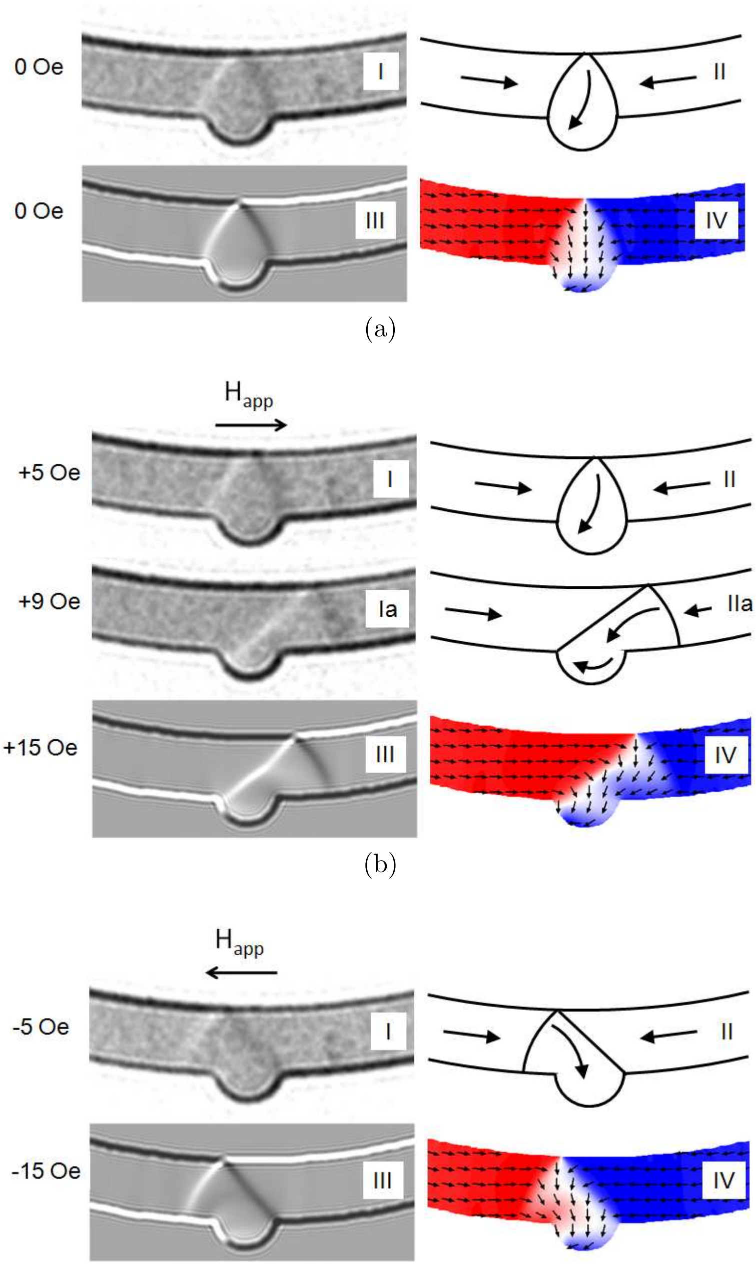

(a)

(b)

(c)

Figure 5.28: In each sub-figure (I) is an experimental Fresnel image, (II) is a corresponding schematic. (III) is the corresponding calculated Fresnel image obtained from the micromagnetic simulation given in (IV). (a) illustrates the form of the domain wall in the trap at remanence. (b), (c) illustrate the depinning of the domain wall at a field $\approx \mathrm{H}_{\mathrm{d}}/2$ in both the forward and reverse directions, respectively.

strongly pinned in the trap, figure 5.28b. However, the simulation predicts that the vertex moves along the wire towards the right, with the trailing domain wall firmly anchored to the corner of the trap at $H_d^+/2$. Additionally, the overall structure of the transverse domain wall distorts to some extent. The component of magnetisation within the wall, parallel to the structure edge, is preserved with the application of this field. Additionally, it was observed that at an applied field of +9 Oe, the domain wall abruptly distorted and extended a significant distance beyond the trap, as illustrated by the Fresnel image given in figure 5.28b(Ia). The domain wall depinned at a field of +10 Oe. The reason for this abrupt extension of the domain wall away from the protrusion is unclear but may be attributed to a random defect in the wire.

With the application of a magnetic field of -5 Oe ($\approx H_d^-/2$), figure 5.28c, the domain wall packet distorted and extended slightly beyond the trap into the wire. In this case the component of magnetisation within the domain wall parallel to the structure edge is parallel to the field direction leading to a smaller extension of the domain wall away from the trap (predicted by simulation) than in figure 5.28b. The domain wall depinned at a field of -9 Oe. The depinning fields for this structure were calculated to be $\pm 27.5 \pm 2.5$ Oe, therefore the asymmetry was predicted to have no effect on the strength of pinning for this structure. The depinning fields were measured to be $H_d^+ = +10.0 \pm 0.5$ Oe and $H_d^- = -9.2 \pm 0.4$ Oe, hence no asymmetry was detected within the precision of the applied field.

The simulation of the perfect structure indicated that the depinning field is dependent on the nature of the asymmetry within the domain wall relative to the direction of the applied field. The depinning fields for a L-asymmetric transverse domain wall under $-H_{app}$ and a R-asymmetric transverse domain wall under $+H_{app}$ are identical, as illustrated in figure 5.29. The simulation of the perfect structure also predicted that depinning field is lower when the nature of the asymmetry is anti-parallel to the direction of the applied field, i.e. for a L-asymmetric transverse domain wall, $H_d^+ = +22.5 \pm 2.5$Oe and $H_d^- = -17.5 \pm 2.5$Oe.

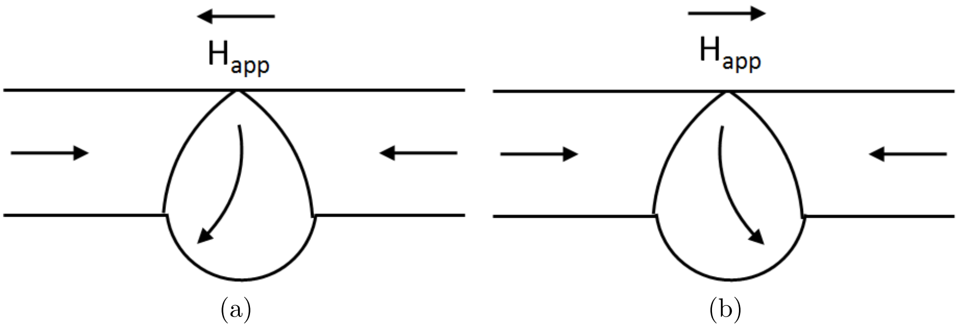

Figure 5.29: Schematic illustration of two equivalent cases. In (a) pulling a L-asymmetric transverse domain wall away from a protrusion is equivalent to pushing a R-asymmetric transverse domain wall through the same protrusion, as in (b).

### Protrusion on inner edge of arc

A different type of interaction was observed if the protrusion was placed on the inner edge of the arc, in other words, if the vertex of the transverse domain wall met the trap, figure 5.30. In this case, the transverse domain wall did not completely occupy the trap at remanence but instead the equilibrium position was to the left of the trap, illustrated in figure 5.30a. The transverse domain wall here also has a component of magnetisation parallel to the wire edge, directed from right to left, as in figure 5.28a. This is confirmed by noting that the dark Fresnel fringe that runs along the outer edge of the arc to the right of the wall also continues along the wire where the central

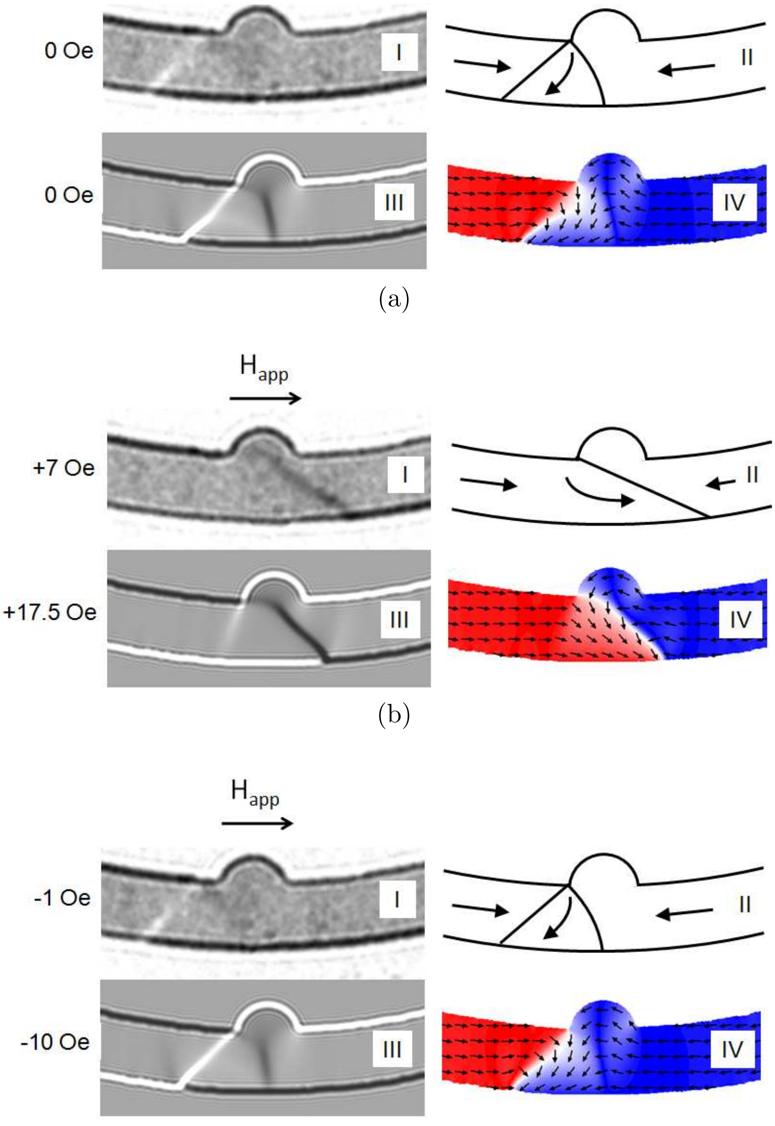

(a)

(b)

(c)

Figure 5.30: In each sub-figure (I) is an experimental Fresnel image, (II) is a corresponding schematic. (III) is the corresponding calculated Fresnel image obtained from the micromagnetic simulation given in (IV). (a) illustrates the form of the domain wall in the trap at remanence. (b), (c) illustrate the depinning of the domain wall at a field $\approx \mathrm{H_d}/2$ in both the forward and reverse directions, respectively.

domain of the asymmetric transverse domain wall is situated. The calculated Fresnel image (III) is in good agreement with the Fresnel image above (I).

The protrusion acted as a barrier to the domain wall and at an applied field of +7 Oe, the leading wall extended considerably beyond the trap, whilst the trailing wall was still pinned at the first corner of the trap (figure 5.30b). Additionally, the nature of the asymmetry in the transverse domain wall must switch in order for the domain wall to progress through the protrusion. The leading wall appears stronger here due to a greater angle of rotation of the atomic spins within the wall; the trailing wall is not visible. The wall depinned at a field of +14 Oe. This behaviour is in very good agreement with that previously reported for wires comprising a similar pinning geometry [16].

In the reverse direction the configuration of the transverse domain wall remained unchanged at a field of -1 Oe (≈ $H_d^-/2$), in agreement with that predicted by the simulation. A non-negligible magnetic field of -2 Oe was required to depin the wall from its position at the side of the trap indicating that the wall was trapped inside a small potential well. The depinning field was calculated to be +35 ± 5/-25 ± 5 Oe, characteristic of a potential barrier with a smaller side well.

A simulation of the perfect structure also showed that a L-asymmetric transverse domain wall transforms to a R-asymmetric transverse domain wall when under the influence of $+H_{app}$. They also showed that a R-asymmetric transverse domain wall depinned at a slightly lower field of -17.5 ± 2.5 Oe when pulled away from the trap. This could not be investigated in experiment as the asymmetry of the domain wall could not be controlled.

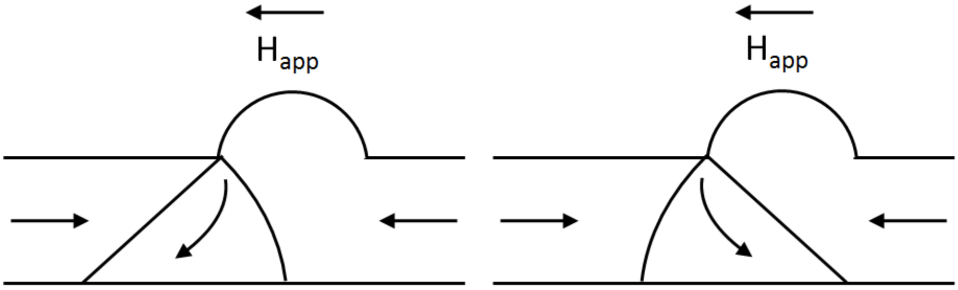

(a) Wall depins at -25 ± 5 Oe (b) Wall depins at -17.5 ± 2.5 Oe

Figure 5.31: Schematic illustration of (a) a L-asymmetric and (b) a R-asymmetric transverse domain wall pinned in the side well of the protrusion. The R-asymmetric transverse domain wall depins at a slightly lower field than the L-asymmetric transverse domain wall, predicted by the perfect simulation.

### 5.4.3 Discussion

A table summarising the depinning fields for transverse domain walls from constrictions and protrusions is given in table 5.3. A schematic illustration of the orientation of the transverse domain wall with respect to the constriction or protrusion is also provided for clarification. It is clear from the experiments performed here that the type of potential presented by either a constriction or protrusion to a transverse domain wall is dependent on its orientation with respect to the pinning site. In two cases, a potential well was observed and in the other two cases a potential barrier was observed. Additionally, in the cases where a potential barrier was observed, the domain wall appeared to be pinned by a small potential well prior to being transmitted through the potential barrier presented by the trap. The presence of a side barrier in the cases where a potential well was observed could not be determined as the domain wall would have to be created outside the pinning site and subsequently driven towards it. However, the presence of small potential barriers either side of a larger potential well have previously been reported for symmetric transverse domain walls [3].

In the cases where a potential well was observed, two completely different types of interaction were observed. In the case where the constriction was placed on the inner edge of the arc, a potential well was observed when the vertex of the domain wall was incident on the constriction. With the application of a field to either transmit the domain wall through or pull it away from the constriction, the nature of the asymmetry

| | Experimental | | Simulated | |
|---|---|---|---|---|
| | $H_d^+$ | $H_d^-$ | $H_d^+$ | $H_d^-$ |
| Constriction outer 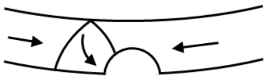 | +31.6 ± 1.5 | -11.2 ± 0.5 | >+65 ± 5 | -36 ± 4 |
| Constriction inner  | +12.5 ± 0.6 | -10.8 ± 0.5 | +36 ± 4 | -45 ± 5 |
| Protrusion outer 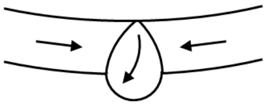 | +10.0 ± 0.5 | -9.2 ± 0.4 | +27.5 ± 2.5 | -27.5 ± 2.5 |
| Protrusion inner  | +14.1 ± 0.7 | -2.1 ± 0.1 | +35 ± 5 | -25 ± 5 |

Table 5.3: Depinning fields, in Oe, of transverse domain walls from both protrusions and constrictions when the wide side and vertex of the wall meets the trap, for example 'Constriction outer' refers to a constriction on the outer edge of the arc.

in the wall readily changed to align with the direction of the applied field. This is due to the vertex being anchored to the constriction; the wide side of the domain wall is influenced by the applied field. As a result, the nature of the domain wall asymmetry was not preserved as it was depinned from the constriction.

When a protrusion was placed on the outer edge of the arc, a potential well was also observed, however in this case, the wide side of the domain wall was anchored to the trap and the vertex moved along the wire in the direction of the applied field. As a result the nature of the asymmetry in the domain wall was not affected by the application of a magnetic field to drive it through, or away from the protrusion.

Where a potential barrier was observed, the favourable position for the domain wall was not in the centre of the trap but to one side of the trap at remanence. In one case, a considerable field was required to transmit the domain wall through the trap. The domain wall asymmetry was determined by its location with respect to the trap in the case of the constriction; a R-asymmetric domain wall was observed on the left side of the constriction and a L-asymmetric domain wall was observed on the right. Furthermore, the constriction provided a significantly stronger barrier to the domain wall than the protrusion, with a field more than twice required to overcome the barrier presented by the constriction than that for the protrusion.

It is evident that a transverse domain wall is efficiently pinned by both constrictions and protrusions regardless of whether its wide side or vertex is incident on the trap. A potential barrier however, provided a bigger obstacle for the domain wall than being pulled from a potential well. When the vertex is incident on the trap, the wide side of the domain wall is free to move in the direction of the applied field, and as a result the asymmetry readily changes to align with the field. The asymmetry was not affected by the applied field when the wide side of the domain wall was incident on the trap.

This geometry provides a highly effective method of pinning transverse domain walls regardless of their orientation and may provide a useful tool for the control of domain walls in magnetic logic devices, for example. Conversely, the effectiveness of the T-shaped trap was entirely dependent on the orientation of the transverse domain wall. However, this property is potentially highly advantageous in gaining control over transverse domain walls. For example, one highly efficient proposed application is its use as a domain wall gate [17], the basic concept of which is illustrated schematically in figure 5.32. By patterning the T on the upper edge of the wire, the T-shaped trap, or gate, either allows or prevents an incoming transverse domain wall to pass through. The gate may be controlled by the application of an external field to reverse its magnetisation. The gate is therefore open when its magnetisation is parallel to that within the central domain of the transverse domain wall, figure 5.32a, and is closed when there is an anti-parallel alignment between the gate and the core of the domain wall (figure 5.32b). Furthermore, in the closed state, the domain wall is blocked in

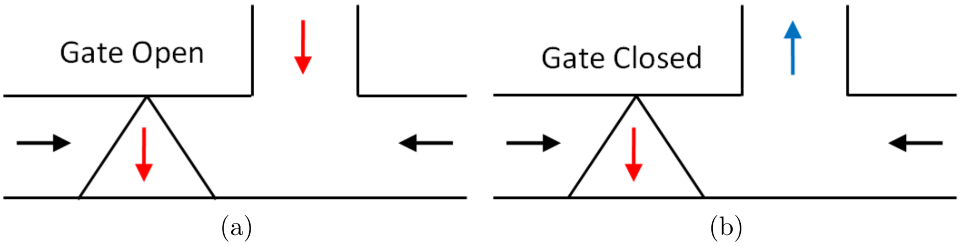

(a) (b)

Figure 5.32: Schematic illustration of a potential application for the T-shaped pinning geometry investigated earlier. The gate can either be (a) open to allow the domain wall to propagate through, or (b) closed to prevent it from travelling further.

front of the gate and may be pulled away from the gate with a small reverse field. Similar concepts have also previously been reported for controlling the propagation of both vortex [18] and transverse [19] domain walls.

It may be concluded that a greater strength of pinning of transverse domain walls is ensured by using elongated traps, where the magnetisation deviates more markedly from the mean direction in the main body of the wire. However, the orientation of the domain wall with respect to the trap is crucial to efficiently obstruct the domain wall. By using smaller, more rounded pinning sites however, the domain wall is efficiently pinned regardless of its orientation, with the main part of the potential profile largely unaffected by the asymmetry of a transverse domain wall. As a result this pinning geometry may provide an attractive method of gaining control over the propagation of domain walls for memory devices, and is perhaps made even more attractive by the reduced area of the trap.

# Bibliography

[1] D. A. Allwood, G. Xiong, C. C. Falkner, D. Atkinson, D. Petit and R. P. Cowburn, Science **309** 1688 (2005).

[2] S. S. P. Parkin, M. Hayashi and L. Thomas, Science **320** 190 (2008).

[3] D. Petit, A.-V. Jausovec, D. Read and R. P. Cowburn, J. Appl. Phys. **103** 114307 (2008).

[4] D. Petit, A.-V. Jausovec, H. T. Zeng, E. Lewis, L. O'Brien, D. Read and R. P. Cowburn, Phys. Rev. B **79** 214405 (2009).

[5] M. Hayashi, L. Thomas, C. Rettner, R. Moriya, X. Jiang and S. S. P. Parkin, Phys. Rev. Lett. **97** 207205 (2006).

[6] S.-H. Huang and C.-H. Lai, Appl. Phys. Lett. **95** 032505 (2009).

[7] M.-Y. Im, L. Bocklage, P. Fischer and G. Meier, Phys. Rev. Lett. **102** 147204 (2009).

[8] A. Himeno, K. Kondo, H. Tanigawa, S. Kasai and T. Ono, J. Appl. Phys. **103** 07E703 (2008).

[9] D. Bedau, M. Kläui, U. Rüdiger, C. A. F. Vaz, J. A. C. Bland, G. Faini, L. Vila and W. Wernsdorfer, J. Appl. Phys. **101** 09F509 (2007).

[10] S.-M. Ahn, D.-H. Kim and S.-B. Choe, IEEE Trans. Magn. **45** 2478 (2009).

[11] S. D. Kim, B. S. Chun and Y. K. Kim, J. Appl. Phys. **101** 09F504 (2007).

[12] R. D. McMichael and M. J. Donahue, IEEE Trans. Magn. **33** 4167 (1997).

[13] M. Kläui, J. Phys.: Condens. Matter **20** 313001 (2008).

[14] A. Himeno, T. Okuno, T. Ono, K. Mibu, S. Nasu and T. Shinjo, J. Magn. Magn. Mater. **286** 167 (2005).

[15] Y. Nakatani, A. Thiaville and J. Militat, J. Magn. Magn. Mater. **290** 750 (2004).

[16] C. W. Sandweg, N. Wiese, D. McGrouther, S. J. Hermsdoerfer, H. Schultheiss, B. Leven, S. McVitie, B. Hillebrands and J. N. Chapman, J. Appl. Phys. **103** 093906 (2008).

[17] D. Petit, A.-V. Jausovec, H. T. Zeng, E. Lewis, L. O'Brien, D. Read and R. P. Cowburn, Appl. Phys. Lett. **93** 163108 (2008).

[18] M. Hara, J. Shibata, T. Kimura and Y. Otani, Appl. Phys. Lett. **89** 192504 (2006).

[19] M. T. Bryan, T. Schrefl and D. A. Allwood, Appl. Phys. Lett. **91** 142502 (2007).

# 6

# Characteristics of Fast Field Pulse Driven Domain Wall Motion

## 6.1 Introduction

Understanding and control over the dynamic in addition to the static behaviour of domain walls is crucial for the development of magnetic storage devices. It is well established that a magnetic domain wall in a nanowire will move under the influence of a magnetic field [1, 2] or spin-polarised current [3, 4], which in turn considerably affects its propagation velocity [5, 6]. The speed at which a magnetic device operates however is entirely dependent on the speed at which a domain wall can be moved and values of up to 1 kms$^{-1}$ have been reported [7]. Under a modest external magnetic field, a domain wall propagates in a uniform manner as a well defined object. Above the Walker field however, the domain wall transforms between various magnetic configurations, i.e. transitions between vortex and anti-vortex states when driven by a magnetic field, as introduced in chapter 1. These transformations have been predicted by simulation [8] and measured from the time evolution of a domain wall's resistance, which is structure-dependent [3]. Additionally, the progress of a domain wall is slowed significantly as a result, thus significantly lowering the propagation velocity. For a 600 nm wide, 20 nm thick Permalloy wire, a Walker field of ≈4 Oe has been reported [6]. In this chapter, two different wire geometries were used to investigate the effect of a magnetic field on the propagation of a domain wall using pulsed magnetic fields. By using a field pulse of a fixed duration rather than a static field, the lower limit of the domain wall velocity can be calculated from the distance the wall travels in a given field duration, assuming uniform motion of the domain wall. Additionally, by repeating a sequence of field pulses, a large number of results can be acquired in a relatively short time. One proposed method of triggering a transformation in domain wall structure involving a gently tapered wire was investigated in this chapter, i.e. a wire in which the width varies gently along its length. At the wider end of the wire a vortex domain wall may be the lowest energy configuration however as the wall is moved towards the narrower end of the wire, the lowest energy configuration will change and may cause the wall to change structure accordingly. Transformations between domain wall configurations have previously been observed through heating [9] or with the application of an electrical current [10], however domain wall transformations triggered by wire geometry have not been widely explored. One study has been carried out using a wire of varying thickness [11], however transformations between vortex and transverse domain walls were not directly observed. In the second part of this chapter, the behaviour of domain walls in straight wires under the influence of pulsed magnetic fields was probed, where domain wall transformations were explored in addition to the velocity-field characteristic of propagating domain walls.

## 6.2 Domain wall propagation in a tapered wire

### 6.2.1 The structure overview

A schematic illustration of the gently tapered wire structure introduced above is given in figure 6.1a. The wire varied in width from 500 nm to 50 nm over a length of 80 $\mu$m and was connected to an ellipse of dimensions 3.4 $\mu$m × 2 $\mu$m. Electron beam lithography and lift off techniques were used to fabricate the wire, made from 10 nm thick thermally evaporated permalloy. In order to illustrate the wire dimensions in terms of the expected domain wall configuration, an image of the domain wall phase diagram for permalloy (introduced in chapter 1) is given in figure 6.1b, where the dashed red line indicates the variation in wire width for a constant thickness of 10 nm. It may be seen that at a wire width of 150 nm, there is a transition between vortex and transverse domain walls for the wire thickness studied here, however it must be noted that the phase diagram is valid for wires with straight edges. This phase boundary is located a distance of around 62 $\mu$m along the wire.

A variety of methods exist, some of which have been employed in this thesis, to generate domain walls in nanowires. In most cases a pair of orthogonal fields are required, with one used to nucleate a domain wall and the other to subsequently drive it along the wire. In this chapter, a larger pad situated at one end of the wire was utilised, meaning that nucleation and propagation of magnetic domain walls could be achieved with a uniaxial field parallel to the wire axis. Head-to-head domain walls were injected into the wire with the application of a magnetic field along the direction indicated by $H_{\text{inject}}$ in figure 6.1a. The initial uniformly magnetised state was set with a field along $H_{\text{reset}}$ to ensure the wire was in the same configuration at the start of each experiment. The direction of both $H_{\text{inject}}$ and $H_{\text{reset}}$ can be interchanged however, and a reset field applied along the direction of $H_{\text{inject}}$ followed by an injection field applied along the direction $H_{\text{reset}}$ will produce a tail-to-tail domain wall in the wire. The direction of

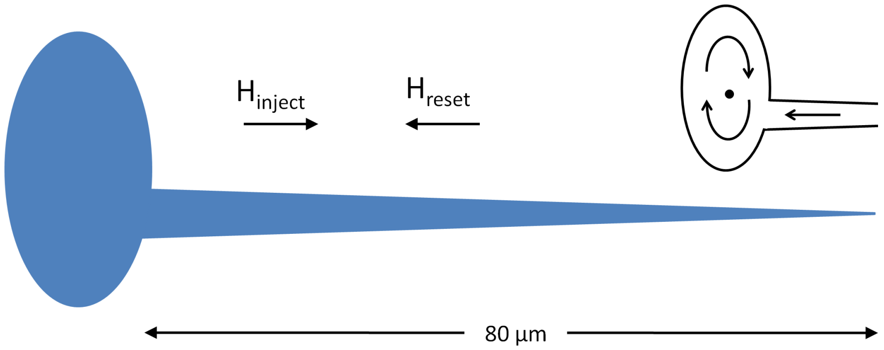

(a)

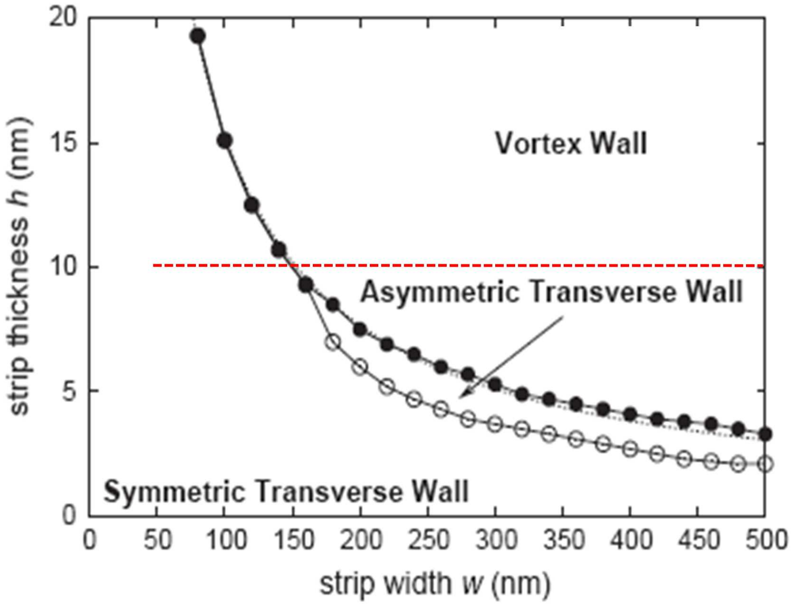

(b)

Figure 6.1: (a) A schematic of the wire geometry used to investigate the propagation of domain walls in a wire of varying width. (b) The red dashed line indicates the dimensions the wire spans in the domain wall phase diagram [12] for permalloy.

field used to inject and subsequently propagate a domain wall along the wire will be indicated in each figure by $H_{inject}$ and $H_{prop}$, respectively. A schematic of the initial configuration of the wire will also be included. $H_{reset}$ was always anti-parallel to $H_{inject}$. With the application of a magnetic field, changes in the magnetisation within the pad result in the creation of a domain wall at the wire/pad junction [13]. With further increase of the applied field, the domain wall detaches from the pad and propagates down the wire. A vortex is still present within the elliptical pad at the value of $H_{inject}$. Nucleation pad shapes with straight edges such as rectangles were discounted as these geometries can support a number of magnetic configurations at remanence and may not provide highly reproducible domain wall injection. An ellipse however, supports the magnetisation circulating around a single vortex and is a more favourable injection pad geometry as the vortex readily forms following saturation. Furthermore, it has been found that by offsetting the pad with respect to the long axis of the wire, the symmetry

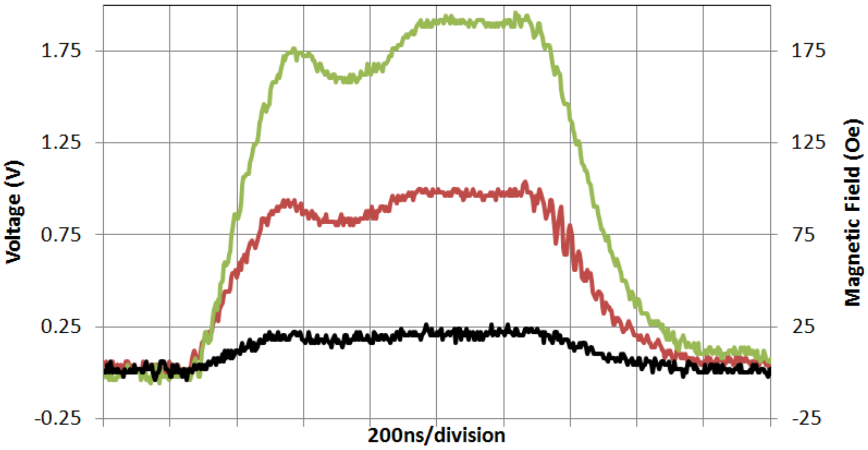

Figure 6.2: Profile of the pulse used to apply the field to the wire. Three different field pulses are given to illustrate the change in profile as the height is increased.

of the system is lowered, thus introducing a degree of control over the chirality of the injected domain wall [14]. The wire was offset from the centre of the ellipse by 250 nm. Additionally, a series of markers, of dimensions 250 × 50 nm were patterned at 5 $\mu$m intervals alongside the wire, at a distance of 2 $\mu$m from the wire. The markers provided a useful tool in quickly determining the position of a given domain wall in the wire. The wire was fabricated by electron beam lithography and lift off techniques; the permalloy was deposited by thermal evaporation. Characterisation of the magnetic behaviour was carried out using the Fresnel mode of Lorentz microscopy.

Time-resolved dynamic studies could not be performed in situ due to the acquisition rate of the CCD array in the Philips CM20 which limits the time resolution to around 20 ms. A solution to this problem was to use a magnetic field pulse in place of the static magnetic fields used in previous experiments. The domain wall velocity was calculated by measuring the distance a wall travels following the application of a field pulse. This method assumes a uniform motion of the domain wall on application of the field pulse and provides a lower limit of the propagation velocity. Therefore all velocities quoted throughout this chapter indicate the lower limit of the velocity. The pulsed magnetic field was generated using the setup described in chapter 2, section 2.4.5. Figure 6.2 shows three pulse profiles of different heights used to deliver the field to the sample. Here the height of the pulse is shown in volts, where 1V provides a magnetic field of 100 Oe at the specimen position in the rod. From the full width at half maximum, the pulse duration is around 1 $\mu$s.

### 6.2.2 Pulsed field experiments

Initially a domain wall was injected into the wire with the application of a 48 Oe field pulse, along the direction shown in the figure, to form a clockwise (cw) tail-to-

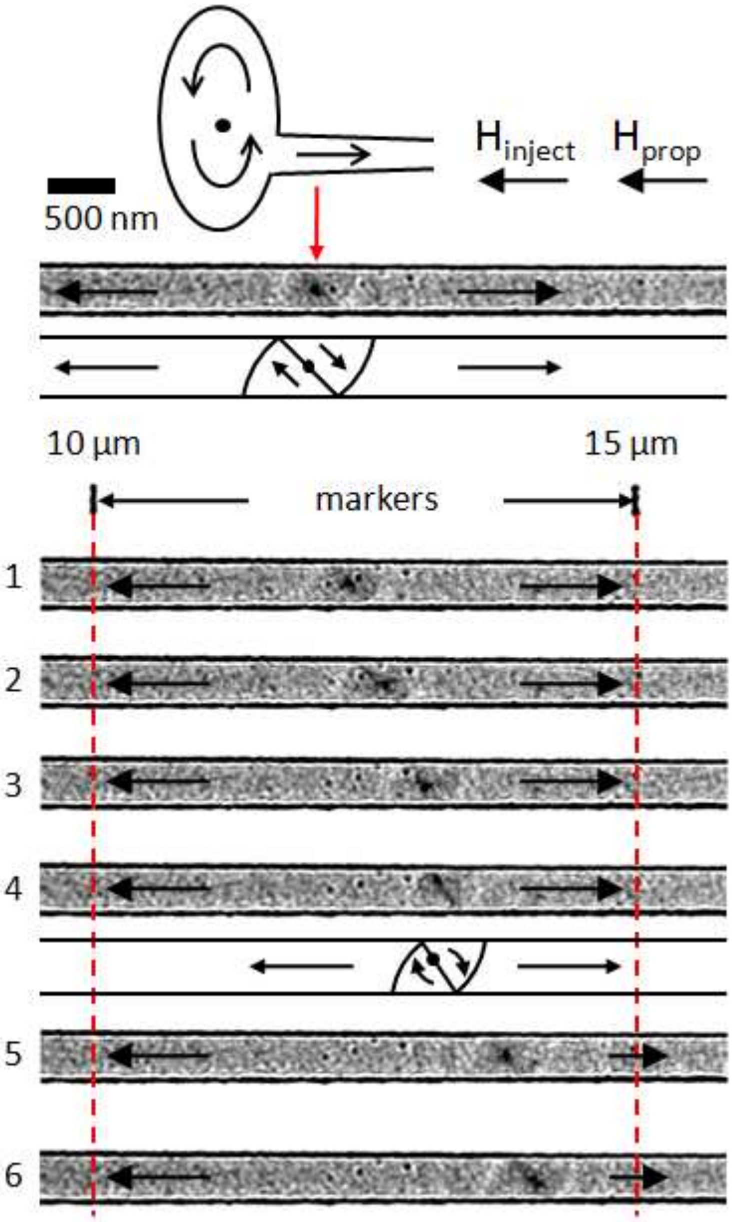

Figure 6.3: A series of Fresnel images illustrating the propagation of a vortex domain wall under the application of a series of field pulses of 33 Oe.

tail domain wall. This value of applied field was chosen as it was found to inject a wall into the wire in the majority of experiments. The top image in figure 6.3 is a Fresnel image with accompanying schematic of the injected domain wall. It may be observed that there is reduced domain wall contrast here compared with previous Fresnel images of domain walls in wires of a similar thickness. In the previous chapter, the permalloy was deposited by thermal evaporation at the Imperial College London, which operates under a higher vacuum during deposition than the permalloy deposited using the thermal evaporator at Glasgow University. As a result, the quality of the wires investigated here may be compromised due to contamination during deposition. However, it is possible to determine the wall structure from the images shown here and some interesting results have been observed. The injected wall is a vortex domain wall, confirmed by the presence of a dark vortex core in the centre of the wall, indicated by the red arrow. A series of field pulses were then applied to the domain wall, along the direction indicated by $H_{\mathrm{prop}}$, to observe its motion along the wire; a value of 33 Oe was used. Smaller field pulses did not have any effect on the domain wall. Figure 6.3 shows a series of Fresnel images acquired after each field pulse; the pulse number is displayed to the left of the Fresnel images. The domain wall did not travel more than a distance of around 2.5 $\mu$m along the wire as indicated by the markers. The chirality of the domain wall did not change as it progressed along the wire, however its structure changed slightly after the 4th pulse to form an asymmetric vortex domain wall. The asymmetric vortex domain wall is similar in appearance to a symmetric vortex domain wall however the core of the vortex is in a non-central location, see schematic below. The vortex core returned to a central location within the domain wall on the next pulse. Here, the domain wall was observed to propagate along the wire in a relatively controlled manner under a series of magnetic field pulses with an interesting change to its spin structure observed. However, this behaviour was not typical and the domain wall tended to travel larger distances along the wire under an applied field pulse, as illustrated in the next sections.

### 6.2.3 Driving domain walls from the wide to narrow end

In the next set of experiments, a series of field pulses were applied to the wire to initially inject a domain wall and to subsequently drive it from the wide end of the wire to the narrow end. The results are presented as a series of Fresnel images acquired after each pulse along with an accompanying schematic of the magnetisation in figure 6.4. A vortex domain wall was initially injected with a field pulse of 48 Oe along the direction $H_{\mathrm{inject}}$ to form a head-to-head vortex domain wall, figure 6.4a. The wall has a clockwise sense of rotation, as indicated by the schematic below. The height of the pulse subsequently applied to the domain wall, along $H_{\mathrm{prop}}$, was increased from zero in increments of around 8 Oe. The pulse was triggered 10 times at each field increment; if no changes to the domain wall were observed, the field was increased and another 10 pulses were triggered. The structure of the domain wall in each Fresnel image is indicated by the schematic below.

No changes to the the domain wall structure or position were observed for field values below 44 Oe. Following the first pulse at a height of 44 Oe, the domain wall travelled a significant distance (around 13 $\mu$m) down the wire; its final structure was unchanged (figure 6.4b). A second pulse of 44 Oe was applied to the wall where in this case it only travelled a short distance compared with the first pulse, however its structure had slightly changed, figure 6.4c. The central vortex core shifted downwards towards the lower edge of the wire to form an asymmetric vortex domain wall. No

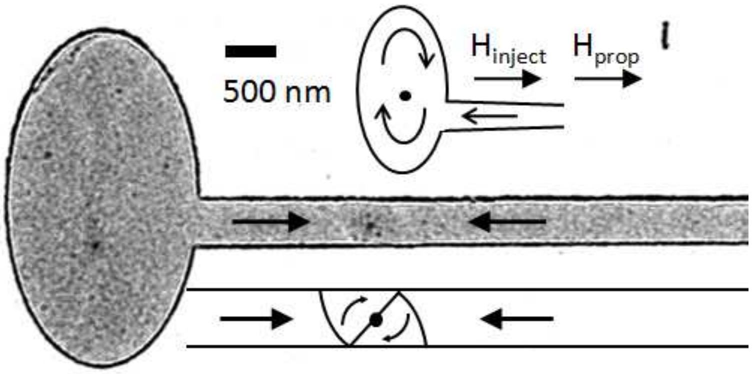

(a) Wall injected with a pulse of 48 Oe

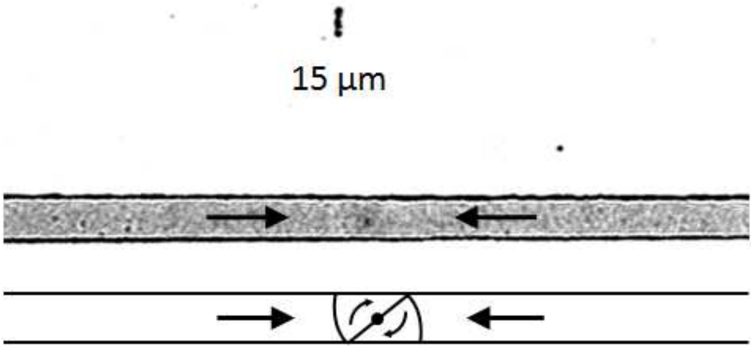

(b) After 1st pulse at 44 Oe

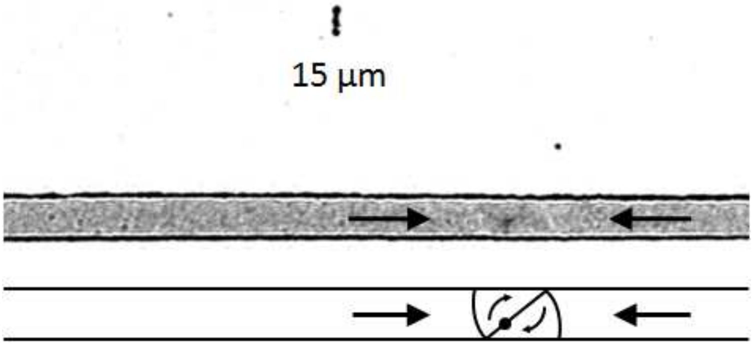

(c) After 2nd pulse at 44 Oe

(d) After 3rd pulse at 51 Oe

Figure 6.4: Figure continues on the following page.

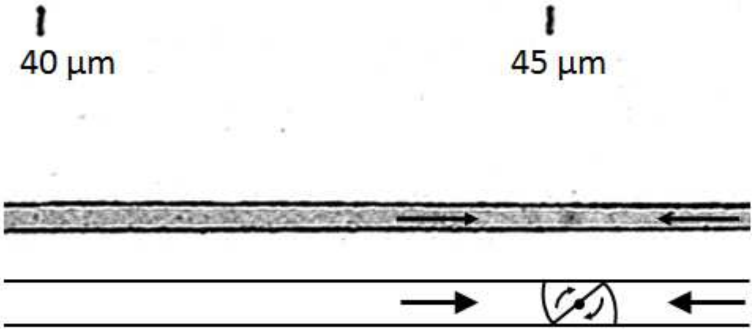

(e) After 5th pulse at 51 Oe

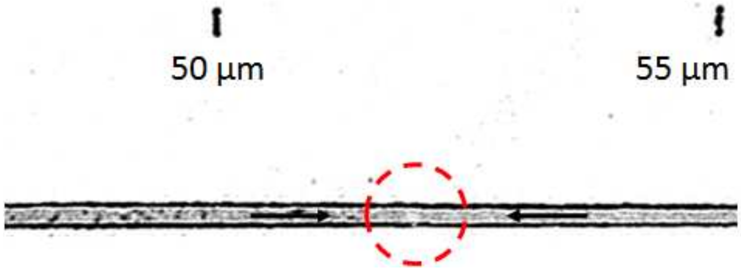

(f) After 6th pulse at 51 Oe

Figure 6.4: A series of Fresnel images illustrating the propagation of a vortex domain wall after injection into the wire in (a) and following the application of a series of field pulses to drive it towards the narrower end of the wire.

further changes to the wall were observed for this pulse height, with the application of 10 pulses. On the third pulse of height 51 Oe, the domain wall travelled a significant distance (around 25 $\mu$m) along the wire, figure 6.4d. The final structure of the wall was still a vortex domain wall, however the chirality had changed from a cw to a ccw vortex domain wall. This is confirmed by observing the bright appearance of the vortex core. The structure of the domain wall changed a second time following the 5th pulse at this field value, figure 6.4e, and comprised a cw vortex domain wall structure. The domain wall moved a distance around 7 $\mu$m further down the wire, its position indicated by the dashed red circle in figure 6.4f. Although the presence of a domain wall at this location was detected, its structure could not be determined conclusively. The structure of the domain wall remained as a vortex domain wall following all pulses applied here, except the final pulse where the structure is unknown; this is not surprising when looking at the domain wall phase diagram shown in figure 6.5. Figure 6.5 is the domain wall phase diagram including each position the domain wall reached in the above experiment, indicated by a red dot with a number to clarify the order. The phase boundary, where a change in domain wall structure may occur, was not reached in these experiments. A total of 5 similar experiments were carried out with no observation of a transformation between a vortex and a transverse domain wall structure.

A summary of the experiments carried out is given in figure 6.6, which illustrates the distance travelled by the domain walls under magnetic field pulses. It may be observed

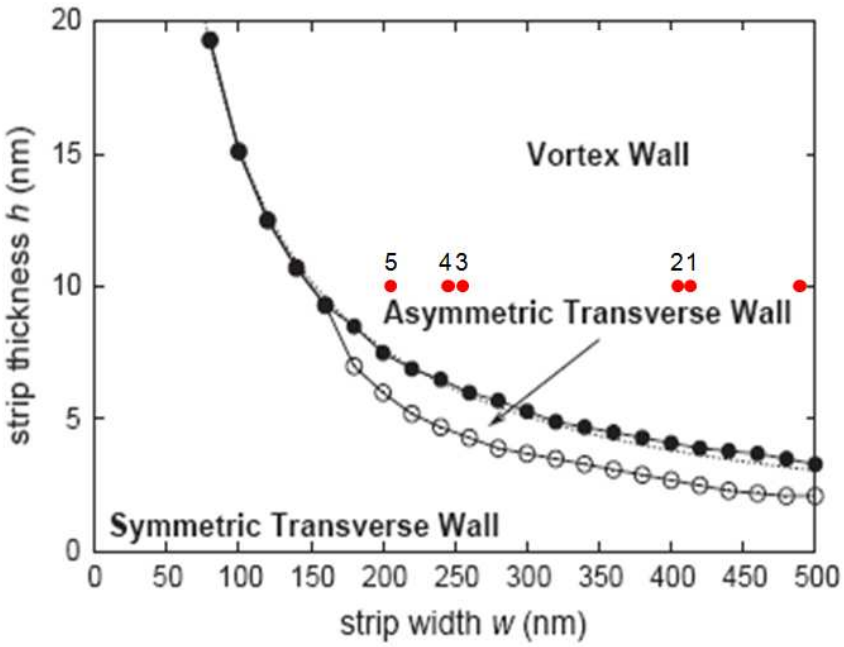

Figure 6.5: Illustration of the region of the domain wall phase diagram probed by the domain wall in the above experiment, where the red dots indicate the position of the domain wall following each pulse (numbered). The domain wall remained within the vortex regime throughout. Plot taken from Y. Nakatani et al J. Magn. Magn. Mater. **290** (2004).

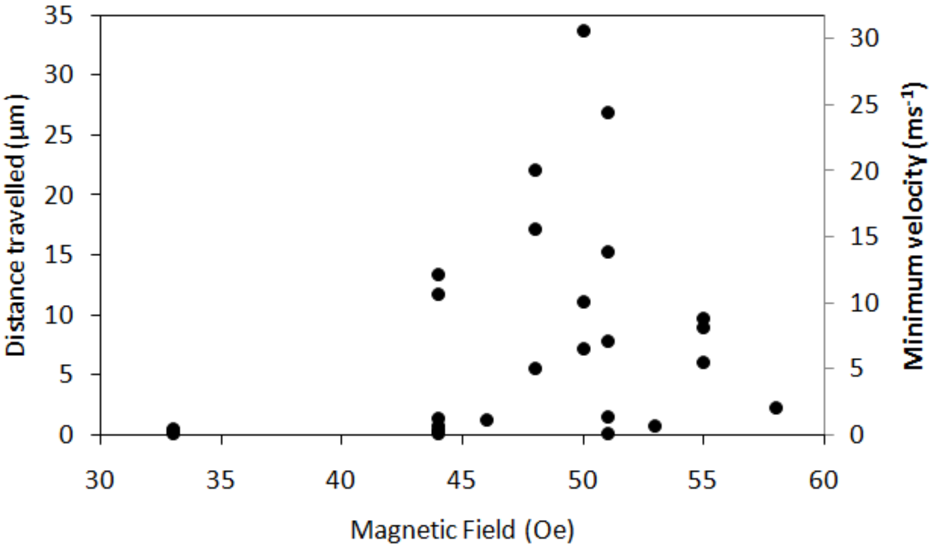

Figure 6.6: Plot of the distance travelled by a domain wall under a magnetic field pulse in a tapered permalloy wire obtained from the experiments driving the domain wall from a wider to a narrower region of wire.

that there is no clear relationship between the magnitude of the field pulse and the distance a wall travels under the influence of such a pulse. Additionally, the field values at which the majority of domain walls move are relatively high, being comparable to those required to depin a domain wall from a deliberately fabricated pinning site, as in chapter 4. The minimum velocity, calculated from the distance travelled by a domain wall, is also included in the plot. As the injection and propagation of a domain wall under a pulsed magnetic field is a stochastic process, there is no guarantee that the domain wall moves at the onset of the pulse. Consequently, only a minimum velocity may be calculated from the distance travelled by a domain wall. All velocities quoted hereafter refer to the minimum domain wall velocity.

### 6.2.4 Driving domain walls from the narrow to wide end

In the next set of experiments, the effect of driving the wall from the narrower end of the wire to the wider end was explored. The experiments were carried out in a similar manner to the previous set, that is a domain wall was injected into the wire and its structure and location was recorded by the acquisition of an image. The direction of the magnetic field was then reversed and incremented in steps of around 8 Oe and field pulses were triggered 10 times for each field increment. Two different types of behaviour observed are illustrated in figures 6.7 and 6.8.

In figure 6.7, a cw vortex domain wall was injected into the wire with a field pulse of 48 Oe, a Fresnel image is given in figure 6.7a. On applying a series of field pulses along the direction $H_{\text{prop}}$ in the diagram, the domain wall did not move or change structure. However, at a pulse height of 36 Oe, a tail-to-tail domain wall was injected into the wire (figure 6.7b). The new domain wall also comprised a dark central vortex core and therefore possessed the same chirality, i.e. a clockwise rotation. On the first pulse at a field of 46 Oe, the new domain wall travelled towards and stopped adjacent to the original domain wall thus creating a complex 360° domain wall structure. The magnitude of the field pulse was increased further to determine the field required to annihilate this 360° domain wall structure. At a field pulse of 103 Oe, the walls annihilated to give a uniformly magnetised wire.

In figure 6.8, a cw vortex domain wall was injected into the wire at a field of 48 Oe and stopped between the 40 $\mu$m and the 45 $\mu$m markers as indicated in figure 6.8a. In a similar manner to the previous experiment, a series of magnetic field pulses were applied along the direction shown in the figure to drive the wall from the narrower end of the wire to the wider end. At a field pulse height of 50 Oe, a tail-to-tail domain wall was again injected into the wire before any changes to the original domain wall were observed, figure 6.8b. The tail-to-tail domain wall appeared with a bright central vortex core and therefore had the opposite sense of rotation to the original head-to-head domain wall, i.e. counterclockwise. The domain wall did not travel any further towards the original wall before annihilating it following the next field pulse of 50 Oe.

The reason for this behaviour is explained in figure 6.9, where a schematic of the domain wall structure is given when both domain walls have the same (figure 6.9a) or opposite (figure 6.9b) chirality. When the adjacent domain walls have the same

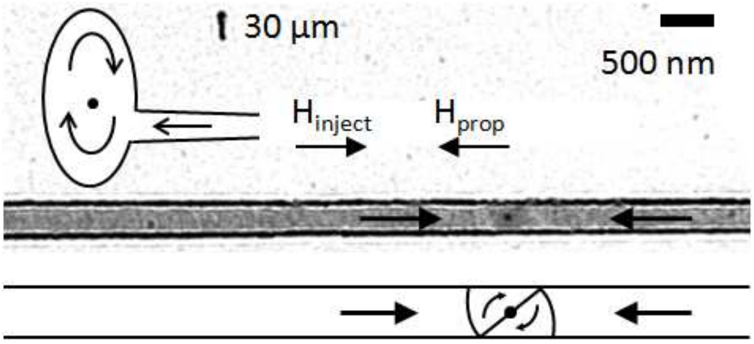

(a) Wall injected with a pulse of 48 Oe

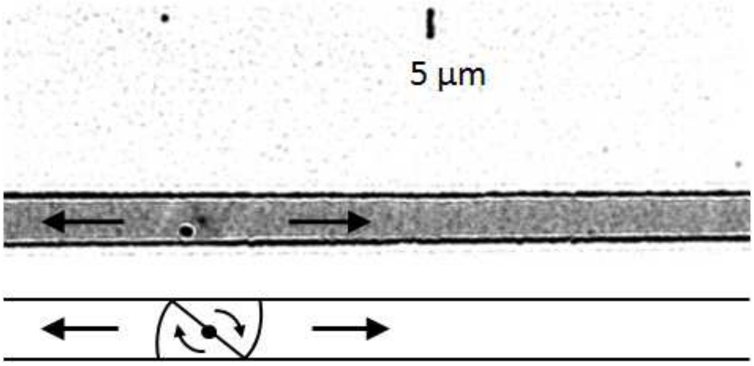

(b) After 1st pulse at 36 Oe

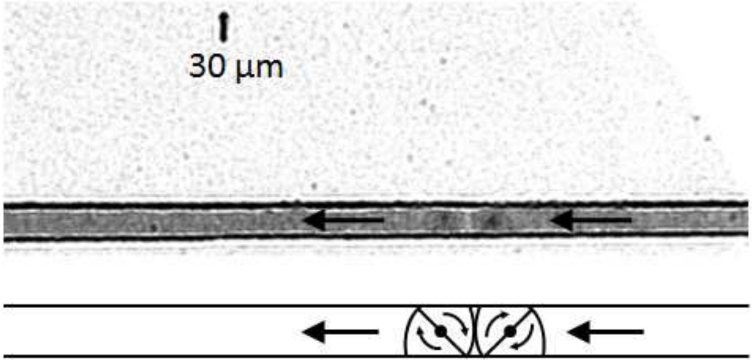

(c) After 1st pulse at 46 Oe, walls annihilated at 103 Oe

Figure 6.7: Sequence of Fresnel images illustrating the behaviour of a vortex domain wall under the application of a series of magnetic field pulses to drive the wall from the narrower to the wider end of the wire. The original wall did not move; a new domain wall of the same chirality was injected and created a complex 360° domain wall.

chirality, the magnetisation within the leading domain of the tail-to-tail domain wall is unfavourably aligned with the magnetisation within the trailing domain of the head-to-head domain wall, indicated by the red arrows in figure 6.9a. As a result, the domain walls do not immediately annihilate when driven together by an external field. A simulation of this behaviour is discussed at the end of the chapter. Conversely, when the adjacent domain walls have the opposite chirality, there is a favourable alignment between the magnetisation in the leading domain of the tail-to-tail domain wall and in the trailing domain of the head-to-head domain wall. This is again indicated by the

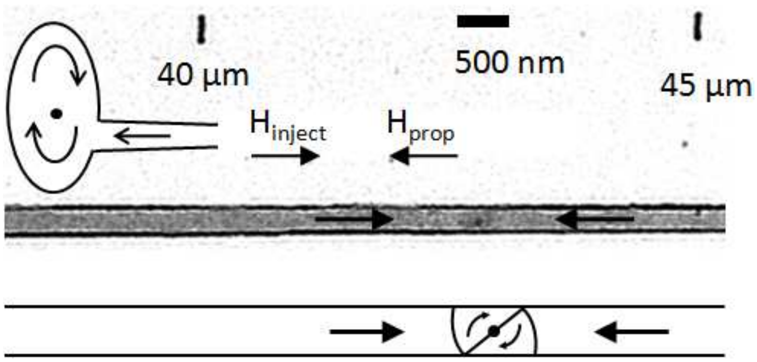

(a) Wall injected with a pulse of 48 Oe

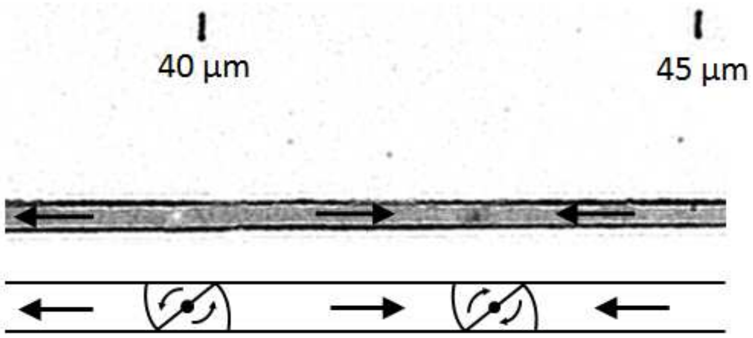

(b) After 1st pulse at 50 Oe

Figure 6.8: Sequence of Fresnel images illustrating the behaviour of a vortex domain wall under the application of a series of magnetic field pulses to drive the wall from the narrower to the wider end of the wire. The original wall did not move; a new domain wall of the opposite chirality was injected and annihilated the original domain wall.

red arrows in figure 6.9b. As a result the domain walls annihilate when driven towards each another.

The behaviour presented in the figures above highlights an issue with this injection pad geometry where additional domain walls may be injected into the wire when a field, opposite in direction to $H_{inject}$, is applied to propagate the original domain wall in a particular direction. It is not possible for an additional domain wall to be injected into

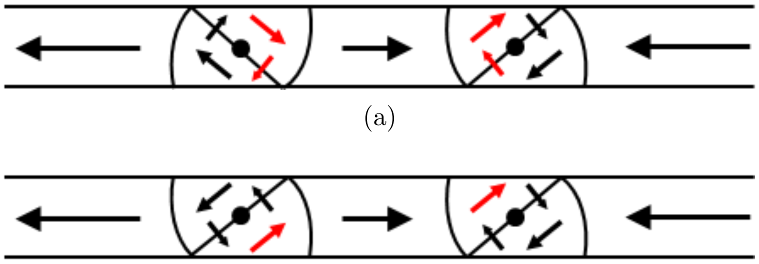

(a)

(b)

Figure 6.9: Schematic illustration of the magnetic spin structure of two adjacent domain walls with (a) the same chirality and (b) the opposite chirality. The red arrows indicate (a) an unfavourable alignment and (b) a favourable alignment of the adjacent domains of the vortex domain walls.

the wire when a field along the direction $H_{\mathrm{inject}}$ is applied to inject and subsequently propagate the domain wall, i.e. when the direction of field is unchanged. Each type of behaviour presented above was observed once out of a total of 5 experiments and is therefore worthy of further study. In the remaining three cases, the domain wall moved short distances along the wire towards the wider end before abruptly reversing it.

### 6.2.5 Effect of increasing the applied field

As a result of the large variation in distance travelled by a domain wall for different fields, the effect of the magnitude of the field pulse on the distance the wall travelled along the wire was then investigated. Due to the fact that the wire varies in width, it was expected that the domain walls would easily propagate towards the narrower end of the wire since the total energy of a domain wall is reduced by decreasing its length. Additionally, a key dynamic parameter of propagating domain walls is the domain wall mobility, $\mu$, which describes the rate of change of domain wall velocity with applied field, $dv/d\mathrm{H}$, as introduced in chapter 1. Values between 30 - 40 ms$^{-1}$ Oe$^{-1}$ are expected for domain walls in permalloy [6], however one study reported a very low $\mu$ of 2.6 ms$^{-1}$ Oe$^{-1}$ for a straight 500 nm wide permalloy wire [5]. This low mobility was attributed to the edge roughness of the structure.

An injection pulse was triggered 10 times at each field value and the distance the domain wall travelled was recorded and is presented in figure 6.10. The reset field pulse was kept the same; a value of 107 Oe was used throughout. The field was incremented in 10 Oe field steps. It is clear from this plot that there is

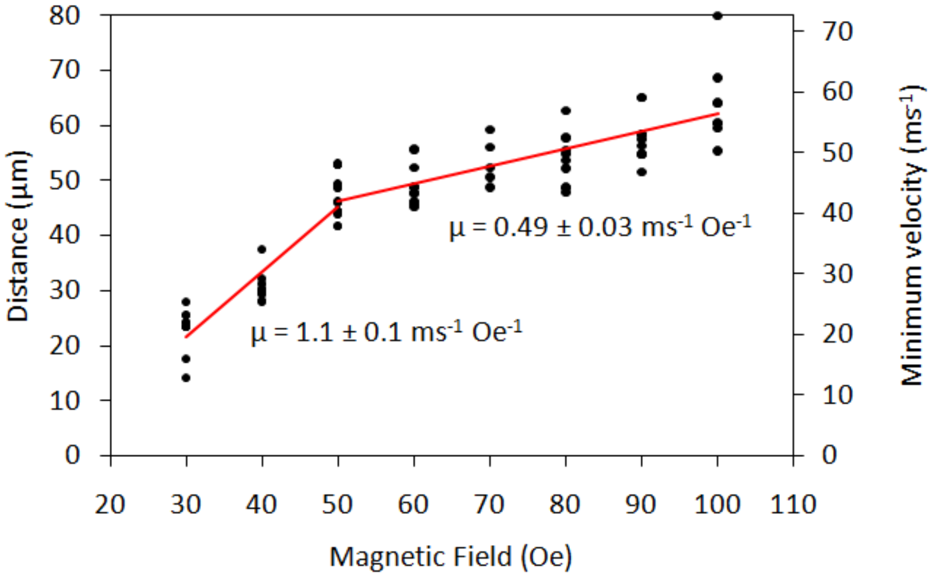

Figure 6.10: The effect of the height of the field pulse on the distance a domain wall travelled along the wire was investigated. Each experiment was repeated 10 times with field increments of 10 Oe. A lower limit of the domain wall mobility is also given.

a general increase in distance travelled by a domain wall with increasing applied field, however there a considerable spread (around 10 $\mu$m) for a given field value. A least squares fit was utilised to calculate the domain wall mobility which was found to be 1.1 ms$^{-1}$ Oe$^{-1}$ for fields of 50 Oe and below and 0.5 ms$^{-1}$ Oe$^{-1}$ for 50 Oe and above. That there is a lower mobility for higher field values indicates a slowing of the domain wall as it propagates towards the narrow end of the wire. Additionally, the wire is 80 $\mu$m long therefore on one occasion the wire reversed. The behaviour observed here may be a result of the poor quality of the wire; bright field images of the tapered wire at the wide and narrow end of the wire are given in figure 6.11. Flagging of the order of 50 nm is visible at the wire edge, which becomes more dominant as the width of the wire decreases. At the wider end of the wire (figure 6.11a), the width of the wire is large compared to the edge flagging. As the domain wall propagates along the wire, the edge flagging becomes more prominent (figure 6.11b), therefore the probability of the domain wall being trapped by a pinning site increases thus interrupting the progress of the domain wall.

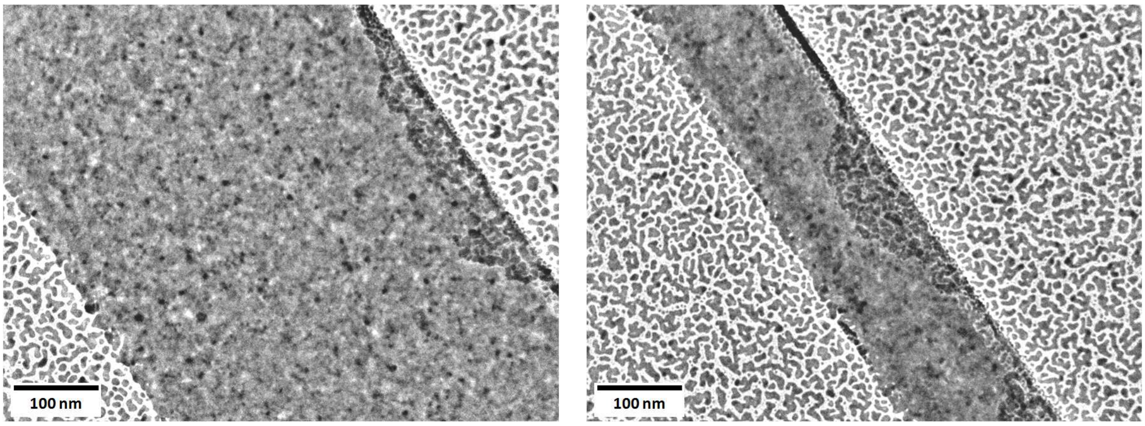

(a) (b)

Figure 6.11: Bright field images of the tapered wire at the (a) the wider end of the wire and (b) the narrower end. Metal flags of the order of 50 nm are present at the wire edge.

### 6.2.6 Summary

It is clear that a wide variety of behaviour is observed when a pulsed magnetic field is used to drive domain walls in a wire of a gradually varying width. In the initial experiments, the domain wall appeared to propagate along the wire in a moderately uniform manner, whilst keeping the overall vortex domain wall structure; the position of the vortex core was observed to change position in more than one case. However, the domain wall did not travel a large distance along the wire under a considerable field of 33 Oe, which may be attributed to pinning sites arising from the presence of flagging at the wire edge. This type of motion was not observed in the majority of experiments however and the domain wall often propagated significant distances along the wire following the application of a field pulse.

Quite different behaviour was observed when applying pulses to domain walls already present in the wire, depending on the direction of the applied field. With a magnetic field set up to drive the wall from a wider to a narrower section of wire, the domain wall structure remained unchanged i.e. the structure was always observed to be a vortex domain wall. The chirality did change however on 2 occasions. The domain wall structure could not be determined conclusively at the wire width where transverse domain walls were expected, thus a transformation from a vortex to a transverse domain wall was not confirmed.

On applying field pulses to drive the wall from a narrower to a wider section of wire, no changes to the original head-to-head domain wall were observed. Instead, a new tail-to-tail domain wall was injected into the wire and, depending on its chirality, either stopped adjacent to the original wall to create a complex 360° structure or stopped a short distance in front of the original wall and annihilated it at a moderate field value.

It was decided that the observed changes in domain wall chirality should be investigated further and separated from the transformations that may occur due to the varying width of the wire. Therefore a straight wire geometry was fabricated for a range of wire widths, detailed in the next section. Experiments on the pulsed field propagation of domain walls in straight wires were carried out and are presented in the next section.

## 6.3 Domain wall propagation in a straight wire

### 6.3.1 The structure overview

The permalloy nanowires studied in this section are shown schematically in figure 6.12. As in the previous section, they comprise an elliptical injection pad at one end of the wire; the other end of the wire is pointed. A greater wire thickness of 20 nm was used here to provide better domain wall contrast using Fresnel imaging. Wire widths ranging from 500 nm to 200 nm in 100 nm steps were investigated. The wires were 40 $\mu$m in length and were fabricated following the same method as for the tapered wires.

In the first set of experiments, a series of reset ($H_{reset}$) and inject ($H_{inject}$) field pulses, of 1.1 $\mu$s duration, described in the previous section, were applied to the wires. The direction of $H_{reset}$ and $H_{inject}$ were kept the same throughout these experiments. Figure 6.12 also shows an inset Fresnel image of the magnetic configuration of the wire after the application of a reset pulse. Here the straight part of the wire is uniformly magnetised,

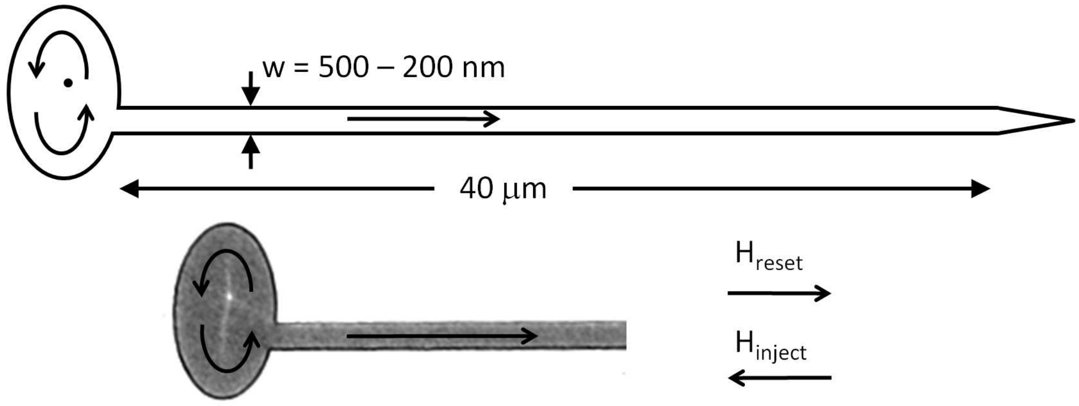

Figure 6.12: A schematic of the nanowire after the application of a reset pulse. A corresponding Fresnel image of this configuration at the pad/wire junction is given.

with a vortex magnetisation state in the elliptical pad. A reset pulse was applied prior to each injection to ensure the initial configuration of the wire was identical each time. An inject pulse could then be applied to inject a domain wall into the wire, in this case tail-to-tail domain walls were injected. After each inject pulse an image was acquired and in this way a large number of results could be generated quickly. From the images, the position and final structure of the wall could be determined. The reset/inject pulse sequence was repeated 50 times for two nominally identical wires of each width.

In the first set of experiments, information on the probability of injecting a domain

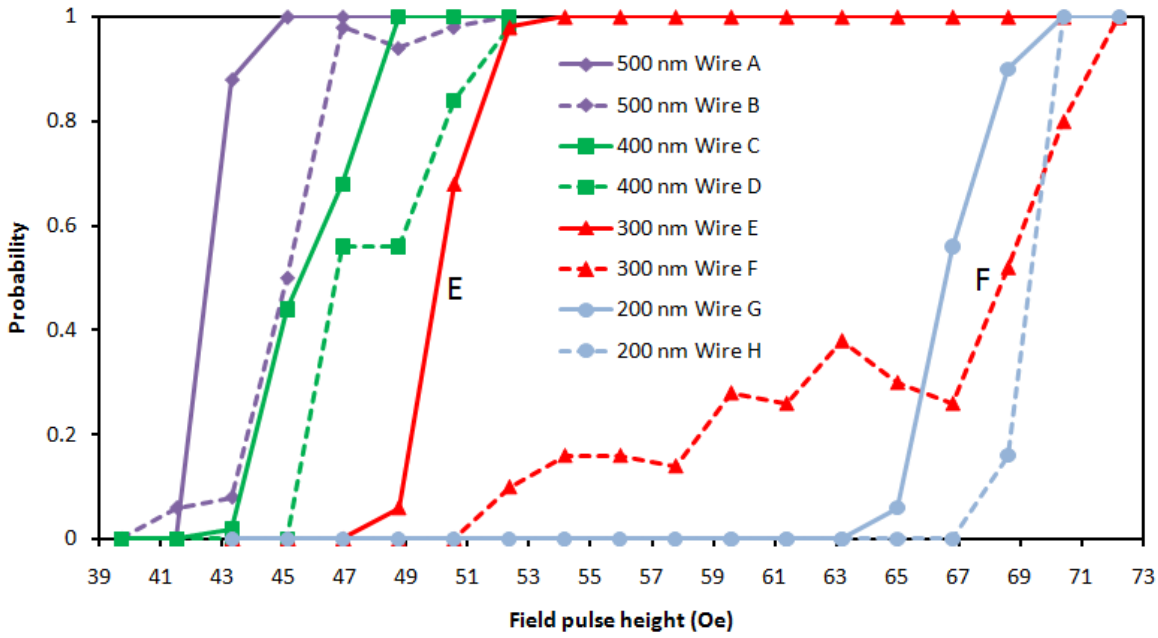

Figure 6.13: Probability of injecting domain walls into wires of a given width. Diamonds (◆) correspond to wires of width 500 nm, squares (■) indicate 400 nm wide wires, triangles (▲) correspond to 300 nm wide wires and circles (●) represent wires of width 200 nm. Solid and dashed lines represent data from two nominally identical wires.

wall into each wire was acquired and is presented in figure 6.13. The probability of injection as a function of applied field was determined from a series of 50 pulses at each field value for two wires of each width. It is clear that the field required to inject a domain wall increases with decreasing wire width. The injection profile of three out of the four wire pairs is very similar, with a variability of around 2-3 Oe between two nominally identical wires. There is significant disagreement however between the 300 nm wide wires (indicated by E and F in figure 6.13). The injection probability of wire F increases very gradually over a field range of around 20 Oe, compared with 7 Oe for wire E. The cause of this difference in behaviour could not be determined as there were no obvious observable physical differences between the wires. Although the field required to inject a domain wall into the 300 nm wide wires differed depending on which wire was used, the same domain wall structures were observed in each wire.

### 6.3.2 Structure of injected domain walls

In the next set of experiments, the structure of the injected domain wall for each wire width was investigated. From the 50 injections, a plot of the domain wall type and its occurrence in each wire width was generated, as shown in figure 6.14. An injection field of 50 Oe was initially used. All of the walls injected into the 500 nm and 400 nm wide wires were vortex domain walls, with a counterclockwise (ccw) sense of rotation; a Fresnel image is given in figure 6.15a. 20% of injections in a 500 nm wide wire and 50% in a 400 nm wide wire had an asymmetric appearance, figure 6.15b.

No transverse domain walls were observed in either the 500 nm or the 400 nm wide wires, however some were observed in the 300 nm wide wire and more than 50% of

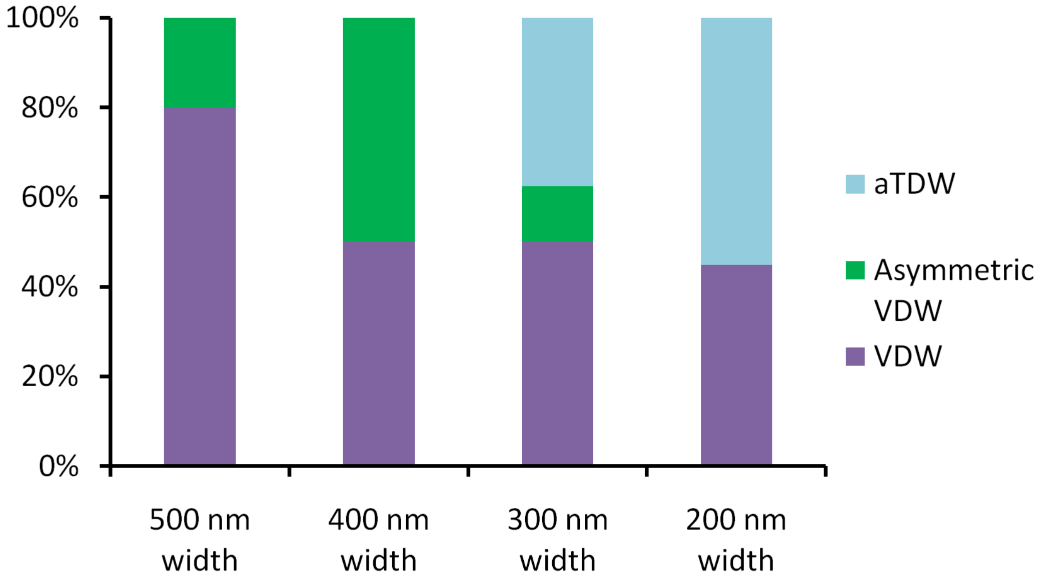

Figure 6.14: The occurrence of each type of domain wall injected into the four wire widths by a magnetic field pulse of duration 1.1 $\mu$s.

walls observed in the 200 nm wide wire were transverse domain walls. The original value of $H_{\text{inject}}$ was insufficient to nucleate walls in this wire; a field of 64 Oe was used. Figures 6.15c,d illustrate the form of the vortex and transverse domain walls observed in the 200 nm wide wire.

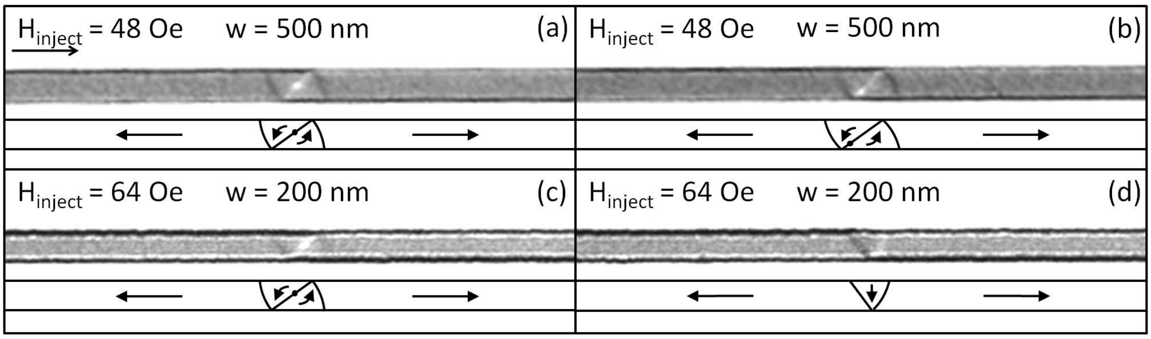

Figure 6.15: Fresnel images of (a) a symmetric and (b) asymmetric vortex domain wall observed in the 500 nm wide wires and (c) a symmetric vortex and (d) a transverse domain wall observed in the 200 nm wide wires.

## 6.3.3 Domain wall transformations

Experiments were then carried out to investigate the behaviour of a domain wall already present in the wire under the influence of a magnetic field pulse. Only the 500 nm wide wire was used in these experiments. A shorter pulse duration was used here to ensure the domain wall did not travel a large distance along the wire and reverse it. To achieve a shorter pulse duration, a slightly different experimental setup was employed. Using the original setup, pulses shorter than 1.1 $\mu$s were significantly distorted due to the inductance associated with the wire connected to the rod.

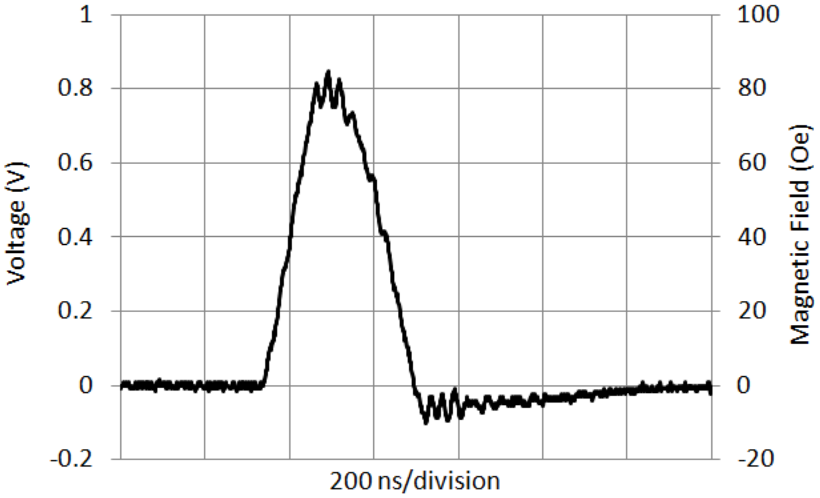

Figure 6.16: Profile of the shorter pulse used to investigate transformations arising from driving domain walls around the wire.

Instead a new setup was constructed by Ray Pallester at the University of Glasgow and was specifically designed to deliver field pulses of height up to 300 Oe with a duration of around 200 ns. A high voltage supply was used to drive the circuit which sends a pulse to the TEM rod through the discharge of a capacitor. The duration of the pulse was fixed however the height of the pulse was adjustable and could provide up to 300 Oe at the specimen position. The polarity of the pulse could also be switched to provide the necessary $H_{\mathrm{inject}}$ and $H_{\mathrm{reset}}$ field pulses. Additionally, a continuous mode was available where pulses with a frequency of 1 kHz could be applied. A diagram of the pulse shape generated from this setup is given in figure 6.16; the pulse duration is 212 ± 2 ns from the full width at half maximum.

Figures 6.17A-C illustrate three different types of transformation observed during these experiments. The form of the initial domain wall is given at the top of each sub-figure; a corresponding schematic is given below. In Figure 6.17A, the initial wall configuration was a cw vortex domain wall. Following domain wall injection, a field pulse was applied along the direction given in the figure and its effect on the domain wall

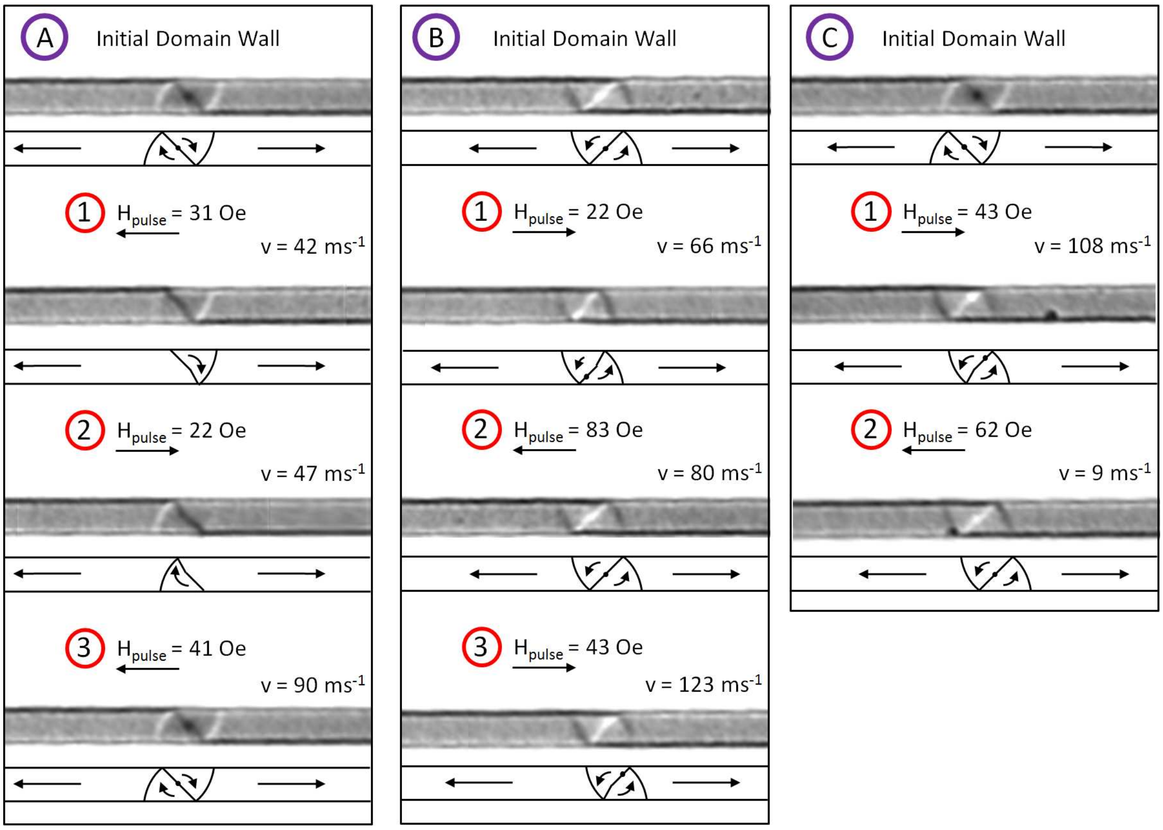

Figure 6.17: A series of Fresnel experiments illustrating the types of transformations observed with the application of shorter field pulses. Three different experiments are displayed. For each transformation, the field required to move the domain wall in addition to the domain wall velocity is given. The velocities quoted here represent the lower limit of the domain wall velocity. A schematic of the magnetisation is included below each Fresnel image.

was assessed. If the domain wall was unchanged, another pulse was triggered. This was repeated 5 times and if the domain wall was still unchanged after 5 repetitions, the field was increased and the process repeated. In figure 6.17A, the first transformation was observed with the application of a 31 Oe field pulse, where the domain wall transformed into an asymmetric transverse domain wall, illustrated by the schematic below. The domain wall travelled a distance of 9 $\mu$m, obtained by observing the location of the wall before and after the pulse and measuring the difference. As the field pulse duration was 212 ns, the domain wall travelled with a velocity of 42 ms$^{-1}$. A second transformation was observed following the application of a 22 Oe field pulse. The domain wall retained the structure of a transverse domain wall however the magnetisation within the central domain reversed. Additionally, the asymmetry in the domain wall also reversed; the asymmetry was originally directed from left to right and then changed to the opposite case. The velocity of the domain wall was slightly higher at 47 ms$^{-1}$. The domain wall changed structure once more following the application of a 41 Oe field pulse into a vortex domain wall with the same chirality as the initial wall (cw). The velocity of this domain wall was significantly higher, a value of 90 ms$^{-1}$ was calculated.

In a second experiment, the initial wall structure was again a vortex domain wall but with a ccw sense of rotation, figure 6.17B. Following the application of a 22 Oe pulse, the domain wall travelled along the wire with a velocity of 66 ms$^{-1}$. The resulting domain wall structure was still vortex however the core had shifted downwards towards the lower edge of the wire, as indicated by the schematic. The wall was strongly pinned at this location as a large field of 83 Oe was required to move the wall from this position. The wall configuration returned to a symmetric vortex structure. In a final case, the domain wall changed to an asymmetric vortex domain wall again, however the vortex core was shifted towards the upper edge of the wire. The domain wall travelled with a considerably higher velocity of 123 ms$^{-1}$.

In a final experiment, the initial wall structure was a cw vortex domain wall, as in the first experiment, figure 6.17C. Following the application of a 43 Oe pulse, the domain wall not only changed structure but also changed chirality. The domain wall transformed into a ccw asymmetric vortex domain wall with the core of the vortex shifted towards the upper edge of the wire. The wall travelled with a velocity of 108 ms$^{-1}$. The final transformation was observed after the application of a 62 Oe field pulse; the ccw vortex domain wall was observed to have a symmetric appearance. This domain wall travelled with a velocity of just 9 ms$^{-1}$.

The processes involved for such transformations to occur is illustrated schematically in figure 6.18. At fields above the Walker field, the domain wall structure oscillates periodically from a transverse domain wall of one sense of rotation to the other, i.e. a change in direction of magnetisation within the central domain. This process occurs via intermediate vortex and anti-vortex states [15]. Figure 6.18a is a schematic illustration

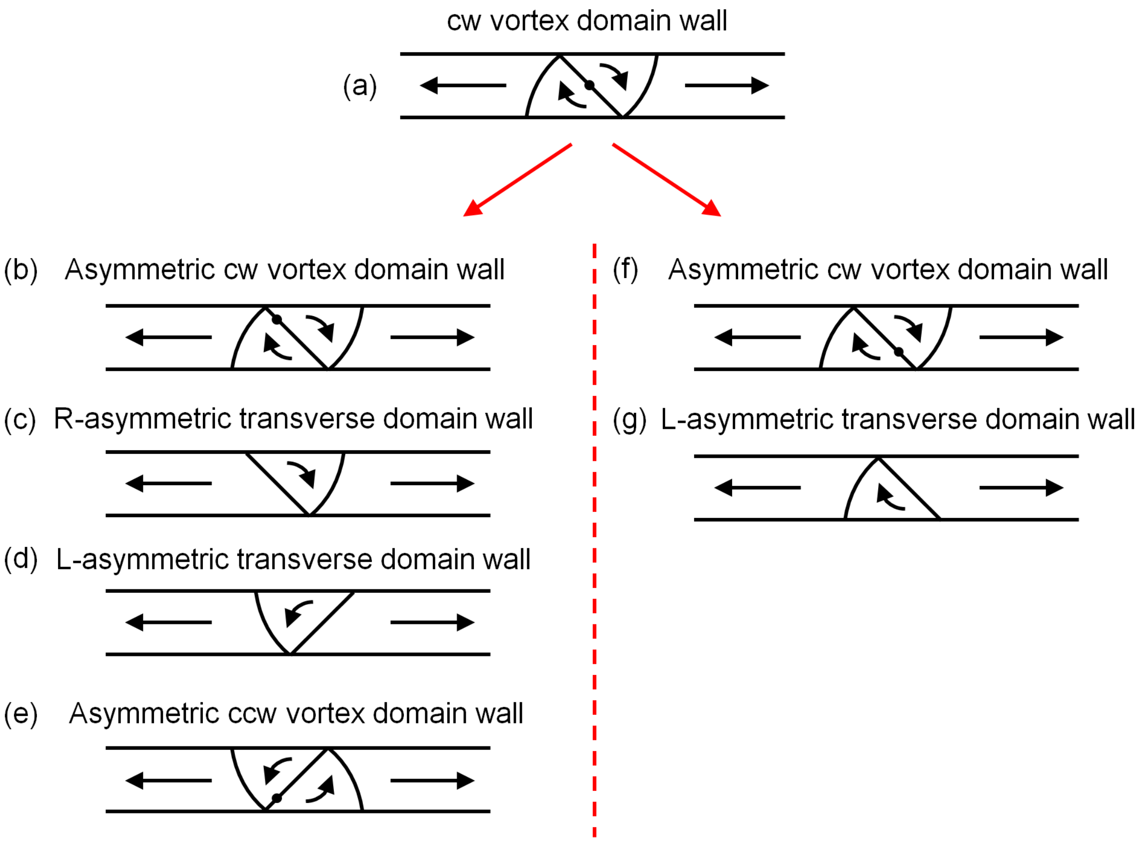

Figure 6.18: Schematic illustration of the transformation of a vortex domain wall by the movement of the vortex core in and out of the wire. (a) An initial cw vortex domain wall. (b)-(e) illustrate possible changes in structure for the domain wall to transform to an asymmetric ccw vortex domain wall. (f),(g) illustration of the change in wall structure if the vortex core moves in the opposite direction.

of an initial domain wall, here a cw vortex domain wall is given. Following the application of a field pulse, the vortex core may be displaced upwards to form an asymmetric vortex domain wall, figure 6.18b. Furthermore, the vortex core may be displaced to the edge of the wire where it is expelled to form a R-asymmetric transverse domain wall as in figure 6.18c. A transformation from a R-asymmetric to a L-asymmetric domain wall may occur with the application of a reverse field, or as a result of a random defect, figure 6.18d. A vortex may be nucleated from the lower edge of the wire to form an asymmetric ccw vortex domain wall, figure 6.18e. This illustrates a possible sequence of structure changes to ultimately change the chirality of a vortex domain wall from cw to ccw, as observed in the previous experiment. Figures 6.18f,g illustrate a possible transformation if the vortex core is displaced downwards and subsequently out of the wire to form a L-asymmetric transverse domain wall with an opposite core magnetisation to that in figure 6.18d.

It is clear from these results that domain walls travel with a wide range of velocities that are independent of their structure and the magnitude of the applied field. A number of similar experiments were carried out, the results of which are presented

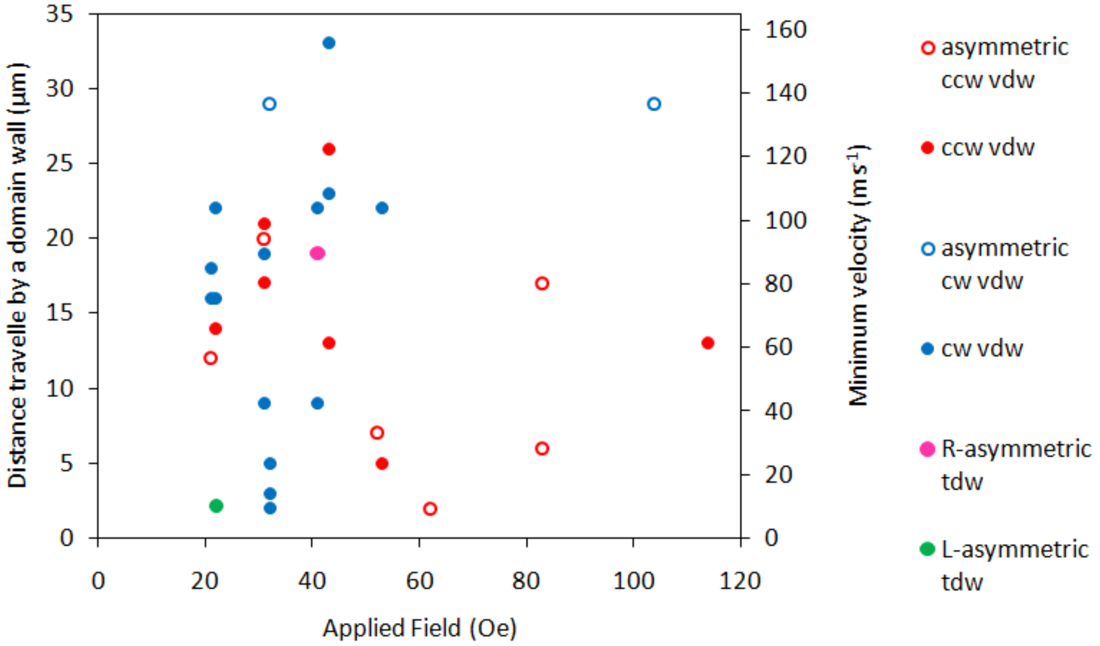

Figure 6.19: An illustration of the distance a domain wall travelled under the influence of a short (212 ns) magnetic field pulse. The velocity obtained from the distance is shown on a secondary axis. The domain wall structures included refers to the initial state of the wall.

in figure 6.19. The distance travelled by a number of domain walls was measured and the corresponding velocity calculated. A large range of domain wall velocities were observed in these experiments, irrespective of the field applied. The domain wall structure indicated in the figure refers to the initial structure of the domain wall. There was no clear dependence of the applied field on the structure of the domain wall and fields values of 50 Oe and below were sufficient to propagate the majority of domain walls. The highest velocity of 156 ms$^{-1}$ was observed for a modest field value of 43 Oe. A possible cause may be attributed to random pinning sites arising from the edge roughness. A quick solution to this problem using focused ion beam milling is discussed in the next section.

### 6.3.4 Ion irradiation of the wire edges

In order to try to reduce the edge roughness and therefore the number of pinning sites along the wire edge, ion irradiation was utilised to remove material along both edges of the wire. Ion irradiation of magnetic thin films has the capability of modifying the magnetic properties of the material. It has been shown, for example, that the coercivity and local anisotropy can be altered in NiFe films [16]. At sufficiently high doses, the ion beam may be used to sputter material, a widely used technique to create patterned structures. Focused ion beam milling was carried out by Dr. Damien McGrouther at

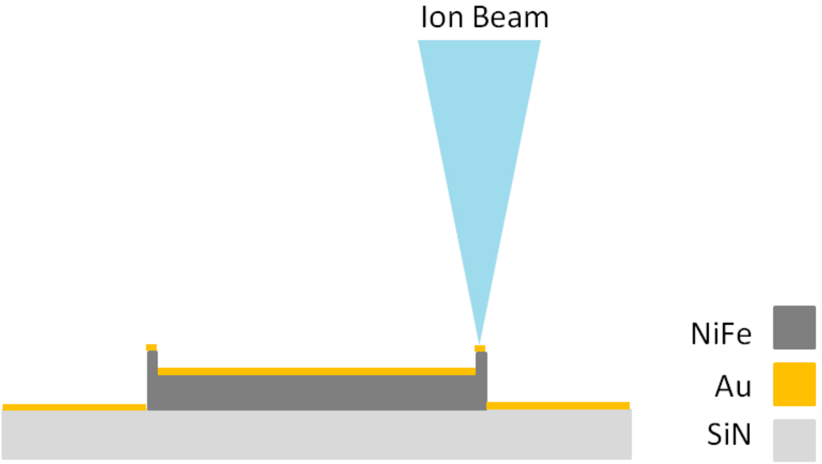

Figure 6.20: A schematic illustration of the wire with attached edge flags under the influence of an ion beam to remove material.

the University of Glasgow with the aim of sufficiently irradiating the wire edges to remove metal flags and reduce the edge roughness. A schematic illustration of the milling is given in figure 6.20, where only the sides of the wire were irradiated; an area in the centre of the wire was not milled. The instrument used was a FEI Dualbeam FIB consisting of an electron column and a Sidewinder Ion column tilted at an angle of 52°. During ion milling, the sample was also tilted to an angle of 52° so that the ion beam was perpendicular to the sample surface. Figure 6.21a shows an SEM image of the 500 nm wide wire prior to ion beam milling. At this tilt angle, the edge flags are clearly visible along the upper edge of the wire; edge flags are also present along the lower edge however they appear with a similar grey level as the wire and are less distinguishable. The presence of the gold layer is also visible on the membrane surrounding the wire. An area 40 $\mu$m × 200 nm was chosen as the milling area for each

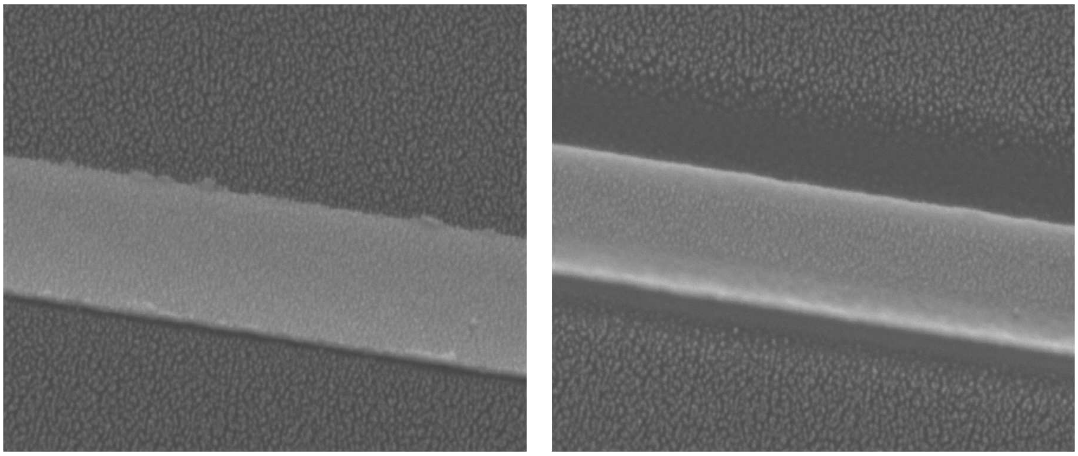

(a) before milling (b) after milling

Figure 6.21: SEM images of the 500 nm wide wire (a) prior to and (b) following ion irradiation of the wire edges.

side of the wire. During ion irradiation, a low magnification value had to be used to ensure the whole wire was in the field of view and, as a result, the accurate positioning of the area to be milled with respect to the wire was difficult, as this was done manually. Additionally, due to time constraints, the milling parameters could not be optimised therefore the parameters used here are the initial conditions used to test whether this technique is feasible for efficiently removing edge flags from structures fabricated by electron beam lithography. A modest milling depth of 2 nm was initially chosen with a duration of 11s. Following irradiation of the first wire edge however, the lower edge in figure 6.21b, it appeared that the edge profile had been altered significantly and it was decided that the milling time for the second edge should be reduced to 5s. It is not clear whether the use of different milling conditions is significant in determining the resulting magnetic behaviour. Both wire edges have been irradiated in figure 6.21b where it may be observed that the wire edges are considerably smoother and the edge flags are no longer visible. The gold adjacent to the wire has also been removed during milling.

### 6.3.5 Behaviour of domain walls in ion irradiated wires

A series of experiments were carried out on these wires prior to and immediately following the ion irradiation of the wire edges to study the effect of the milling. On closer inspection of the milled wires, it was clear that the whole length of the wire had not been affected by the ion beam; the irradiated area began a distance of around 500 nm along the wire. This was expected due to the challenging task of manually positioning the area to be milled correctly. A bright field image of the area of wire that was not irradiated is given in figure 6.22a, where part of the elliptical injection pad can be seen in the upper right part of the image. A bright field image of a section of wire that was irradiated is given in figure 6.22b, where the effects of the ion beam at either side of the wire are clearly observed. A higher magnification image is given alongside in figure 6.22c. The gold film on the surrounding membrane and part of the wire has been removed; the gold still remains in the centre of the wire and on the surrounding film away from the wire. Additionally, some larger grains, highlighted by red circles, may be seen towards the right edge of the wire. The effect of FIB irradiation grain growth has previously been reported for NiFe films [17]. That such large grains are not observed on the left side of the wire is a consequence of the different milling times used for each side of the wire. The effect of the ion irradiation on the behaviour of propagating magnetic domain walls will now be presented.

Only results from one of the 500 nm wide wires will be discussed here. A series of 50 injection and reset field pulses were applied to the wires for a range of field values to asses the most common domain wall configuration and also to calculate the domain wall velocity following ion irradiation. The results are presented in figures 6.23 and

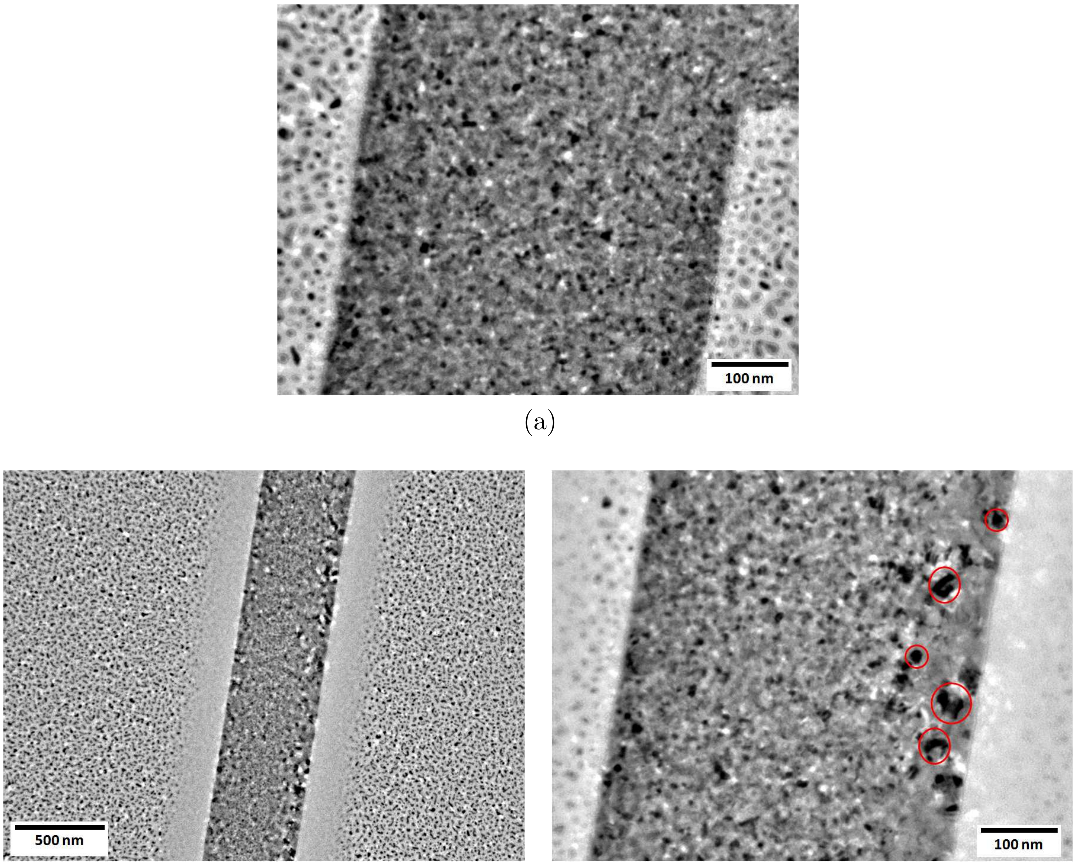

(a)

(b)

(c)

Figure 6.22: (a) A bright field image of the 500 nm wide at an unmilled region close to the injection pad. (b) A bright field image of a milled area of the same wire. (c) A higher magnification bright field image, where the effect of the ion beam is clearly observed at the right side of the wire where some grain growth has occurred, highlighted by red circles.

6.24. The field of view was centred on the lower half of the wire (20 $\mu$m section) for the duration of the field pulses. An image of this section of the wire was acquired after each pulse was triggered. From the images the position and structure of the domain wall could be determined. It could also be determined whether the wire had completely reversed with the application of a given pulse. In the cases where no domain wall was observed and the wire had not reversed, no distinction could be made between the case where no domain wall was injected into the wire and the case where an injected domain wall did not travel as far as the lower half of the wire. This is referred to as 'No injection >20 $\mu$m' in the figure. It was also ensured that the sense of rotation of magnetisation within the injection pad was the same in both sets of experiments, i.e. counterclockwise, as this has a direct impact on the chirality of the injected domain wall [14].

From figure 6.23, it can be seen that the number of cases labelled 'No injection >20 $\mu$m' decreased with increasing field. This was expected as the probability of injecting a domain wall into the wire increased with increasing field as observed in the

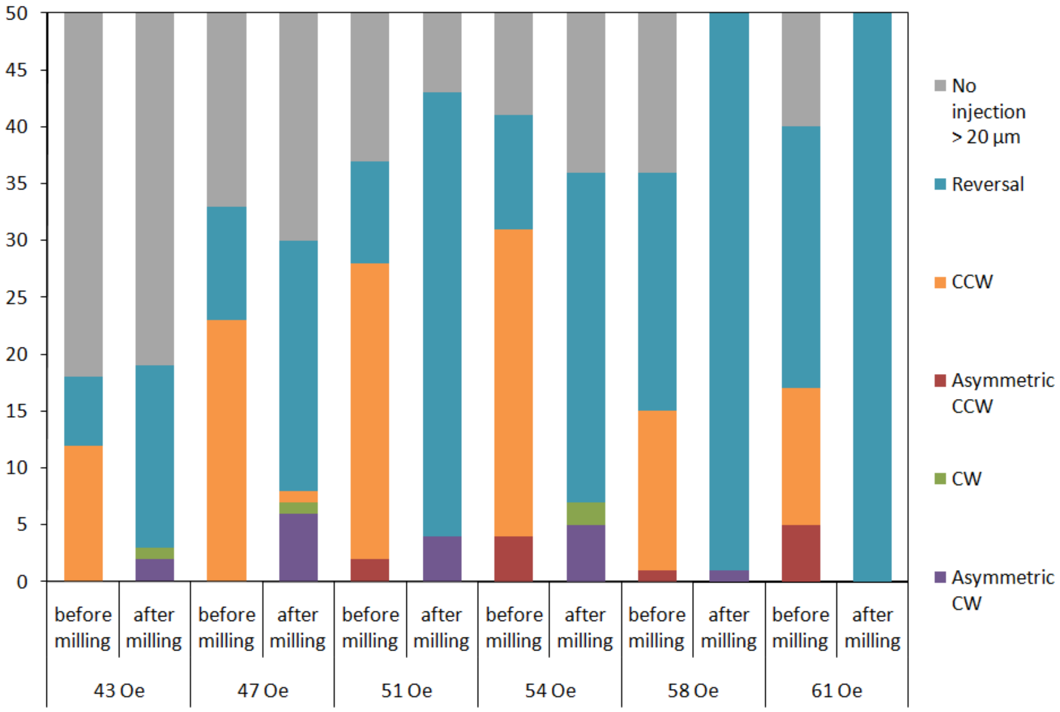

Figure 6.23: The outcome of a series of injection and reset field pulses applied to a 500 nm wide wire prior to and following ion irradiation to remove the metal flags.

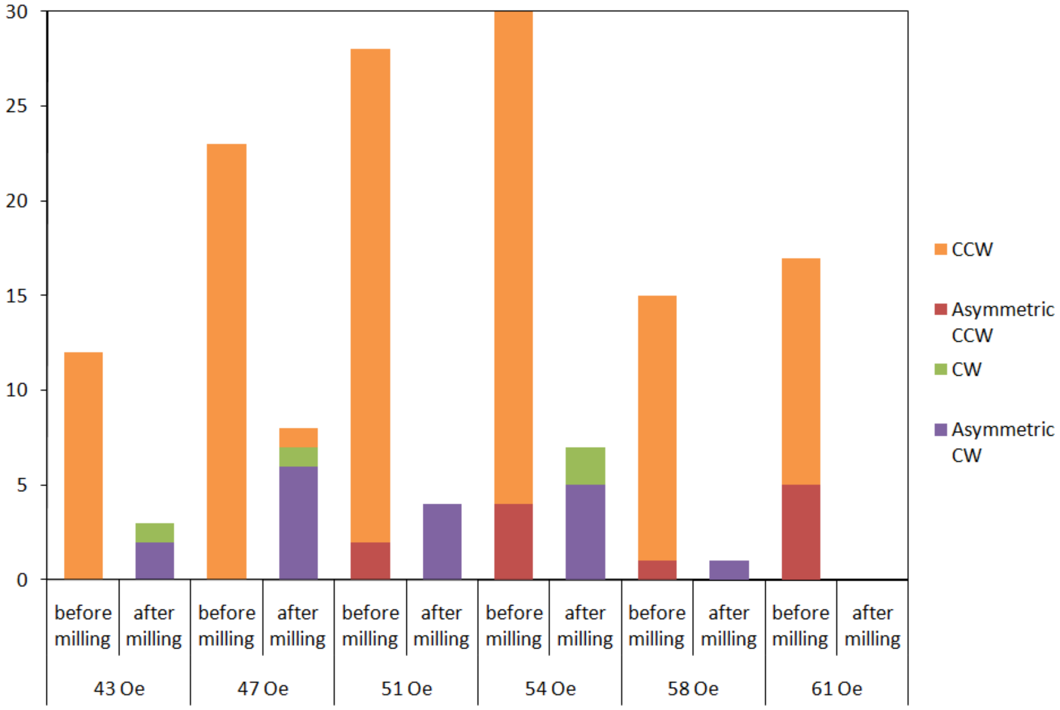

Figure 6.24: The type and occurrence of domain walls observed in a 20 $\mu$m section of the wire furthest from the pad both prior to and following ion irradiation to remove the metal flags.

previous section. Additionally, any random defects in the wire that act as pinning sites for an injected domain wall are more likely to be overcome with increasing field.

Furthermore, this percentage remained similar for experiments carried out on both the original wire and after ion irradiation for field values up to and including 54 Oe. This may be attributed to a random defect located in the upper half of the wire that was not completely smoothed out during ion irradiation acting as a pinning site for injected domain walls. Additionally, the elliptical injection pad was not irradiated therefore any defects acting as random pinning sites will not have been altered by this process. It may also be seen that the number of cases where the wire completely reversed following the application of a field pulse increased with increasing field, as expected. At a field of 61 Oe, the ion irradiated wire reversed in 100% of experiments. The types of domain walls observed and their occurrence are also included in this figure but have been extracted into a new figure to ease interpretation of the results. Only information on the domain walls observed in these experiments is displayed in figure 6.24; cases where no injection was observed or reversal of the wire occurred have been omitted. [14].

The effect of ion irradiation on the domain wall configurations observed is significant. From figure 6.24, it can immediately be seen that the number of domain walls observed in the 20 $\mu$m section of wire furthest from the pad is higher prior to ion irradiation of the edges. Additionally, prior to ion irradiation, the most common domain wall type observed was a ccw vortex domain wall; a Fresnel image is given in figure 6.25a. In some cases the ccw vortex domain wall had an asymmetric appearance, figure 6.25b. Following ion irradiation of the wire edges however, a vortex domain wall was still observed, however the chirality was instead cw, as in figure 6.25c. In the majority of cases, the cw vortex domain wall had an asymmetric appearance, as in figure 6.25d. A ccw vortex domain wall was observed in the wire in one case following ion irradiation of the edges, at a field pulse of 47 Oe. The reason for this behaviour is unclear as it was ensured that the chirality of the magnetisation within the elliptical injection pad was

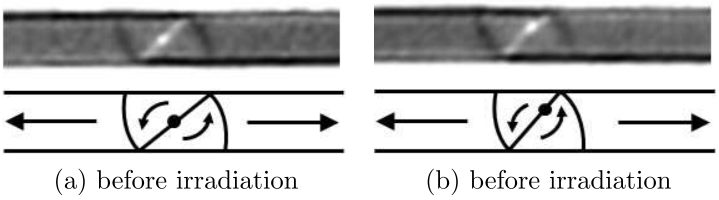

(a) before irradiation

(b) before irradiation

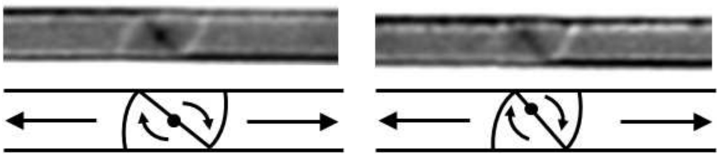

(c) after irradiation

(d) after irradiation

Figure 6.25: Fresnel images of the most common domain wall types observed in the 500 nm wide wire (a), (b) prior to ion beam irradiation and (c), (d) following ion beam irradiation.

the same both prior to and following irradiation, i.e. counterclockwise. It was expected that domain walls of the same chirality as the pad would be injected into the wire

In the original wire, the number of domain walls observed increases steadily with field until a field of 54 Oe is reached, above which the number of domain walls observed drops significantly. This is attributed to complete reversal of the wire occurring in a greater number of experiments. The number of domain walls observed for a given field pulse in the irradiated wire was more variable, however the number of domain walls observed above 54 Oe also dropped considerably.

Furthermore, milling the wire edges did not have a significant effect on the velocity of domain walls injected into the wire, as illustrated in figure 6.26. The values shown represent the distance a domain wall travelled along the wire under a field pulse of 1.1 $\mu$s. This pulse duration was sufficient to completely reverse the irradiated wire in the majority of cases and as a result few domain walls were observed in this section of wire, indicated by the red points in figure 6.26. The blue points represent domain walls observed in the wire prior to irradiation where a large range of velocities were calculated as observed previously. The behaviour of domain walls in the irradiated wires is worthy of further study and it would be instructive to study the velocity of domain walls under the influence of fast field pulses to ensure the domain walls do not travel large distances and reverse the wire.

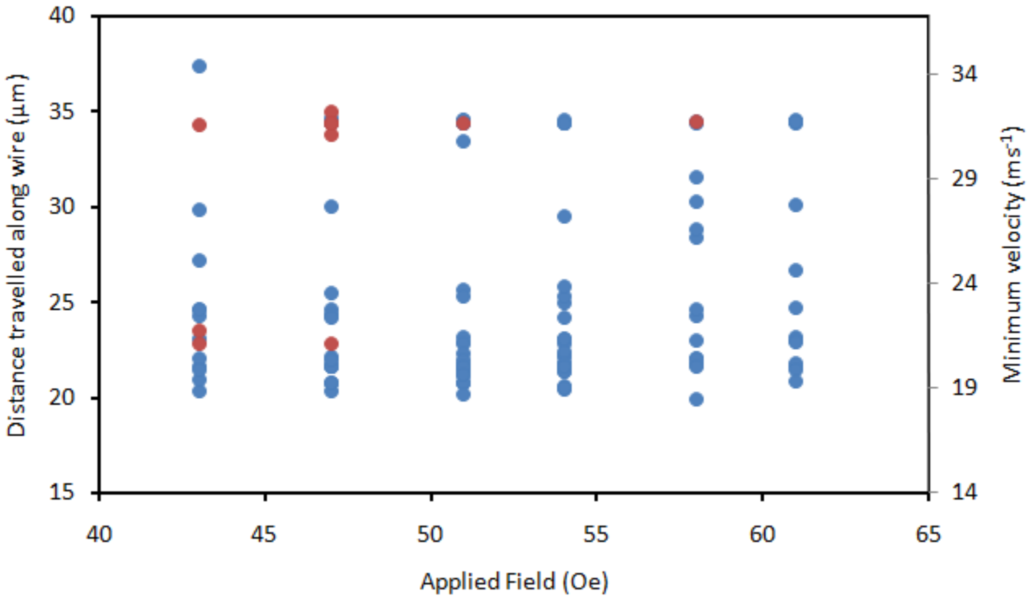

Figure 6.26: Plot of the distance an injected wall travelled along the wire both prior to (blue points) and following (red points) ion irradiation. The lower limit of the velocity is also given.

The same experiment was also performed on the 20 $\mu$m section of wire closest to the injection pad for completeness and the results are presented in figure 6.27. For field pulses of 47 Oe and above, domain walls were injected into the wire in 100%

of experiments. The number of domain walls observed in this portion of the wire generally decreased following ion irradiation, as observed for the bottom half of the wire, indicating that domain walls are able to move more easily along the wire. For a field value of 54 Oe however, the number of domain walls observed prior to ion irradiation was 7 compared with 19 after ion milling. On closer inspection of the results, the domain walls observed after milling were located at the same position along the wire in every case, that is a distance of around 18 $\mu$m along the wire. Clearly this location is a preferred pinning site for a domain wall that was not effectively removed with the ion beam.

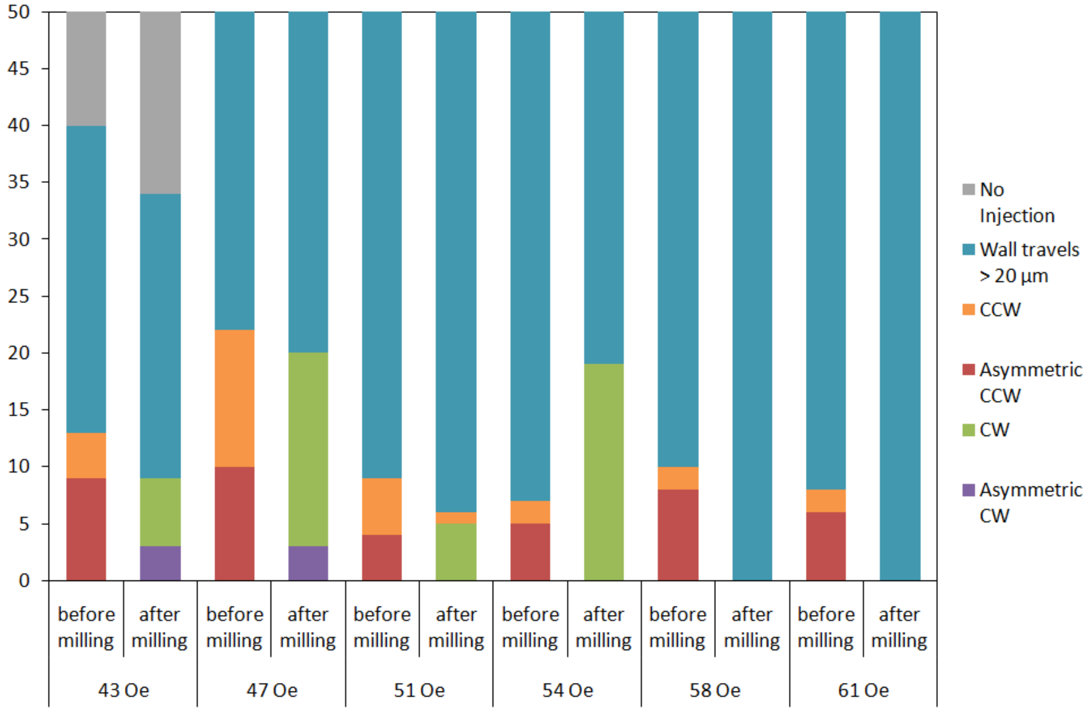

Figure 6.27: The type and occurrence of domain walls observed in the half of the 500 nm wide wire closest to the injection pad prior to and following ion irradiation to remove the metal flags.

## 6.4 Discussion

In the previous chapters, static magnetic fields were utilised to drive domain walls along the wires, where the field was increased relatively slowly. Here, pulsed magnetic fields were used to drive domain walls along a variety of wires. The main difference here is that the field was applied for a significantly shorter time than for the cases where static fields were used. Additionally, the field reached its maximum value in a significantly shorter time. Here the pulse rise time was 300 ± 5 ns for the 1.1 $\mu$s pulse duration and 125 ± 5 ns for the 212 ns pulse duration. It has previously been reported that the pulse rise time for pulsed magnetic field driven domain wall motion has a significant effect on the average domain wall velocity [18]. However, as the respective pulse rise times did not change throughout these experiments, any variability in domain wall velocity cannot be attributed to this parameter.

No transformations on the domain wall structure, i.e. from vortex to transverse, were observed in the tapered wire. However, transformations in the vortex domain wall structure occurred and a new structure was observed, the asymmetric vortex domain wall. It was not clear whether these transformations in domain wall structure were attributed to the varying width of the wire or due to the poor quality of the wire. The bright field images clearly indicated the presence of the metal flags at the wire edges, which became comparable to the wire width as the wire narrowed. The presence of these metal flags may support the nucleation of an asymmetric vortex domain wall; the wire is thicker at the edges where the flags are located therefore a favourable position for the vortex core is at the wire edge, thus creating an asymmetric vortex domain wall. Asymmetric transverse domain walls were also observed as the core of the vortex domain wall was forced out of the wire. Similar asymmetric transverse domain walls have also been observed in permalloy wires, described as buckled transverse domain walls, as an intermediate configuration that occurs prior to vortex nucleation [19].

It was extremely difficult to determine the domain wall structure at the wire width where transitions between vortex and transverse domain walls were expected due to the quality of the wire. Additionally, a wire thickness of 10 nm was used here, giving reduced Fresnel contrast when compared with the 20 nm thick wires studied in the second set of experiments. Some interesting behaviour was observed however, when two domain walls were nucleated in the wire. The behaviour observed was dependent on whether the two walls comprised the same or opposite chirality. A complex 360° domain

(a) Initial magnetic configuration

(b) OOMMF calculation

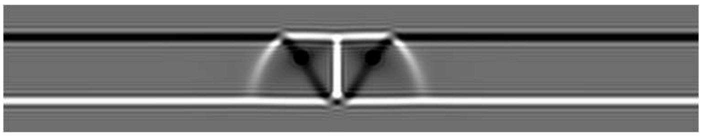

(c) Fresnel image

Figure 6.28: (a) The initial configuration of a simulation performed to determine whether two cw vortex domain walls could form a stable 360° domain wall. (b) The result of the simulation observed in OOMMF. (c) Fresnel image calculated from the result of the simulation using the magnetic phase only and a defocus of 500 $\mu$m.

wall structure was formed when both walls had the same chirality. A micromagnetic simulation was performed to observe whether such a domain wall would be stable in a straight wire of width 300 nm. The simulation was initialised to contain two cw vortex domain walls and was relaxed in the absence of an external field. The initial configuration is given in figure 6.28a; the final configuration is given in figure 6.28b, where it can be seen that a 360° domain wall is stable at remanence. A Fresnel image was calculated from the simulation using the magnetic phase only and a defocus of 500 $\mu$m (figure 6.28c) and is in good agreement with the experimental image.

The importance of the edge structure became apparent from the plot of distance travelled by an injected domain wall with applied field. It was expected that the distance would increase rapidly with increasing field as the domain wall energy is reduced by reducing its length. It could be seen that from the bright field images, the extent of the edge flags became comparable to the width of the wire at the narrower end, and a low domain wall mobility was calculated as a result. Static fields were also used to try to create a transformation from vortex to transverse, however the wire completely reversed before any transformations could be observed.

Straight wires were then fabricated to try to understand the origin of the changes in vortex domain wall structure observed in the tapered wire. Again, the importance of microstructure was highlighted from the injection probability experiments. It was clear that a small variability occurred between three out of the four nominally identical pairs of wires, however for one pair the injection probability was significantly different with no obvious cause.

It was observed that the most common domain wall observed was dependent on the wire width. Asymmetric transverse domain walls were observed in the 300 nm and 200 nm wide wires despite the fact that these wire geometries lie distinctly in the vortex domain wall regime of the phase diagram [12]. However, periodic transformations in domain wall structure have been observed for domain walls under the influence of magnetic fields higher than the Walker field, where the structure oscillates between vortex and transverse [3]. Only the initial and final structure of the domain wall could be established in these experiments, however a schematic illustration of a series of changes in structure were given as an illustration of the likely intermediate states.

A wide range of domain wall velocities were calculated for the domain walls driven by the 212 ns pulse. A large range of field values were also required to move the domain walls suggesting that the wire comprises a number of pinning sites, which require varying fields to depin domain walls from. Ion irradiation was proposed as a quick solution to gently smooth the wire edges. The main result of this was that the wire reversed in more cases, suggesting that the domain walls move more easily through the wire, with fewer defects acting as pinning sites. It has been reported that ion irradiation of permalloy films causes an associated grain growth [17]. Larger grains at the wire edges results in fewer grain boundaries and may mean that domain wall propagation is easier, thus lowering the coercivity of the wire. Clearly, focused ion beam milling provides a quick and effective tool for improving the quality of structures fabricated by electron beam lithography. That the number of cases where 'No Injection >20 $\mu$m' was observed remained relatively constant prior to and following irradiation suggests a region of the structure not irradiated by the ion beam may be responsible, i.e. the elliptical injection pad. Furthermore, it was expected that the chirality of the injected domain walls would remain the same as in the original wire due to the injection pad comprising the same magnetic state prior to injection, however this was not the case. Most of the domain walls injected into the irradiated wire had the opposite chirality to that observed in the original wire. These experiments highlight the importance of the edge structure for domain wall propagation. The results presented here suggest that the behaviour observed is dominated by random pinning from edge defects which mask the intrinsic behaviour being probed. If sufficient changes to the fabrication process can be made to eliminate metal flagging at the wire edges, the intrinsic behaviour of domain walls will be revealed.

Transformations of domain walls have been observed for current driven experiments [20, 21], with domain wall velocities comparable to that observed here. However domain wall velocities of up to 1 kms$^{-1}$ have been reported for field driven domain walls. The quality of the wires used in this chapter are likely to be the cause for the modest velocities reported here. Unfortunately, due to time constraints, further experiments could not be carried out to improve the quality of the wires.

# Bibliography

[1] Y. Nakatani, A. Thiaville and J. Miltat, Nat. Mater. **2** 521 (2003).

[2] J. Y. Lee, K. S. Lee, S. Choi, K. Y. Guslienko and S. K. Kim, Phys. Rev. B **76** 184408 (2007).

[3] M. Hayashi, L. Thomas, C. Rettner, R. Moriya, X. Jiang and S. S. P. Parkin, Phys. Rev. Lett. **97** 207205 (2006).

[4] M. Klaüi, P.-O. Jubert, R. Allenspach, A. Bischof, J. A. C. Bland, G. Faini, U. Rüdiger, C. A. F. Vaz, L. Vila and C. Vouille, Phys. Rev. Lett. **95** 026601 (2005).

[5] T. Ono, H. Miyajima, K. Shigeto, K. Mibu, N. Hosoito and T. Shinjo, Science **284** 468 (1999).

[6] G. S. D. Beach, C. Nistor, C. Knutson, M. Tsoi and J. L. Erskine, Nature Mater. **4** 741 (2004).

[7] D. Atkinson, D. A. Allwood, G. Xiong, M. D. Cooke, C. C. Faulkner and R. P. Cowburn, Nature Mater. **2** 85 (2003).

[8] A. Kunz, IEEE Trans. Magn. **42** 3219 (2006).

[9] M. Laufenberg, D. Backes, W. Bührer, D. Bedau, M. Klaüi, U. Rüdiger, C. A. F. Vaz, J. A. C. Bland, L. J. Heyderman, F. Nolting, , S. Cherifi, A. Locatelli, R. Belkhou, S. Heun and E. Bauer, Appl. Phys. Lett. **88** 052507 (2006).

[10] M. Klaüi, P.-O. Jubert, R. Allenspach, A. Bischof, J. A. C. Bland, G. Faini, U. Rüdiger, C. A. F. Vaz, L. Vila and C. Vouille, Phys. Rev. Lett. **95** 026601 (2005).

[11] O. Petracic, P. Szary, H. Zabel, D. Gorlitz and K. Nielsch, Superlattices and Microstructures **46** 728 (2009).

[12] Y. Nakatani, A. Thiaville and J. Militat, J. Magn. Magn. Mater. **290** 750 (2004).

[13] L. Thomas, C. Rettner, M. Hayashi, M. G. Samant and S. S. P. Parkin, Appl. Phys. Lett. **87** 262501 (2005).

[14] D. McGrouther, S. McVitie, J. N. Chapman and A. Gentils, Appl. Phys. Lett. **91** 022506 (2007).

[15] M. Hayashi, L. Thomas, C. Rettner, R. Moriya and S. S. P. Parkin, Nature Physics **3** 21 (2007).

[16] W. M. Kaminsky, G. A. C. Jones, N. K. Patel, W. E. Booij, M. G. Blamaire, S. M. Gardiner, Y. B. Xu and J. A. C. Bland, Appl. Phys. Lett. **78** 1589 (2001).

[17] C.-M. Park and J. A. Bain, J. Appl. Phys. **91** 6830 (2002).

[18] K. Weerts, P. Neutens, L. Lagae and G. Borghs, J. Appl. Phys. **103** 094307 (2008).

[19] D. Backes, C. Schieback, M. Kläui, F. Junginger, H. Ehrke, P. Nielaba, U. Rüdiger, L. J. Heyderman, C. S. Chen, T. Kasama, R. E. Dunin-Borkowski, C. A. F. Vaz and J. A. C. Bland, Appl. Phys. Lett. **91** 112502 (2007).

[20] W. C. Uhlig, M. J. Donahue, D. T. Pierce and J. Unguris, J. Appl. Phys. **105** 103902 (2009).

[21] L. Heyne, J. Rhensius, A. Bisig, S. Krzyk, P. Punke, M. Klaüi, L. J. Heyderman, L. Le Guyader and F. Nolting, Appl. Phys. Lett. **96** 032504 (2010).

# 7

# Conclusions

## 7.1 Introduction

The ability to control the nucleation, propagation and annihilation of magnetic domain walls in nanostructures is crucial for the development of exciting future magnetic technologies [1–3]. The behaviour of magnetic domain walls in thin film permalloy nanostructures has been extensively studied using Lorentz microscopy, a particular focus being the interaction of transverse and vortex domain walls with deliberately fabricated pinning features driven by magnetic fields. The form of the domain walls that arise at the intersection of two straight wires was also investigated with a castellated wire which proved to be a particularly interesting structure as domain walls were not only observed at the corners, but also in the straight sections. The behaviour of domain walls in longer wires under pulsed magnetic fields was also investigated as domain walls undergo interesting oscillations in structure as they progress along a wire at fields greater than the Walker breakdown field. It is clear that the interaction a domain wall undergoes with a geometrical pinning feature is dependent on the spin structure of the domain wall relative to the magnetisation within the pinning site. This proved to affect both the type and strength of interaction observed. Micromagnetic simulations were also carried out to aid interpretation of some of the results and to provide a useful comparison to the experimental data. In this chapter, the key outcomes are discussed and some avenues to explore in the future are also described.

## 7.2 Conclusions

The work in this thesis has demonstrated that the form of domain walls in permalloy nanowires can easily be controlled using various techniques. A nucleation pad is a particularly useful tool for the creation of domain walls and, depending on its geometry, can also be used to control the domain wall chirality. If a uniaxial field is available, an elliptical injection pad is the most effective method of injecting domain walls with a predetermined chirality, as explored in chapter 6. However, a significant field of around

40 Oe for a 500 nm wide wire was required to inject a wall with this method; the injection field increased with decreasing wire width. A significant injection field may be undesirable in some cases as it could cause the injected domain wall to travel large distances through the wire. Nucleation pads with straight edges, such as rectangles, are not suitable for highly reproducible domain wall injection due to the multiple remanent states that can form.

If the field direction is variable, a better option for nucleating domain walls is the use of a diamond shaped nucleation pad. The frequency with which a given domain wall chirality is nucleated is increased by varying the orientation of the nucleation field with respect to the short axis of the wire. Using this geometry, a degree of control over the chirality of the nucleated domain wall is achieved and separate fields are used to nucleate and propagate the domain wall, as demonstrated in chapter 4. This may be useful for devices where domain walls are to be moved short distances with small magnetic fields.

Artificial pinning sites proved to be extremely effective tools for interrupting the propagation of a domain wall along a nanowire. The specific shape of the notch is not particularly important as all geometries were found to interrupt the progress of a domain wall efficiently. It was observed that either a potential well or a potential barrier was presented to an incoming wall. If the potential disruption is such that a barrier is presented to a domain wall, the strength of the pinning is increased by increasing the height of the anti-notch. The pinning strength was unaltered by increasing the anti-notch height where a potential well was presented. In the majority of cases, the domain wall structure was largely preserved at each pinning site. In general, if the height of the trap is kept to a minimum and the width of the trap is comparable to the wire width, the domain wall structure is preserved.

A transverse arm patterned along one side of a wire provides the capability of filtering out unwanted domain wall chiralities and is recommended for experiments or devices where knowledge of the chirality is important, as presented in chapter 5. One domain wall chirality is not pinned by this trap and is effectively filtered out whereas a field around 25 Oe is required to depin the opposite chirality from the same trap. Furthermore this geometry either permits or blocks the motion of a domain wall with a given chirality by switching the magnetisation within the trap and can be used as a domain wall gate. This is highly advantageous for device applications such as domain wall logic or for experiments on the properties of a single domain wall, such as domain wall resistance. However, the simultaneous control of multiple gates in close proximity is more complicated as a field applied to either open or close one gate will affect a number of gates. If knowledge of the domain wall chirality is not important, then a small notch or anti-notch provides a useful tool for trapping domain walls at specific locations with a relatively small depinning field compared with that needed for a geometry that filters chirality.

## 7.3 Future Outlook

A key outcome from this work is that domain walls can be propagated towards and stopped by an artificial pinning site. It would therefore be instructive to test whether a depinned domain wall may be subsequently pinned at additional notches or anti-notches along the wire. For racetrack memory to be successful, it is essential to be able to reliably move a sequence of 10-100 domain walls from one pinning site to another. The minimum achievable distance between adjacent pinning sites could also be explored, as this determines the bit length. For magnetic memory devices such as racetrack memory, sequences of domain walls must be moved with spin-polarised electrical currents, as magnetic fields eventually annihilate a series of domain walls. As demonstrated in chapter 6, injecting multiple domain walls into a nanowire using a magnetic field for subsequent current driven motion is not straightforward, as the domain walls eventually annihilate. It would be simpler to use a geometry where a series of domain walls can be generated easily and the effect of an electrical current passed through the wire can be investigated. The problem of injecting domain walls using an electrical current can be tackled later. One geometry where a series of domain walls can be generated using a uniaxial field is a zigzag wire [4]. The wire geometry and nucleation of domain walls is illustrated in figure 7.1. The optimum angle between adjacent straight wire sections may be explored to obtain a geometry where domain walls can easily be propagated along the wire yet also nucleated under a hard axis

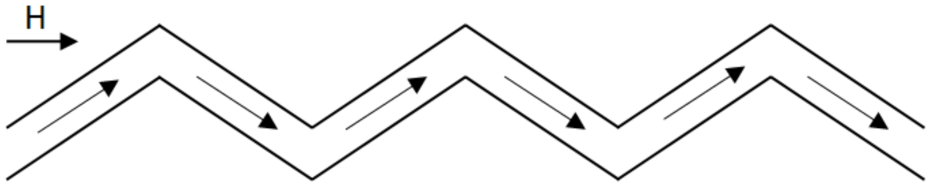

(a) Zigzag wire in initial state

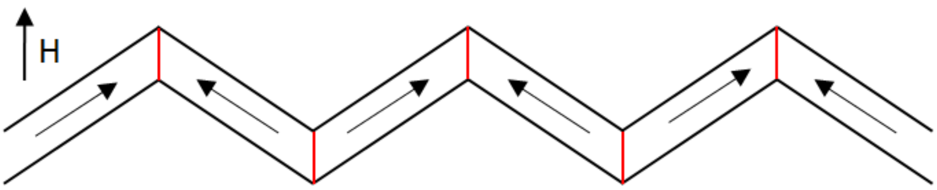

(b) Zigzag wire after the application of a nucleation field

Figure 7.1: Schematic illustration of a wire geometry suitable for the nucleation of multiple domain walls using a magnetic field. (a) The initial configuration of the wire, (b) after the application of a nucleation field along the direction shown. The red lines indicate the positions of the domain walls.

magnetic field.

Current induced domain wall motion has previously been demonstrated using a customised TEM rod for use in the Philips CM20 at Glasgow University [5]. This type of experiment is particulary challenging however, as the large current density required causes significant Joule heating. Moreover, the SiN substrate is thermally insulating and therefore does not provide an efficient sink for the heat. This is problematic as the wires tend to heat significantly during experiments and cause complex domain structures to form. In extreme cases the material may heat such that the ferromagnetic order is completely destroyed. It is possible to deposit a thin layer of metal on the backside of the membrane to act as a heat sink however this also reduces the magnetic contrast and is not a particularly effective solution. A better solution would be to use a more thermally conducting material as a substrate, such as SiC. More research needs to be carried out to determine the most suitable substrate material for such experiments, as the fabrication of TEM membranes is non-trivial.

Physical defects are clearly important in magnetic nanowires as they tend to disturb the progress of a propagating domain wall thus reducing its velocity. The wires in chapter 6 clearly had serious edge defects therefore other fabrication methods could be explored to improve the quality of the wires. One straightforward change to reduce the metal flagging at the edges of the wires would be to use a different resist to replace the bottom layer of resist. One example is LOR (Lift-Off Resist) as it is insensitive to electrons. This layer is wet-etched following processing of the top layer of PMMA. The development of LOR occurs isotropically with time thus a controllable undercut is achieved. Improving the resist profile would form the first step in improving the quality of the wires.

Other avenues to explore include the scalability of the behaviour observed here. The conventional means of developing cheaper and faster devices relies on reducing the size of individual memory elements or data storage bits. In this case cheaper and faster devices will be developed by a greater domain wall density in addition to smaller wire dimensions, which may introduce issues with the magnetic field or current density required to depin a domain wall from a notch. If the wire width and thickness are scaled together, the shape anisotropy remains constant thus the field required to overcome pinning from random defects and edge roughness also remains unchanged. If electrical currents are involved, one method of reducing the critical current density required for current induced domain wall motion is by resonant amplification [3]. The trajectory of a domain wall during and after current excitation depends strongly on the duration of the current pulse and if the pulse duration is matched to a half integer of the domain wall precession period then it is provided with greater energy than if the pulse duration is an integer value of the precession period. Ultimately, the interplay between the thermodynamic stability and the required depinning field or current density will determine the limit in the miniaturisation of magnetic nanowires for device applications.

# Bibliography

[1] D. A. Allwood, G. Xiong, C. C. Falkner, D. Atkinson, D. Petit and R. P. Cowburn, Science **309** 1688 (2005).

[2] D. Atkinson, D. S. Eastwood and L. K. Bogart, Appl. Phys. Lett. **92** 022510 (2008).

[3] S. S. P. Parkin, M. Hayashi and L. Thomas, Science **320** 190 (2008).

[4] E.-S. Wilhelm, D. McGrouther, L. Heyne, A. Bisig and M. Kläui, Appl. Phys. Lett. **95** 252501 (2009).

[5] D. McGrouther, private communication (2010).